246850-1-F

Final Report

PRISM SENSOR MODELING

M.T. Eismann, J.R. Fienup, A.M. Tai, R.L. Sullivan, and D.A. Carrara

Environmental Research Institute of Michigan
P.O. Box 134001
Ann Arbor, MI 48113-4001

DTIC
ELECTE
AUG 04 1995
S D
B

MARCH 1995

DISTRIBUTION STATEMENT A
Approved for public release;
Distribution Unlimited

Sponsored by:

ARPA/ASTO
3701 North Fairfax Drive
Arlington, VA 22203-2724

Wright Laboratory/AARI-2
Wright-Patterson AFB, OH 45433-6543

Contract No.: DLA900-88-D-0392
Delivery Order: 39

19950803 021

ERIM P.O. Box 134001
Ann Arbor, MI 48113-4001

DTIC QUALITY INSPECTED 5

ERIM-320

REPORT DOCUMENTATION PAGE

Form Approved
OMB No. 0704-0188

Public reporting burden for the collection of information is estimated to average 1 hour per response, including the time for reviewing instructions, searching existing data sources, gathering and maintaining the data needed, and completing and reviewing the collection of information. Send comments regarding this burden estimate or any other aspect of this collection of information, including suggestions for reducing this burden, to Washington Headquarters Services, Directorate for Information Operations and Reports, 1215 Jefferson Davis Highway, Suite 1204, Arlington, VA 22202-4302, and to the Office of Management and Budget, Paperwork Reduction Project (0704-0188), Washington, DC 20503.

1. AGENCY USE ONLY (*Leave Blank*)

2. REPORT DATE
March 1995

3. REPORT TYPE AND DATES COVERED
Final 2/93 - 3/95

4. TITLE AND SUBTITLE
PRISM Sensor Modeling

5. FUNDING NUMBERS
DLA900-88-0392
Delivery Order 39

6. AUTHOR(S)
M.T. Eismann, J.R. Fienup, A.M. Tai, R.L. Sullivan, D.A. Carrara

7. PERFORMING ORGANIZATION NAME(S) AND ADDRESS(ES)
Environmental Research Institute of Michigan
P.O. Box 134001
Ann Arbor, MI 48113-4001

8. PERFORMING ORGANIZATION REPORT NUMBER
ERIM 246850-1-F

9. SPONSORING/MONITORING AGENCY NAME(S) AND ADDRESS(ES)
ARPA
3701 North Fairfax Dr.
Arlington, VA 22203-2724

Avionics Directorate
Wright Laboratory
Air Force Materiel Command
Wright-Patterson AFB, OH45433-7409

10. SPONSORING/MONITORING AGENCY REPORT NUMBER

11. SUPPLEMENTARY NOTES

12a. DISTRIBUTION/AVAILABILITY STATEMENT
Unlimited

12b. DISTRIBUTION CODE

13. ABSTRACT (*Maximum 200 words*)

The Passive Range-angle-angle Imaging with Spectral Measurements (PRISM) sensor is a novel three-dimensional imaging modality conceived by ERIM researchers. The PRISM sensor uses thermal (passive) radiation to form a three-dimensional (range-angle-angle) image. The passive nature of this sensor makes it attractive for imaging applications for which stealth is important. Three-dimensional imaging provides a significant increase in information for detection, classification, and general interpretation over the two-dimensional counterpart.

The goal of the effort described in this report was to develop, exercise, and evaluate detailed sensor and target signature models. Such models are expected to serve several purposes. First, they serve as an important tool for designing PRISM sensors based on a set of top-level performance requirements. Second, they provide a capability for synthetically generating realistic 3-D target signatures, which yields insight into the unique nature of PRISM imagery. Thirdly, they provide a platform for generating PRISM test data for evaluating and processing algorithms, such as phase error correction and automatic target detection and/or recognition algorithms.

14. SUBJECT TERMS
Infrared, 3-D Sensor, Performance Modeling

15. NUMBER OF PAGES
206

16. PRICE CODE

17. SECURITY CLASSIFICATION OF REPORT
Unclassified

18. SECURITY CLASSIFICATION OF THIS PAGE
Unclassified

19. SECURITY CLASSIFICATION OF ABSTRACT
Unclassified

20. LIMITATION OF ABSTRACT
Unlimited

Intentionally Left Blank

PREFACE

This report documents the results of a study called "PRISM Sensor Modeling" performed by the Optical & Infrared Science Laboratory of the Environmental Research Institute of Michigan, Ann Arbor, Michigan, for the Advanced Research Projects Agency (ARPA) and the Air Force Wright Laboratory (WL), during the period February 1993 through March 1995. This study was performed under Delivery Order 37 within the Infrared Information Analysis Center (IRIA) program, contract number DLA900-88-D-0392, for which the Defense Electronic Supply Center (DESC), Dayton, Ohio, serves as the contracting agency. The ARPA program manager was Paul White and the Wright Laboratory project manager was Patrick Woodworth. The ERIM program manager was James P. Mills, and the principal investigator was Michael T. Eismann. The authors of this report are Michael T. Eismann, James R. Fienup, Anthony M. Tai, Richard L. Sullivan, and David A. Carrara.

Accession For
NTIS GRA&I ☑
DTIC TAB ☐
Unannounced ☐
Justification
By
Distribution/
Availability Codes
Avail and/or
Dist Special
A-1

Intentionally Left Blank

CONTENTS

PREFACE iii

FIGURES viii

TABLES xi

1.0 INTRODUCTION 1
1.2 REFERENCES 2

2.0 SENSOR SIGNAL MODEL 3
2.1 THEORETICAL FOUNDATIONS 3
2.2 RADIOMETRIC SIGNAL MODEL 11
2.3 SINGLE SURFACE MODEL 13
2.4 HEIGHT ESTIMATION 16
2.5 BIAS SIGNAL SUBTRACTION 17
2.6 HEIGHT AMBIGUITY 18
2.6.1 Discrete Phase Modulation 18
2.6.2 Linear Phase Modulation 19
2.6.3 Wideband FM 19
2.7 DATA FORMATTING 20
2.8 PIXEL WALK COMPENSATION 21
2.9 REFERENCES 21

3.0 SENSOR PERFORMANCE MODEL 23
3.1 MODEL INPUTS 24
3.1.1 Target Parameters 24
3.1.2 Viewing Geometry Parameters 27
3.1.3 Sensor Parameters 28
3.1.4 Optical Throughput Parameters 29
3.1.5 Modulation Error Parameters 30
3.1.6 Phase Error Parameters 31
3.1.7 Detector Parameters 32
3.2 INTERMEDIATE PARAMETERS 32
3.3 SCENE RADIANCE 33
3.4 OPTICAL THROUGHPUT 33
3.5 SCENE SPATIAL CONTRAST 34
3.5.1 Edge Target 34
3.5.2 Bar Target 35
3.5.3 Surface Target 35
3.6 RADIOMETRIC BIAS 36
3.7 MODULATION DEPTH 36
3.7.1 Target Contrast 36
3.7.2 Throughput Ratio 36
3.7.3 Random Wavefront Errors 37
3.7.4 Low Order Wavefront Errors 37
3.7.5 Near Field Wavefront Curvature 38
3.7.6 Interferometer Achromaticity 38
3.7.7 Mean Input Grating Misalignment 39
3.7.8 Differential Input Grating Misalignment 39
3.7.9 Grating Piston Error 40

CONTENTS (Continued)

3.7.10 Grating Frequency Mismatch 41
3.7.11 Lateral Grating Vibration 41
3.7.12 Within Frame LOS Jitter 41
3.7.13 Frame Integration 42
3.7.14 Aero-Optical Turbulence 42
3.8 NOISE 43
3.9 INTERFEROMETRIC SIGNAL AMPLITUDE 44
3.10 INTERFEROMETRIC SIGNAL PHASE 44
3.11 PHASE ERRORS 45
3.11.1 Wideband Phase Errors 45
3.11..2 Low Order Phase Errors 46
3.12 2-D IMAGE SENSITIVITY 47
3.13 3-D IMAGE SENSITIVITY 48
3.13.1 Phase History Sensitivity 48
3.13.2 Signal Loss Factors 48
3.13.3 Image Sensitivity 50
3.14 SPATIAL RESOLUTION 50
3.14.1 3-D Image Resolution 50
3.14.2 Spatial Sampling Distance 51
3.14.3 Height Estimation Accuracy 51
3.15 SPATIAL COVERAGE 51
3.16 REFERENCES 52

4.0 GROUND SENSOR DESIGN 53
4.1 DESIGN GOALS AND CONSTRAINTS 53
4.2 PARAMETRIC SENSOR DESIGN 54
4.2.1 Wavelength Band Selection 55
4.2.2 Interferometer Design 55
4.2.3 Basic Design Parameters 57
4.3 SENSOR PERFORMANCE 58
4.4 REFERENCES 58

5.0 SIMULATION-BASED SENSOR MODEL 69
5.1 MODELING APPROACH 69
5.2 TEST TARGET MODELING (MKSEQ) 71
5.3 SIRIM TARGET MODELING 74
5.3.1 SIRIM Overview 74
5.3.2 Modifications to Model 76
5.4 BACKGROUND MODELING 78
5.5 SENSOR PHASE HISTORY MODELING (SEQTOPH) 80
5.6 3-D IMAGE FORMATION (PHT03D) 84
5.7 IMAGE ANALYSIS AND DISPLAY 87
5.8 REFERENCES 88

6.0 COLLECTED IMAGERY/MODEL COMPARISON 89
6.1 TEST TARGET COMPARISON 89
6.2 COMPLEX TARGET SIGNATURE COMPARISON 98
6.2.1 Daytime Imaging Case 98
6.2.2 Nighttime Imaging Case 106
6.3 COMPARISON SUMMARY 116

CONTENTS (Continued)

7.0 AIRBORNE DEMO SENSOR DESIGN 125
7.1 REFERENCES 129

8.0 RANGE ESTIMATION ALGORITHM DEVELOPMENT 131
8.1 SENSOR OUTPUT SIGNAL 131
8.2 IMAGE FORMATION 135
8.3 IMPULSE RESPONSE CHARACTERISTICS 142
8.4 ESTIMATING RANGE OF EXTENDED SURFACES 147

9.0 PRISM FOCUSING 153
9.1 SIGNAL MODEL 153
9.2 PHASE-ERROR CORRECTION ALGORITHMS 154
9.3 EXTENSION OF SHEAR AVERAGING ALGORITHM 155
9.4 BIAS TERM 158
9.5 SIMULATION RESULTS 158
9.6 REFERENCES 172

10.0 COMPARISON OF PRISM VS. MOTION STEREO 173
10.1 DESCRIPTION OF THE MOTION STEREO ALGORITHM 173
10.2 ANALYTICAL COMPARISON 176
10.2.1 Motion Stereo Depth Estimation Precision 176
10.2.2 PRISM Depth Estimation Precision 178
10.2.3 Comparison of Depth Estimation Precision 179
10.2.4 Multiple Depth Scenario 182
10.3 EMPIRICAL COMPARISON 183
10.3.1 Motion Stereo Processing 183
10.3.2 PRISM Processing 192
10.3.3 Results and Comparisons 192
10.3.4 Conclusion 193
10.4 REFERENCES 194

FIGURES

2-1. Imaging Geometry Assumed by van Cittert-Zernike Theorem 4

2-2 Imaging Geometry for 3-D Generalization of van Cittert-Zernike Theorem 6

2-3 Pictorial Drawing of PRISM Sensor Concept 8

2-4 Airborne Imaging Geometry 9

2-5 Illustration of Bias and Signal Scene Radiance Terms 15

3-1 Performance Model Block Diagram 25

4-1 Grating Interferometer Designs 56

5-1 PRISM Sensor Modeling Components 70

5-2 Definition of R, θ Coordinates 73

5-3 SIRIM Functional Flow 75

5-4 SIRIM Viewing Geometry 77

6-1 Range Response Functions for LTEST1 91

6-2 Range Response Functions for LTEST2 92

6-3 Range Response Functions for LTEST3 93

6-4 Range Response Functions for KTEST1 94

6-5 Range Response Functions for KTEST2 95

6-6 Range Response Functions for KTEST3 96

6-7 Range Response Functions for KTEST4 97

6-8 Simulated Viewing Geometry 101

6-9 M35 Truck Model Perspectives 103

6-10 High Resolution Frame Sequence for Daytime Image Simulation 107

6-11 Orthogonal 3-D Image Projections for Daytime Image Simulation 108

6-12 3-D Imaging Results for Daytime Image Simulation 109

6-13 Line-of-Sight Photograph of Imaged Area Corresponding to Daytime and Nighttime Simulations 111

6-14 Orthogonal 3-D Image Projections for Daytime Field Collection 112

FIGURES (Continued)

6-15 3-D Imaging Results for Daytime Field Collection 113

6-16 High Resolution Frame Sequence for Nighttime Image Simulation 115

6-17 Orthogonal 3-D Image Projections for Nighttime Image Simulation 117

6-18 3-D Imaging Results for Nighttime Image Simulation 119

6-19 Orthogonal 3-D Image Projections for Nighttime Field Collection 121

6-20 3-D Imaging Results for Nighttime Field Collection 123

8-1 Imaging Geometry of PRISM Sensor 132

8-2 Shape of Detector IFOV and Sampling Frequency of Virtual Fringes 134

8-3 Imaging with a Single Large Detector Pixel 136

8-4 Aperture Fill and Impulse Response with a Single Detector and a Single Wavelength 137

8-5 Jumping of Point Image from One Detector Element to Another with Change in Viewing Angle 138

8-6 Outputs of Three Adjacent Detector Elements Due to a Single Point Radiator at Different Target Locations 140

8-7 Back-projecting Complex Virtual Fringes (Linear Phases) Along the IFOVs of Detector Elements 141

8-8 Simulated Image of a Point Radiator 5m Above Reference Plane 143

8-9 Simulated Images of Point Radiators at Different Locations 5m Above Reference Plane 144

8-10 Image of Point Radiator Located Near the Reference Plane 145

8-11 Simulated Images of Point Radiators at Different Locations 0.5m above Reference Plane 146

8-12 Using Sampling Period 1/4 of the Pixel Width to Limit Signal Loss to Less Than 12.5% 148

8-13 Speckle Effect when Imaging Extended Surface with Random Texture 149

8-14 Surface Estimation by Grouping Four Sample Lines Together and Determining the Location of the Peak 151

8-15 Speckle Effect in the Range Direction when Imaging Range Dispersed Targets 152

FIGURES (Continued)

9-1 Example SIRIM Image of a Truck (the 10th of 30 Images) Used in the Signal History Simulations 159

9-2 The 2-D X, Y, and Z Projections of the 3-D PRISM Image Used in the Simulations 160

9-3 The Result of Applying Shear Averaging to a PRISM Signal History with a Peak Quadratic Phase Error of 1/4 Wave 162

9-4 Applied Phase Error vs. Shear Averaging Correction for 1/4 Wave Peak Quadratic Error 163

9-5 The Result of Applying Shear Averaging to a PRISM Signal History with a Peak Quadratic Phase Error of 1/2 Wave 164

9-6 Applied Phase Error vs. Shear Averaging Correction for 1/2 Wave Peak Quadratic Error 165

9-7 The Result of Applying Shear Averaging to a PRISM Signal History with a Peak Quadratic Phase Error of One Wave 166

9-8 Applied Phase Error vs. Shear Averaging Correction for 1 Wave Peak Quadratic Error 167

9-9 The Result of Applying Shear Averaging to a PRISM Signal History with a Peak Linear Phase Error of 1/4 Wave 168

9-10 Applied Phase Error vs. Shear Averaging Correction for 1/4 Wave Peak Linear Error 169

9-11 The Result of Applying Shear Averaging without Linear Trend Removal to a PRISM Signal History with a Peak Quadratic Phase Error of 1/4 Wave 170

9-12 Applied Phase Error vs. Shear Averaging Correction without Linear Trend Removal for 1/4 Wave Peak Quadratic Error 171

10-1 Motion Stereo Data Collection Geometry 174

10-2 Factors in Height Precision in the Spatial Frequency Domain 181

10-3 Comparison of PRISM and Motion Stereo Imagery for TEST2 Data Set 185

10-4 Comparison of PRISM and Motion Stereo Imagery for SCENE2 Data Set 187

10-5 Comparison of PRISM and Motion Stereo Imagery for RUN25 Data Set 189

TABLES

4-1 Top Level Sensor Design Specifications 54

4-2 Ground Demo Sensor Design Parameters 58

4-3 Ground Demo Sensor Performance Estimates 59

4-4 Model Output for Ground Demo Design: Mode #2, Center of Field 60

4-5 Model Output for Ground Demo Design: Mode #2, Edge of Field 64

6-1 Modeled Test Target Conditions 90

6-2 Image Performance Metric Definitions 99

6-3 Measured Image Performance Metrics 100

6-4 Simulation Weather History 105

7-1 Baseline Airborne Imaging Geometry 126

7-2 Parametric MWIR Airborne Design 127

7-3 Parametric LWIR Airborne Design 128

9-1 Correction Algorithms for Spatially Invariant Phase Errors 154

10-1 Collection and Processing Parameters 191

Intentionally Left Blank

1.0 INTRODUCTION

The Passive Range-angle-angle Imaging with Spectral Measurements (PRISM) sensor is a novel three-dimensional imaging modality conceived by ERIM researchers. The PRISM sensor uses thermal (passive) radiation to form a three-dimensional (range-angle-angle) image. The passive nature of this sensor makes it attractive for imaging applications for which stealth is important. Three-dimensional imaging provides a significant increase in information for detection, classification, and general interpretation over the two-dimensional counterpart. In addition, a spectral signature can be measured leading to a four-dimensional dataset, although this report only considers the monochromatic embodiment of the sensor. Reports from previous programs document the theoretical development and various laboratory demonstrations of the PRISM concept and sensor [1.1-1.4].

The goal of the effort described in this report was to develop, exercise, and evaluate detailed sensor and target signature models. Such models are expected to serve several purposes. First, they serve as an important tool for designing PRISM sensors based on a set of top-level performance requirements. Second, they provide a capability for synthetically generating realistic 3-D target signatures, which yields insight into the unique nature of PRISM imagery. Thirdly, they provide a platform for generating PRISM test data for evaluating and processing algorithms, such as phase error correction and automatic target detection and/or recognition algorithms.

This report is laid out in the following manner. Section 2 provides a mathematical description of the sensor signal model, along with some discussion of height estimation and other important sensor issues. Section 3 overviews a metric-based sensor performance model that was developed primarily for use as a sensor design tool. Based on this model, the parametric design of the ground demo sensor is detailed in Section 4. Synthetic target signatures can be generated utilizing a model based on the 3-D thermal target model. This procedure is described in Section 5, and a comparison of synthetic and measured target signatures is given in Section 6. Based on insight gained from this modeling effort as well as the ground demonstration effort [1.5], Section 7 overviews parametric designs of MWIR and LWIR airborne demonstration sensors, the next step along the PRISM sensor development path. Sections 8 and 9 focus on algorithms investigated during this effort to produce enhanced imagery by providing better range estimation and correction of sensor phase errors, respectively. Finally, Section 10 overviews the results of an assessment of passive motion stereo imaging as compared with PRISM.

1.2 REFERENCES

[1.1] *Passive Range-Angle Interferometric Imaging*, ERIM Report No. 179200-110-F, AD No. C 049116L, November 1991.

[1.2] *Interferometric Sensor Study*, ERIM IR&D Report, ERIM Report No. 617116-1-X, January 1992.

[1.3] *PRISM Sensor Technology Development for Passive 2-D and 3-D Imaging*, ERIM Final Report No. 219600-2-F, Air Force Report No. WL-TR-92-1041, August 1992.

[1.4] *PRISM System Requirement*, ERIM Final Report No. 240400-15-F, December 1992.

[1.5] *PRISM Ground Experiment*, ERIM Final Report No. 246840-1-F to Air Force WL/AARI on Contract DLA900-88-D-0392, Delivery Order 38, March 1995.

2.0 SENSOR SIGNAL MODEL

The theoretical basis of the PRISM sensor concept is the van Cittert-Zernike theorem. In this section, this theoretical foundation is briefly overviewed and the sensor signal model is derived, both in the form of a more generalized radiometric signal model, and a more simplified model based on a single surface approximation. Also, several important issues related to this signal model are discussed.

2.1 THEORETICAL FOUNDATIONS

The theoretical foundations of passive interferometric imaging have been described elsewhere [2.1, 2.2, 2.3], but are repeated here for continuity. The basis of the sensor concept is the van Cittert-Zernike theorem, which states that the mutual intensity between two points of a wave field is related to the Fourier Transform of the source intensity distribution provided that the measurements are in the far-field of the source [2.1]. With reference to the geometry of Figure 2-1:

$$\begin{aligned} J(x_1',y_1';x_2',y_2') &= \langle u(x_1',y_1',t)u^*(x_2',y_2',t)\rangle \\ &= \frac{e^{-i\psi}}{(\lambda R)^2}\iint I(x,y)e^{-i\frac{2\pi}{R\lambda}(\Delta x'x+\Delta y'y)}dxdy \end{aligned} \tag{2-1}$$

where (x_1',y_1') and (x_2',y_2') are the measurement points, $J(x_1',y_1';x_2',y_2')$ is the mutual intensity function of the propagated wavefield $u(x,y,t)$ between the measurement points, $I(x,y)$ is the source intensity distribution, R is the distance between source and measurement planes, λ is the optical wavelength, $\Delta x' = x_2' - x_1'$, $\Delta y' = y_2' - y_1'$, and

$$\psi = \frac{\pi}{\lambda R}\left[\left(x_2'^2 + y_2'^2\right) - \left(x_1'^2 + y_1'^2\right)\right] \tag{2-2}$$

Under the assumption that the range extent (Δz) of the source is small relative to the distance between the source and measurement planes, this theorem can be generalized to a three dimensional source distribution $I(x,y,z)$ such that

$$J(x_1',y_1';x_2',y_2') = \frac{e^{-i\psi}}{(\lambda R)^2}\iint \int_{\Delta z} I(x,y,z)e^{-i\frac{2\pi}{R\lambda}(\Delta x'x+\Delta y'y)}dxdydz \tag{2-3}$$

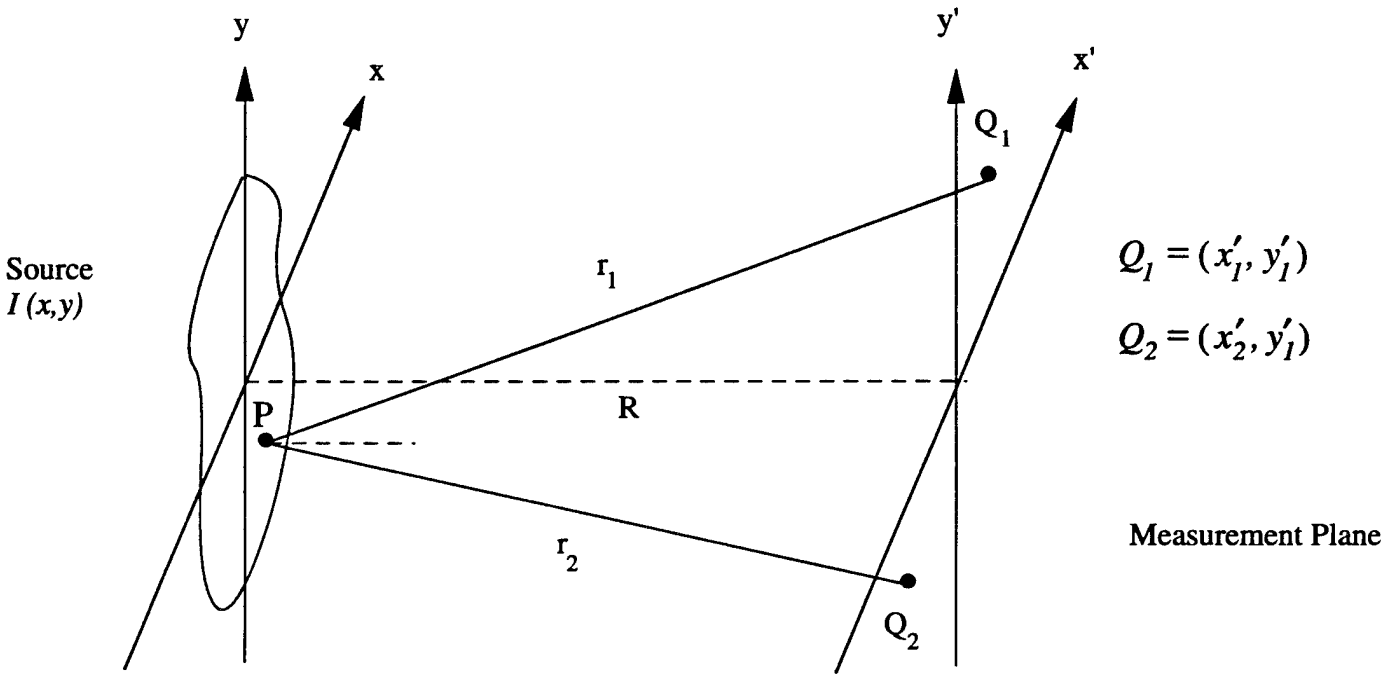

Figure 2-1. Imaging geometry assumed by van Cittert-Zernike Theorem.

In other words, the mutual intensity function is related by a Fourier Transform to the line-of-sight projection of the 3-D source intensity distribution. The underlying assumption to this equation is that $I(x,y,z)$ contains only source contributions that are in the line-of-sight of both measurement points (i.e., "shell" model of the source).

This generalization can be taken one step further to incorporate measurement points not constrained to a plane [Figure 2-2]. If $\bar{s}$ is the vector between measurement points and $\bar{r}$ is a vector in the source space, it can be shown [2.2] that

$$J(\bar{f}) = \frac{e^{-i\psi}}{(\lambda R)^2} \iiint I(\bar{r}) e^{i2\pi \bar{f} \bullet \bar{r}} d\bar{r} \tag{2-4}$$

where

$$\bar{r} = x\hat{x} + y\hat{y} + z\hat{z} \tag{2-5}$$

and

$$\bar{f} = \frac{\bar{s}}{\lambda R} = \frac{\Delta x\hat{x} + \Delta y\hat{y} + \Delta z\hat{z}}{\lambda R} \tag{2-6}$$

Equation [2-4] was written to explicitly show the 3-D Fourier Transform relationship between the source intensity distribution and the mutual intensity function. The previously stated approximations still apply along with the added approximation that $I(\bar{r})$ does not change (much) with $\bar{s}$.

In theory, full 3-D information of the source can be acquired by making a series of measurements in which $\bar{f}$ is varied in all three directions by adjusting the magnitude and/or orientation of the separation vector. In this manner, a synthetic aperture is created. The spatial resolution in any dimension is related to the inverse of the corresponding width of the synthetic aperture.

At infrared wavelengths, measurement of the mutual intensity function requires the use of an interferometer. We have specifically been investigating the use of a grating interferometer, which has the important practical advantage of being achromatic. That is, the dispersion of the interferometer gratings actually compensates the wavelength dependence of the Fourier Transform

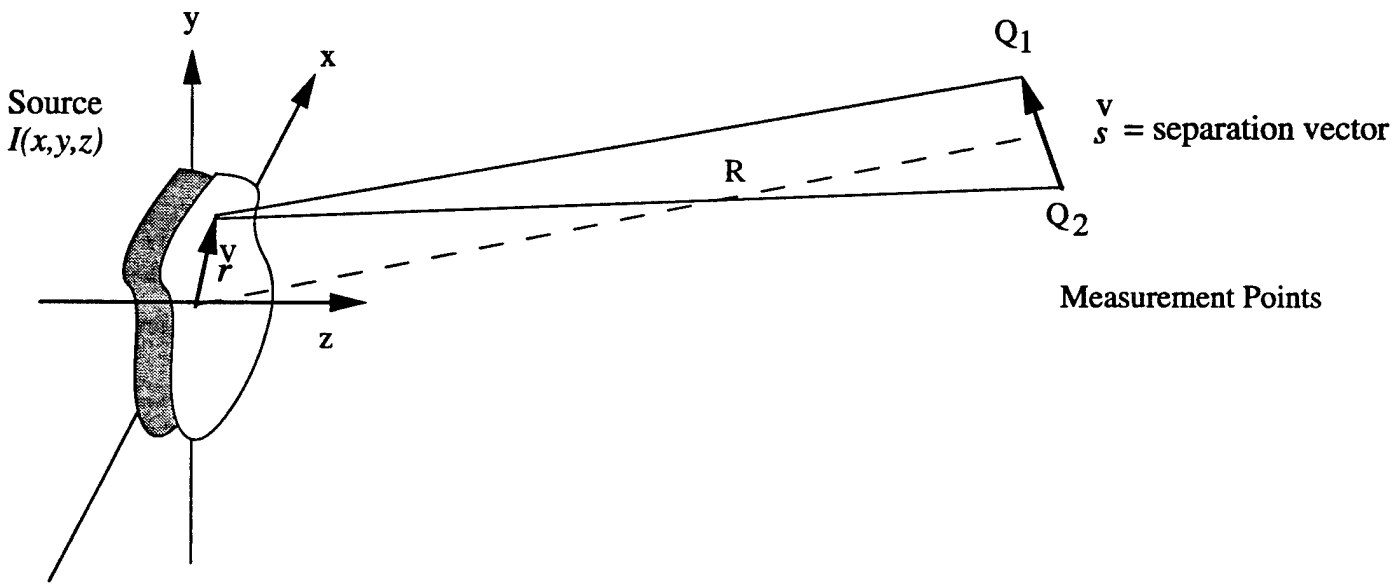

Figure 2-2: Imaging geometry for 3-D generalization of van Cittert-Zernike Theorem.

kernel [see Eq. (2-6)] such that the mutual intensity measurements can be made over sufficiently broad wavelengths to provide adequate sensitivity. This occurs because the wavefront shear upon propagation through the interferometer is given, to first order, by

$$s = 2d\lambda F \tag{2-7}$$

where F is the grating periodicity and d is the separation between gratings (longitudinally). Inserting Eq. (2-7) into Eq. (2-6), we see that the spatial frequency vector is wavelength independent, or achromatic.

While 3-D synthetic aperture imaging is theoretically achievable through this technique, in most cases it is impractical to achieve the required degrees of freedom in relative scene/object motion to generate a 3-D synthetic aperture. It is also generally unnecessary since good 2-D image information can be provided by a conventional staring array imager. We have, therefore, investigated the augmentation of such a sensor with an interferometer to add a (relative) ranging capability.

A pictorial drawing of the sensor concept is given in Figure 2-3. A conventional staring array imager is placed behind a grating interferometer and views a 3-D object in the far-field. The effect of the array is to segment the detected object radiation into spatial pixels (i.e., 2-D imaging). The interferometer imposes a modulation characteristic onto the detected intensity of each detector panel that takes the form of the biased real part of the mutual intensity function:

$$I_{ij} = K \iiint_{FOV_{ij}} I(\bar{r})\left[1 + \cos\left\{2\pi\left(\frac{2dF}{R}\right)\hat{s} \bullet \bar{r} + \phi\right\}\right] d\bar{r} \tag{2-8}$$

where I_{ij} is the detected intensity of the i, j detector, FOV_{ij} is the 3-D portion of the object viewed by the i, j detector, ϕ is an interferometer phase term, and K is a radiometric constant.

To synthesize an aperture in the range (z) dimension, we use relative sensor/object motion in the x direction. The imaging geometry is shown pictorially for an airborne scenario in Figure 2-4. Note that it is a strict requirement that the sensor line-of-sight be precisely pointed to a phase reference point in the object (arbitrarily defined to be the center of the coordinate system) during the generation of the synthetic aperture. When this condition is met, we see from Eq. (2-6) that

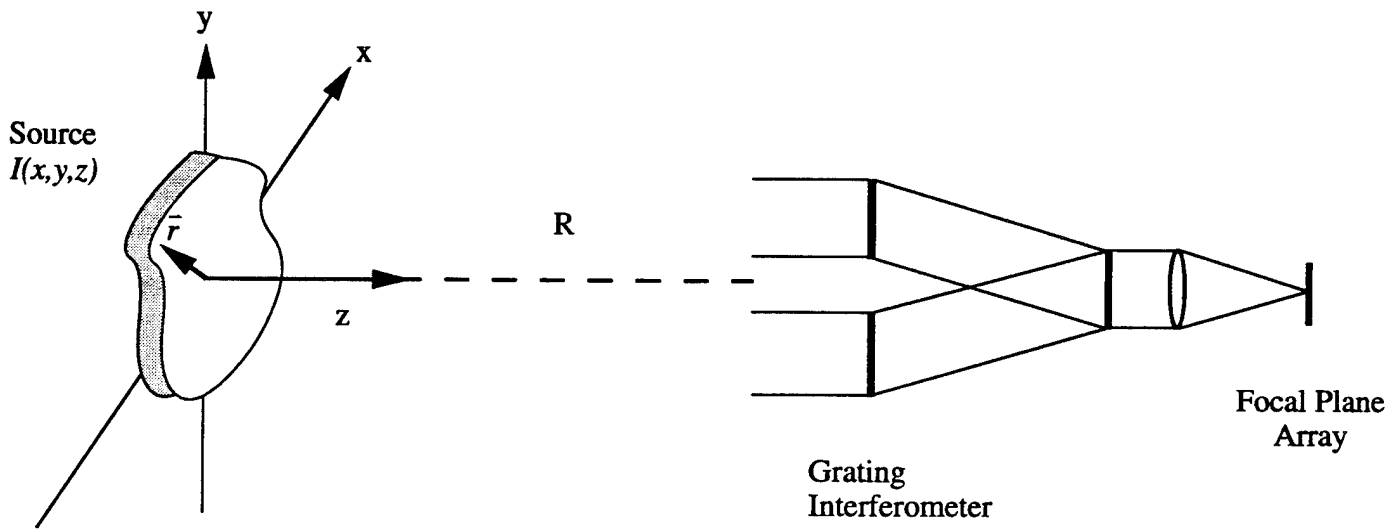

Figure 2-3: Pictorial drawing of PRISM sensor concept.

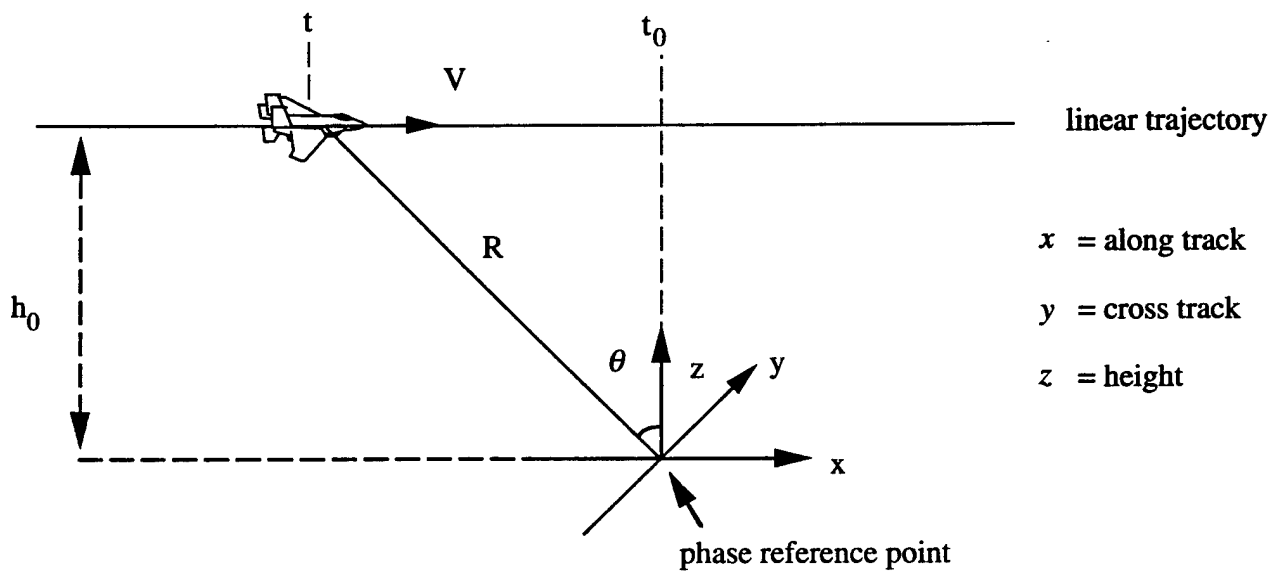

Figure 2-4: Airborne imaging geometry.

$$\bar{f} = \frac{2dF}{h_0}\left(\cos^2\theta\hat{x} + \sin\theta\,\cos\theta\hat{z}\right) \tag{2-9}$$

where

$$\theta = \tan^{-1}\left[\frac{v(t-t_0)}{h_0}\right] \tag{2-10}$$

In Eq. (2-10), v is the platform velocity, t is the time, and t_0 is the reference time when $\theta = 0$.

Under a small angle approximation, $(\cos\theta \sim 1,\ \sin\theta \sim \tan\theta)$, we can substitute Eq. (2-9) into Eq. (2-8):

$$I_{ij}(t) = K \iiint_{FOV_{ij}} \left[1 + \cos\left\{2\pi\left(\frac{2dF}{h_0}\right)\left(x + \frac{zv(t-t_0)}{h_0}\right) + \phi\right\}\right] d\bar{r} \tag{2-11}$$

This represents a detected frame sequence upon which a temporal modulation is imposed. This temporal modulation can be separated from the temporally constant component, and provides the signal component that is related to the mutual intensity function for each pixel field-of-view. In fact, by adjusting the phase term ϕ, we can truly measure the complex mutual intensity function through its quadrature (real and imaginary components).

If we examine the phase function of Eq. (2-11), we notice that it contains x- and z-dependent terms. The x-dependent term is temporally constant and results in a spatially bandpass image characteristic (i.e., sensor is sensitive only to scene content with high frequency structure in the x direction). The z-dependent term is a temporal signal whose frequency content is related to the range distribution of the pixel. By Fourier transforming the detected frame sequence along the time axis, a 3-D image is produced. The height resolution (peak-to-null width of range impulse response) is a function of the total collection time T_a for the sequence:

$$\rho_z = \frac{h_0^2}{2dFvT_a} \tag{2-12}$$

The along and cross track resolutions are defined by the staring array imaging system (detector size and optics point spread function).

2.2 RADIOMETRIC SIGNAL MODEL

Equations (2-8), (2-9) and (2-10) combine to form the basis of the sensor signal model. We note, however, that these equations do not include any sensor and target radiometric factors as well as sensor degradation such as non-unity modulation depth, phase errors, and noise. Since such factors can significantly impact sensor performance, they must be included in any signal model intended to form the basis of a sensor design tool.

We begin by introducing radiometric constants into Eq. (2-8). In order to do this, however, we first must take into account that any practical sensor will have some spectral bandwidth over which radiation is sensed. Therefore, it is possible that the variables in Eq. (2-8) are wavelength dependent. We will accommodate this fact in the model by defining a scene radiance distribution $L(\bar{r})$ which is corrected to the sensor spectral response:

$$L(\bar{r}) = \frac{1}{\eta\,\tau}\int L_\lambda(\bar{r})\,\eta(\lambda)\,\tau(\lambda)\,d\lambda \qquad (2\text{-}13)$$

where $L_\lambda(\bar{r})$ is the scene spectral radiance, $\eta(\lambda)$ is the detector quantum efficiency, $\tau(\lambda)$ is the sensor throughput, and η and τ are the corresponding means over the spectral band.

To account for the spatial limits of the three-dimensional integral of Eq. (2-8), we define a scene footprint function of the $(i,j)^{th}$ array pixel, $W_{ij}(\bar{r},t)$, where

$$\iint W_{ij}(\bar{r},t)\,d\bar{r} = 1 \qquad (2\text{-}14)$$

Note both the spatial and temporal dependence of this function, the latter to include effects due to the change in view angle during the collection time. The data collected over this time period is called the phase history (note the analogy to synthetic aperture radar).

With radiometric terms included, the phase history of the $(i,j)^{th}$ detector array pixel is given by

$$N_{ij}(t) = \frac{\pi D^2}{4}\frac{IFOV^2}{hc}\eta\,\tau\,\Delta\lambda\,T_f \iiint W_{ij}(\bar{r},t)\,L(\bar{r})\,d\bar{r}$$
$$+\frac{\pi D^2}{4}\frac{IFOV^2}{hc}\eta\,\tau\,\Delta\lambda\,T_f \iiint W_{ij}(\bar{r},t)\,L(\bar{r})\cos\left(2\pi\bar{f}\bullet\bar{r}\right)d\bar{r} \qquad (2\text{-}15)$$

where D is the effective sensor aperture diameter, $IFOV$ is the angular instantaneous pixel field-of-view, $\Delta\lambda$ is the effective sensor spectral bandwidth, Tf is the frame integration time, and $N_{ij}(t)$ is the number of photoelectrons integrated during a single frame for the $(i,j)^{th}$ pixel at time t.. Note that this equation has intentionally been separated into non-interferometric (bias) and interferometric (modulated) terms. The former is the conventional passive image. The latter is the signal from which the height information is derived.

Several sensor degradations will be added into Eq. (2-15). The first of these is additional radiance due to the atmospheric path, optics, and higher interferometer orders. This can be included as a constant radiance L_{path} added into the bias integral. The second effect is the non-unity sensor modulation depth due to limited achromaticity, sampling effects, wavefront errors, etc. Since this can be spatially dependent, it can be included by a term $m(\bar{r})$ in the interferometric integral. Temporally dependent phase terms should also be included, both in the form of intentionally induced phase shifts $\phi_i(t)$ by tuning the interferometer, as well as phase errors $\phi_e(t)$ due to pointing jitter, turbulence, etc. Finally, a noise process $n_{ij}(t)$ is included to account for all sources of sensor noise.

After including all of the terms described above, we arrive at the non-ideal radiometric signal model

$$N_{ij}(t) = \frac{\pi D^2}{4}\frac{IFOV^2}{hc}\eta\,\tau\,\Delta\lambda\,T_f \iiint W_{ij}(\bar{r},t)\left[L(\bar{r})+L_{path}\right]d\bar{r}$$
$$+\frac{\pi D^2}{4}\frac{IFOV^2}{hc}\eta\,\tau\,\Delta\lambda\,T_f \iiint m_s(\bar{r})W_{ij}(\bar{r},t)\,L(\bar{r})\cos\left[2\pi\bar{f}\bullet\bar{r}+\phi_i(t)+\phi_e(t)\right]d\bar{r} \qquad (2\text{-}16)$$
$$+n_{ij}(t)$$

which realistically describes the phase history of the $(i,j)^{th}$ detector array pixel.

2.3 SINGLE SURFACE MODEL

In many cases of interest, the imaged scene consists of approximately a single radiating surface over the spatial footprint of a detector array pixel. In these cases, the radiometric signal model can be simplified to a more tractable form for estimating sensor performance in terms of image signal-to-noise ratio, height estimation uncertainty, and detection performance.

The primary approximation is to represent $L(\bar{r})$ as

$$L(\bar{r}) = L(x,y)\ \delta(z - z_o) \tag{2-17}$$

where $\delta(z)$ is the Dirac delta function. Under this assumption

$$W_{ij}(\bar{r},t) = \tilde{h}\left[x - i\Delta x\ \cos^2\theta - z_o \sin\theta\cos\theta,\ y - j\Delta y\right]\frac{1}{\rho_x\rho_y} \tag{2-18}$$

where $\tilde{h}(x,y)$ is the normalized point spread function of the 2-D imaging system, Δx and Δy are the scene spatial sample spacings of the detector array, and $\rho_{x,y}$ is the 2-D spatial resolution such that

$$\rho_x\rho_y = \iint \tilde{h}(x,y)dxdy \tag{2-19}$$

In Eq. (2-18), we have also explicitly shown the airborne imaging geometry

$$\bar{f} \bullet \bar{r} = \frac{2dF}{h_o}\left[x\cos^2\theta + z_o \sin\theta\cos\theta\right] \tag{2-20}$$

By further ignoring any spatial dependence in modulation depth across a pixel,

$$m_s(\bar{r}) = \left[m_s(z_o)\right]_{ij} \tag{2-21}$$

the pixel phase history becomes

$$N_{ij}(t) = \frac{\pi D^2}{4}\frac{IFOV^2}{hc}\frac{\eta\,\tau\,\Delta\lambda\,T_f}{\rho_x\rho_y}\iint \tilde{h}\left[x - i\Delta x\,\cos^2\theta - z_o\sin\theta\cos\theta,\; y - j\Delta y\right]\left[L(x,y) + L_{path}\right]dxdy$$

$$+\frac{\pi D^2}{4}\frac{IFOV^2}{hc}\frac{\eta\,\tau\,\Delta\lambda\,T_f}{\rho_x\rho_y}\left[m_s(z_o)\right]_{ij}\iint \tilde{h}\left[x - i\Delta x\,\cos^2\theta - z_o\sin\theta\cos\theta,\; y - j\Delta y\right]L(x,y)$$

$$\cos\left[2\pi\left(\frac{2dF}{h_o}\right)\left(x\cos^2\theta + z_o\sin\theta\cos\theta\right) + \phi_i(t) + \phi_e(t)\right]dxdy$$

$$+\,n_{ij}(t)$$

(2-22)

To put this equation in a more manageable form, we will make a few definitions. First, we will define a bias and signal scene radiance (by "signal" we refer to interferometric modulation). The bias scene radiance is defined as the mean scene radiance over the sensor spatial footprint:

$$\left(L_B\right)_{ij} = \frac{1}{\rho_x\rho_y}\iint \tilde{h}\left[x - i\Delta x\,\cos^2\theta - z_o\sin\theta\cos\theta,\; y - j\Delta y\right]L(x,y)\,dxdy \quad (2\text{-}23)$$

Analogously, the signal scene radiance is defined as the mean scene radiance in the sensor spatial passband:

$$\left(L_S\right)_{ij} = \frac{1}{\rho_x\rho_y}\left|\iint \tilde{h}\left[x - i\Delta x\,\cos^2\theta - z_o\sin\theta\cos\theta,\; y - j\Delta y\right]L(x,y)\,e^{i2\pi\left(\frac{2dF}{h_o}\right)x\cos^2\theta}\,dxdy\right| \quad (2\text{-}24)$$

Figure 2-5 pictorially illustrates the meaning of these radiance terms with respect to the spatial spectrum of the portion of the scene viewed by the pixel [i.e., Fourier transform of $L(x,y)$]. We note that both $\left(L_B\right)_{ij}$ and $\left(L_S\right)_{ij}$ can vary in time, although this temporal dependence is not explicitly shown.

Three more definitions will be made. First, we will define the signal bias level as

$$N_{ij}^{B}(t) = \frac{\pi D^2}{4}\frac{IFOV^2}{hc}\eta\,\tau\,\Delta\lambda\,T_f\left[\left(L_B\right)_{ij} + L_{path}\right] \quad (2\text{-}25)$$

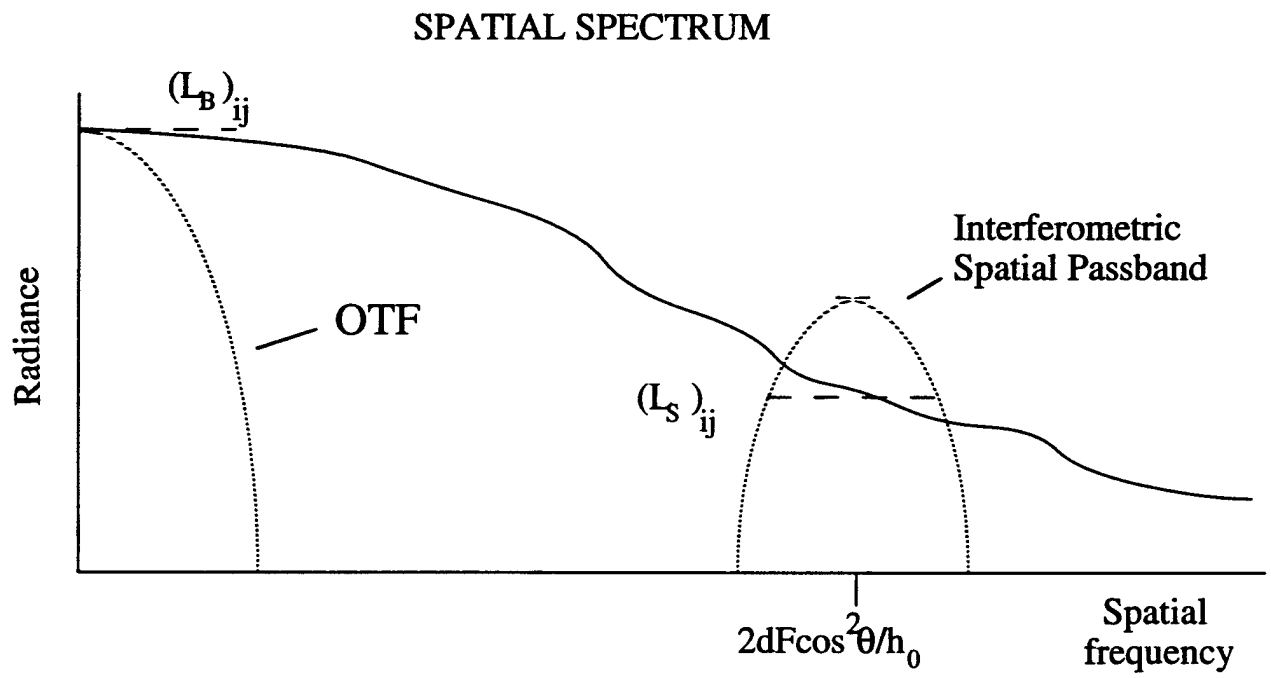

Figure 2-5: Illustration of bias and signal scene radiance terms

Next, we define the interferometric signal modulation depth as

$$m_{ij}(z_o,t) = \left[m_s(z_o)\right]_{ij} \frac{(L_S)_{ij}}{(L_B)_{ij} + L_{path}} \tag{2-26}$$

Finally, we define the interferometric signal phase as

$$\phi_{ij}(z_o,t) = 2\pi\left(\frac{2dF}{h_o}\right)\left(\mathrm{x}_0 \cos^2\theta + z_o \sin\theta\cos\theta\right) \tag{2-27}$$

With these defined parameters, the single surface pixel phase history model becomes

$$N_{ij}(t) = N_{ij}^B(t)\left[1 + m_{ij}(z_o,t)\cos\left\{\phi_{ij}(z_o,t) + \phi_i(t) + \phi_e(t)\phi'_{ij}\right\}\right] + n_{ij}(t) \tag{2-28}$$

where ϕ'_{ij} has been inserted to represent the generally unknown, scene dependent offset phase, which is given by the phase of the signal scene radiance integral [Eq.(2-24)].

2.4 HEIGHT ESTIMATION

Significant insight into how height information is established by the PRISM sensor can be obtained by the single surface model provided in Eq. (2-28). Ideally, the signal bias and modulation depth will be constant and the viewing angle θ will be small. Under these approximations, the pixel phase history simplifies to a sinusoidal signal in noise:

$$N_{ij}(t) = N_{ij}^B\, m_{ij} \cos\left\{\frac{4\pi dF}{h_o} z_o v(t - t_o) + \phi_{ij}\right\} n_{ij}(t) \tag{2-29}$$

The determination of z_o then becomes a frequency estimation problem, which is optimally performed by matched filtering and peak detection. Mathematically, the height estimate $\hat{z}_o$ is given by $I_{ij}(z_o) > I_{ij}(z) \forall z$ where

$$I_{ij}(z) = \left|\frac{1}{T_a}\int N_{ij}(t) e^{-i\frac{4\pi dF}{h_o} z v(t-t_o)} dt\right| \tag{2-30}$$

It can be shown [2.5] that the Cramer-Rao lower bound for the height estimation uncertainty is given by

$$\delta_z = \begin{cases} \dfrac{\sqrt{6}\rho_z}{\pi SNR_{3d}} & SNR_{3d} > SNR_t \\ \alpha & SNR_{3d} < SNR_t \end{cases} \tag{2-31}$$

where SNR_{3d} is the signal-to-noise ratio of the matched filtered height distribution $I_{ij}(z)$, $SNR_t \approx 3.5$, and ρ_z is the peak-to-null width of $I_{ij}(z)$, or height resolution:

$$\rho_z = \frac{h_o^2}{2dFvT_a} \tag{2-32}$$

2.5 BIAS SIGNAL SUBTRACTION

One problem confronted in the practical use of a PRISM sensor is the fact that the bias signal $N_{ij}^B(t)$ can be somewhat temporally dependent due to the changing viewing angle. The problem is that the characteristics of this fluctuation may be such that it exhibits frequency content that overlaps with the desired interferometric signal term and spoils the height measurement capability, especially near the phase reference point where the temporal modulation frequency goes to zero.

The solution to this problem is to introduce an additive but known phase $\phi_i(t)$ into the interferometric term (which can be performed by a relative lateral shift of the gratings) to differentially remove the bias. For example,

$$\begin{aligned} N'_{ij}(t) &= \left[N_{ij}(t)\right]_{\phi_i(t)=0} - \left[N_{ij}(t)\right]_{\phi_i(t)=\pi} \\ &= 2N_{ij}^B(t)m_{ij}(z_o,t)\cos\left\{\phi_{ij}(t)+\phi_{ij}\right\} + n'_{ij}(t) \end{aligned} \tag{2-33}$$

represents a bias-subtracted signal where $n'_{ij}(t)$ is a noise process that has twice the variance of $n_{ij}(t)$. We note that bias signal fluctuations still impact the amplitude of the interferometric signal (which is generally a small effect), but the bias signal is otherwise removed.

2.6 HEIGHT AMBIGUITY

Because the PRISM sensor only measures the real part of the source coherence function, as represented by the cosine in the signal model as opposed to a complex exponential, a natural ambiguity about $z = 0$ arises. That is, the measured signal is identical for sources at $\pm z_o$, and in fact, the matched filtering (image formation) process superimposes mirror images about $z = 0$ of the true height distributions.

There are several ways to resolve this ambiguity. The first is merely to insure that the phase reference point is either above or below all radiation sources in the scene, such that the ambiguity can be ignored. The second is to introduce a known phase modulation $\phi_i(t)$ into the interferometric signal such that both the real (in-phase) and imaginary (quadrature) components of the pixel phase history are measured. In the latter case, the height ambiguity will no longer exist.

Generally, one of three phase modulation schemes are used to extract the complex phase history: discrete, linear, and wideband FM. The tradeoffs between the three are mainly at the sensor implementation level. All three approaches also remove the bias signal.

2.6.1 Discrete Phase Modulation

This is the most straightforward approach in which four measurements are made (either sequentially or via parallel channels) with $\phi_i(t) = 0, \pi/2, \pi$, and $3\pi/2$. The in-phase I(t), quadrature Q(t), and bias B(t) signal components of the signal are then extracted by

$$\begin{aligned} I(t) &= \frac{1}{2}\left\{\left[N_{ij}(t)\right]_{\phi_i(t)=0} - \left[N_{ij}(t)\right]_{\phi_i(t)=\pi}\right\} \\ &= N_{ij}^B(t) m_{ij}(z_o,t)\cos\left\{\phi_{ij}(t)+\phi_{ij}\right\} + n'_{ij}(t) \end{aligned} \tag{2-34}$$

$$\begin{aligned} Q(t) &= \frac{1}{2}\left\{\left[N_{ij}(t)\right]_{\phi_i(t)=\pi/2} - \left[N_{ij}(t)\right]_{\phi_i(t)=3\pi/2}\right\} \\ &= N_{ij}^B(t) m_{ij}(z_o,t)\sin\left\{\phi_{ij}(t)+\phi_{ij}\right\} + n'_{ij}(t) \end{aligned} \tag{2-35}$$

$$\begin{aligned} B(t) &= \frac{1}{4}\left\{\left[N_{ij}(t)\right]_{\phi_i(t)=0} + \left[N_{ij}(t)\right]_{\phi_i(t)=\pi/2} + \left[N_{ij}(t)\right]_{\phi_i(t)=\pi} + \left[N_{ij}(t)\right]_{\phi_i(t)=3\pi/2}\right\} \\ &= N_{ij}^B(t) + n''_{ij}(t) \end{aligned} \tag{2-36}$$

where $n'_{ij}(t)$ and $n''_{ij}(t)$ are noise processes with $1/\sqrt{2}$ and $1/2$ times the variance of $n_{ij}(t)$, respectively.

2.6.2 Linear Phase Modulation

This approach entails introducing a linear phase $\phi_i(t) = 2\pi f_m t$ where f_m is a frequency sufficiently high to separate the interferometric signal from the bias signal, but low enough to avoid signal sampling problems. The in-phase, quadrature, and bias signal components are then extracted by demodulation:

$$\begin{aligned} I(t) &= \frac{2}{F_s T_f} \int_t^{t+F_s T_f} N_{ij}(t)\, \cos 2\pi f_m t\, dt \\ &= N_{ij}^B(t)\, m_{ij}(z_o, t) \cos\{\phi_{ij}(t) + \phi_{ij}\} + n'_{ij}(t) \end{aligned} \tag{2-37}$$

$$\begin{aligned} Q(t) &= \frac{2}{F_s T_f} \int_t^{t+F_s T_f} N_{ij}(t)\, \sin 2\pi f_m t\, dt \\ &= N_{ij}^B(t)\, m_{ij}(z_o, t) \sin\{\phi_{ij}(t) + \phi_{ij}\} + n'_{ij}(t) \end{aligned} \tag{2-38}$$

$$\begin{aligned} B(t) &= \frac{1}{F_s T_f} \int_t^{t+F_s T_f} N_{ij}(t)\, dt \\ &= N_{ij}^B(t) + n''_{ij}(t) \end{aligned} \tag{2-39}$$

where $n'_{ij}(t)$ and $n''_{ij}(t)$ are noise processes with $\sqrt{2/F_s}$ and $\sqrt{1/F_s}$ times the variance of $n_{ij}(t)$, and $F_s T_f$ contains an integral number of cycles of the induced phase $(f_m = N / F_s T_f)$.

2.6.3 Wideband FM

This approach involves introducing a sinusoidal phase term $\phi_i(t) = b_m \sin 2\pi f_m t$ where f_m is a frequency sufficiently high to separate the interferometric signal from the bias signal, but low enough to avoid signal sampling problems. The in-phase, quadrature, and bias signal components are then extracted by

$$I(t) = \frac{1}{F_s T_f} \frac{1}{J_2(b_m)} \int_t^{t+F_s T_f} N_{ij}(t) \cos 4\pi f_m t \, dt$$
$$\cong N_{ij}^B(t) m_{ij}(z_o, t) \cos\{\phi_{ij}(t) + \phi_{ij}\} + n'_{ij}(t) \tag{2-40}$$

$$Q(t) = \frac{1}{F_s T_f} \frac{1}{J_1(b_m)} \int_t^{t+F_s T_f} N_{ij}(t) \sin 2\pi f_m t \, dt$$
$$\cong N_{ij}^B(t) \, m_{ij}(z_o, t) \sin\{\phi_{ij}(t) + \phi_{ij}\} + n''_{ij}(t) \tag{2-41}$$

$$B(t) = \frac{1}{F_s T_f} \int_t^{t+F_s T_f} N_{ij}(t) \, dt - J_0(b_m) I(t)$$
$$= N_{ij}^B(t) + \mathrm{J}_1(b_m) N_{ij}^B(t) \, m_{ij}(z_o, t) \cos\{\phi_{ij}(t) + \phi_{ij}\} + n'''_{ij}(t) \tag{2-42}$$

where $n'_{ij}(t)$, $n''_{ij}(t)$ and $n'''_{ij}(t)$ are noise processes with $\sqrt{1/F_s \, J_2(b_m)}$, $\sqrt{1/F_s \, J_1(b_m)}$, and $\sqrt{1/F_s}$ times the variance of $n_{ij}(t)$, and $F_s T_f$ contains an integral number of cycles of the induced phase $(f_m = N / F_s T_f)$. A modulation parameter b_m=2.4 rad provides optimal performance in terms the noise characteristics of the interferometric signal.

2.7 DATA FORMATTING

The discussion regarding height estimation in Section 2.4 was based on a small angle approximation, which resulted in a sinusoidal single surface phase history. In actuality, the phase term $2\pi \bar{f} \bullet \bar{r}$ is not exactly linear in time and, therefore, matched filtering with sinusoids is no longer optimal for height estimation. Rather, the optimal matched filter is

$$I_{ij}(z) = \left| \frac{1}{T_a} \int N'_{ij}(t) e^{-i\hat{\phi}_{ij}(z,t)} dt \right| \tag{2-43}$$

where $\hat{\phi}_{ij}(z,t)$ is the expected phase for a radiator at z in the $(i,j)^{th}$ pixel. In this case, this is defined by Eq. (2-27), but other known phase deviations (such as measured motion and pointing errors) can also be incorporated into the matched filter. When this phase term is significantly altered, the height estimation uncertainty may also be affected.

2.8 PIXEL WALK COMPENSATION

Thus far in the discussion of the single surface signal model, we have assumed that the source of the interferometric signal does not drift from pixel to pixel during the aperture time T_a. In fact, this generally does occur as described by the argument of the footprint function $\tilde{h}$ in Equations (2-23) and (2-24). If the matched filtering process does not accommodate this drift, height estimation will be non-optimal and potentially very poor [see Reference 2.2 for a more detailed discussion].

The current solution is to compensate this drift through a space-variant matched filtering algorithm:

$$I_{ij}(z) = \left| \frac{1}{T_a} \int N'_{ij}(t) e^{-i\hat{\phi}_{ij}(z,t)} dt \right| \tag{2-44}$$

where

$$i' = \left\| i\cos^2\theta + \frac{z\sin\theta}{\Delta x} + \frac{1}{2} \right\| \tag{2-45}$$

and $\|\bullet\|$ is the greatest integer function. This pixel walk compensation algorithm is optimal for a point radiator at the center of the $(i,j)^{th}$ pixel, but results in higher sidelobes elsewhere. Section 8 discusses other approaches and more detail with regard to pixel walk compensation. One approach that was used to achieve better performance is to compute $I_{ij}(z)$ on an oversampled i axis to better compensate features non-centered within a pixel (an oversampling of four provides excellent results). For features distributed across a pixel, this oversampling provides minimal gain, but the effects of pixel walk are also less significant.

2.9 REFERENCES

[2.1] J.D. Gorman, et al., "Assessing the Benefits of 3-D in a FLIR/Laser Radar Sensor," 1992 Meeting of the Iris Specialty Group on Active Systems, Vol. II, p. 72 (October 1992).

[2.2] A. Tai, et al., "Three-dimensional Passive Imaging," 1993 National Infrared Information Symposium, Vol. II, p. 43 (May 1993).

[2.3] I. Cindrich, et al., *PRISM Sensor Technology Development for Passive 2-D and 3-D Imaging*, ERIM Report No. 219600-2-F to Air Force WL/AARI, Contract No. F33615-84-C-1508, January 1992 (SECRET).

Intentionally Left Blank

3.0 SENSOR PERFORMANCE MODEL

This section describes a sensor performance model developed under this program to be used as a sensor design and evaluation tool. This model is metric-based as opposed to simulation-based. That is, as an output it computes estimated sensor performance such as sensitivity and 3-D resolution based on a detailed set of scene, sensor, and error budget parameters. The model is based on a signal-surface target assumption, but is sufficiently detailed to be useful as a sensor design program.

Under a single surface approximation, it has been shown that the form of the detected signal is given by

$$N_{ij}(t) = N_{ij}^{B}(t)\left[1 + m_{ij}(t)\cos\left\{\phi_{ij}(z_o,t) + \phi_i(t) + \phi_e(t) + \phi'_{ij}\right\}\right] + n_{ij}(t) \qquad (3\text{-}1)$$

where $N_{ij}(t)$ is the detected photoelectron count for detector element i,j at time t. The remaining parameters are defined as follows:

$N_{ij}^{B}(t)$	Bias signal level in photoelectrons
$m_{ij}(t)$	Interferometric signal modulation depth
$\phi_{ij}(z_o,t)$	Interferometric signal phase for surface at height z_O
$\phi_i(t)$	Induced additive phase (deterministic)
$\phi_e(t)$	Phase error
ϕ'_{ij}	Offset phase (unknown, scene dependent)
$n_{ij}(t)$	Additive noise

The signal representation given above will be referred to as the phase history. Height estimation in this model is assumed to consist of matched filtering to the interferometric modulation for a range of z_O values followed by peak detection. We will refer to the matched filtered signal as a function of z_O as the range impulse response function.

The primary assumptions of the sensor performance model are: (1) single surface per sensor IFOV, (2) small range of viewing angles such that aspect effects are negligible (i.e., N_{ij}^{B} and m_{ij} are time independent), and (3) use of current DFT with pixel walk compensation approach

resolution, and field-of-view of a PRISM sensor through a procedure outlined in Figure 3-1. The remainder of this section describes this procedure in a step-by-step manner. In general, the technical basis for this model is found in Reference 3.1. Other specific technical references are given within.

3.1 MODEL INPUTS

3.1.1 Target Parameters

Along track position	x_o	Distance in ground plane coordinates between target and phase reference point in direction coincident with interferometer baseline
Cross track position	y_o	Distance in ground plane coordinates between target and phase reference point in direction orthogonal to interferometer baseline
Vertical position	z_o	Distance orthogonal to ground plane between target and phase reference point
Mean emissivity	ε	Target emissivity averaged over spatial footprint
Illumination	$E\lambda$	Solar spectral irradiance of target
Target type	–	Edge, bar, or surface

Three target types are supported: edge, bar, and surface. An "edge" target consists of an interface between surfaces at the same height with different apparent temperatures. The following parameters are defined:

Left side temperature	T_1
Right side temperature	T_2

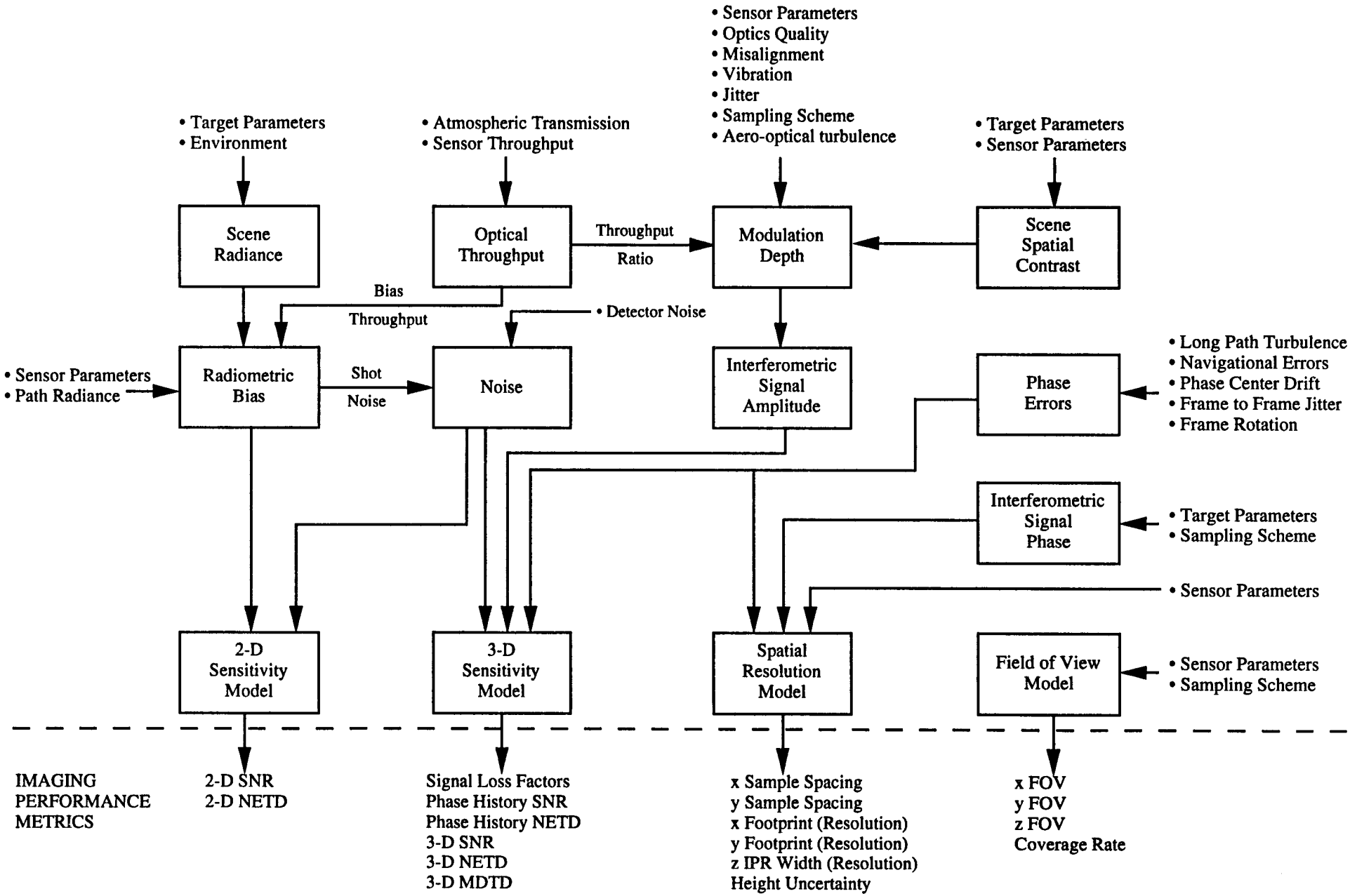

Figure 3-1: Performance model block diagram

Relative centration	r_C	Deviation of edge interface from pixel center in along track direction relative to pixel width (ranges -0.5 to 0.5)
Orientation angle	β	Angle of edge interface to cross track axis

A "bar" target consists of a rectangular object at one apparent temperature in a uniform background at another apparent temperature. The following parameters are defined:

Bar temperature	T_1	
Background temperature	T_2	
Bar width	W	Bar dimension in along track direction when β=0
Bar height	H	Bar dimension in cross track direction when β=0
Orientation angle	β	Angle of bar to cross track axis

Centration is assumed perfect (r_C=0).

A "surface" target consists of a homogeneous textured surface, which is assumed to extend over a large enough region such that the spatial statistics are stationary with respect to the sensor pixel. The following parameters are defined:

Edge Equivalent ΔT	ΔT_{eq}	Differential temperature of perfectly oriented and centered edge, which produces equivalent spatial passband energy as textured surface. This is a measure of surface spatial structure and contrast.
Mean temperature	T_{avg}	Surface temperature averaged over spatial footprint

3.1.2 Viewing Geometry Parameters

Platform altitude	h_o	Sensor height above ground plane
Side angle	ϕ	Angle from nadir between sensor position at center of track and phase reference point measured from height/track plane
Forward angle	α	Angle from nadir between sensor position at center of track and phase reference point measured in height/track plane
Collection type	–	Linear trajectory, step stare

"Linear trajectory" collection type refers to the collection of data from a platform moving at constant velocity along a line parallel to the ground plane x axis. The following parameters are defined:

Platform velocity	v	Ground speed in x direction
Stare time	T_a	Total time over which frames are collected and processed

"Step stare" collection type refers to the collection of data from a sensor which moves from point to point along a track parallel to the ground plane x-axis, but is stationary during the collection at each position. The following parameters are defined:

Track length	L	Distance between endpoints of track
Number of positions	N_p	Separate measurement positions (linearly dispersed)

3.1.3 Sensor Parameters

Center wavelength	λ_o	Center of overall sensor spectral response
Spectral bandwidth	$\Delta\lambda$	3dB width of overall sensor spectral response function
Aperture diameter	D	Effective diameter of limiting aperture
Interferometer shear	s	Wavefront shear distance at λ_o
Grating periodicity	F	
Detector element width	δ	Assumed identical in x and y
Detector pitch	p	Assumed identical in x and y
Optics blur circle	B	RMS spot size due to aberrations or defocus
Number of detector elements	N_x, N_y	Potentially different in x and y
Imaging lens focal length	f	
Detector frame time	T_f	
Downsampling factor/ integrated frames	F_s	For linear trajectory data collection, defines pre-filtering width. For step stare data collection, defines number of integrated frames
Achromaticity expansion	–	None, optimal, or intermediate
Achromaticity expansion	F_a	Equals unity for no expansion. Equals $2.5\ \lambda_o/\Delta\lambda$ for optimal expansion. Defined for intermediate

Wavefront collimation	–	Yes or no. Refers to collimation before interferometer to compensate near field wavefront curvature
Phase history sampling method	–	Single channel; real part only Single channel; linear phase modulation Single channel; wideband FM Dual channel; real part only Quadrature channel; I/Q samples
Modulation frequency	f_m	Temporal modulation frequency for linear phase modulation or wideband FM $\left[\phi_i(t) = 2\pi f_m t \text{ or } b_m \sin\left(2\pi f_m t\right)\right]$
Modulation amplitude	b_m	For wideband FM, $\phi_i(t) = b_m \sin\left(2\pi f_m t\right)$

3.1.4 Optical Throughput Parameters

Atmospheric transmission	τ_a	Sensor to phase reference point transmission averaged over sensor spectral response
Cold filter throughput	τ_c	Peak transmission of cold filter
Interferometer throughput	τ_{int}	Ratio of energy of interfered outputs in desired orders to input energy normalized to aperture diameter D
Imaging optics throughput	τ_{opt}	Transmission of optical train, excluding cold filter, averaged over sensor spectral response. Optics are assumed to be at ambient temperature
Additional path radiance	L_{path}	Added spectral radiance from other sources (e.g., scattering) referenced to the scene plane

3.1.5 Modulation Error Parameters

Optical quality (random)	σ_w	RMS wavefront irregularity of interfered wavefronts due to optics, including only wideband spatial frequency components
Optical quality (quadratic)	ϕ_m	Peak wavefront irregularity of interfered wavefronts due to optics, including only low order spatial components
Tilt misalignment	$\delta\theta_t$	Angular deviation of mean input grating vector from demodulation grating vector away from demodulation grating plane
Rotational misalignment	$\delta\theta r$	Angular deviation of mean input grating vector from demodulation grating vector in demodulation grating plane
Differential x-tilt misalignment	$\delta\theta_x$	Angular deviation between input grating planes about vertical axis
Differential y-tilt misalignment	$\delta\theta_y$	Angular deviation between input grating planes about baseline axis
Differential rotational misalignment	$\delta\theta_z$	Angular deviation between input grating vectors in mean input grating plane
Piston Error	δ_z	Longitudinal deviation between input grating planes along line-of-sight axis
Relative grating mismatch	δF	Difference between input and demodulation grating periodicities

Lateral grating vibration	σ_x	RMS differential motion between input and demodulation gratings in baseline direction during data collection
Within frame jitter	σ_j	RMS line-of-sight pointing jitter during F_s frames
Boundary layer thickness	t_{bl}	Depth of airborne platform turbulent boundary layer at sensor window

3.1.6 Phase Error Parameters

Atmosphere index structure parameter at 1 m altitude	$C_n^2(1m)$	Characterizes long path atmospheric turbulence; 1/h model is assumed
Frame to frame jitter	σ_p	Unknown RMS line-of-sight pointing jitter over T_a not including σ_j component and low order drift components
Along track navigational error	dx	Unknown variation (peak) in along track location from ideal or estimated location over T_a
Vertical navigational error	dz	Unknown variation (peak) in vertical sensor location from ideal or estimated location over T_a
Along track PRP drift	Δx	Unknown drift (peak) in phase reference point in along track direction over T_a
Vertical PRP drift	Δz	Unknown drift (peak) in phase reference point in vertical direction over T_a
Frame rotation drift	Δ_{rot}	Unknown drift (peak) in sensor baseline to along track axis over T_a

3.1.7 Detector Parameters

Quantum efficiency	η	Detector quantum efficiency averaged over sensor spectral response
Dark current density	J_d	Thermally-generated dark current density
Read noise per frame	σ_{read}	RMS noise of detector readout chain referred to input (photoelectrons)
Quantization levels	b	Assumed to cover charge storage capacity
Charge storage capacity	N_{FW}	Photoelectron saturation level per frame

3.2 INTERMEDIATE PARAMETERS

Several derived, intermediate parameters are used in the sensor modules to be described. These include:

Target slant range:

$$R = \frac{h_o}{\cos\alpha \cos\phi} \tag{3-2}$$

Viewing angle diversity:

$$\Delta\theta = 2\tan^{-1}\left(2L\cos\theta/h_o\right) \tag{3-3}$$

LOS fringe period:

$$\Lambda_{los} = R\lambda_o/s \tag{3-4}$$

Ground fringe period:

$$\Lambda_g = R\lambda_o/s\cos\alpha \tag{3-5}$$

Pixel-limited IFOV:

$$IFOV_{xy} = \delta/f \tag{3-6}$$

Optics-limited IFOV:

$$IFOV_{opt} = B/f \tag{3-7}$$

Diffraction-limited IFOV:

$$IFOV_{dl} = \lambda_o/D \tag{3-8}$$

Longitudinal grating separation:

$$d = \frac{s}{2\tan\left[\sin^{-1}(\lambda_o F)\right]} \tag{3-9}$$

Number of collected frames: $$M_f = T_a / T_f \tag{3-10}$$

3.3 SCENE RADIANCE

The mean target temperature and spectral radiance are computed via standard radiometric equations. Depending on target type, T is obtained by averaging over the spatial footprint

Edge: $$T = T_1(0.5 + r_c) + T_2(0.5 - r_c) \tag{3-11}$$

Bar: $$T = T_1 \frac{WH}{A_p} + T_2\left(1 - \frac{WH}{A_p}\right) \tag{3-12}$$

$$A_p = R^2 IFOV_{xy}^2 / \cos\alpha \ \cos\phi \tag{3-13}$$

Surface: defined as input variable

Scene spectral radiance is computed as a gray body with diffuse illumination:

$$L_\lambda = \frac{2hc^2}{\lambda^5} \frac{\varepsilon}{e^{hc/\lambda KT} - 1} + \frac{(1-\varepsilon)E_\lambda}{\pi} \tag{3-14}$$

3.4 OPTICAL THROUGHPUT

The optical throughput of the sensor is characterized separately for the radiometric bias (τ_{bias}) and the interferometric signal (τ_{sig}).

The bias throughput relates the total detected energy to the mean scene energy and is given by

$$\tau_{\text{bias}} = \tau_c \frac{L_\lambda + L_{path}}{L_\lambda} \tag{3-15}$$

This expression assumes the atmosphere, optics, and regions viewed through higher orders are roughly at the same temperature as the scene so that the absorbed and reradiated spectra are identical. The interferometric signal is further reduced by the atmosphere, optics, and higher interferometer orders:

$$\tau_{sig} = \tau_a \tau_c \tau_{\text{int}} \tau_{opt} \tag{3-16}$$

3.5 SCENE SPATIAL CONTRAST

Scene spatial contrast is described either by the edge equivalent temperature differential (ΔT_{eq}) or the combination of radiometric contrast (C_R) and spatial frequency factor (C_S). The edge equivalent temperature differential is that of a perfectly oriented and centered edge that produces the equivalent energy in the sensor spatial passband as the target. The radiometric contrast is the scene radiance variability across the spatial footprint relative to the mean. Analogously, the spatial frequency factor is the passband energy for a spatial footprint relative to the mean.

3.5.1 Edge Target

By definition,

$$\begin{aligned} C_s &= \frac{\left| \int_0^{0.5+r_c} e^{i2\pi x/\Lambda_g} dx \right|}{\int_0^{0.5+r_c} dx} \\ &= \frac{\Lambda_g \cos\beta}{\pi \rho_x} \frac{1}{1+2r_c} sinc\left(\frac{\rho_x \tan\beta}{\Lambda_g} \right) \end{aligned} \tag{3-17}$$

Utilizing a linear approximation for dL/dT:

$$C_R = \frac{hc}{\lambda k T^2} \frac{|T_2 - T_1|}{2} (1+2r_c) \tag{3-18}$$

By comparison,

$$\Delta T_{eq} = |T_2 - T_1| \cos\beta \, \mathrm{sinc}\left(\frac{\rho_x \tan\beta}{\Lambda_g}\right) \tag{3-19}$$

3.5.2 Bar Target

Centration with regard to the bar target is ignored. Through the definition,

$$C_s = \left| \frac{\iint rect\left(\frac{x}{W}, \frac{y}{H}\right) e^{i2\pi x/\Lambda_g} dxdy}{\iint rect\left(\frac{x}{W}, \frac{y}{H}\right) dxdy} \right| \tag{3-20}$$

$$= sinc\ \left(W/\Lambda_g\right)$$

for an oriented bar. At arbitrary orientation:

$$C_s = sinc\left(W/\Lambda_g\right) cos\beta \ \ sinc\left(\frac{\rho_x \, tan\beta}{\Lambda_g}\right) \tag{3-21}$$

By comparison

$$C_R = \frac{hc}{\lambda k T^2} |T_2 - T_1| \frac{WH}{\rho_x \rho_y} \tag{3-22}$$

and

$$\Delta T_{eq} = 2|T_2 - T_1| \frac{WH}{\rho_x \rho_y} \frac{\pi \rho_x}{\Lambda_g} \mathrm{sinc}\left(W/\Lambda_g\right) \cos\beta \, \mathrm{sinc}\left(\frac{\rho_x \tan\beta}{\Lambda_g}\right) \tag{3-23}$$

3.5.3 Surface Target

A surface target, by definition, is defined by ΔT_{eq}.

$$C_R = \frac{hc}{\lambda k T^2} \frac{\Delta T_{eq}}{2} \tag{3-24}$$

and

$$C_s = \frac{\Lambda_g}{\pi \rho_x} \tag{3-25}$$

Orientation and centration are ignored.

3.6 RADIOMETRIC BIAS

The radiometric bias (N_B) is the mean detected photoelectrons per frame.

Since all parameters are normalized to the sensor spectral response:

$$N_B = \frac{\pi D^2 \, IFOV_{xy}^2 \, T_f \, \eta \, \tau_{bias} L_\lambda \lambda_o \Delta\lambda}{4hc} \tag{3-26}$$

This expression assumes that the scene spectral radiance L_λ is roughly linear over $\Delta\lambda$.

3.7 MODULATION DEPTH

The overall sensor modulation depth is given by the product of its individual constituents (defined as m_i). Each are individually discussed.

3.7.1 Target Contrast

The target modulation depth is determined from the radiometric contrast and spatial frequency factor:

$$m_o = C_R C_S \tag{3-27}$$

3.7.2 Throughput Ratio

The relative signal to bias throughput ratio results in a corresponding reduction in modulation depth:

$$m_1 = \tau_{sig} \, / \, \tau_{bias} \tag{3-28}$$

3.7.3 Random Wavefront Errors

The model used for random wavefront errors is a differential phase variance σ_w^2 between interfering wavefronts with a correlation distance much smaller than aperture diameter. Under this assumption, the interference contrast is given by

$$m_2 = \langle \cos\ \delta\phi \rangle \tag{3-29}$$

where $\delta\phi$ is the phase difference. If $\delta\phi$ is a zero mean gaussian random variable with variance σ_w^2, this expression can be determined by integrating the probability density function to show

$$m_2 = e^{-\sigma_w^2/2} \tag{3-30}$$

3.7.4 Low Order Wavefront Errors

A quadratic model is used for low order wavefront errors such that

$$\phi(r) = \frac{4\phi_m r^2}{D} \tag{3-31}$$

where r is a radial parameter $\left(r^2 = x^2 + y^2\right)$ in the pupil plane. After sheared interference, this produces a differential phase error in the demodulation grating plane (x', y') given by

$$\delta\phi(x', y') = \frac{8\phi_m}{D} x's \tag{3-32}$$

The reduction in modulation depth is given by the normalized integration of $\cos\ \delta\phi$ over the aperture diameter:

$$m_3 = \frac{2J_1\left(2\phi_m\ s/D\right)}{\left(2\phi_m\ s/D\right)} \tag{3-33}$$

3.7.5 Near Field Wavefront Curvature

If collimating optics are used in front of the interferometer, $m_4 = 1$. If not, a quadratic wavefront error exists such that

$$\phi(r) = \frac{\pi}{\lambda R} r^2 \tag{3-34}$$

where is a radial parameter $\left(r^2 = x^2 + y^2\right)$ in the pupil plane. After sheared interference, this produces a differential phase error in the demodulation grating plane (x', y') given by

$$\delta\phi(x', y') = \frac{2\pi}{\lambda R} x's \tag{3-35}$$

The reduction in modulation depth is given by the normalized integration of cos $\delta\phi$ over the aperture diameter

$$m_4 = \frac{2\,\mathrm{J}_1\left(\pi D/\Lambda_{LOS}\right)}{\left(\pi D/\Lambda_{LOS}\right)} \tag{3-36}$$

3.7.6 Interferometer Achromaticity

Using a third order series approximation to the interferometric phase as a function of incident angle and wavelength, the reduction in modulation depth is given by

$$m_5 = \frac{1}{\Delta\lambda}\left|\int_{\lambda} W(\lambda) e^{i\frac{2\pi d F^3 x \lambda^2}{R}} d\lambda\right| \tag{3-37}$$

For no achromaticity expansion, this is solved numerically assuming $W(\lambda) = 1$ over the range $\left[\lambda_0 - \Delta\lambda/2,\ \lambda_0 + \Delta\lambda/2\right]$. With achromaticity expansion, a narrow band approximation $\Delta\lambda >> \lambda_0$ is used along with the achromaticity expansion factor to estimate m_5:

$$m_5 = \operatorname{sinc}\left(\frac{2\mathrm{d}\mathrm{F}^3 \lambda_0 \Delta\lambda}{R F_a} x\right) \tag{3-38}$$

3.7.7 Mean Input Grating Misalignment

Here we define the modulation depth reductions due to misalignment between mean input grating and demodulation grating wave vectors.

Tilt misalignment will result in an equivalent error independent of orientation β_t under the approximation that $\delta\theta_t << \theta_{FOV}$. In this case, the phase error in the demodulation plane (x', y') is given by

$$\delta\phi(x', y') \cong 2\pi \frac{Fx \tan \delta\theta_t}{2R}(x' \cos \beta_t + y' \sin \beta_t) \tag{3-39}$$

Integrating $\cos \delta\phi$ over the aperture diameter results in

$$m_6 = \frac{2J_1(\pi DFx \tan \delta\theta_t / 2R)}{(\pi DFx \tan \delta\theta_t / 2R)} \tag{3-40}$$

For in-plane rotational misalignment

$$\delta\phi(x', y') = 4\pi Fx'(1 - \cos \delta\theta_r) + 4\pi Fy' \sin \delta\theta_r \tag{3-41}$$

resulting in

$$m_7 = \frac{2J_1(4\pi DF \sin(\delta\theta_r/2))}{(4\pi DF \sin(\delta\theta_r/2))} \tag{3-42}$$

3.7.8 Differential Input Grating Misalignment

Here we define the modulation depth reductions due to differential misalignments between input gratings. These misalignments are modeled as the multiplicative effect of each and opposite errors in each grating.

For each $\delta\theta_x, \delta\theta_y$, and $\delta\theta_z$ error, respectively,

$$\delta\phi(x', y') \cong \frac{2\pi}{\lambda_0} y' \tan 2\delta\theta_x \tag{3-43}$$

$$\cong \frac{4\pi}{\lambda_0} y' \sin \delta\theta_y \tag{3-44}$$

$$\cong 2\pi F(1-\cos \delta\theta_z)x' - 2\pi F \sin \delta\theta_z \, y' \tag{3-45}$$

The modulation depth is the square of the normalized integral of $\cos \delta\phi$ over the aperture diameter for each case:

$$m_8 = \frac{4J_1^2(\pi D \tan 2\delta\theta_x/\lambda)}{(\pi D \tan 2\delta\theta_x/\lambda)^2} \tag{3-46}$$

$$m_9 = \frac{4J_1^2\left(2\pi D \sin\left(\delta\theta_y\right)/\lambda\right)}{\left(\pi D \sin\left(\delta\theta_y\right)/\lambda\right)^2} \tag{3-47}$$

$$m_{10} = \frac{4J_1^2\left(2\pi FD \sin\left(\delta\theta_z/2\right)\right)}{\left(2\pi FD \sin\left(\delta\theta_z/2\right)\right)^2} \tag{3-48}$$

3.7.9 Grating Piston Error

Piston error is the longitudinal difference between input grating positions. The piston error model is based on a reflective grating design. For a transmission design, the effect is significantly smaller. Piston error has the effect of reducing the interferometer achromaticity by introducing a wavelength dependent phase term given by

$$\psi(\lambda) = \frac{2\pi}{\lambda}\delta_z\left[1+\sqrt{1-\lambda^2F^2}\right] \tag{3-49}$$

The modulation depth is then given by

$$m_{11} = \frac{1}{\Delta\lambda}\left|\int W(\lambda)e^{i\psi(\lambda)}d\lambda\right| \tag{3-50}$$

Using a narrow band approximation and analytically computing the integral

$$m_{11} \approx \operatorname{sinc}^2\left(\frac{\pi D \delta_z}{4 s \lambda_0}\right) \tag{3-51}$$

3.7.10 Grating Frequency Mismatch

Mismatch of input and demodulation grating periodicities causes a linear wavefront error in the demodulation grating plane given by

$$\delta\phi(x', y') = 4\pi(\delta F)x' \tag{3-52}$$

Integrating $\cos\ \delta\phi$ over the aperture diameter, it can be shown that

$$m_{12} = \frac{2J_1(2\pi\delta FD)}{(2\pi\delta FD)} \tag{3-53}$$

3.7.11 Lateral Grating Vibration

Lateral vibration of the demodulation grating relative to the input gratings with variance σ_x^2 will cause a detected phase variance of

$$\sigma_\phi^2 = 16\pi^2 F^2 \sigma_x^2 \tag{3-54}$$

Assuming this vibration is wideband relative to the frame integration time

$$m_{13} = \langle \cos\ \phi \rangle = e^{-\sigma_\phi^{2/2}} = e^{-8\pi^2 F^2 \sigma_x^2} \tag{3-55}$$

3.7.12 Within Frame LOS Jitter

Jitter in the sensor LOS with variance σ_j^2 in the x-direction produces an additive phase variance of

$$\sigma_\phi^2 = 4\pi^2 \sigma_j^2\ \mathrm{s}^2/\lambda_o^2 \tag{3-56}$$

Assuming this jitter is wideband relative to the frame integration time

$$m_{14} = \langle \cos\phi \rangle = e^{-\sigma_\phi^{2/2}} = e^{-2\pi^2 \sigma_j^2 \, s^2/\lambda_o^2} \tag{3-57}$$

3.7.13 Frame Integration

For step-stare data collection, frame integration has no effect on modulation depth. With a moving platform, however, it will reduce modulation depth as the signal frequency increases. The effect will also be dependent on the relative phase between the signal and samples. It can be shown [3.2] that

$$m_{15} = \frac{[\cos(\psi) - \cos(\psi + k\beta')]}{\alpha + [\cos(\psi) + \cos(\psi + k\beta')]} \tag{3-58}$$

where

$$\beta' = \pi T_f \, f_{sig} \tag{3-59}$$

$$n = \mathrm{int}\left(1/T_f \, f_{sig}\right) + 1 \tag{3-60}$$

$$\psi^* = \pi - \left(n - \tfrac{1}{2}\right)\beta' \tag{3-61}$$

$$k = \begin{cases} n & \psi \le \psi^* \\ n-1 & \psi > \psi^* \end{cases} \tag{3-62}$$

ψ^* represents relative phase from 0 (best case) to β (worse case). The model numerically averages m_{15} over this range of cases.

3.7.14 Aero-Optical Turbulence

Aero-optical turbulence is modeled as a high temporal and spatial frequency random wavefront disturbance within each of the sensor apertures. A boundary layer turbulence model [3.3] is used. If x_{b1} is the along track distance to the boundary layer leading edge, the boundary layer thickness is approximately

$$t_{bl} \cong 0.015 x_{b1} \tag{3-63}$$

The rms density variation is given roughly by

$$\rho' = 0.2(\rho_0 - \rho) \tag{3-64}$$

where

$$\rho = \rho_0 \{1 + r[(\gamma - 1)/2] M^2\}^{-1} \tag{3-65}$$

where ρ_0 is the free stream air density $\sim(1\ kg/m^3$ at 2 km$)$, r = 0.89 for turbulent flow, γ is the adiabatic index (1.4 for air), and M is the Mach number $(\mathrm{v}/(305\ \mathrm{m/s}))$. The correlation lengths are approximately $L_z = 0.2 t_{bl}$, $L_x = 2L_z$, and $L_y = L_z$. The RMS optical phase variation is

$$\sigma_{b1} = \frac{2\pi}{\lambda_0} \int G\rho' dz \cong \frac{2\pi}{\lambda_0} G\rho' (2 L_z t_{bl})^{1/2} \tag{3-66}$$

where G is the Gladstone Dale constant $(0.22 \times 10^{-3}\ m^3/kg)$ for $0.6\ \mu m < \lambda_0 < 10\ \mu m$. Since the phase variations are highly uncorrelated in space and time as well as between the apertures,

$$m_{16} = \langle cos\ \phi_{b1} \rangle^2 = e^{-\sigma_{b1}^2} \tag{3-67}$$

assuming a gaussian model.

3.8 NOISE

All noise sources are assumed independent, additive zero mean gaussian random processes. The shot noise variance is signal dependent.

$$(\sigma_n)_1^2 = N_B \tag{3-68}$$

Detector noise is specified by the dark current density

$$(\sigma_n)_2^2 = \frac{J_d \delta^2 T_f}{q} \tag{3-69}$$

and/or additional sources

$$(\sigma_n)_3^2 = \sigma_{read}^2 \tag{3-70}$$

Finally, quantization noise is modeled analogously [3.4] with

$$(\sigma_n)_4^2 = \frac{2^{-2b} N_{FW}^2}{6} \tag{3-71}$$

Assuming independence, the total noise variance is the sum of these four constituents.

3.9 INTERFEROMETRIC SIGNAL AMPLITUDE

The interferometric signal amplitude is the product of the radiometric bias and modulation depth

$$N_S = mN_B \tag{3-72}$$

3.10 INTERFEROMETRIC SIGNAL PHASE

The exact equation for the interferometric signal phase is

$$\phi_{ij}(z_o,t) = \frac{2\pi(x_o \cos\theta + z_o \sin\theta)}{\Lambda_{LOS}} \tag{3-73}$$

where

$$\theta = \tan^{-1}\left[\frac{vt}{h_o} - \tan\alpha\right] \tag{3-74}$$

Under a small angle approximation for θ, we see that

$$\phi(z_o,t) \approx 2\pi f_{sig} t \tag{3-75}$$

where

$$f_{sig} = \frac{v(x_o \sin\alpha + z_o \cos\alpha)}{h_o \Lambda_{LOS}} \tag{3-76}$$

3.11 PHASE ERRORS

Phase errors are separated into wideband and low-order, depending on their frequency content relative to the sensor total collection time T_a.

3.11.1 Wideband Phase Errors

The total wideband phase error variance σ_e is the sum of the variances of its individual constituents.

3.11.1.1 Atmospheric Turbulence

Atmospheric turbulence is modeled [3.5] with a $1/h$ index structure parameter model:

$$C_n^2(h) = C_n^2(h_1) h_1 / h \tag{3-77}$$

With this model, the correlation distance r_o for propagation from the PRP $(h = 0)$ to the sensor $(h = h_o)$ is given by

$$\begin{aligned} r_o &= \left[\frac{0.4233(2\pi)^2}{\lambda_o^2 \cos\alpha \cos\phi} \int_o^{h_o} C_n^2(h_1) \frac{h_1}{h} h^{5/3} dh \right]^{-3/5} \\ &= \left[10 \frac{C_n^2(h_1) h_1}{\lambda_o^2 \cos\alpha \cos\phi} \right]^{-3/5} \end{aligned} \tag{3-78}$$

The phase variance across the interferometer baseline is given by

$$\begin{aligned} (\sigma_e)_1^2 &= 6.884 [s/r_o]^{5/3} \\ &= 8.3 \left[\frac{C_n^2(h_1) h_1}{\lambda_o^2 \cos\alpha \cos\phi} \right] s^{5/6} \end{aligned} \tag{3-79}$$

This model assumes r_o is larger than D and v/r_o is on the order of signal sampling rate.

3.11.1.2 Frame Pointing Jitter

If σ_p^2 is the angular LOS pointing variance in the along track direction, not including low order drifts or high frequency content beyond the sampling bandwidth, then

$$(\sigma_e)_2 = 2\pi s\ \sigma_p/\lambda_o \tag{3-80}$$

3.11.2 Low Order Phase Errors

The total low order phase error is the sum of its constituents in the worst case assumption used.

3.11.2.1 Navigational Uncertainties

For a point source at x_o, z_o:

$$\phi = \frac{2\pi s}{R\lambda_o}(x_o \cos\theta + z_o \sin\theta) \tag{3-81}$$

If there are unknown errors in R and θ:

$$\begin{aligned} d\phi &\cong \frac{\partial\phi}{\partial R}dz + \frac{\partial\phi}{R\partial\theta}dx \\ &\cong \frac{2\pi}{\Lambda_{LOS}}\left(\frac{x_o}{R}dz + \frac{z_o}{R}dx\right) \end{aligned} \tag{3-82}$$

where dx, dz are the peak uncertainties in the sensor position. Separating the errors for the x and z errors

$$(\phi_e)_1 = \frac{2\pi z_o}{R\Lambda_{LOS}}dx \tag{3-83}$$

$$(\phi_e)_2 = \frac{2\pi x_o}{R\Lambda_{LOS}}dz \tag{3-84}$$

This is modeled as a quadratic error.

3.11.2.2 Phase Reference Point Drift

A low order drift in the phase reference point, given by peak-to-peak values Δx and Δz for the along track and height directions, result in peak phase errors of

$$(\phi_e)_3 = \frac{2\pi}{\Lambda_{LOS}} \Delta x \cos\alpha \tag{3-85}$$

$$(\phi_e)_4 = \frac{2\pi}{\Lambda_{LOS}} \Delta z \sin\alpha \tag{3-86}$$

for $\theta = 0$. For $\theta \neq 0$, $(\phi_e)_4$ will be somewhat higher, but this is ignored. This phase error is modeled as a quadratic.

3.11.2.3 Frame Rotation Drift

Frame rotation (including interferometer baseline) by an angle Δ_{rot} will laterally (x) translate the fringe planes by an amount of $\Delta_{rot}\, y_0/\Lambda_g$ where Δ_{rot} is in radians. The resulting phase error, assuming Δ_{rot} corresponds to the peak-to-peak drift, is

$$(\phi_e)_5 = \frac{2\pi}{\Lambda_g} \Delta_{rot} y_0 \tag{3-87}$$

This ignores a slight (but negligible) height dependence and is modeled as a quadratic.

3.12 2-D IMAGE SENSITIVITY

The signal-to-noise ratio of the 2-D frame is defined with respect to the full bias pedestal after integration or downsampling

$$SNR_{2d} = \frac{\sqrt{F_s} N_b}{\sigma_n} \tag{3-88}$$

The noise equivalent ΔT, however, is defined with regard to the spatial contrast signal

$$NETD_{2d} = \frac{\sigma_n}{\left(\frac{t_{sig}}{t_{bias}}\right)\left(\frac{hc}{\lambda kT^2}\right)\sqrt{F_s}N_b} \tag{3-89}$$

Once again, this is defined for the 2-D integrated or downsampled bias frame

3.13 3-D IMAGE SENSITIVITY

The sensitivity of the 3-D image is traced from the interferometric signal through the image formation process.

3.13.1 Phase History Sensitivity

The amplitude signal to rms noise ratio for the interferometric phase history is defined as

$$SNR_{ph} = \frac{m\sqrt{F_s}N_b}{\sigma_n} \tag{3-90}$$

The noise equivalent ΔT is defined with respect to the edge equivalent spatial structure

$$NETD_{ph} = \frac{\Delta T_{eq}}{SNR_{ph}} \tag{3-91}$$

3.13.2 Signal Loss Factors

Three factors are defined that result in an SNR loss in the image formation process.

3.13.2.1 Phase History Sampling

This factor represents the increase or reduction in the range IPR peak as a function of the type of phase history data sampled by the sensor. The baseline $(R_s = 1)$ is I and Q data with a signal-to-noise ratio of SNR_{ph}. The cases, signal loss factors, and explanations are given below:

Single channel, Real Part Only: $R_s = 0.5$

Reduction due to Hermitean symmetry

Single channel, Linear Phase Modulation: $-R_s = 0.5$

Reduction due to temporal multiplexing of I and Q components

Single channel, wideband FM: $R_s = \sqrt{\frac{J_1^2(b_m) + J_2^2(b_m)}{2}}$

Reduction due to temporal multiplexing of I and Q components and losses to harmonics

Dual channel, Real Part Only: $R_s = 0.707$

Reduction due to Hermitean symmetry, partially offset by increases due to differential channels

Quadrature channel, I and Q samples: $R_s = 1.414$

Increase due to differential channels

3.13.2.2 Phase Errors

The IPR reduction is modeled as being multiplicative between the contributions due to the wideband random, quadratic (low order), and sinusoidal phase error components. For wideband random phase errors,

$$R_e = \langle \cos\ \phi_e(t) \rangle = e^{-\sigma_e^2/2} \tag{3-92}$$

For the quadratic component

$$R_e = \frac{1}{T_a} \left| \int_o^{T_a} e^{i\phi_e(t)} dt \right| \tag{3-93}$$

which is evaluated numerically. For the sinusoidal component

$$R_e = J_o(b_e) \tag{3-94}$$

3.13.2.3 Pixel Walk

Decentration of an edge pixel causes a loss in signal in the matched filtering process using the current pixel walk compensation approach. The resulting IPR reduction is:

$$R_{pw} = 1 - r_c \tag{3-95}$$

3.13.3 Image Sensitivity

Assuming matched filter frequency estimation, the image peak signal to rms noise ratio is defined as

$$SNR_{3d} = \frac{m\sqrt{M_f}\, N_b}{\sigma_n} R_e R_s R_{pw} \tag{3-96}$$

The noise equivalent ΔT is defined with respect to the edge equivalent spatial structure

$$NETD_{3d} = \frac{\Delta T_{eq}}{SNR_{3d}} \tag{3-97}$$

The threshold SNR is defined at the level at which a non erroneous height estimate can be made. This has been found to be roughly $SNR_t = 3.5$. The detectability threshold is defined with respect to SNR_t:

$$MDTD = SNR_t \bullet NETD_{3d} \tag{3-98}$$

3.14 SPATIAL RESOLUTION

3.14.1 3-D Image Resolution

If the imaging system is blur - limited $\left(IFOV_{opt} > IFOV_{xy}\right)$, then the along and cross track (ground plane) resolutions are given by

$$\rho_x = R\, IFOV_{opt}/\cos\,\alpha \tag{3-99}$$

$$\rho_y = R\, IFOV_{opt}/\cos\,\phi \tag{3-100}$$

Otherwise, they are pixel $IFOV$ - limited:

$$\rho_x = R\, IFOV_{xy}/\cos\,\alpha \tag{3-101}$$

$$\rho_y = R\, IFOV_{xy}/\cos\,\phi \tag{3-102}$$

Note that $IFOV_{opt}$ cannot be less than $IFOV_{dl}$. For orthogonal plane resolution, the cosine factors are ignored. The height resolution (3dB width) is determined by the synthetic aperture:

$$\rho_z = \frac{R^2 \lambda_o \cos \phi}{sL} \tag{3-103}$$

3.14.2 Spatial Sampling Distance

The ground pixel sample spacing is determined from the array pitch

$$P_x = Rp / f \cos \alpha \tag{3-104}$$

$$P_y = Rp / f \cos \phi \tag{3-105}$$

3.14.3 Height Estimation Accuracy

For the height estimation procedure employed, the estimation accuracy is approximately

$$\sigma_z = \frac{\sqrt{3}\rho_z}{\pi \, SNR_{3d}} \tag{3-106}$$

This is the Cramer-Rao bound for frequency estimation of a sinusoid in white noise [3.6]. At the detectability threshold,

$$(\sigma_z)_t = \frac{\sqrt{3}\rho_z}{\pi \, SNR_t} \tag{3-107}$$

3.15 SPATIAL COVERAGE

The sensor ground plane field of view is determined by the focal plane array size

$$FOV_x = N_x P_x \tag{3-108}$$

$$FOV_y = N_y P_y \tag{3-109}$$

This results in an effective ground coverage rate of

$$CR = FOV_x \, FOV_y / T_a \tag{3-110}$$

The height field of view is determined by the sampling rate and frame integration. For I and Q sampling

$$FOV_z = \frac{N_{pos}\rho_x}{\cos\alpha} - FOV_x \tan\alpha \qquad (3\text{-}111)$$

for step stare collection and

$$FOV_z = \frac{2M_f\rho_z}{3F_s \cos\alpha} - FOV_x \tan\alpha \qquad (3\text{-}112)$$

for linear trajectory collection. For real (I) sampling only, FOV_z is effectively halved due to the range ambiguity.

3.16 REFERENCES

[3.1] *PRISM Sensor Technology Development for Passive 2-D and 3-D Imaging*, ERIM Final Report No. 219600-2-F, Air Force Report No. WL-TR-92-1041, August 1992.

[3.2] J.C. Feltz and M.A. Raim, "Modulation Transfer Function of Charge Coupled Devices," Appl. Opt. 5, pp. 717-722 (1990).

[3.3] L.J. Otten, K.G. Gilbert, and W.C. Rose, "Aerodynamic Effects," Ch. 3 in "Atmospheric Propogation of Radiation," Vol. 2 of IR handbook (to be published).

[3.4] A.V. Oppenheim and R.W. Shafer, Digital Signal Processing, (Prentice Hall, 1975), pp. 413-418.

[3.5] *Phase Error Source Assessment/Correction Approach*, ERIM Final Report 232301-1-F, pp. 15-28.

[3.6] D.C. Rife and R.R. Boorstyn, "Single-Tone Parameter Estimation from Discrete-Time Observations," IEEE Trans. Info. Theory, Vol. IT-20, pp.591-598 (Sept., 1974).

4.0 GROUND SENSOR DESIGN

This section describes the use of the performance model detailed in Section 3 to design a PRISM sensor for a ground-based MWIR demonstration of the imaging concept.

4.1 DESIGN GOALS AND CONSTRAINTS

The overall objectives of the ground sensor demonstration were the following:

- Design and fabricate a ground-based mid-IR PRISM sensor capable of collecting imagery of full-sized targets in natural backgrounds.

- Use the sensor to compile an image database consisting of targets under a variety of operational conditions.

- Analyze the resulting imagery to gain a better understanding of the robustness of PRISM target signatures under this variety of operational conditions.

- Extract statistical information on targets and backgrounds that can be used for validation and refinement of sensor and detection performance models.

Based on these objectives, a set of top level sensor specifications were defined and are summarized in Table 4-1.

These top level specifications were determined from a variety of considerations. For example, the near-nadir viewing geometry and 10° angle diversity limits arise from the need to obtain a clear line-of-sight to targets hidden in a forested environment. The resolution specifications, on the other hand, are expectations of what might be required to detect and perhaps recognize such objects in clutter from passive 3-D imagery.

The sensitivity specification is based on prior estimates of high spatial frequency target and background contrast. Because of the bandpass nature of the sensor, its ability to range is dependent not only on scene contrast, but also on subpixel spatial structure. The NETD specification provides a metric for contrast and spatial structure based on a target of known spatial structure - an edge aligned orthogonally to the sensor shear direction. This metric was determined

through prior high resolution IR image measurements of a limited set of targets and backgrounds. Most of these measurements showed higher contrast in the 10-20 cycles/m spatial frequency range than a 0.1C edge; therefore, a sensor designed to provide an accurate range to a 0.1C edge would also be expected to range to such targets and backgrounds in most environments.

Table 4-1: Top Level Sensor Design Specifications

Imaging Geometry:	Near nadir spotlight 0 to 30 degrees off nadir
Angular Diversity:	≤10° in vertical plane along track
Along/Cross Track Resolution:	0.2-0.5 meters (spatial footprint)
Range (height) Resolution:	0.2-0.5 meters (IPR 3dB width)
Along/Cross Track FOV:	>20 m
Height FOV:	>10 m
Sensitivity:	NETD (edge) = 0.1 C or less
Scene:	Full-sized military vehicles in natural clutter background

In addition to these top level specifications, two other issues formed the basis of the sensor design. The first of these is the decision to implement a ground-based demonstration from the Kinzua bridge site in Bradford, Pennsylvania [4.1]. This set the operating range to approximately 90m. The second was the decision to utilize an off-the-shelf Cincinnati Electronics IRC-160 InSb camera as the thermal imaging sensor. This was driven by cost and lead time constraints. Two modifications, however, were made to the camera prior to delivery. First, the standard cold filter was replaced with a 160 nm bandpass filter centered at 4.7μm to allow the sensor to operate in the thermally-dominated portion of the MWIR atmospheric window. Second, the detector preamplifier gain was increased to provide an improved sensitivity at the expense of lower saturation level (45C versus 60C). This tradeoff is required because the digitizer dynamic range (12 bit) is lower than that of the detector array. The chosen spectral filter provided roughly 33% saturation at full frame integration (19.44 msec) for a 25C blackbody.

4.2 PARAMETRIC SENSOR DESIGN

This subsection outlines the process by which the initial sensor design was obtained. Using the sensor performance model, iterations in this design were made to optimize performance in light of the various constraints and performance of the optical components. The description of

this design process contained in this report will be largely parametric in scope. For more detail on the details of the optical, mechanical, and electrical hardware, the reader is referred to Ref. 4-1.

4.2.1 Wavelength Band Selection

Selection of the spectral band of the sensor was based on four considerations: detector sensitivity, atmospheric transmission, LWIR extrapolation, and detector saturation. The IRC-160 camera contains an InSb array sensitive over roughly the 2-5 micron spectral band. In order to extrapolate the ground demo sensor measurements to the LWIR, however, the upper end of this band was selected where thermal emission dominates. Specifically, a 4.7 μm center wavelength places the sensor in an atmospheric transmission window where the thermal target and background signatures are similar to the LWIR.

The spectral bandwidth of 160 nm was chosen to match the camera dynamic range. Based on the maximum integration time of 19.44 msec, a 300K blackbody target generates a mean signal corresponding to roughly one-third of the detector full well, resulting in good SNR, but also leaving additional overhead for significantly warmer targets.

4.2.2 Interferometer Design

The critical component of the sensor design is that of the interferometer. In general, it is preferred to utilize a reflective grating interferometer arrangement [Figure 4-1(a)] since this maximizes sensor throughput and minimizes interferometric (higher orders) and non-interferometric (stray light and component radiation) spurious signals. Because of the near range relative to the desired FOV, however, such a design was not feasible for the ground demonstration sensor since the shear distance (roughly 5-10 mm for 0.2-0.5 m range resolution with 10° angle diversity) is less than the aperture size (11 mm). Instead, a transmissive grating interferometer design [Figure 4-1(b)] was utilized based on square wave phase gratings designed to optimize ±1 diffracted order efficiency.

The selection of grating periodicity is another critical design issue. On one hand, the periodicity must be sufficient to place singly diffracted scene energy off the detector array. This occurs for

$$F > \sin \theta_{FOV} / \lambda \qquad (4\text{-}1)$$

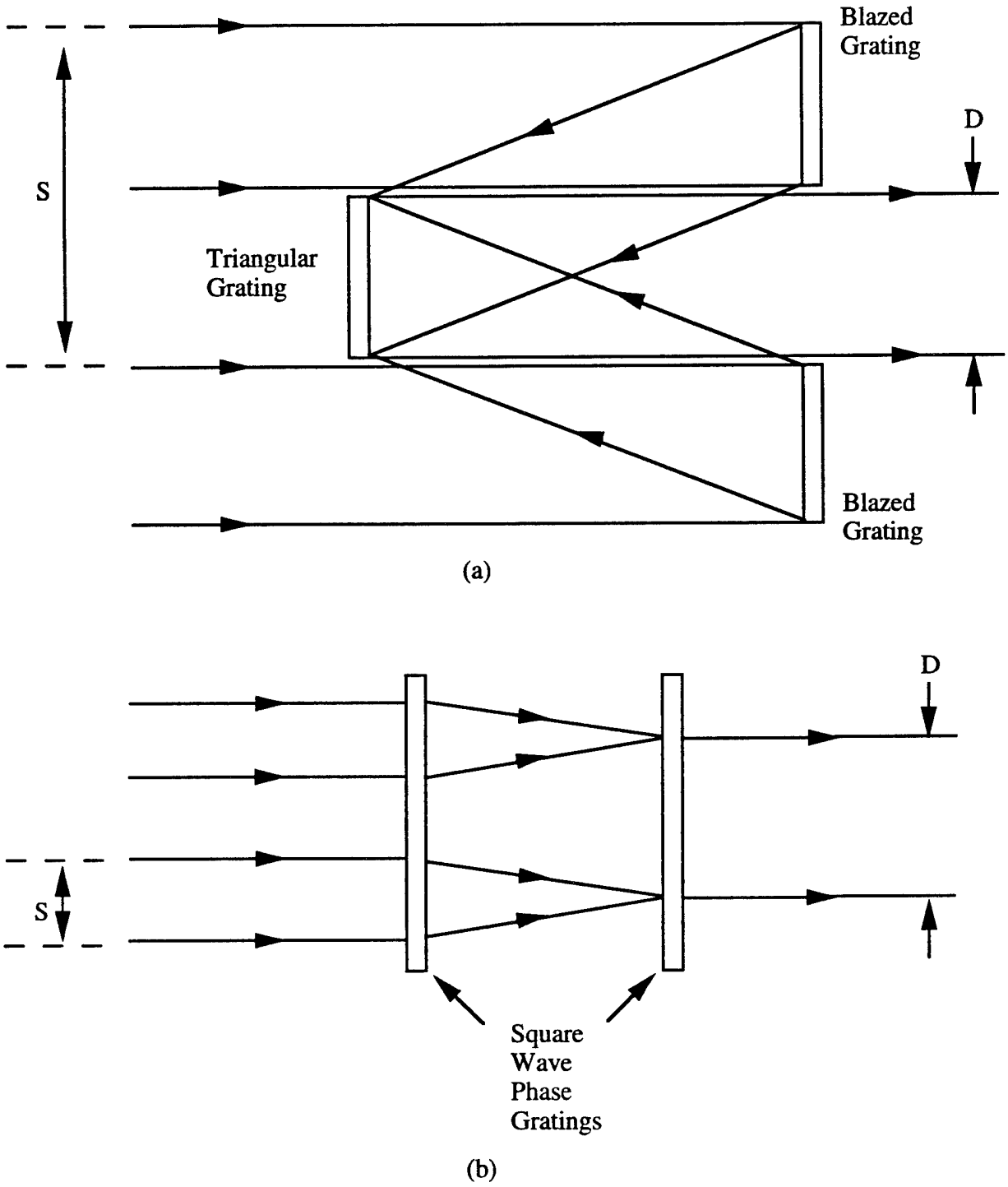

Figure 4-1: Grating interferometer designs. Reflective design (a) is preferred due to higher throughput, but design (b) is required when the shear distance S is less than or comparable to the aperture size D.

On the other hand, increasing the grating periodicity has the effect of decreasing the achromaticity of the interferometer, which in turn, reduces the field of view [4.2]. This constraint is given by

$$F < \sqrt{\frac{1}{s\Delta\lambda \tan\theta_{FOV}}} \qquad (4\text{-}2)$$

For s=6.3 mm, $\Delta\lambda$=160 nm, and θ_{FOV}=13.6°, both constraints are satisfied for the periodicity range F=50-65 1p/mm. Note that a 13.6° FOV is obtained by using only a 120 x 120 section of the IRC-160 detector array (160 x 120 in full) with a 25 mm imaging lens.

4.2.3 Basic Design Parameters

Based on the design issues described above, the resulting ground demo sensor parameters are summarized in Table 4-2. The sensor was designed to operate in four basic modes with differing levels of achievable spatial resolution:

MODE 1:	No pixel binning, 9.2 mm shear distance 53.2 mm LOS fringe spacing Roughly 0.3 m resolution in all 3 dimensions
MODE 2:	2 x 2 pixel binning, 6.3 mm shear distance 79.4 mm fringe spacing Roughly 0.4 m resolution in all 3 dimensions
MODE 3:	3 x 3 pixel binning, 4.7 mm shear distance 106.4 mm fringe spacing Roughly 0.5 x .4 resolution, 0.5 m height resolution
MODE 4:	3 x 3 pixel binning, 3.8 mm shear distance 131.6 mm fringe spacing Roughly 0.6 m resolution in all 3 dimensions

Table 4-2: Ground Demo Sensor Design Parameters

Center Wavelength:	4.7μm
Spectral Bandwidth:	160 nm
Aperture Diameter:	1.1 cm
Imaging Lens Focal Length:	25 mm
Interferometer Shear:	3.8-9.4 mm
Grating Periodicity:	50 1p/mm
Grating Separation:	1.3 cm
Detector Pitch:	50 μm (30% fill)
Along Track Detector Elements:	120 (40 unused)
Cross Track Detector Elements:	120
Detector Frame Time:	19.44 msec

4.3 SENSOR PERFORMANCE

The sensor performance model was exercised iteratively in conjunction with the hardware design effort [4.1] to arrive at the detailed sensor design parameters and corresponding performance estimates. The overall performance estimates at the center and edge (10m, 10m, 5m) of the 3-D sensor field-of-view for each of the sensor modes are summarized in Table 4-3. Of the four modes, Mode #2 exhibits the best balance of spatial resolution and 3-D sensitivity relative to the performance goals. Detailed sensor model output for this case is given in Tables 4-4 and 4-5.

4.4 REFERENCES

[4.1] *PRISM Ground Experiment*, ERIM Final Report No. 246840-1-F to Air Force WL/AARI on Contract DLA900-88-D-0392, Delivery Order 38, March 1995.

Table 4-3: Ground Demo Sensor Performance Estimates

Mode	Field Position	Resolution			3d MDTD
		X	Y	Z	
#1	(0m, 0m, 0m)	0.319m	0.340m	0.266m	0.41°C
	(10m, 10m, 5m)	0.319m	0.346m	0.266m	0.56°C
#2	(0m, 0m, 0m)	0.426m	0.453m	0.397m	0.09°C
	(10m, 10m, 5m)	0.426m	0.453m	0.397m	0.10°C
#3	(0m, 0m, 0m)	0.639m	0.653m	0.532m	0.04°C
	(10m, 10m, 5m)	0.639m	0.679m	0.532m	0.05°C
#4	(0m, 0m, 0m)	0.639m	0.679m	0.658m	0.03°C
	(10m, 10m, 5m)	0.629m	0.679m	0.658m	0.04°C

Table 4-4: Model Output for Ground Demo Design: Mode #2, Center of Field

```
Apr 30 1993 15:58:20                    case2c.out                    Page 2

  Diff. rot. misalignment        =   0.000 arcsec
  Piston error                   =   0.000 microns
  Grating frequency mismatch     =   0.005 lp/mm
  Lateral grating vibration      =   0.500 microns rms
  Within frame LOS jitter        =  20.000 microrad rms
  Boundary layer thickness       =   0.000 m

Phase error parameters:
  Atmosphere Cn2 at 1m         = 1.000000e-12 m-2/3
  Frame to frame jitter        =  20.000 microrad rms
  Along track nav. error       =   0.100 meters peak
  Vertical nav. error          =   0.100 meters peak
  Along track PRP drift        =   0.002 meters peak
  Vertical PRP drift           =   0.002 meters peak
  Frame rotation drift         =   1.000 arcmin peak

Detector parameters:
  Quantum efficiency           =   0.700
  Dark current density         =   0.000 microamp/cm2
  Read noise per frame         = 2000 electrons rms
  Quantization levels          = 14
  Charge storage capacity      = 120000000 electrons

INTERMEDIATE PARAMETERS
-----------------------

Imaging Geometry
  Slant range                  =   0.106 km
  Angle diversity              =  10.737 degrees
  Effective integration time   =  18.662 sec

Sensor Parameters
  LOS fringe spacing           =   7.939 cm
  Ground fringe spacing        =   7.939 cm
  Total number of frames       = 960
  Pixel limited IFOV           =   2.240 mrad
  Optics limited IFOV          =   3.000 mrad
  Diffraction limited IFOV     =   0.427 mrad
  Grating separation           =   1.303 cm

Target Parameters
  Mean temperature             = 300.000 K
  Edge equivalent dT           =   1.000 K
  Radiometric contrast         = 0.0170
  Spatial frequency factor     = 0.0792
  Scene spectral radiance      = 189.211 microflicks

ERROR BUDGET PARAMETERS
-----------------------

Optical Throughput
  Bias throughput              = 0.8500
  Signal throughput            = 0.1377

Modulation Depth
  Spatial contrast             = 0.0013
  Optical throughput           = 0.1620
  Random wavefront errors      = 0.9518
  Quadratic wavefront errors   = 0.8945
  Near field effect            = 0.9765
  Achromaticity                = 1.0000
  Mean tilt misalignment       = 1.0000
  Mean in-plane misalignment   = 0.9688
  Diff. x-tilt misalignment    = 1.0000
  Diff. y-tilt misalignment    = 1.0000
  Diff. in-plane misalignment  = 1.0000
  Piston error                 = 1.0000
  Grating frequency mismatch   = 0.9851
```

1

Table 4-4: Model Output for Ground Demo Design: Mode #2, Center of Field (Cont.)

```
Apr 30 1993 15:58:20                    case2c.out                    Page 1

DESIGN DESCRIPTION
------------------

Design:    MWIR ground demo sensor: Case #2

Date:      April 30, 1993

Comments: 2x2 binning, 6.3 mm baseline, center of field


INPUT PARAMETERS
----------------

Target parameters:
  Along track position          =   0.000 meters
  Cross track position          =   0.000 meters
  Vertical position             =   0.000 meters
  Mean emissivity               =   1.000
  Mean reflectance              =   0.000
  Illumination                  =   0.000 uW/cm2/um
  Target type                   = edge
  Left side temperature         = 299.500 K
  Right side temperature        = 300.500 K
  Relative centration           =   0.000
  Orientation angle             =   0.000 deg

Viewing geometry parameters:
  Collection type               = step stare
  Platform altitude             =   0.100 km
  Track length                  =  20.000 m
  Number of positions           = 40
  Side angle                    =  20.000 deg
  Forward angle                 =   0.000 deg

Sensor parameters:
  Center wavelength             =   4.700 microns
  Spectral bandwidth            =   0.160 microns
  Aperture diameter             =   1.100 cm
  Interferometer shear          =   0.630 cm
  Grating periodicity           =  50.000 lp/mm
  Achromaticity expansion       = none
  Expansion factor              =   1.000
  Wavefront collimation         = no
  Detector pitch                = 100.000 microns
  Detector element width        =  56.000 microns
  Optics blur circle            =  75.000 microns
  Along track elements          = 60
  Cross track elements          = 60
  Imaging lens focal length     =   2.500 cm
  Detector frame time           =  19.440 msec
  Number of integrated frames = 24
  Quadrature channel; I/Q samples

Optical throughput parameters:
  Atmospheric transmission      = 0.9000
  Cold filter transmission      = 0.8500
  Interferometer throughput     = 0.2000
  Optics throughput             = 0.9000
  Added path radiance           =    0.00 microflicks

Modulation error parameters:
  Optical quality (random)      = 0.0500 waves rms
  Optical quality (quadratic)   = 0.1300 waves peak
  Tilt misalignment             =  60.000 arcsec
  Rotational misalignment       =  30.000 arcsec
  Diff. x-tilt misalignment     =   0.000 arcsec
  Diff. y-tilt misalignment     =   0.000 arcsec
```

Table 4-4: Model Output for Ground Demo Design: Mode #2, Center of Field (Cont.)

```
Apr 30 1993 15:58:20                    case2c.out                    Page 3

  Lateral grating vibration     = 0.9518
  Within frame LOS jitter       = 0.9859
  Finite sampling interval      = 1.0000
  Aero-optical turbulence       = 1.0000

System Noise
  Signal shot noise             = 6281 electrons rms
  Detector dark noise           = 0 electrons rms
  Detector read noise           = 2000 electrons rms
  Quantization noise            = 2990 electrons rms

Random Phase Errors
  Atmospheric turbulence        = 0.0043 waves rms
  Frame to frame jitter         = 0.0268 waves rms

Deterministic Phase Errors
  Along track nav. error        = 0.0000 waves peak
  Vertical nav. error           = 0.0000 waves peak
  Along track PRP drift         = 0.0252 waves peak
  Vertical PRP drift            = 0.0000 waves peak
  Frame rotation                = 0.0000 waves peak

Sinusoidal Phase Errors
  None included

OBSERVABLE PARAMETERS
---------------------

Bias Signal
  Mean level                    = 39456147 electrons

Modulation Depth
  Mean level                    = 0.00016

Additive Noise
  Standard deviation            = 7238 electrons

Signal Phase
  Mean frequency                =   0.000 Hz

Phase Errors
  Random phase error            = 0.0271 waves rms
  Deterministic phase error     = 0.0252 waves peak
  Sinusoidal phase error        =   0.000 waves peak
  Resonant frequency            =   0.000 Hz

Signal Loss factors
  Signal sampling               =   1.414
  Phase errors                  =   0.984

PERFORMANCE PARAMETERS
----------------------

Radiometric Sensitivity Metrics
  NETD (2d imagery)             = 0.0136 C
  NETD (phase history)          = 0.2302 C
  NETD (3d imagery)             = 0.0261 C
  MDTD (3d imagery)             = 0.0915 C
  Threshold 3d SNR              = 3.5000 C

Target Detectability
  SNR (2d imagery)              = 26703.47
  SNR (phase history)           =    4.34
  SNR (3d imagery)              =   38.25

Spatial Resolution
  Along track sample spacing    =   0.426 m
  Cross track sample spacing    =   0.453 m
```

Table 4-4: Model Output for Ground Demo Design: Mode #2, Center of Field (Cont.)


```
  Along track footprint (3dB) =   0.319 m
  Cross track footprint (3dB) =   0.340 m
  Height resolution (IPR 3dB) =   0.397 m

Height Estimation (Cramer Rao)
  Height accuracy (threshold) =   0.063 m
  Height accuracy (target)    =   0.006 m

Spatial Coverage
  Along track field-of-view   =   19.16 m
  Cross track field-of-view   =   20.38 m
  Height field-of-view        =   15.88 m
  Coverage rate               =    0.00 km2/min
```

2

Table 4-5: Model Output for Ground Demo Design: Mode #2, Edge of Field

```
Apr 30 1993 16:29:01                    case2e.out                    Page 1

DESIGN DESCRIPTION
------------------

Design:    MWIR ground demo sensor: Case #2

Date:      April 30, 1993

Comments: 2x2 binning, 6.3 mm baseline, edge of field


INPUT PARAMETERS
----------------

Target parameters:
  Along track position          =  10.000 meters
  Cross track position          =  10.000 meters
  Vertical position             =   5.000 meters
  Mean emissivity               =   1.000
  Mean reflectance              =   0.000
  Illumination                  =   0.000 uW/cm2/um
  Target type                   = edge
  Left side temperature         = 299.500 K
  Right side temperature        = 300.500 K
  Relative centration           =   0.000
  Orientation angle             =   0.000 deg

Viewing geometry parameters:
  Collection type               = step stare
  Platform altitude             =   0.100 km
  Track length                  =  20.000 m
  Number of positions           = 40
  Side angle                    =  20.000 deg
  Forward angle                 =   0.000 deg

Sensor parameters:
  Center wavelength             =   4.700 microns
  Spectral bandwidth            =   0.160 microns
  Aperture diameter             =   1.100 cm
  Interferometer shear          =   0.630 cm
  Grating periodicity           =  50.000 lp/mm
  Achromaticity expansion       = none
  Expansion factor              =   1.000
  Wavefront collimation         = no
  Detector pitch                = 100.000 microns
  Detector element width        =  56.000 microns
  Optics blur circle            =  75.000 microns
  Along track elements          = 60
  Cross track elements          = 60
  Imaging lens focal length     =   2.500 cm
  Detector frame time           =  19.440 msec
  Number of integrated frames = 24
  Quadrature channel; I/Q samples

Optical throughput parameters:
  Atmospheric transmission      = 0.9000
  Cold filter transmission      = 0.8500
  Interferometer throughput     = 0.2000
  Optics throughput             = 0.9000
  Added path radiance           =    0.00 microflicks

Modulation error parameters:
  Optical quality (random)      = 0.0500 waves rms
  Optical quality (quadratic)   = 0.1300 waves peak
  Tilt misalignment             =  60.000 arcsec
  Rotational misalignment       =  30.000 arcsec
  Diff. x-tilt misalignment     =   0.000 arcsec
  Diff. y-tilt misalignment     =   0.000 arcsec
```

Table 4-5: Model Output for Ground Demo Design: Mode #2, Edge of Field (Cont.)


```
  Diff. rot. misalignment        =   0.000 arcsec
  Piston error                   =   0.000 microns
  Grating frequency mismatch     =   0.005 lp/mm
  Lateral grating vibration      =   0.500 microns rms
  Within frame LOS jitter        =  20.000 microrad rms
  Boundary layer thickness       =   0.000 m

Phase error parameters:
  Atmosphere Cn2 at 1m           = 1.000000e-12 m-2/3
  Frame to frame jitter          =  20.000 microrad rms
  Along track nav. error         =   0.100 meters peak
  Vertical nav. error            =   0.100 meters peak
  Along track PRP drift          =   0.002 meters peak
  Vertical PRP drift             =   0.002 meters peak
  Frame rotation drift           =   1.000 arcmin peak

Detector parameters:
  Quantum efficiency             =   0.700
  Dark current density           =   0.000 microamp/cm2
  Read noise per frame           = 2000 electrons rms
  Quantization levels            = 14
  Charge storage capacity        = 120000000 electrons

INTERMEDIATE PARAMETERS
-----------------------

Imaging Geometry
  Slant range                    =   0.106 km
  Angle diversity                =  10.737 degrees
  Effective integration time     =  18.662 sec

Sensor Parameters
  LOS fringe spacing             =   7.939 cm
  Ground fringe spacing          =   7.939 cm
  Total number of frames         = 960
  Pixel limited IFOV             =   2.240 mrad
  Optics limited IFOV            =   3.000 mrad
  Diffraction limited IFOV       =   0.427 mrad
  Grating separation             =   1.303 cm

Target Parameters
  Mean temperature               = 300.000 K
  Edge equivalent dT             =   1.000 K
  Radiometric contrast           = 0.0170
  Spatial frequency factor       = 0.0792
  Scene spectral radiance        = 189.211 microflicks

ERROR BUDGET PARAMETERS
-----------------------

Optical Throughput
  Bias throughput                = 0.8500
  Signal throughput              = 0.1377

Modulation Depth
  Spatial contrast               = 0.0013
  Optical throughput             = 0.1620
  Random wavefront errors        = 0.9518
  Quadratic wavefront errors     = 0.8945
  Near field effect              = 0.9765
  Achromaticity                  = 0.9085
  Mean tilt misalignment         = 0.9999
  Mean in-plane misalignment     = 0.9688
  Diff. x-tilt misalignment      = 1.0000
  Diff. y-tilt misalignment      = 1.0000
  Diff. in-plane misalignment    = 1.0000
  Piston error                   = 1.0000
  Grating frequency mismatch     = 0.9851
```

1

Table 4-5: Model Output for Ground Demo Design: Mode #2, Edge of Field (Cont.)

```
Apr 30 1993 16:29:01                case2e.out                    Page 3

  Lateral grating vibration    = 0.9518
  Within frame LOS jitter      = 0.9859
  Finite sampling interval     = 1.0000
  Aero-optical turbulence      = 1.0000

System Noise
  Signal shot noise            = 6281 electrons rms
  Detector dark noise          = 0 electrons rms
  Detector read noise          = 2000 electrons rms
  Quantization noise           = 2990 electrons rms

Random Phase Errors
  Atmospheric turbulence       = 0.0043 waves rms
  Frame to frame jitter        = 0.0268 waves rms

Deterministic Phase Errors
  Along track nav. error       = 0.0592 waves peak
  Vertical nav. error          = 0.1184 waves peak
  Along track PRP drift        = 0.0252 waves peak
  Vertical PRP drift           = 0.0000 waves peak
  Frame rotation               = 0.0366 waves peak

Sinusoidal Phase Errors
  None included

OBSERVABLE PARAMETERS
---------------------

Bias Signal
  Mean level                   = 39456147 electrons

Modulation Depth
  Mean level                   = 0.00015

Additive Noise
  Standard deviation           = 7238 electrons

Signal Phase
  Mean frequency               =   0.675 Hz

Phase Errors
  Random phase error           = 0.0271 waves rms
  Deterministic phase error    = 0.1396 waves peak
  Sinusoidal phase error       =   0.000 waves peak
  Resonant frequency           =   0.000 Hz

Signal Loss factors
  Signal sampling              =   1.414
  Phase errors                 =   0.951

PERFORMANCE PARAMETERS
----------------------

Radiometric Sensitivity Metrics
  NETD (2d imagery)            = 0.0136 C
  NETD (phase history)         = 0.2534 C
  NETD (3d imagery)            = 0.0298 C
  MDTD (3d imagery)            = 0.1043 C
  Threshold 3d SNR             = 3.5000 C

Target Detectability
  SNR (2d imagery)             = 26703.47
  SNR (phase history)          =    3.95
  SNR (3d imagery)             =   33.57

Spatial Resolution
  Along track sample spacing   =   0.426 m
  Cross track sample spacing   =   0.453 m
```

Table 4-5: Model Output for Ground Demo Design: Mode #2, Edge of Field (Cont.)


```
  Along track footprint (3dB) =   0.319 m
  Cross track footprint (3dB) =   0.340 m
  Height resolution (IPR 3dB) =   0.397 m

Height Estimation (Cramer Rao)
  Height accuracy (threshold) =   0.063 m
  Height accuracy (target)    =   0.007 m

Spatial Coverage
  Along track field-of-view   =   19.16 m
  Cross track field-of-view   =   20.38 m
  Height field-of-view        =   15.88 m
  Coverage rate               =    0.00 km2/min
```

Intentionally Left Blank

5.0 SIMULATION-BASED SENSOR MODEL

This section overviews a simulation-based sensor model developed to produce simulated PRISM phase histories and 3-D imagery to, among other things, compare with signatures collected with the ground demonstration sensor.

5.1 MODELING APPROACH

Figure 5-1 shows a block diagram of the sensor modeling components. The upper line contains the performance model (named *psmodel*) described in Section 3. As discussed earlier, *psmodel* takes detailed sensor design parameters and computes performance metrics useful for sensor design (ground and airborne) and detection modeling. As will be described, these metrics are also used to parameterize sensor performance in the signature simulation process.

Two types of target signatures can be simulated by the tools generated in this program. The first type includes test targets such as bar and edge targets, and the second includes complex targets. In both cases, the simulation begins by generating a sequence of high spatial resolution frames, each corresponding to a particular sensor look angle during the synthetic aperture time. The frames are calibrated with respect to in-band scene radiance, and are assumed to exhibit spatial resolution of roughly an order of magnitude finer than the virtual fringe period of the sensor being modeled.

In the case of the test targets, the high resolution frame sequence is generated directly with program named *mkseq*. Complex targets are generated in a three step process. In the first step, a 3-D thermal target model is generated by the SIRIM [5.1] program from a constructed solid geometry (CGS) model of the target. In parallel, a background model is generated by "painting" a ground surface with a background pattern described by a power spectral density (PSD). Finally, the target and background are combined and raytraced for each sensor line-of-sight. This last step is also performed within the SIRIM program.

Once a high resolution frame sequence has been generated, the next step in the simulation is to simulate the PRISM phase history. This is performed by the program *seqtoph*, which performs the bandpass filtering and introduces realizations of the various sensor error sources (such as noise and phase errors) based on performance metrics output from *psmodel*. The resulting phase history

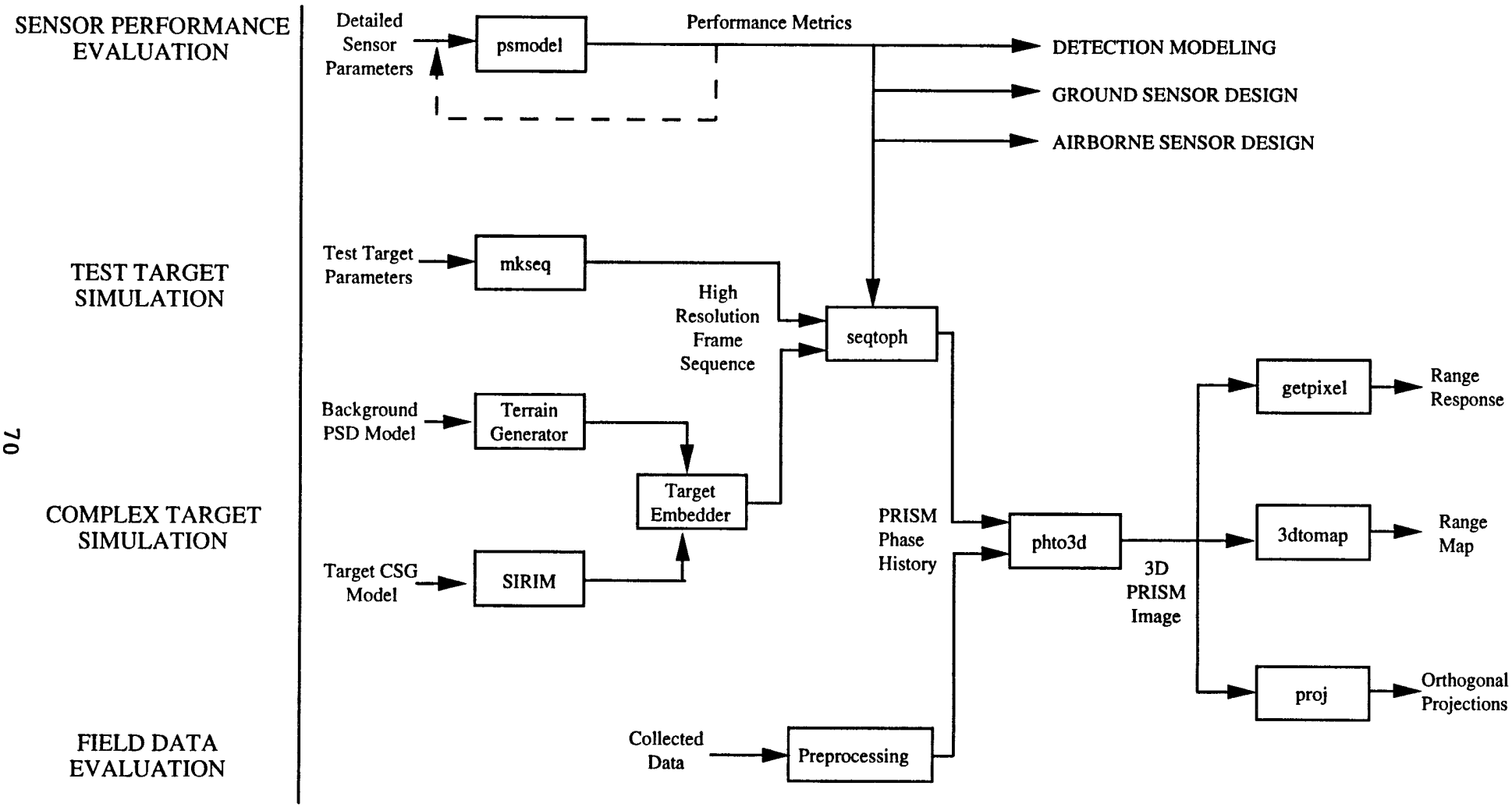

Figure 5-1: PRISM sensor modeling components

contains in-phase (I), quadrature (Q), and bias (B) components of the same form as the ground demonstration sensor.

Because they are of the same form, simulated and collected phase histories are processed into 3-D images, using the same image formation program, *phto3d*. Once processed into this form, various utilities have been written for image analysis and display, including the generation of range response function (*getpixel*), thresholded and range-gated range maps (*3dtomap*), and orthogonal projections (*proj*).

5.2 TEST TARGET MODELING (MKSEQ)

The program *mkseq* generates a simulated high resolution image sequence for a PRISM sensor viewing geometry of a uniform rectangular target in a uniform background with different apparent temperatures, but on the same surface. By altering the input parameters, bar and edge targets can be accommodated.

The following parameters are input to the model:

N_x	number of along track samples
N_y	number of cross track samples
x_0	along track target center
y_0	cross track target center
z_0	range target center
W	target width (along track)
H	target height (cross track)
T_t	target apparent temperature
T_b	background apparent temperature
type	target type (bar or edge)
λ_0	center wavelength
$\Delta\lambda$	spectral bandwidth
x_{min}	minimum along track position of frame sequence
x_{max}	maximum along track position of frame sequence
y_{min}	minimum cross track position of frame sequence
y_{max}	maximum cross track position of frame sequence
R_k	sensor slant range for M_f frames
θ_k	sensor angular position in slant plane for M_f frames

Figure 5-2 illustrates the definitions of R and θ.

Let L_t and L_b denote the target and background radiance as computed by

$$L_{t,b} = \frac{2hc^2 \Delta\lambda}{\lambda^5} \frac{1}{e^{hc/\lambda k T_{t,b}} - 1} \tag{5-1}$$

For an edge target

$$L_k(x,y) = \begin{cases} L_b & x > d_{cntr} \text{ or } |y| > H/2 \\ L_t & x < d_{cntr} \text{ and } |y| < H/2 \end{cases} \tag{5-2}$$

where

$$d_{cntr} = x_0 \cos\theta_k + z_0 \sin\theta_k \tag{5-3}$$

For a bar target

$$L_k(x,y) = \begin{cases} L_b & x < d_{\min} \text{ or } x > d_{\max} \text{ or } |y| > H/2 \\ L_t & x > d_{\min} \text{ or } x < d_{\max} \text{ and } |y| < H/2 \end{cases} \tag{5-4}$$

where

$$d_{\min} = \left(x_0 - \frac{W}{2}\right) \cos\theta_k + z_0 \sin\theta_k \tag{5-5}$$

$$d_{\max} = \left(x_0 + \frac{W}{2}\right) \cos\theta_k + z_0 \sin\theta_k \tag{5-6}$$

$L_k(x,y)$ defines the kth high resolution frame for each angle θ_k of the sequence.

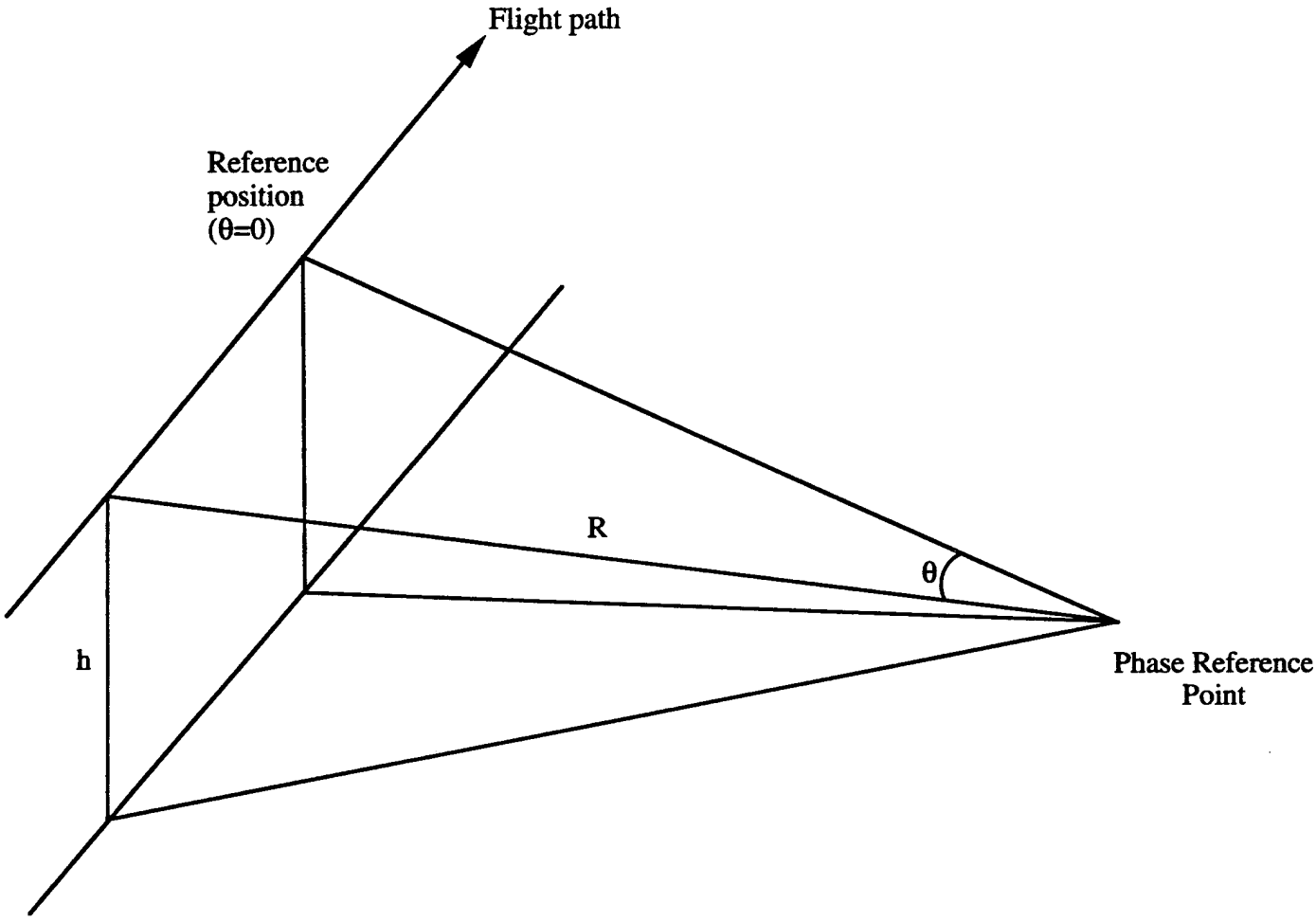

Figure 5-2: Definition of R, θ coordinates.

5.3 SIRIM TARGET MODELING

5.3.1 SIRIM Overview

The Simulated Infrared Image (SIRIM) software package consists of four modules: VOXCRE, VOXSUN, SVOXTMP and RADCLC. The system function diagram follows in Figure 5-3. For initial input, SIRIM relies upon a target geometry description in a specified format. The principle outputs of SIRIM are a set of one to four digital simulated infrared images corresponding to polarization modes.

The SIRIM model provides a unique approach to the thermal modeling of objects. This uniqueness is primarily manifested in an automatic method to discretize a three-dimensional object in the VOXCRE code. The volume of the object is subdivided into elements called voxels. The voxels are simply cubic solids that fill the volume of the object. The SIRIM model is unique also in that it combines the CSG geometry model, an automatic voxel mesh generator, a thermal diffusion model and the radiance calculation into one integrated thermal signature prediction code.

In the SVOXTMP module, thermal prediction is performed by advancing, in time, the differential equation which models thermal diffusion. The voxel discretization of the volume allows thermal transport throughout the object to be modeled numerically using a finite difference approach. Thermal source inputs at any fixed spatial location are defined as a function of time. The discretization of time is selectable by the user. SVOXTMP produces the three-dimensional temperature distribution of the object as a function of time but independent of sensor or viewing geometry. The temperature distribution may be saved at any interval chosen by the user. The temperature prediction calculations for complex and fine resolution objects are intensive and time consuming. They represent the major processing load of the simulation.

The calculation of the absolute radiance is done in the RADCLC module. It is based on the surface temperatures as well as the reflectance effects of the surrounding environment. The energy that is emitted and that which is reflected is computed based on the observer viewing angle and a desired wavelength band. RADCLC projects the radiance data into the imaging plane using ray tracing techniques. Typically, RADCLC produces imagery in radiance units of watts per meters squared per steradian. The generation of the radiance over a defined sensor spectral band can be accomplished and can be weighted as a function of wavelength. To compute the radiance values, Stokes vector and Mueller matrix analysis is used.

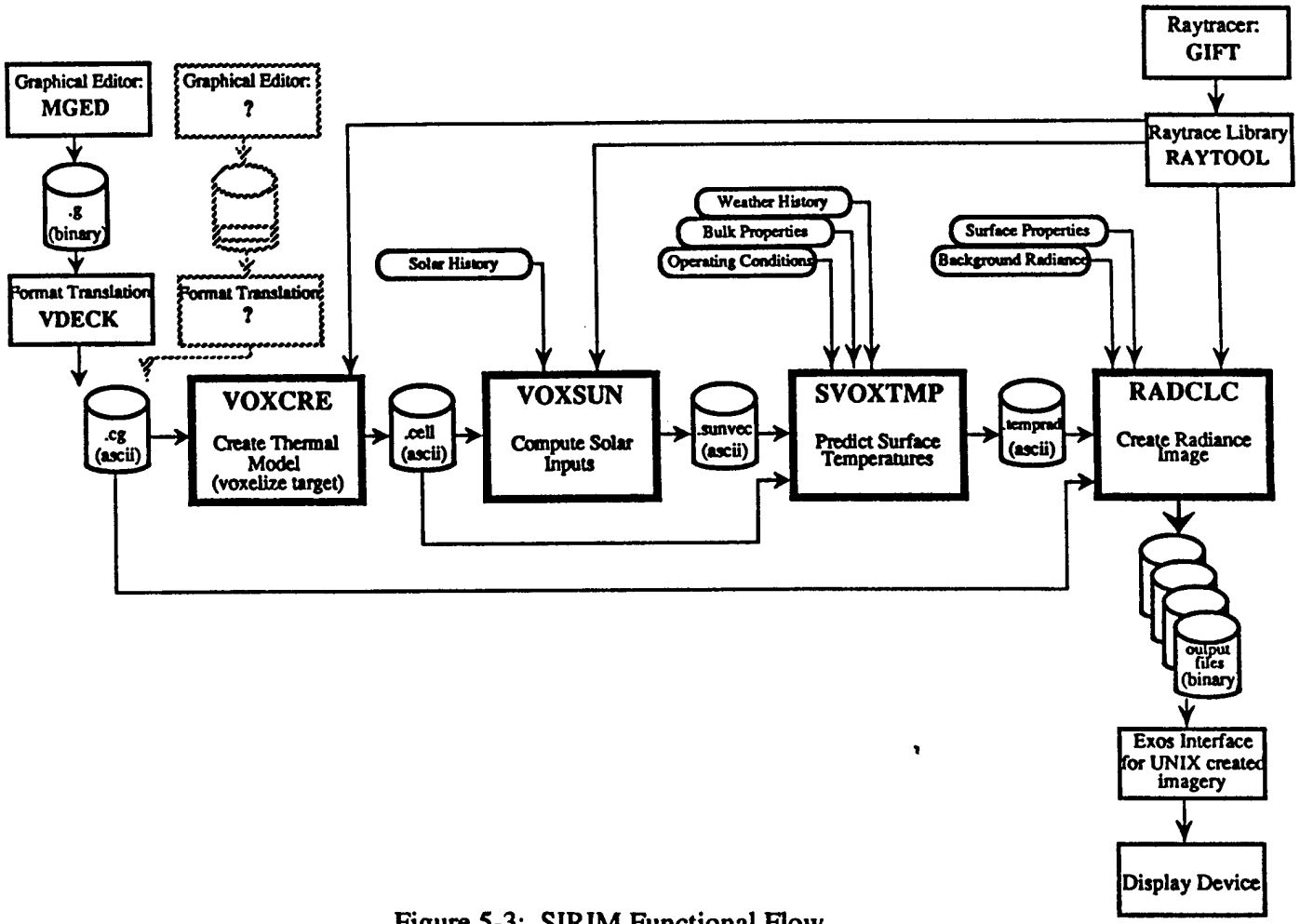

Figure 5-3: SIRIM Functional Flow

5.3.2 Modifications to Model

Two modifications were made to SIRIM to accommodate PRISM signature simulation. The first involved improving the spatial resolution provided. Prior to this effort, thermal modeling was performed using 2 cm voxels, which is marginal for PRISM simulations with roughly 5-10 cm fringe spacing. This was improved to 1 cm for this effort. The penalty for this modification was a significantly increased run time.

The second modification involved altering the ray trace program to provide for perspective viewing and to insure that the in-plane rotation of the frames maintain proper orientation with respect to the rotation axis defined in the ground experiment by two beacons. With respect to Figure 5-4, the normal convention for SIRIM is to maintain the frame column vector in the vertical (z,y) plane. In the PRISM operation, however, the sensor is rotated about the line-of-sight vector such that the column vector $\hat{c}$ is always colinear with $\hat{w}$.

The amount of rotation can be determined by the difference between the normal to the vertical plane at each sensor location and the normal to the plane defined by the rotation and line-of-sight vectors. For a sensor position L along the collection track, the line-of-sight unit vector is given by

$$\hat{R}_L = \frac{1}{\sqrt{L^2 + h^2/\cos^2\phi}}\left(-L\hat{x} + h\tan\phi\hat{y} + h\hat{z}\right) \qquad (5\text{-}7)$$

The row vector for the conventional SIRIM raytrace is the normal to the vertical plane:

$$\begin{aligned} {}_L &= \frac{\hat{h}\,x\,\hat{R}}{\left|\hat{h}\,x\,\hat{R}\right|} \\ &= \frac{1}{\sqrt{L^2 + h^2\tan^2\phi}}\left(h\tan\phi\,\hat{x} + L\hat{y}\right) \end{aligned} \qquad (5\text{-}8)$$

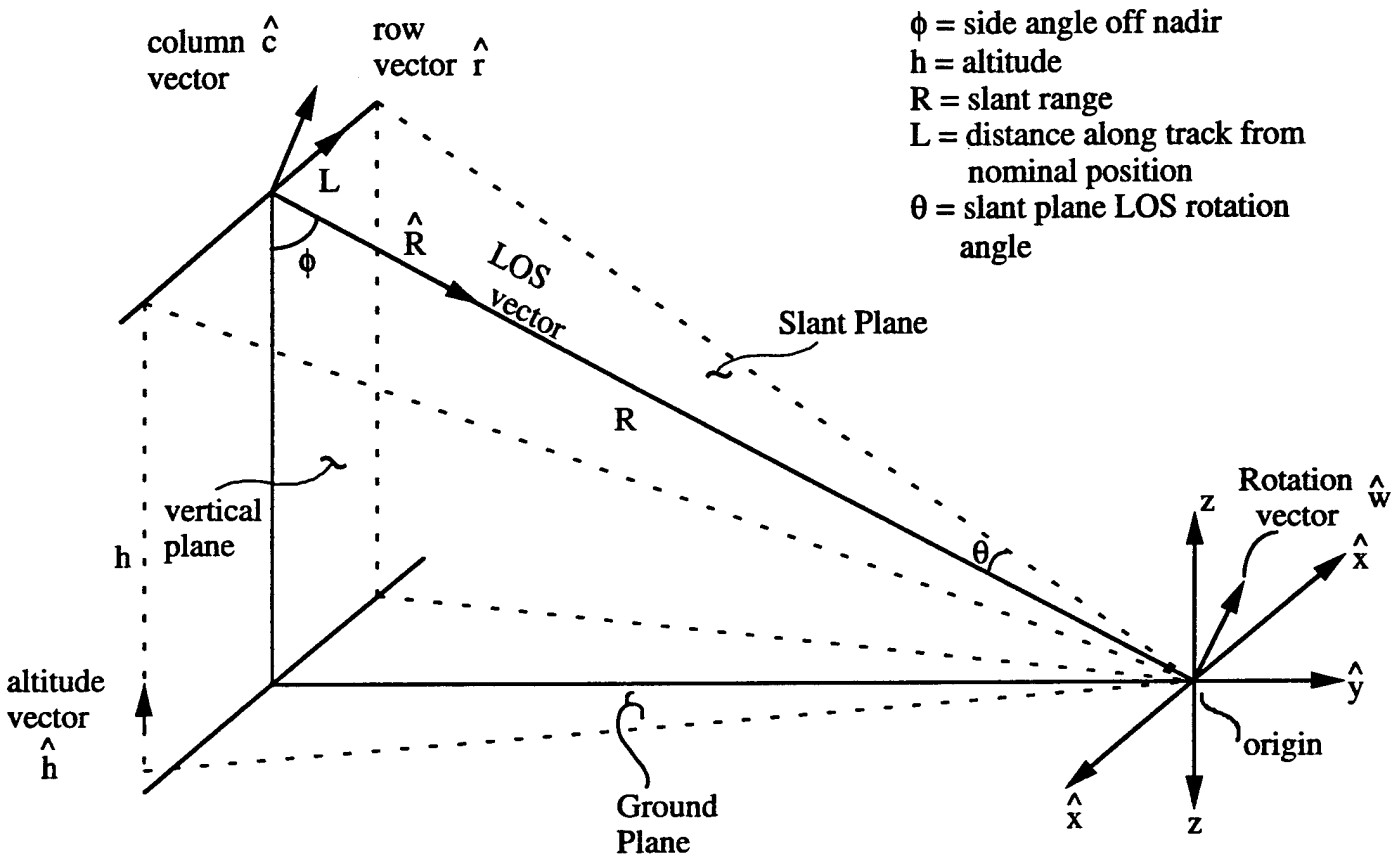

$\hat{x}$, $\hat{y}$, $\hat{z}$ are fixed ground plane coordinates with origin at rotation center

Figure 5-4: SIRIM Viewing Geometry

For the properly rotated frame, the row vector is given by

$$\begin{aligned}\hat{r}_L &= \frac{\hat{c}_L \, x \, \hat{R}_L}{\left|c_L \, x \, \hat{R}_L\right|} \\ &= \frac{1}{\sqrt{L^2 + h^2/\cos^2\phi}}\left[(h\cos\phi + h\sin\phi\tan\phi)\hat{x} + L\sin\phi\hat{y} + L\cos\phi\hat{z}\right]\end{aligned} \tag{5-9}$$

where the column vector $\hat{c}_L$ is colinear with the rotation vector

$$\hat{c}_L = \hat{w} = \cos\phi\hat{y} - \sin\phi\hat{z} \tag{5-10}$$

The amount of rotation is the angular difference between $\hat{r}_L$ and $\hat{n}_L$:

$$\begin{aligned}\theta_{rot} &= \sin^{-1}\left\{\left|\hat{n}_L \, x \, \hat{r}_L\right|\right\} \\ &= \sin^{-1}\left\{\frac{-L\cos\phi}{\sqrt{L^2 + h^2\tan^2\phi}}\right\}\end{aligned} \tag{5-11}$$

This was implemented by numerically rotating the frame sequence after the conventional SIRIM raytrace was performed.

5.4 BACKGROUND MODELING

Due to its bandpass nature, the PRISM sensor is very sensitive to target edge effects, or transition regions between a target and the surrounding background. Therefore, to realistically model PRISM 3-D target signatures, it is necessary to imbed the target in some sort of local background. Full 3-D background modeling at high spatial resolution in the infrared is very difficult. On the other hand, we can certainly envision cases in which the local terrain around a target is fairly flat and random. In this case, it is sufficient to model the background as a ground plane with a pseudo-random spatial radiance pattern.

This approach was employed in the PRISM signature modeling of complex targets. First, a ground plane was defined and "painted" with a radiance pattern, and views of the painted ground plane were generated for each of the sensor aspects. Next, a corresponding set of images were generated within SIRIM for the synthetic target on a ground plane of negative radiance. Finally,

the radiance values for all rays landing on the ground plane (flagged by the negative radiance) during target ray trace were substituted with the corresponding values of the background image.

The pattern of the background ground plane is a gaussian random process defined through its power spectral density (PSD). The PSD is defined as the expected value of the squared magnitude of the Fourier Transform of the background radiance pattern

$$P(f_x, f_y) = E\left[\left|\Im\{L(x,y)\}\right|^2\right] \tag{5-12}$$

A background model based on a parametric rotationally symmetric PSD was used:

$$P(f) = \frac{L_0^2}{1+(f/f_0)^2} \tag{5-13}$$

where

$$f = \sqrt{f_x^2 + f_y^2} \tag{5-14}$$

Two parameters define the background PSD: the mean radiance L_0, and the break frequency f_0. The latter characterizes the spatial frequency content of the background pattern, and can be related to an edge equivalent temperature difference, ΔT_{eq}. By definition of ΔT_{eq}:

$$\frac{P(1/\Lambda)}{P(0)} = \left[\frac{\Lambda}{2\pi\rho_x}\left(\frac{hc}{\lambda K T^2}\Delta T_{eq}\right)^{-1}\right] \tag{5-15}$$

Combining Eqs. 5-13 and 5-15 and solving for f_0:

$$f_0 = \left[\frac{4\pi^2\rho_x^2\lambda^2K^2T^4}{h^2c^2\Delta T_{eq}^2} - \Lambda^2\right] \tag{5-16}$$

Normally the fringe spatial frequency is significantly higher than the background pattern break frequency $(f_0 << 1/\Lambda)$ and Eq. (5-16) can be approximated by

$$f_0 \cong \frac{1}{2\pi\rho_x}\frac{hc}{\lambda K T^2}\Delta T_{eq} \tag{5-17}$$

5.5 SENSOR PHASE HISTORY MODELING (SEQTOPH)

The program *seqtoph* generates a simulated PRISM phase history from a high resolution image sequence based on sensor parameters and performance metrics. This accommodates both test target and complex target modeling.

The following parameters are input to the model:

δ_x	input image sample spacing in x (along track)
δ_y	input image sample spacing in y (cross track)
N_x	number of x samples in input image
N_y	number of y samples in input image
M_f	number of frames in input image sequence
ρ_x	along track spatial footprint of sensor
ρ_y	cross track spatial footprint of sensor
P_x	along track sampling spacing of sensor
P_y	cross track sample spacing of sensor
wtype	shape of pixel spatial footprint: rectangular, gaussian, sinc or airy
h_{pk}	peak of spatial footprint function
Λ	virtual fringe period
λ_0	center wavelength of sensor
Ω	solid angle of sensor aperture from target
T_f	frame integration time
η	detector quantum efficiency over band
samp	sampling method 1) single channel; real part only 2) single channel; linear phase modulation 3) single channel; wideband FM 4) dual channel; real part only 5) quadrature channel; I/Q samples
b_m	FM modulation depth (where applicable)
F_s	downsampling/integration factor
t_b	bias optical sensor throughput
m_s	sensor modulation depth
σ_d	additive sensor noise in rms electrons
σ_e	wideband rms phase error in radians

ϕ_e	peak quadrature phase error in radians
b_e	sinusoidal phase error amplitude in radians
n_e	number of sinusoidal phase error cycles in total collection time
minsub	switch providing subtraction of subpatch minimum radiance where desired

The generation of the PRISM phase history proceeds on a frame by frame basis. Let $L_k(x,y)$ denote the *kth* frame of M_f input images. First, the bias photoelectron level is computed for each PRISM sensor pixel

$$N_b(x_0,y_0) = K \iint_{subpatch} \tilde{h}(x-x_0, y-y_0) L_k(x,y)\,dxdy \tag{5-18}$$

where K is a radiometric constant, $\tilde{h}(x,y)$ is the sensor spatial footprint function, and the limits of the subpatch integration are $-\rho_x \le x - x_0 \le \rho_x$ and $-\rho_y \le y - y_0 \le \rho_y$ where $(x_0, y_0)$is the center of a PRISM sensor pixel.

The radiometric constant K is given by

$$K = \frac{\Omega T_f \eta\, t_b \lambda_0}{hc} \tag{5-19}$$

The sensor spatial footprint function $\tilde{h}(x,y)$ is user-selectable, depending on whether the sensor is diffraction, detector, or blur limited. Four options have been implemented

$$\tilde{h}(x,y) = \begin{cases} h_{pk}\, rect\left(\dfrac{x}{\rho_x}, \dfrac{y}{\rho_y}\right) & \text{RECTANGULAR} \\ h_{pk}\, e^{-2.7726\left[\left(\frac{x}{\rho_x}\right)^2 + \left(\frac{y}{\rho_y}\right)^2\right]} & \text{GAUSSIAN} \\ h_{pk}\, \mathrm{sinc}^2\left[\dfrac{2.784}{\pi\rho_x}(x), \dfrac{2.784}{\pi\rho_y}(y)\right] & \text{SINC} \\ h_{pk}\, \mathrm{jinc}^2\left[\dfrac{3.24x}{\rho_x}, \dfrac{3.24y}{\rho_y}\right] & \text{AIRY} \end{cases} \tag{5-20}$$

where

$$rect\,(x,y) = \begin{cases} 1 & |x| \le \frac{1}{2} \text{and } |y| \le \frac{1}{2} \\ 0 & \text{otherwise} \end{cases} \tag{5-21}$$

$$\text{sinc}\,(x,y) = \frac{\sin(\pi x)\,\sin(\pi y)}{(\pi x)\,(\pi y)} \tag{5-22}$$

$$jinc\,(x,y) = \frac{2J_1(x)}{x}\frac{2J_1(y)}{y} \tag{5-23}$$

Computation of the in-phase (I), quadrature (Q), and bias (B) components of the phase history is dependent on the signal sampling method. This process is not simulated directly, but its impact on the phase history is approximated. For all sampling methods, we begin with a realization of the signal phase error

$$\phi_{error} = \mathbf{N}(0,\sigma_e) + \frac{4\phi_e\left(k - \frac{M_f}{2}\right)^2}{M_f^2} + b_e \sin\left(2\pi n_e \frac{k}{M_f}\right) \tag{5-24}$$

where $\mathbf{N}(\mu,\sigma)$ is a Gaussian random process with mean μ and variance σ^2.

For single channel, real part only sampling, the quadrature signal component is not measured $\left[Q_k(x_0,y_0) = 0\right]$. The in-phase component is given initially by

$$\begin{aligned} I_k'(x_0,y_0) = m_s K \iint_{subpatch} \tilde{h}(x-x_0, y-y_0) L_k(x,y) \cos\left(\frac{2\pi x}{\Lambda} + \theta_{error}\right) dxdy \\ + \mathrm{N_b}(x_0,y_0) + \mathbf{N}\left[0, \sqrt{\frac{\mathrm{N_b}(x_0,y_0) + \sigma_d^2}{F_S}}\right] \end{aligned} \tag{5-25}$$

For this sampling method, the measured in-phase component contains a bias that is estimated and then extracted from $I'(x_0,y_0)$:

$$B_k(x_0,y_0) = \frac{1}{M_f}\sum_{k=1}^{M_f} I_k'(x_0,y_0) \tag{5-26}$$

$$I_k(x_0,y_0) = I'(x_0,y_0) - B(x_0,y_0)\ \forall k \tag{5-27}$$

For single channel, linear phase modulation sampling, all three phase history components and generated directly:

$$\begin{aligned} I'_k(x_0,y_0) = m_s K \iint_{subpatch} \tilde{h}(x-x_0,y-y_0) L_k(x,y) \cos\left(\frac{2\pi x}{\Lambda} + \phi_{error}\right) dxdy \\ + \mathbf{N}\left[0, \sqrt{\frac{4\mathrm{N_b}(x_0,y_0) + 4\sigma_d^2}{F_S}}\right] \end{aligned} \tag{5-28}$$

$$\begin{aligned} Q_k(x_0,y_0) = m_s K \iint_{subpatch} \tilde{h}(x-x_0,y-y_0) L_k(x,y) \sin\left(\frac{2\pi x}{\Lambda} + \phi_{error}\right) dxdy \\ + \mathbf{N}\left[0, \sqrt{\frac{4\mathrm{N_b}(x_0,y_0) + 4\sigma_d^2}{F_S}}\right] \end{aligned} \tag{5-29}$$

$$B_k(x_0,y_0) = N_b(x_0,y_0) + \mathbf{N}\left[0, \sqrt{\frac{\mathrm{N_b}(x_0,y_0) + \sigma_d^2}{F_S}}\right] \tag{5-30}$$

For single channel, wideband FM sampling, the in-phase and quadrature components are generated using Eqs. (5-28) and (5-29) with a slightly different noise standard deviation σ_n. For the I component

$$\sigma_n = \sqrt{\frac{\mathrm{N_b}(x_0,y_0) + \sigma_d^2}{F_S J_2^2(b_m)}} \tag{5-31}$$

For the Q component

$$\sigma_n = \sqrt{\frac{\mathrm{N_b}(x_0,y_0) + \sigma_d^2}{F_S J_1^2(b_m)}} \tag{5-32}$$

The bias component is computed by

$$B_k(x_0,y_0) = \mathrm{J}_0(b_m)m_s K \iint_{subpatch} \tilde{h}(x-x_0,y-y_0)L_K(x,y)\cos\left(\frac{2\pi x}{\Lambda}+\theta_{error}\right)dxdy$$
$$+\mathrm{N_b}(x_0,y_0)+\mathrm{N}\left[0,\sqrt{\frac{\mathrm{N_b}(x_0,y_0)+\sigma_d^2}{F_S}}\right] \tag{5-33}$$

For dual channel, real part only sampling, the quadrature component is not measured $\left[Q_k(x_0,y_0)=0\right]$. The in-phase component is generated using Eq. (5-28) with a slightly different noise standard deviation

$$\sigma_n = \sqrt{\frac{\mathrm{N_b}(x_0,y_0)+\sigma_d^2}{2F_S}} \tag{5-34}$$

The bias component is computed using Eq. (5-30), but with the same noise standard deviation given by Eq. (5-34).

For quadrature channel sampling, Eqs. (5-28), (5-29), and (5-30) are used, but with noise standard deviations defined by Eq. (5-34) for the I and Q components and

$$\sigma_n = \sqrt{\frac{\mathrm{N_b}(x_0,y_0)+\sigma_d^2}{4F_S}} \tag{5-35}$$

for the bias component.

The minimum subtraction switch allows the user to eliminate some of the effects of the residual bias signal. This is accomplished by determining and removing the minimum level of $L_k(x,y)$ over each subpatch. All spatial integrations are performed discretely at the sampling provided by the input image sequence.

5.6 3-D IMAGE FORMATION (PHTO3D)

The formation of a three-dimensional image from a PRISM phase history is accomplished through the pixel-walk compensated matched filtering process described in Section 2.8. This is computed as a series of one-dimensional, formatted Discrete Fourier Transforms (DFTs) where the

input signal window walks along spatial along track pixels as sensor aspect changes. To improve the pixel walk compensation, the 3-D image is generally computed on an oversampled along track spatial grid.

The following parameters are input to the model:

M_x	number of along track samples
M_y	number of cross track samples
M_f	number of frames in sequence
Λ'	angular virtual fringe period
P'_x	angular along track sample spacing
P'_y	angular cross track sample spacing
x'_{ctr}	angle of along track center of rotation
y'_{ctr}	angle of along track center of LOS
R_K	sensor slant range for M_f frames
θ_K	sensor angular position in slant plane for M_f frames
M_z	number of computed samples in LOS range
$z_{\min}$	minimum LOS range position
$z_{\max}$	maximum LOS range position
n_x	upsampling factor in x direction
n_y	upsampling factor in y direction
I_{norm}	normalization factor
ptype	processing algorithm
bsub	bias subtraction method

Bias subtraction is performed prior to transformation to remove residual signal bias. One of three methods can be chosen: no bias subtraction, standard bias subtraction, and drift compensated bias subtraction. Standard bias subtraction merely removes the mean value of the I and Q signals over the M_f frames, independently for each spatial pixel. Drift compensated bias subtraction attempts to remove bias leakage into the I and Q channels. It is performed first by computing the means of the three signals over the M_f frames $\left[\mu_I(x_0,y_0),\mu_Q(x_0,y_0),\mu_B(x_0,y_0)\right]$ and then extracting a proportional part of the bias signal from the I and Q signals:

$$I_k(x_0,y_0) = I'_k(x_0,y_0) - \frac{\mu_I(x_0,y_0)}{\mu_B(x_0,y_0)} B_k(x_0,y_0) \qquad (5\text{-}36)$$

$$Q_k(x_0,y_0) = Q'_k(x_0,y_0) - \frac{\mu_Q(x_0,y_0)}{\mu_B(x_0,y_0)} B_k(x_0,y_0) \tag{5-37}$$

The primed I and Q signals refer to the uncompensated phase histories.

Three image formation algorithms exist. The baseline algorithm is a DFT with no pixel walk compensation and no fringe curvature correction. Using this method, the image magnitude is given by

$$I(x,y,z) = I_{norm} \left| \sum_{k=1}^{M_f} \left[I_k(x',y') + i\, Q_k(x',y') \right] e^{-i\frac{2\pi d_k(x',y')}{R_k}} \right| \tag{5-38}$$

where $d_k(x',y')$ is the along track pixel distance

$$d_k(x',y') = (x' - x'_{ctr}) R_k \cos\theta_k + z \sin\theta_k \tag{5-39}$$

and (x',y') are angular along and cross track coordinates. This is computed on a spatial grid in the three dimensions given by

$$x = (ip'_x - x'_{ctr})\overline{R} \qquad \mathrm{i} = 0 \text{ to } \mathrm{M_x} - 1 \tag{5-40}$$

$$y = (jp'_y - y'_{ctr})\overline{R} \qquad \mathrm{j} = 0 \text{ to } \mathrm{M_y} - 1 \tag{5-41}$$

$$z = z_{\min} + \frac{\ell(z_{\max} - z_{\min})}{M_z - 1} \qquad \ell = 0 \text{ to } \mathrm{M_z} - 1 \tag{5-42}$$

where $\overline{R}$ is the mean scene range, $x' = ip'_x$, and $y' = jp'_y$.

Pixel walk compensation is incorporated by drifting through the phase history in the DFT process, and upsampling in the along track dimension:

$$I(x,y,z) = I_{norm} \left| \sum_{k=1}^{M_f} \left[I_k(i'p'_x,y') + i\, Q_k(i'p'_x,y') \right] e^{-i\frac{2\pi d_k(x',y')}{R_k}} \right| \tag{5-43}$$

where

$$i' = \left\| \frac{d_k\left(x' + \frac{\left(m + \frac{1}{2}\right)p'_x}{n_x}, y\right)}{p'_x R_k} + \frac{x'_{ctr}}{p'_x} \right\| \tag{5-44}$$

and m is the upsampling index $(m = 0 \text{ to } n_x - 1)$. The along track spatial grid is now given by

$$x = \left[ip'_x - x_{ctr} + \frac{\left(m + \frac{1}{2}\right)p'}{n_x} \right] \overline{R} \tag{5-45}$$

Fringe curvature refers to the change in virtual fringe period across an image volume due to a change in range. This occurs for imaging geometries for which the LOS range extent $(z_{\max} - z_{\min})$ is not significantly less than the near range. The effect of fringe curvature, if not corrected, is a distortion or warping of the 3-D image onto equal range contours. This is corrected in the DFT kernel by changing R_k to

$$R'_k(x, y, z, \theta_k) = \sqrt{(R_k \sin\theta_k + x)^2 + y^2 + (R_k \cos\theta_k - z)^2} \tag{5-46}$$

5.7 IMAGE ANALYSIS AND DISPLAY

Results presented in the following section will display 3-D imaging results in one of four forms. The first form consists of a range response function. This is a one-dimensional distribution in range extracted from a 3-D image at a specified (x, y) location. In many cases, the distribution with maximum SNR among the upsampled along track pixel is extracted. The second form is an image projection in one of the orthogonal axes. This is merely a two-dimensional representation of the 3-D image volume generated by integrating along the projection axis. The third form is a peak or interferometric signal image, which is an (x, y) representation of the peak intensity value in range. Once again, this generally also corresponds to the peak among the upsampled along track pixel. The final form is a range map, which contains the height (range) value associated with the peak signal image. This is generally color-coded, and possibly thresholded and range gated such that range peaks below threshold or out of the range gate are assigned a flag value (black).

5.8 REFERENCES

5.1 B. Morey et al, "Infrared Image Simulation Based on Solids Modeling," Proc. SPIE Vol. 1098, p. 28 (1989).

6.0 COLLECTED IMAGERY/MODEL COMPARISON

The critical point of the sensor modeling effort described in this report was the comparison of simulated and field collected PRISM imagery. This comparison is essential for both validating the sensor performance and simulation-based models, as well as verifying that the sensor operated to design specifications. This comparison was made in two ways. First, characteristics of the range response function were compared for geometric test targets (bars and edges) placed in the field collected scenes in a well ground truth manner. This provided quantitative metrics for comparing sensor operation to designed expectations. Second, 3-D signatures of a more complicated hard target (M35 truck) were compared. This comparison was significantly more qualitative due to the lack of detailed ground truth, but provided some insight into how well the simulation works. No attempt was made to model complex backgrounds or camouflaged (netted) vehicles.

6.1 TEST TARGET COMPARISON

The simulation-based PRISM sensor model provides a detailed capability for simulating range response signatures for geometric test targets such as bar and edge targets. This provided the best opportunity for a quantitative comparison between measured and modeled 3-D signatures since such targets can be and were deployed in a well ground truth manner. That is, the orientations and surface temperatures were well controlled and monitored.

Table 6-1 summarizes the test target conditions that were modeled. The name in the first column is the simulation case name. The corresponding experiment name in the second column refers to a field collection scenario that contained a test target under similar conditions. The first three cases (LTEST#) correspond to local imaging tests at ERIM in Ann Arbor, Michigan. The final four cases (KTEST#) correspond to remote field collections at the Kinzua Bridge site in Pennsylvania. In all cases, the test targets were optimally oriented to the sensor.

Figures 6-1 to 6-7 illustrate the range response functions along with the corresponding measured responses for the (along track, cross track) pixel containing the strongest signal peak for each simulation case. Qualitatively, there is a strong similarity in the response functions.

To provide a more quantitative comparison, a set of eight performance metrics were defined (see Table 6-2) which characterize the signal level, noise, sidelobe characteristics, and main lobe width of the range response functions. These metrics are summarized in Table 6-3 for each of the

Table 6-1. Modeled Test Target Conditions

Name	Experiment	Target	T1(C)	T2(C)	W(cm)	H(m)	X(m)	Y(m)	Z(m)
LTEST1	LCLE	BAR	38	28	3.8	1	0.8	0.0	3.00
LTEST2	LCLE	BAR	38	28	3.8	1	-2.8	-1.5	-1.50
LTEST3	LCLE	EDGE	38	28	0	1	-1.6	0.0	0.60
KTEST1	KNZUS,T	EDGE	17	2	0	1	-7.7	0.0	-1.65
KTEST2	KNZUS,T	BAR	17	2	3.8	1	-8.4	0.0	2.10
KTEST3	KNZUD,E	EDGE	27	17	3.8	1	-2.4	0.0	-0.30
KTEST4	KNZUD,E	BAR	27	17	3.8	1	-11.8	0.0	0.30

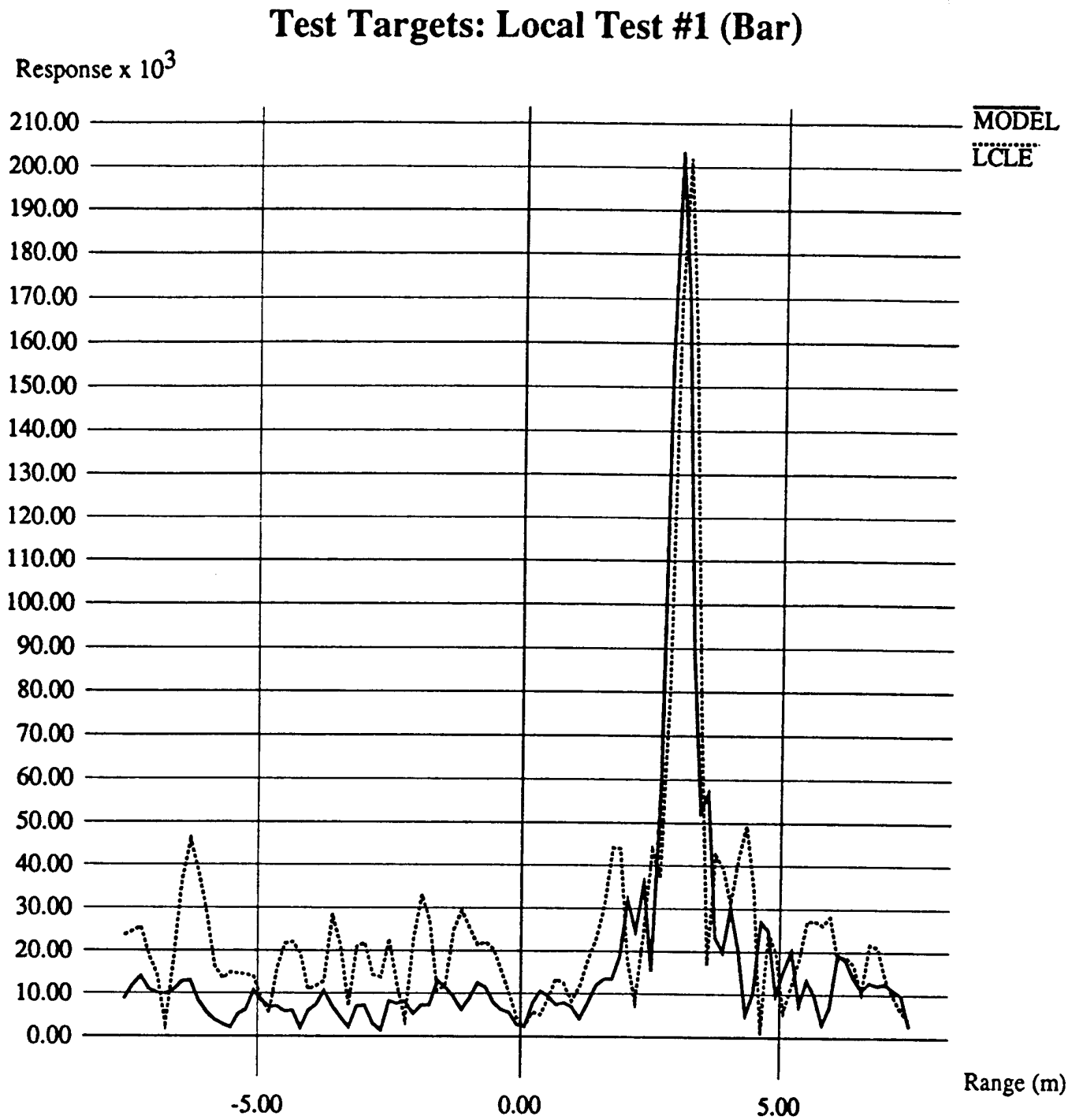

Figure 6-1: Range response functions for LTEST1.

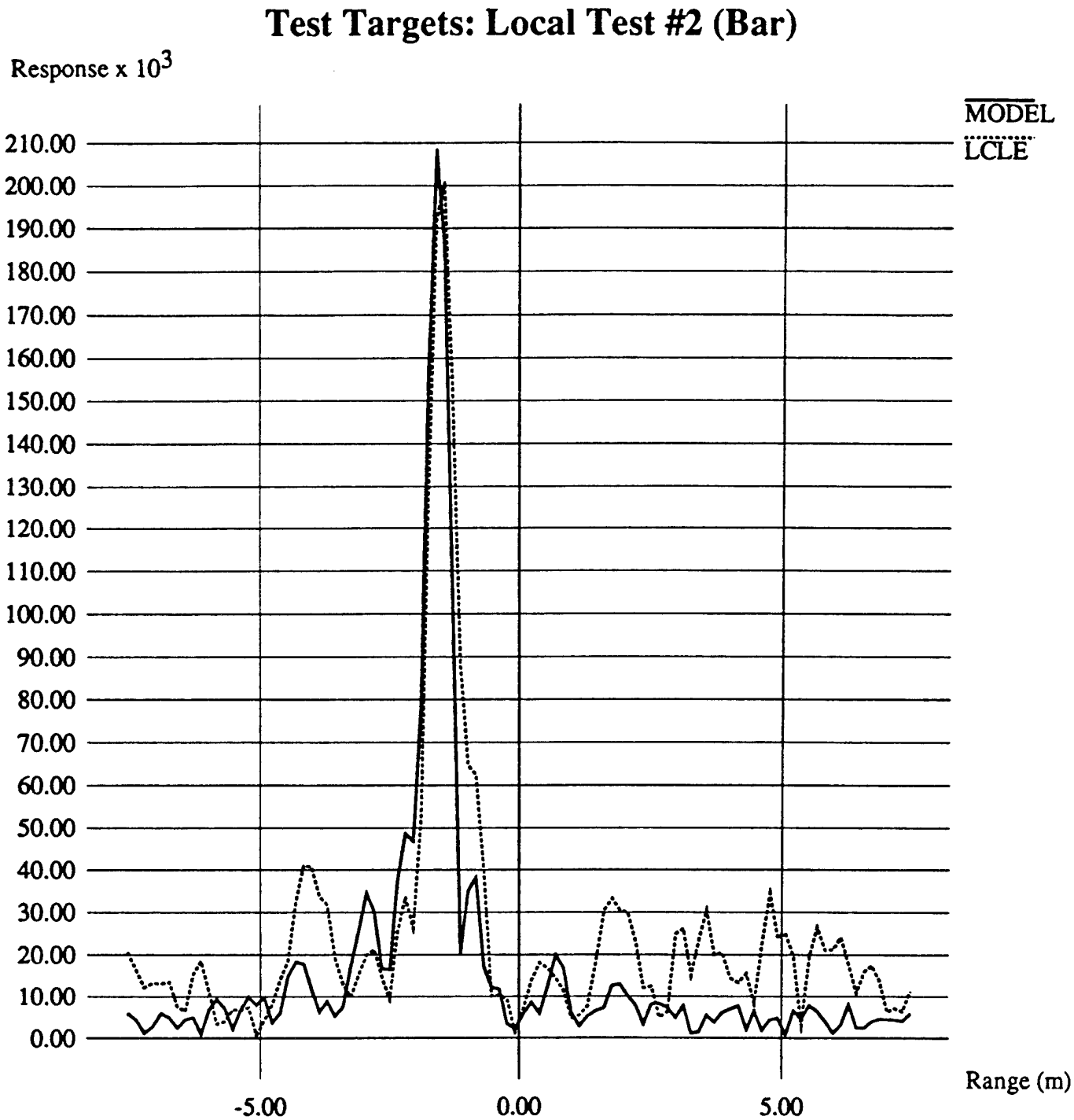

Figure 6-2: Range response functions for LTEST2.

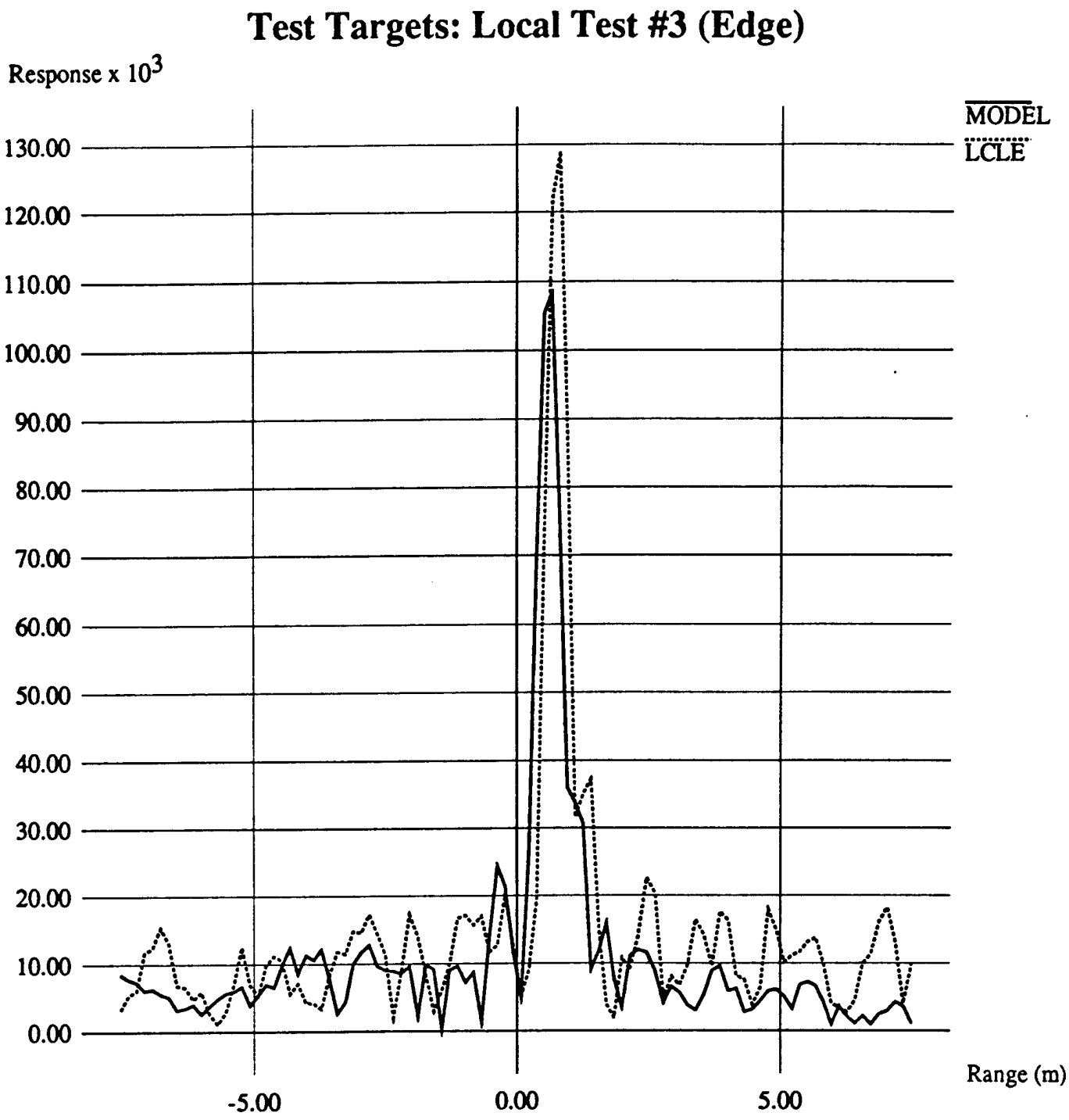

Figure 6-3: Range response functions for LTEST3.

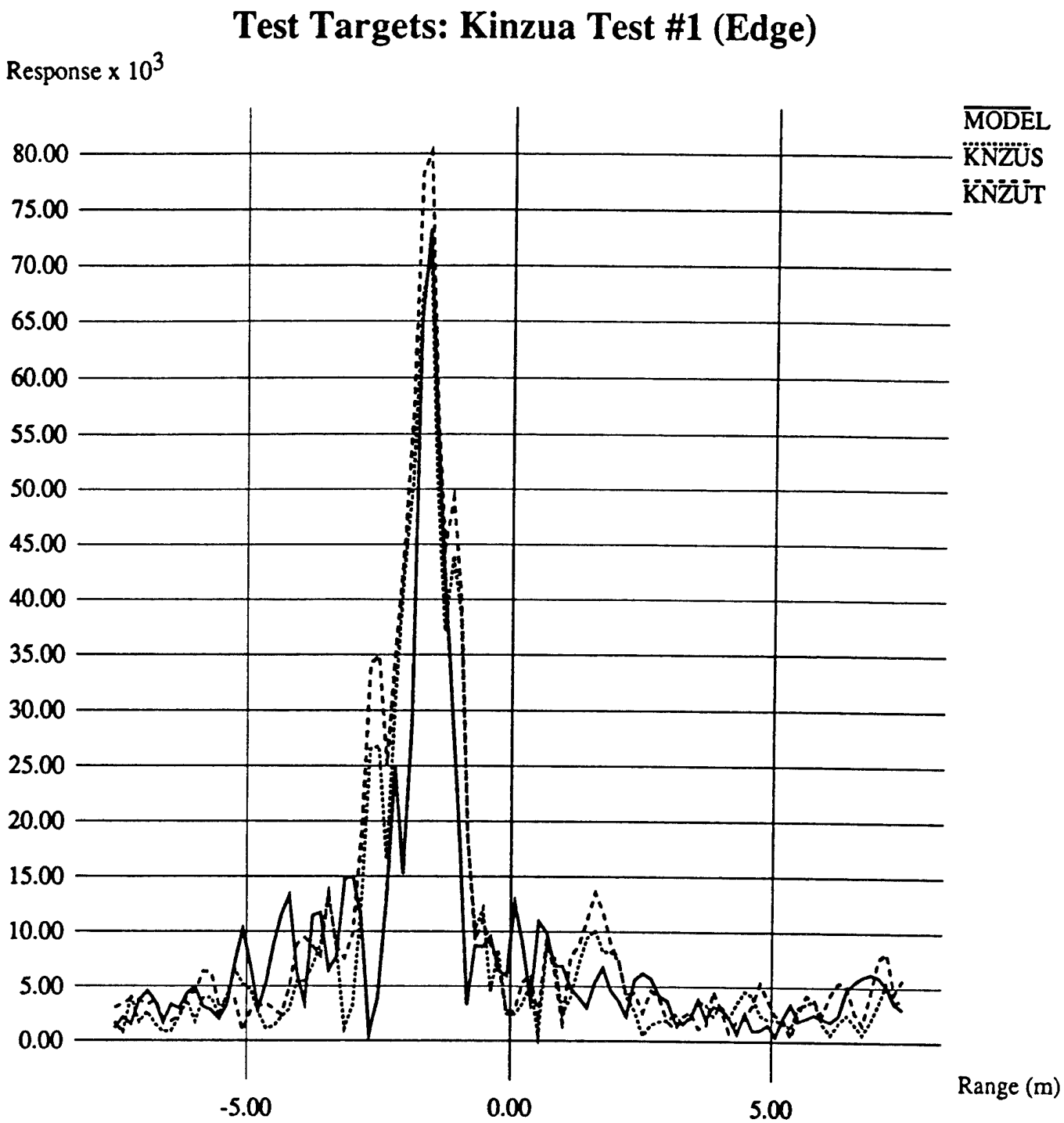

Figure 6-4: Range response functions for KTEST1.

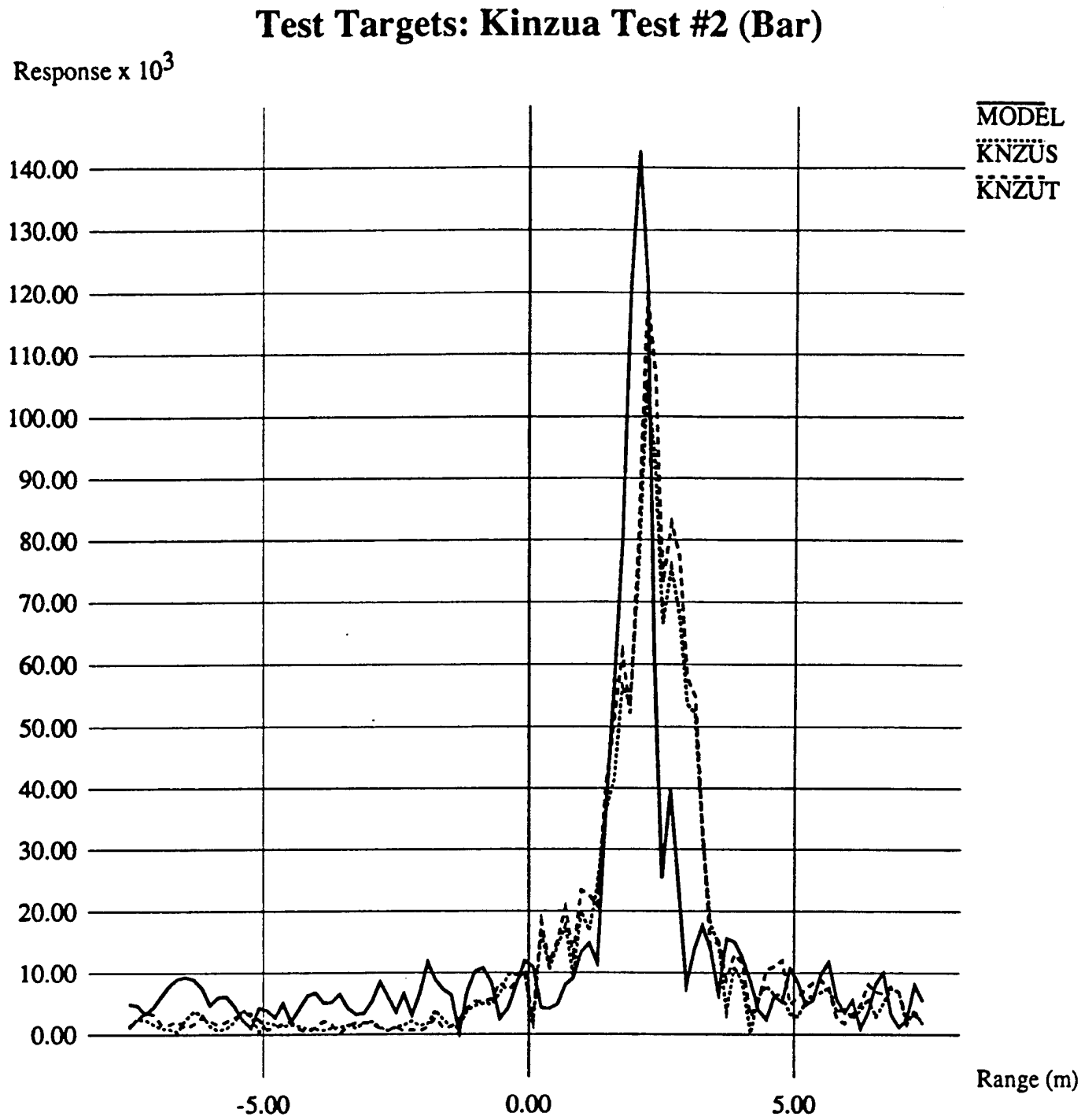

Figure 6-5: Range response functions for KTEST2.

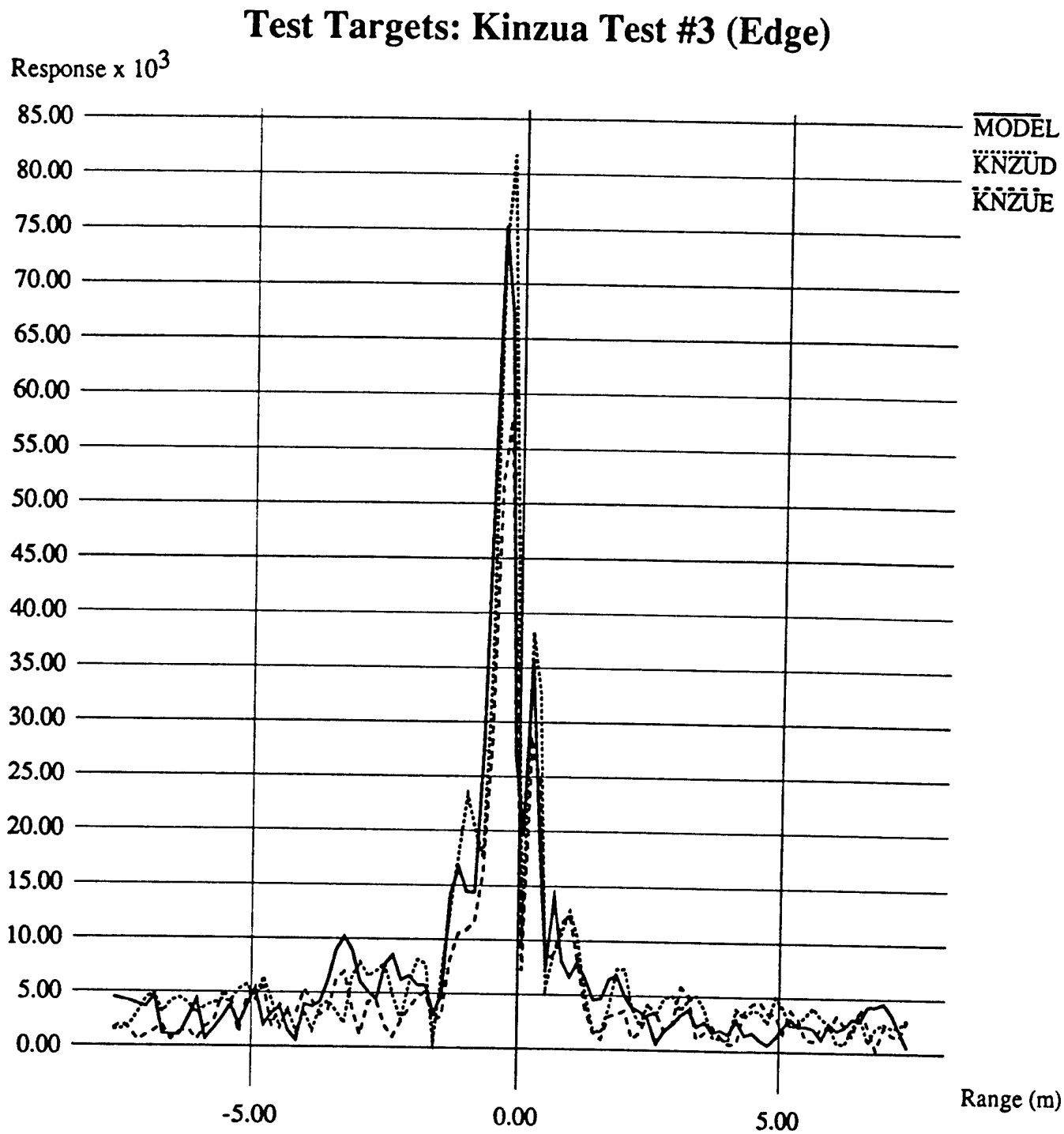

Figure 6-6: Range response functions for KTEST3.

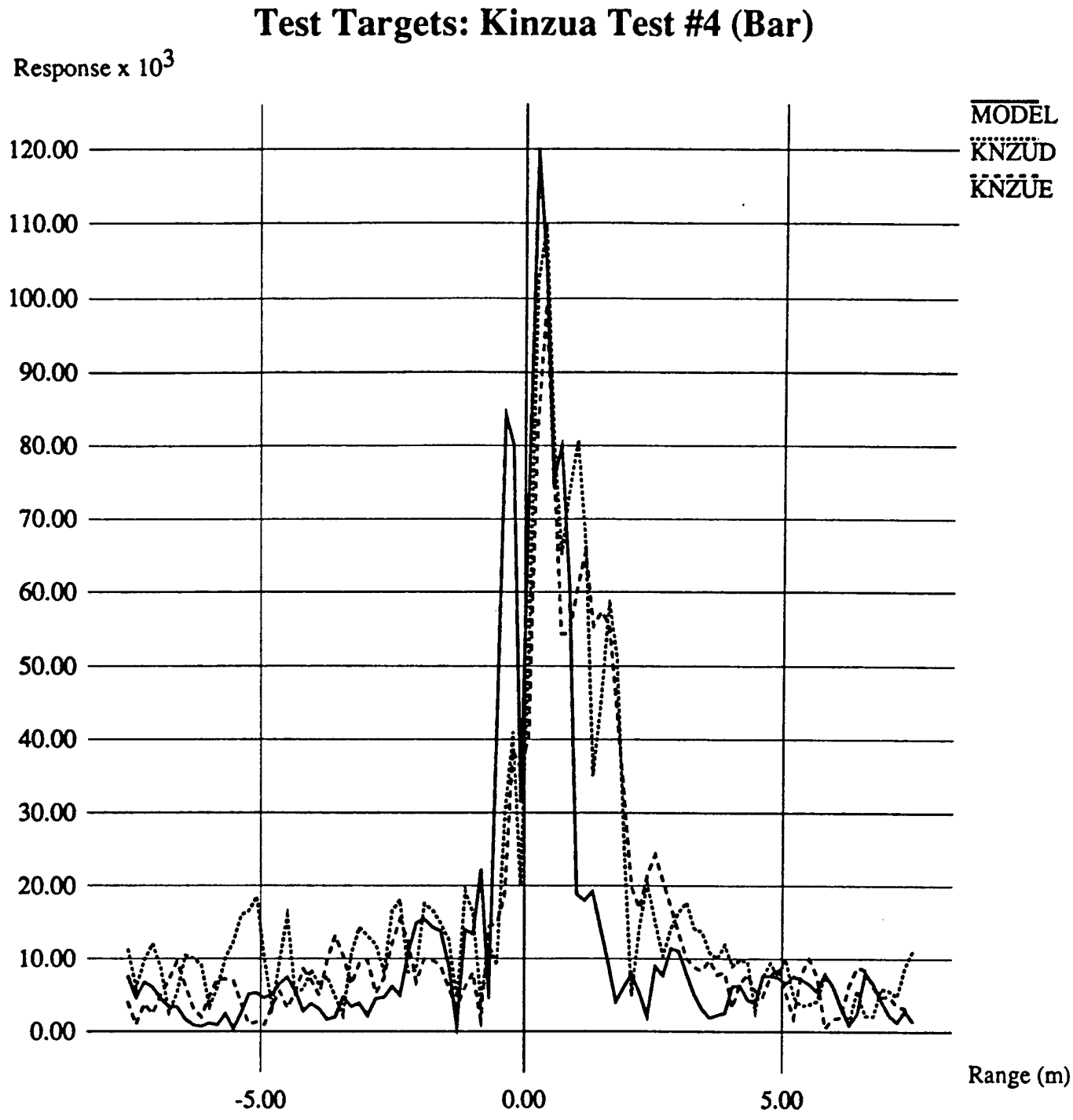

Figure 6-7: Range response functions for KTEST4.

simulated and measured test cases. Corresponding simulated and measured cases are grouped together, along with an "average" of the measured cases where applicable.

A few remarks can be made with regard to each metric. In the case of SNR, there was excellent agreement between the simulated and measured responses, generally within 10-20%. Good agreement was also achieved with regard to the PPNSR metric with some exception. These discrepancies were probably pixel walk related, and cause a discrepancy in RMLW as well. The PPFSR, SSR, and PMSR metrics were also very similar for the simulated and measured Kinzua test cases, but were off by about a factor of two between the simulated and measured local test cases. The source of this discrepancy has not been identified. The 3-D NETD and SETD metrics track the SNR and SSR, respectively, such that the comparison does as well.

6.2 COMPLEX TARGET SIGNATURE COMPARISON

A comparison of simulated and modeled PRISM signatures of a complex target was performed using a passively-heated M35 truck (without the canvas cover) in an open area as a baseline target. Both daytime and nighttime cases were simulated, and corresponding field imagery collected. The common viewing geometry consisted of a 90m sensor height moving along a 20m track at 32m ground range broadside to the scene center. The geometry is illustrated in Figure 6-8. Perspective and LOS views of the M35 target model are shown along with a LOS range map in Figure 6-9. The range map is color coded by the colors of the rainbow (red to yellow to green to blue moving away from the sensor in range).

Since detailed meteorological data was not collected during the field collection, an estimated weather history was used to drive the thermal target simulation. This weather history is summarized in Table 6-4. The sky conditions were assumed clear at all times. The solar angles correspond to the latitude (41°46'), longitude (-78°36'), and time of year (September 15, 1993) for the Kinzua field collection. The thermal portion of the target simulation proceeded by running the model through at least two days of the weather history and stopping at the specified time on the third day.

6.2.1 Daytime Imaging Case

The daytime case was modeled for a 10:00 a.m. local time with clear cloud conditions. The background model parameters were $L_0 = 20\mu W / cm^2 sr$ and $f_0 = 4.5 \times 10^{-3} m^{-1}$, which correspond to roughly a 15 C mean apparent temperature and 0.3 C edge equivalent temperature

Table 6-2: Image Performance Metric Definitions

ACRONYM	NAME	DEFINITION
SNR	Signal to Noise Ratio	$\frac{\text{Peak response}}{\text{Global noise standard deviation}}$
PPNSR	Peak to Peak Near Sidelobe Ratio	$\frac{\text{Peak response}}{\text{Seconday peak response}}$
PPFSR	Peak to Peak Far Sidelobe Ratio	$\frac{\text{Peak response}}{\text{Maximum sidelobe}}$
SSR	Signal to Sidelobe Ratio	$\frac{\text{Peak response}}{\text{Sidelobe standard deviation}}$
PMSR	Peak to Mean Sidelobe Ratio	$\frac{\text{Peak response}}{\text{Mean sidelobe level}}$
RMLW	Relative Main Lobe Width	$\frac{\text{3 dB main lobe width}}{\text{Ideal 3 dB main lobe width}}$
3D NETD	3D Noise Equivalent Temperature Difference	$\frac{\Delta T\ C_s(\text{target})}{\text{SNR}\ C_s(\text{edge})}$
3D SETD	3D Sidelobe Equivalent Temperature Difference	$\frac{\Delta T\ C_s(\text{target})}{\text{SSR}\ C_s(\text{edge})}$

Table 6-3: Measured Image Performance Metrics

Experiment	Target	DT	SNR	PPNSR	PPFSR	SSR	PMSR	PMSR	RMLW	3D NETD	3D SETD
LTEST1	BAR	10C	203	5.6	10.7	65.5	27.1	27.1	1.07	0.10C	0.31C
LCLE	BAR	10C	202	4.6	4.1	22.4	10.8	10.8	1.10	0.10C	0.89C
LTEST2	BAR	10C	209	5.5	10.5	55.0	34.8	34.8	1.08	0.10C	0.36C
LCLE	BAR	10C	201	5.9	4.9	23.3	11.8	11.8	1.31	0.10C	0.86C
LTEST3	EDGE	10C	108	4.5	8.3	36.0	15.0	15.0	1.18	0.09C	0.28C
LCLE	EDGE	10C	129	3.5	5.6	26.3	13.4	13.4	1.10	0.08C	0.38C
KTEST1	EDGE	15C	73	2.9	4.9	28.1	17.8	17.8	1.38	0.21C	0.53C
AVERAGE	EDGE	15.3C	75.5	1.6	5.5	28.2	19.3	19.3	2.02	0.21C	0.56C
KNZUS	EDGE	14C	71	1.6	5.1	29.6	20.3	20.3	1.67	0.20C	0.47C
KNZUT	EDGE	17C	80	1.6	5.7	26.7	18.2	18.2	2.36	0.21C	0.64C
KTEST2	BAR	15C	143	3.6	7.9	52.9	24.7	24.7	1.35	0.21C	0.57C
AVERAGE	BAR	16C	113	1.4	5.7	40.5	40.0	40.0	2.13	0.29C	0.92C
KNZUS	BAR	16C	106	1.4	6.2	26.5	32.1	32.1	2.19	0.30C	1.21C
KNZUT	BAR	17C	120	1.4	5.2	54.5	48.0	48.0	2.07	0.28C	0.62C
KTEST3	EDGE	10C	75	7.5	7.5	31.3	17.4	17.4	1.06	0.13C	0.32C
AVERAGE	EDGE	8.5C	70	5.6	5.6	32.8	20.5	20.5	0.99	0.13C	0.26C
KNZUD	EDGE	8.5C	82	6.3	6.3	31.5	21.0	21.0	0.98	0.10C	0.27C
KNZUE	EDGE	8.5C	58	4.8	4.8	34.1	20.0	20.0	1.00	0.15C	0.25C
KTEST4	BAR	10C	120	1.4	5.4	24.5	20.7	20.7	1.69	0.17C	0.82C
AVERAGE	BAR	10.5C	104.5	1.5	4.8	25.6	13.2	13.2	1.91	0.20C	0.83C
KNZUD	BAR	10.5C	110	1.4	5.5	22.9	10.7	10.7	2.25	0.19C	0.92C
KNZUE	BAR	10.5C	99	1.5	4.1	28.3	15.7	15.7	1.56	0.21C	0.74C

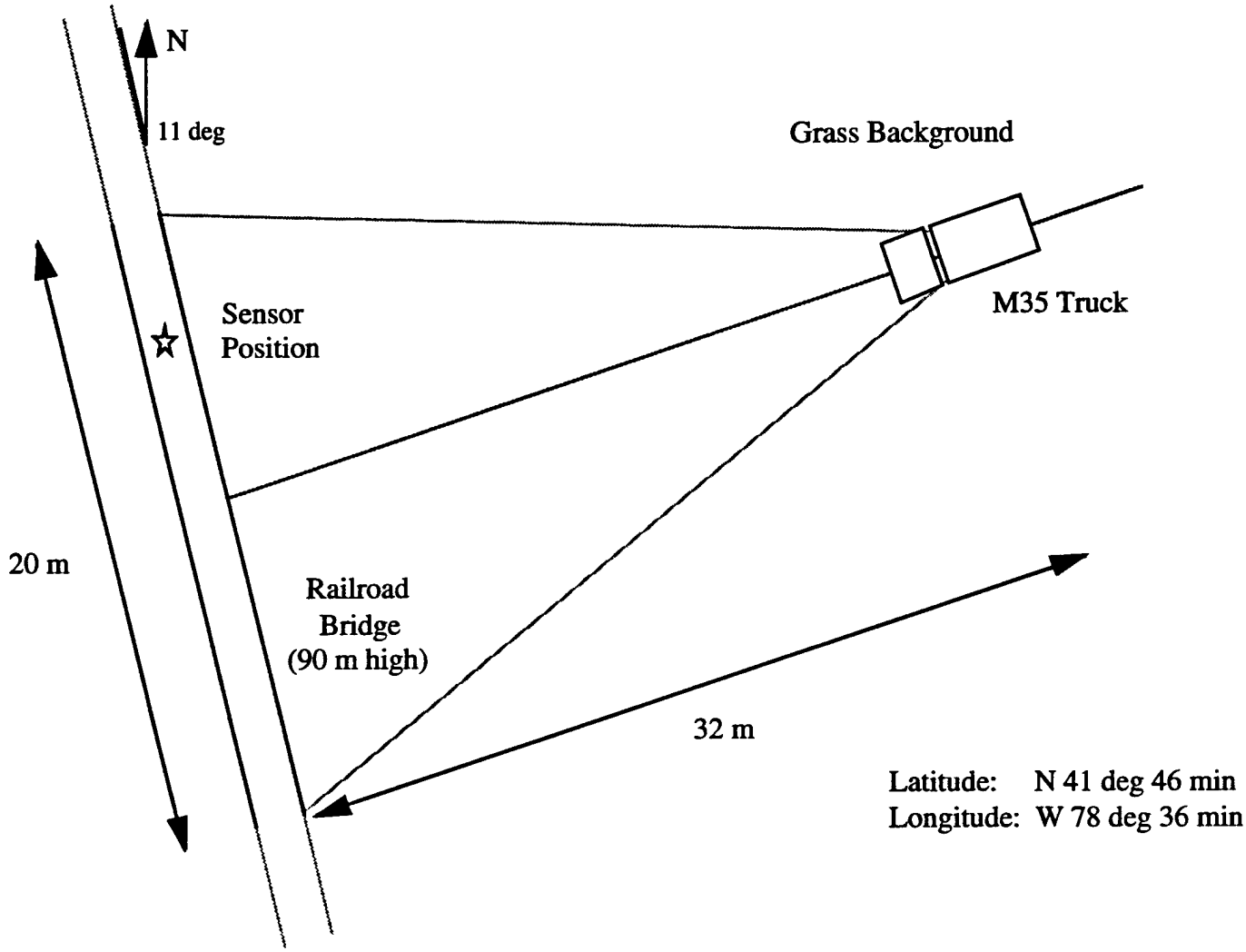

Figure 6-8: Simulated Viewing Geometry

Intentionally Left Blank

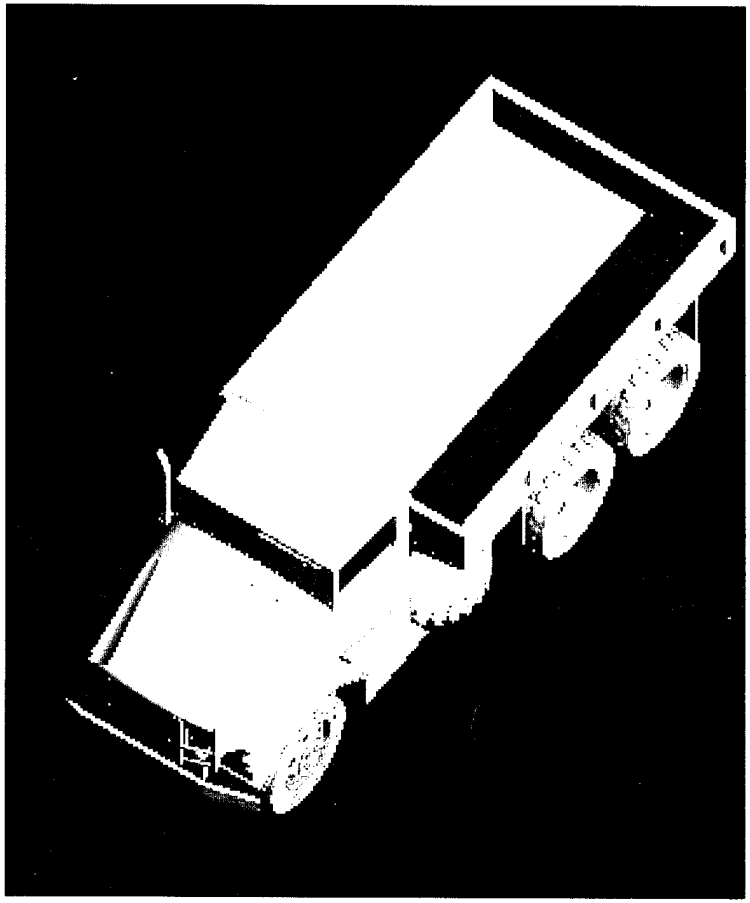

Perspective View

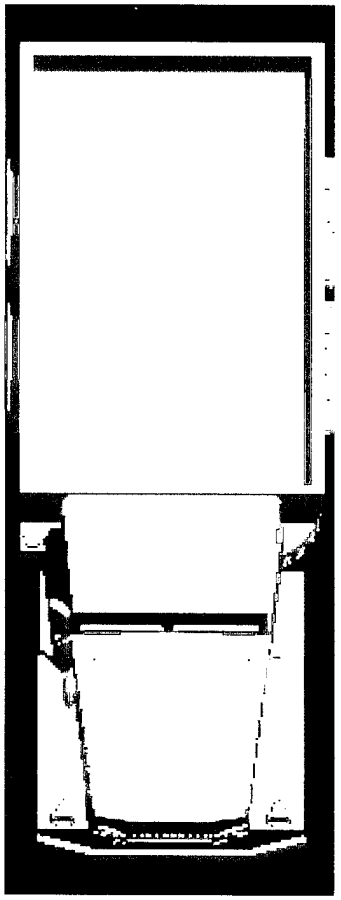

Line-of-Sight View

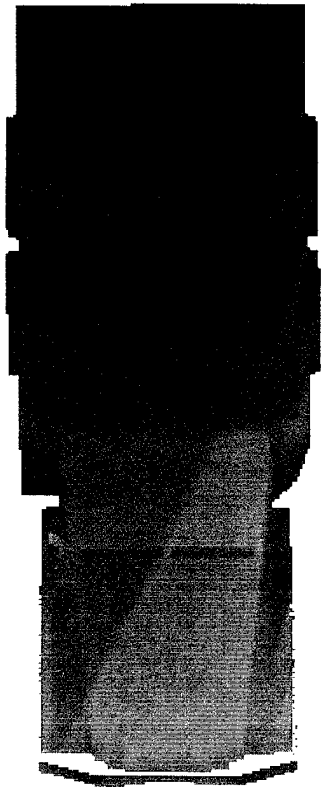

Range Map

Figure 6-9: M35 truck model perspectives

Table 6-4: Simulation Weather History

Time (LST)	Sun Elevation (deg above horizon)	Sun Azimuth (deg from north)	Air Temperature (Kelvin)
0:00	-41.722	356.809	283
1:00	-40.412	16.558	285
2:00	-35.574	34.487	284
3:00	-28.065	49.673	283
4:00	-18.785	62.409	282
5:00	-8.425	73.451	281
6:00	2.526	83.589	282
7:00	13.696	93.573	284
8:00	24.737	104.199	287
9:00	35.22	116.469	290
10:00	44.491	131.741	293
11:00	51.465	151.528	299
12:00	54.633	175.875	303
13:00	52.961	201.109	306
14:00	47.03	222.5	309
15:00	38.349	239.064	310
16:00	28.164	252.124	310
17:00	17.248	263.152	308
18:00	6.08	273.247	303
19:00	-4.979	283.255	283
20:00	-15.573	293.926	295
21:00	-25.261	306.034	289
22:00	-33.424	320.371	287
23:00	-39.218	337.455	286

difference. Figure 6-10 shows the first, middle and last frames of the modeled, high spatial resolution frame sequence. Thirty frames were modeled in all.

Figure 6-11 illustrates the orthogonal axis projections of the simulated 3-D image. The bandpass nature of the signature is clearly evident in that truck side boundaries and wheels generate the strongest image features. Figure 6-12 illustrates these results in the form of a bias image, interferometric signal (peak of range response) image, range map, and thresholded range map. Valid range information exists at the target boundaries (corresponding to target height) and along the ground plane. The target center "disappears" due to a lack of sufficient spatial structure.

The corresponding field collected signature was measured at 3:25 p.m. on October 5, 1993 (KNZUP). The actual weather conditions were clear skies with a very light wind. A color photograph of the target setup taken along the sensor line-of-sight is given in Figure 6-13.

The 3-D imaging results of the field collection are shown in the same form as for the simulated data in Figures 6-14 and 6-15. It is apparent from the bias image that the target to background mean temperature differential was significantly less in the field data, probably due to wind and cloud effects that were not accurately modeled. The interferometric signal images are similar; however, the measured results exhibit significantly more signal in the center of the target. This results in a more "filled" range map (i.e., valid ranges more distributed within the target). The sensor was not able to make valid range measurements to the ground plane, however, due probably to less spatial structure as compared to the modeled background. Note the bright target feature at one side of the cab, which is the warm exhaust pipe.

6.2.2 Nighttime Imaging Case

The nighttime case was modeled for a 3:00 a.m. local time with clear cloud conditions. The background model parameters were $L_0 = 15\ \mu W / cm^2 sr$ and $f_0 = 5.0 \times 10^{-3} m^{-1}$, which correspond to roughly a 8 C mean apparent temperature and 0.3 C edge equivalent temperature difference. Figure 6-16 shows the first, middle, and last frames of the modeled, high spatial resolution frame sequence. Note the significantly reduced mean target to background contrast relative to the daytime case.

The simulation results are shown in Figures 6-17 and 6-18. The target to background contrast of the bias image is significantly reduced as expected. The features of the interferometric

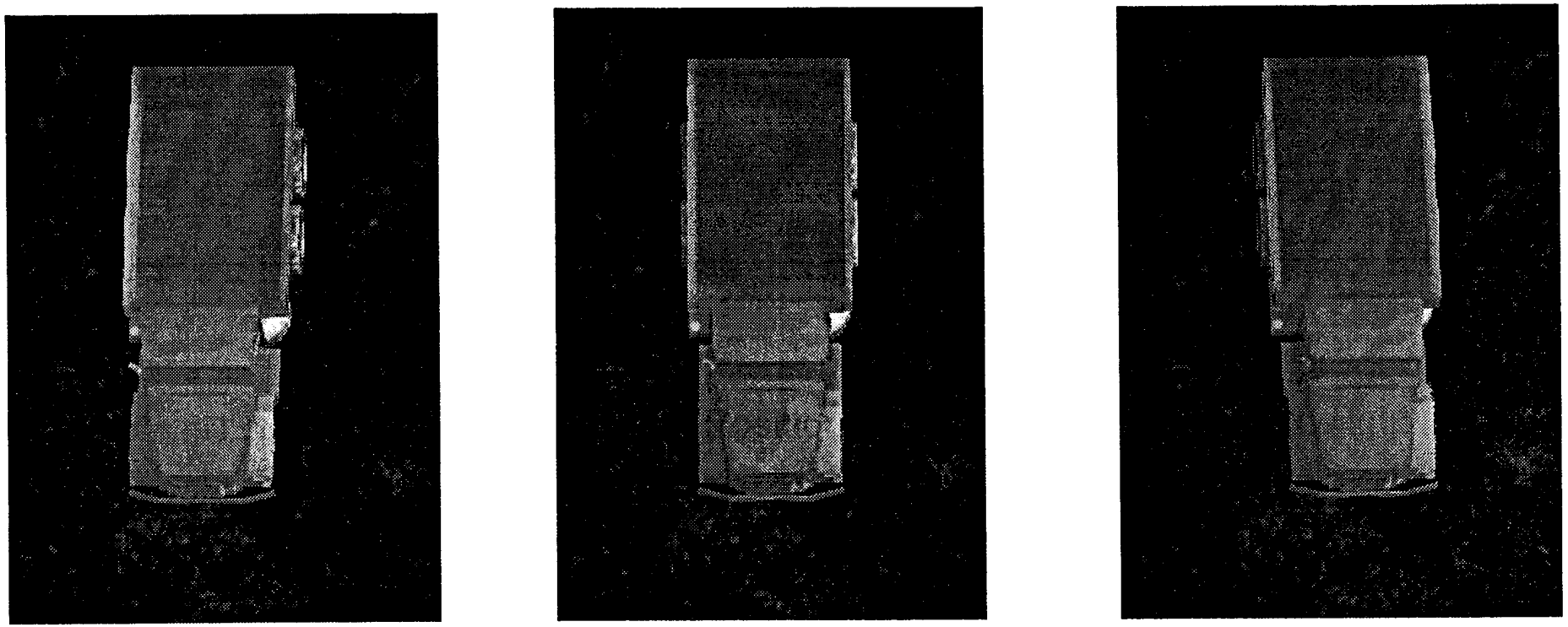

Track Position = -10 m Track Position = 0 m Track Position = 10 m

Figure 6-10: High resolution frame sequence for daytime image simulation

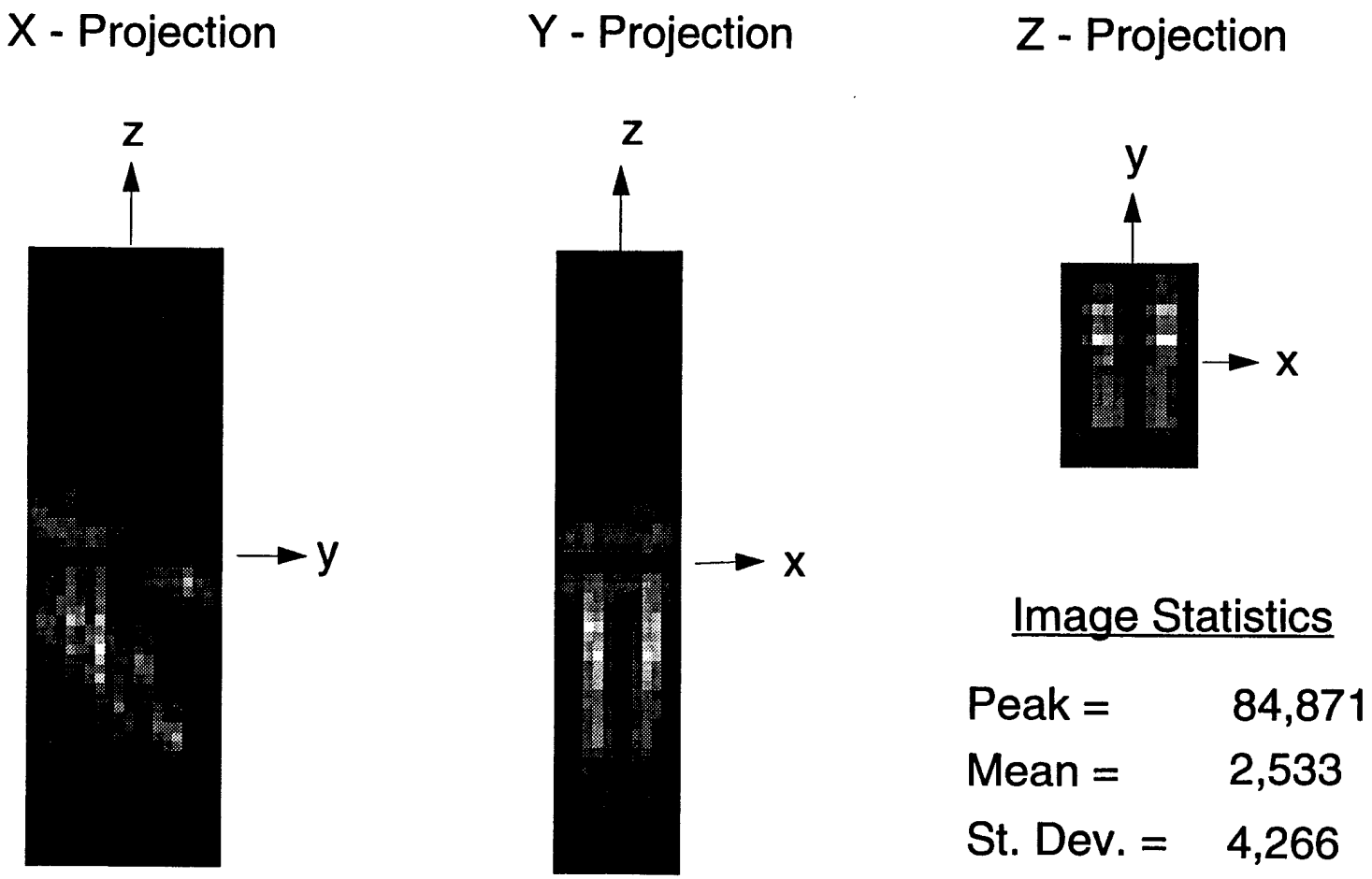

Figure 6-11: Orthogonal 3-D image projections for daytime image simulation

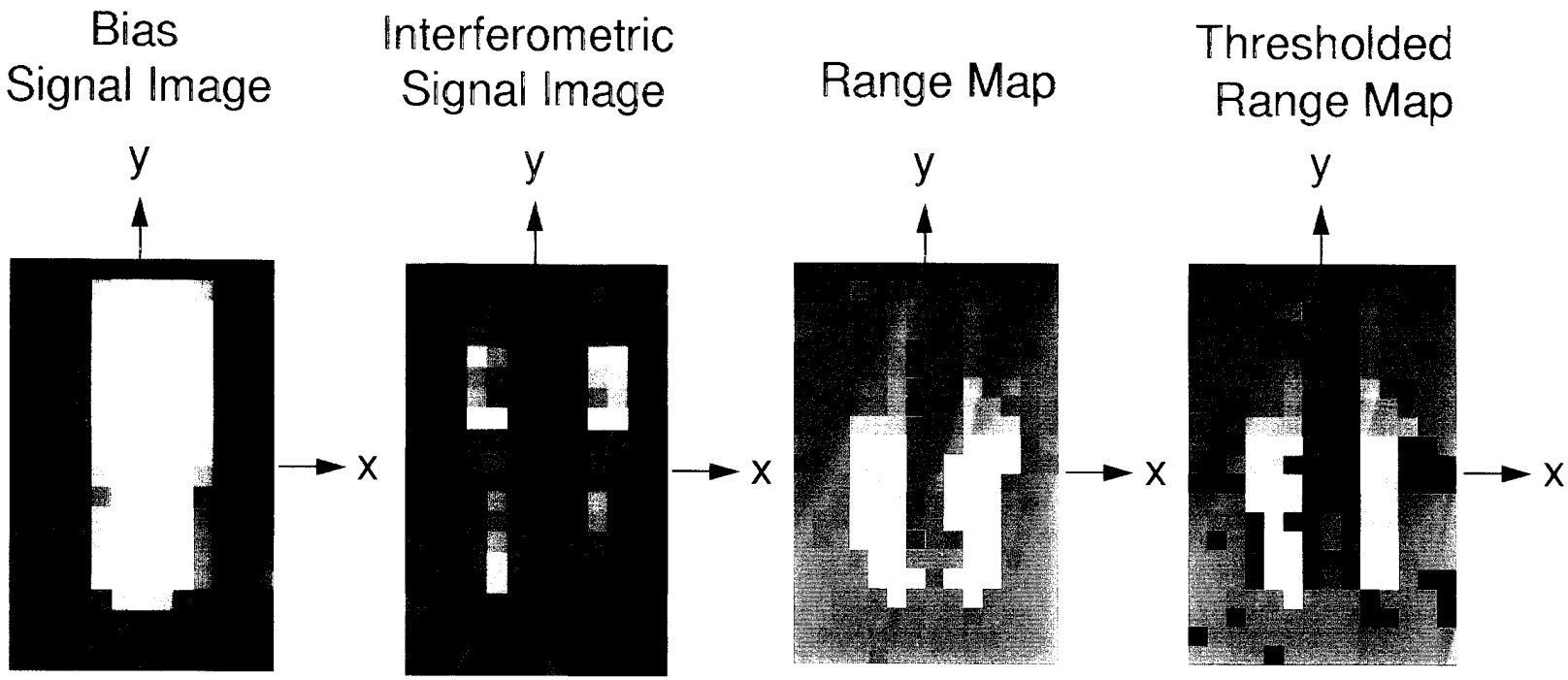

Signal Threshold Level = 5,000

Peak to Sidelobe Threshold Level = 1.5

Figure 6-12: 3D imaging results for daytime image simulation

Figure 6-13: Line-of-sight photograph of imaged area corresponding to daytime and nighttime simulations

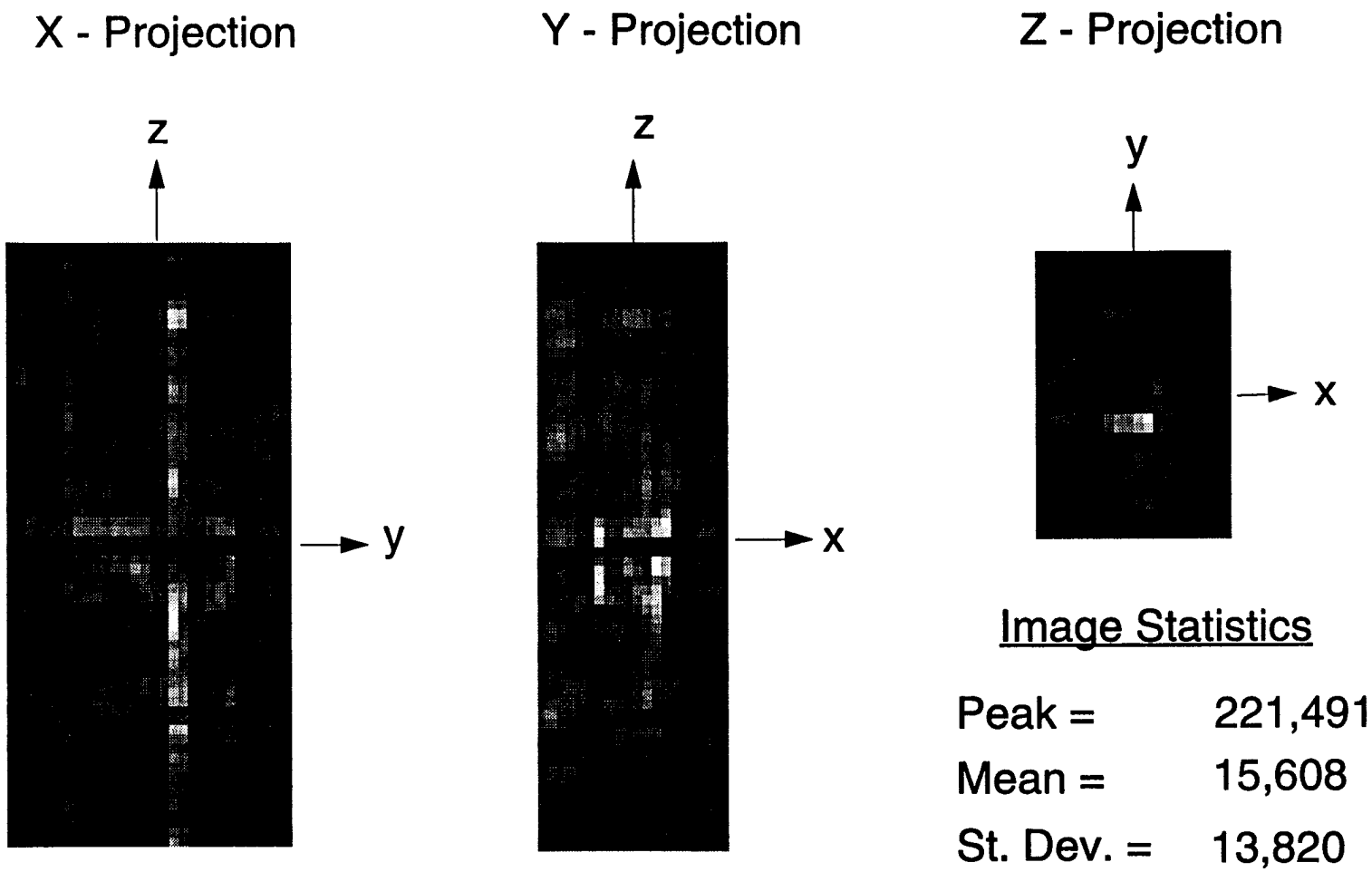

Figure 6-14: Orthogonal 3-D image projections for daytime field collection

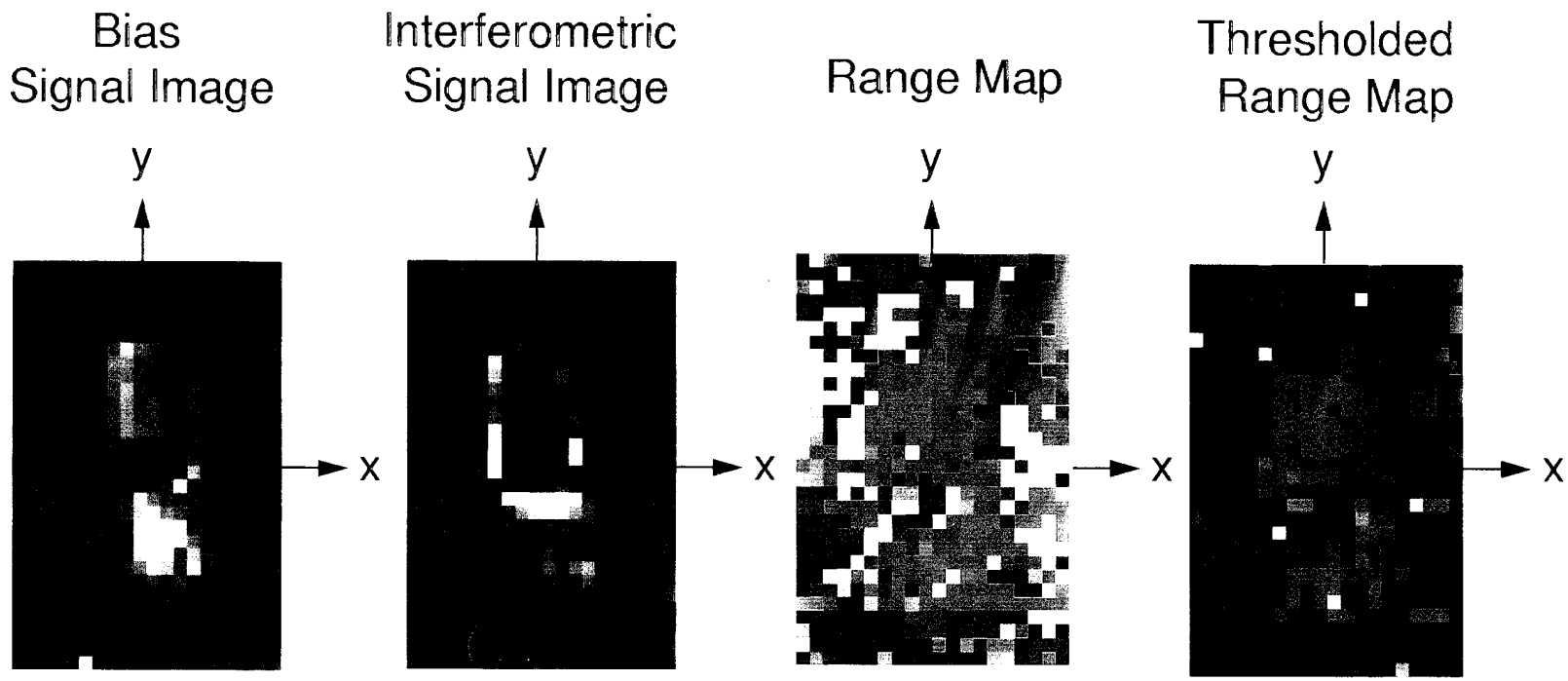

Signal Threshold Level = 10,000

Peak to Sidelobe Threshold Level = 1.5

Figure 6-15: 3-D imaging results for daytime field collection

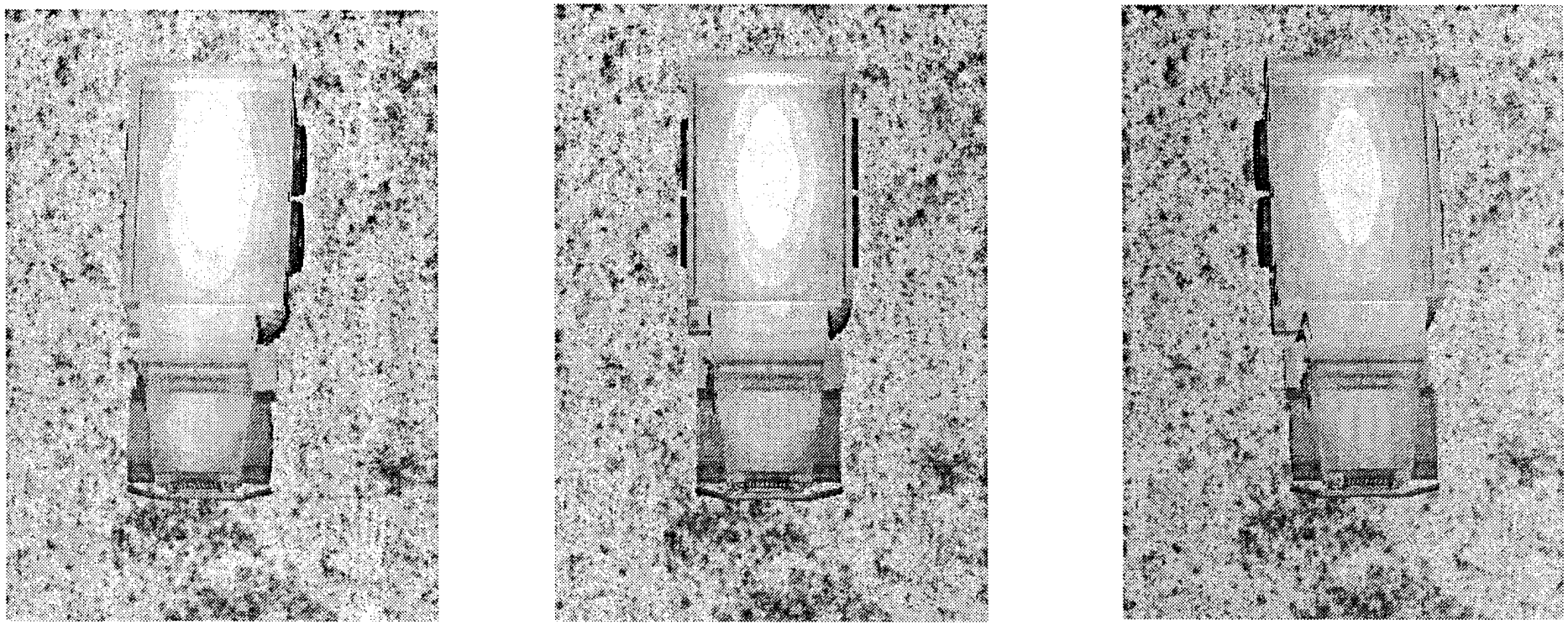

Track Position = -10 m Track Position = 0 m Track Position = 10 m

Figure 6-16: High resolution frame sequence for nighttime image simulation

3-D image, however, are not significantly different to the daytime image. The signal level is somewhat reduced, resulting in less target fill for valid ranges.

The corresponding field collected signature was measured at 8:33 p.m. on October 5, 1993 (KNZUU). The actual weather conditions were partly cloudy with a light wind. The target setup was exactly the same as for the daytime case (Figure 6-13).

The field collected results are shown in Figures 6-19 and 6-20. In terms of the bias (or conventional 2-D thermal) image, the target is at zero contrast to the background. In the interferometric image, however, there seems to be some signal clustered at the target height above the ground plane, but the signal-to-noise ratio is marginal. This result does not agree terribly well with the simulated result due to the significantly lower target contrast.

6.3 COMPARISON SUMMARY

The results of the collected imagery/model comparison generally indicate the validity of the sensor performance and simulation based models. In the case of the test targets, the similarity in results is striking (within 10-20% for many of the quantitative metrics). Discrepancies between the modeled and measured responses are generally due to sidelobes near the peak response, which is most likely due to pixel walk artifacts not precisely modeled or other spurious effects of the field test targets (temperature drift, motion, etc.).

The comparison of modeled and collected 3-D M35 truck signatures also exhibits some commonality in features, but the agreement quickly breaks down at a quantitative level. We feel there are two main reasons for this. First, the field collections were not well ground truthed in terms of environmental and background parameters, which can dramatically influence thermal target signatures. Second, the PRISM sensor (in both modeled and real forms) is very sensitive to subtle, high spatial frequency target contrast. In this vein, the SIRIM-based simulations are perhaps too "clean". For example, the truck bed, cab roof, and hood are modeled as somewhat uniform surfaces and, therefore, show up in the high resolution image sequence as such. In reality, however, some thermal structure exists due to a variety of sources, including paint inhomogenities, dirt, and small target details not contained in the CGS model. This is most likely the reason for the increased "fill" in the range map for the field collected data.

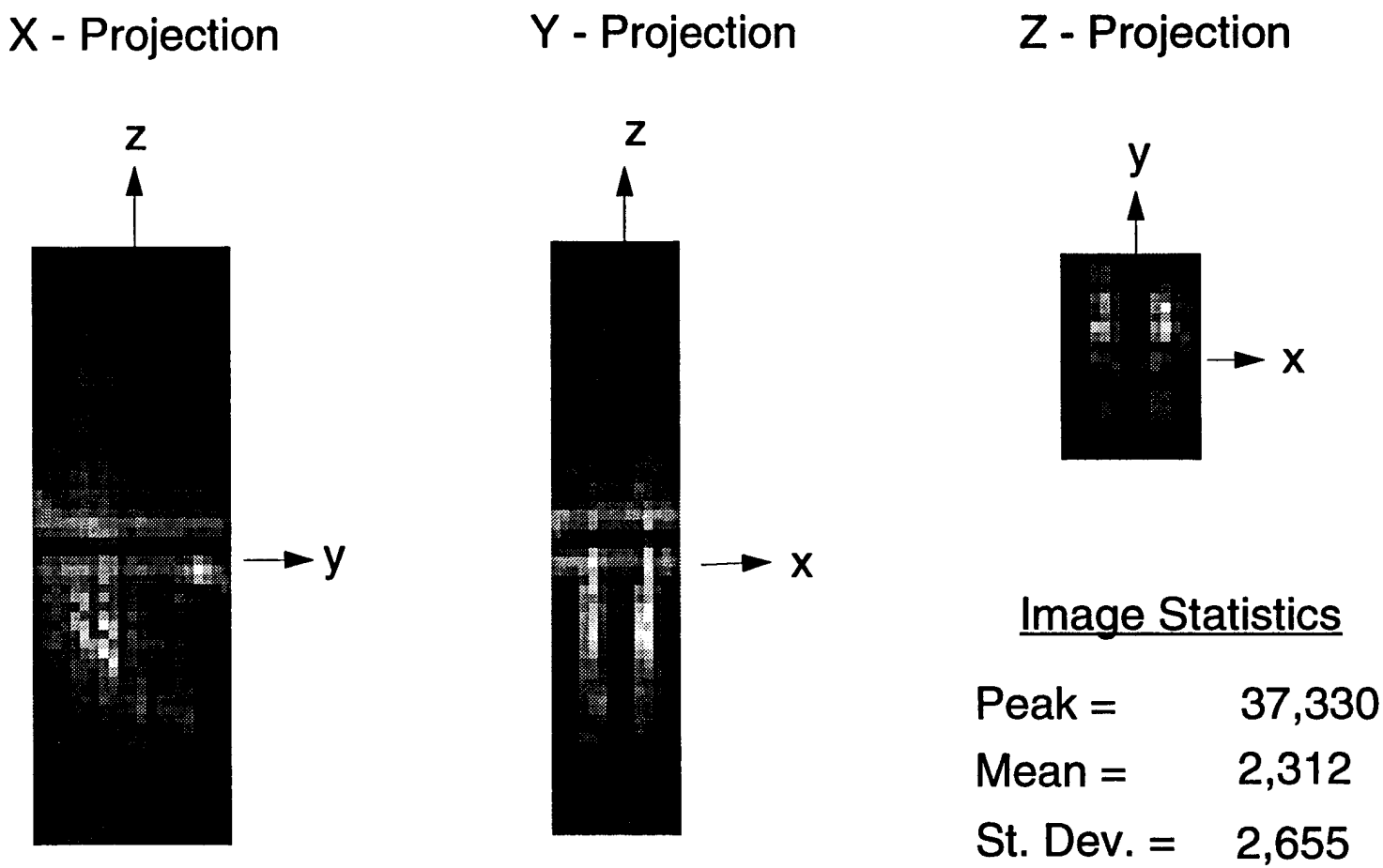

Figure 6-17: Orthogonal 3-D image projections for nighttime image simulation

Intentionally Left Blank

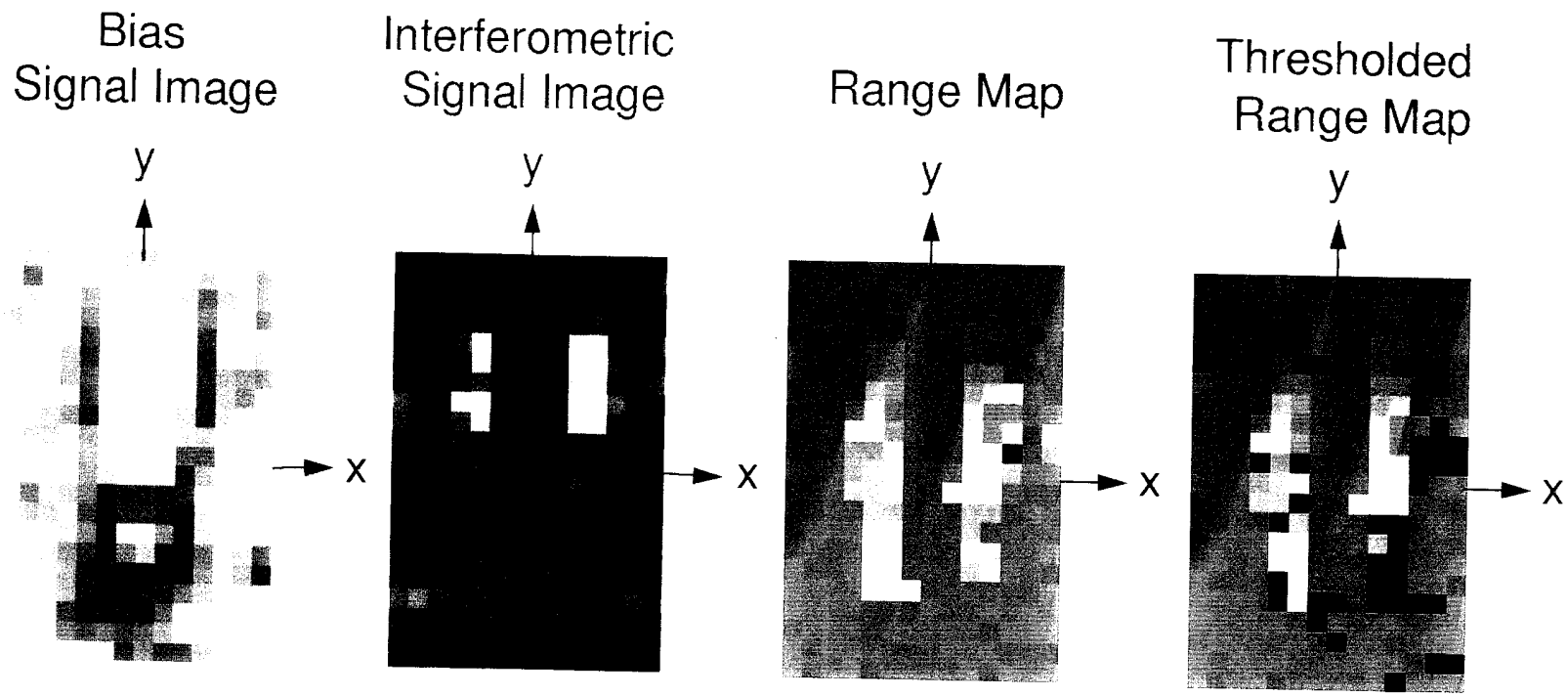

Signal Threshold Level = 5,000

Peak to Sidelobe Threshold Level = 1.5

Figure 6-18: 3-D imaging results for nighttime image simulation

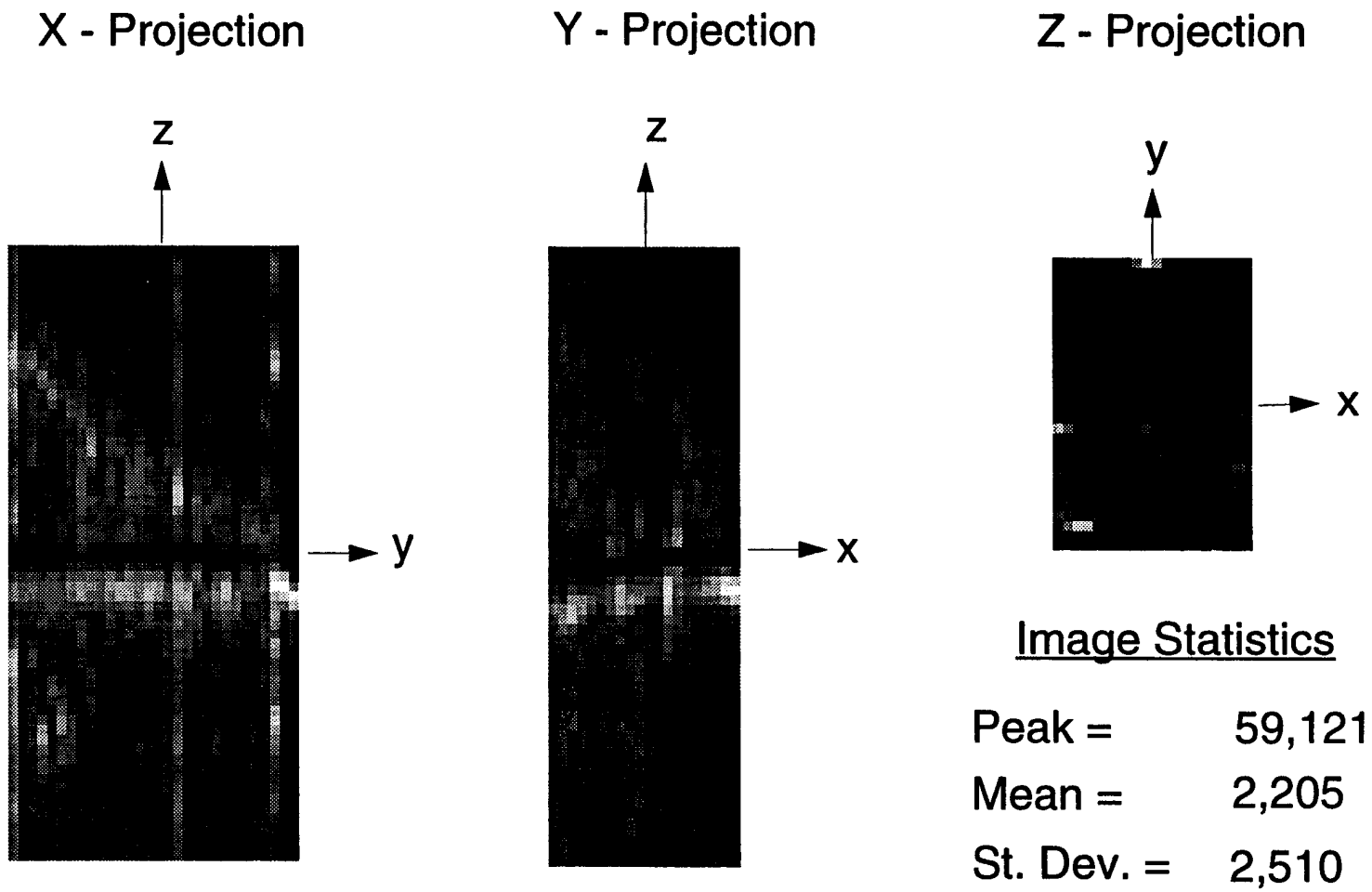

Figure 6-19: Orthogonal 3-D image projections for nighttime field collection

Intentionally Left Blank

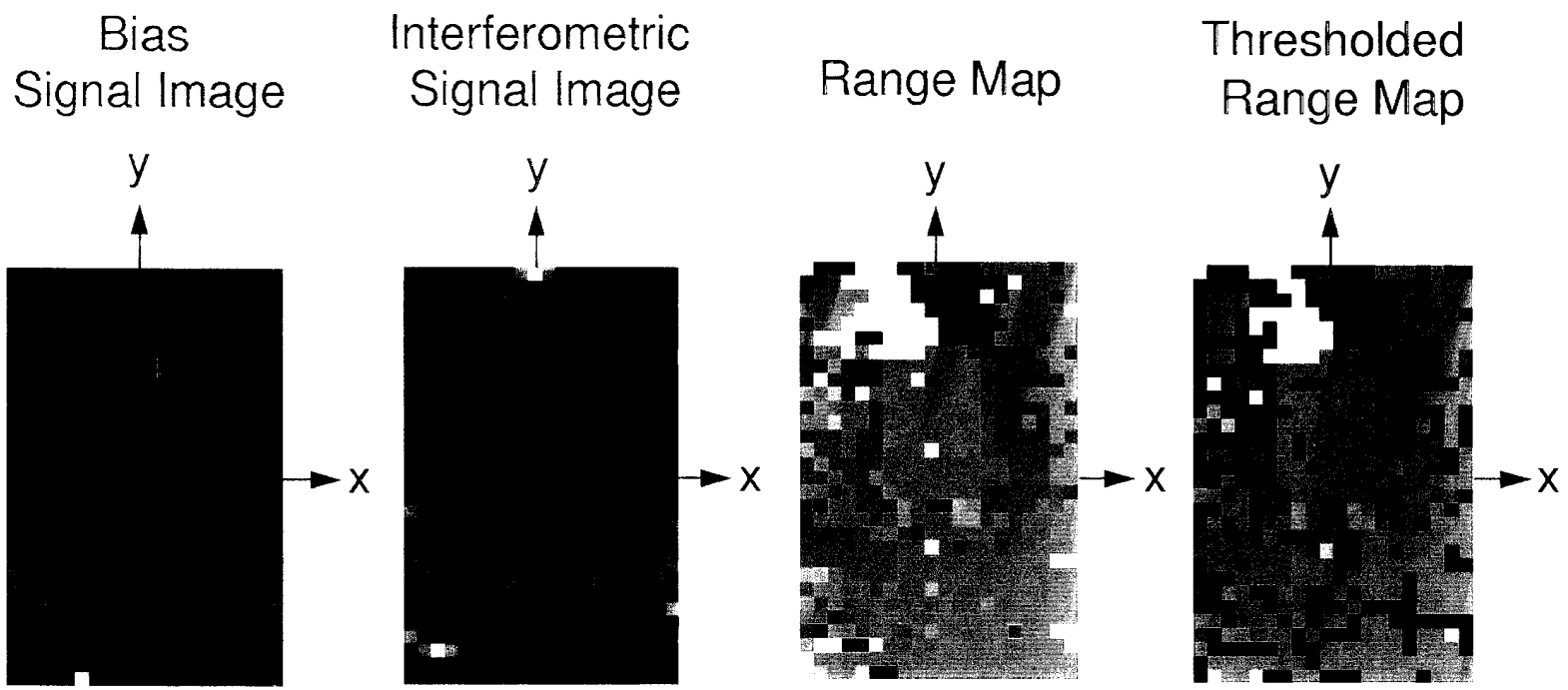

Signal Threshold Level = 5,000

Peak to Sidelobe Threshold Level = 1.5

Figure 6-20: 3-D imaging results for nighttime field collection

7.0 AIRBORNE DEMO SENSOR DESIGN

The next logical step in the development of PRISM sensor technology is the design, implementation, and testing of an airborne demonstration system. This level of demonstration is needed to address probably the most critical implementation issue, that is, the feasibility of a sufficiently capable pointing and stabilization system. At this time, such a design has not been performed.

This section provides a sanity check with regard to the fundamental performance expectations of an airborne PRISM sensor for concept demonstration. Under the hypothesis that a suitable pointing and stabilization system could be implemented, could an airborne demo system be built with suitable performance? Even answering this question is not straightforward given the uncertainty in the metric "suitable".

To circumvent these issues, "suitable" was defined as providing 3-D imagery of better performance than the ground demo sensor. Furthermore, a legitimate demonstration scenario was defined as emulating the ground demo imaging geometry (side angle and angular diversity), but from an airborne platform at 2 km altitude flying at 100 m/s airspeed. Table 7-1 summarizes the baseline imaging geometry.

Using the sensor performance model, parametric designs of both an MWIR and LWIR sensor were generated. The design philosophy was to circumvent the detailed error budgeting process by designing for a sensitivity two times better than the ground demo sensor. This provides a 50% cushion for detailed error budgeting, which would not have been too meaningful at this stage of the design.

The parametric MWIR sensor design is summarized in Table 7-2. This is a reflective interferometer design with barely overlapping 4" apertures. A fairly high readout rate (400 Hz) of the 128 x 128 array is required to maximize sensitivity and provide adequate signal sampling. From a sensor implementation standpoint, this MWIR design is not particularly high risk.

An analogous LWIR sensor design is summarized in Table 7-3. This would also be a reflective interferometer design with 4" apertures, but with a significantly larger (10") separation. To accommodate the higher photon flux in the LWIR, a higher detector frame rate (800 Hz) is needed.

Table 7-1: Baseline Airborne Imaging Geometry

Altitude	2 km
Airspeed	100 m/sec
Stare Time	3.5 sec
Track Length	350.0 m
Side Angle	20 deg off nadir
Forward Angle	0 deg off nadir

Table 7-2: Parametric MWIR Airborne Design

Center Wavelength	4.7 microns
Spectral Bandwidth	0.5 microns
Aperture Diameter	10.0 cm
Interferometer Shear	13.0 cm
Grating Periodicity	20.0 1p/mm
Detector Size	50.0 microns
Detector Array Size	128 x 128
Focal Length	25.0 cm
Frame Rate	400 frames/sec
Down Sampling Factor	4
Modulation Scheme	Single channel, linear phase
Modulation Frequency	200.0 Hz
Detector Charge Capacity	40 million electrons
Quantization Levels	16
2D NETD	0.008 C
3D MDTD (edge)	0.054 C
Along Track Resolution	0.43 m
Cross Track Resolution	0.45 m
Range Resolution	0.44 m
Coverage Rate	0.05 km^2/min
Height Field-of-View	102.6 m

Table 7-3: Parametric LWIR Airborne Design

Center Wavelength	9.0 microns
Spectral Bandwidth	0.2 microns
Aperture Diameter	10.0 cm
Interferometer Shear	25.0 cm
Grating Periodicity	20.0 1p/mm
Detector Size	50.0 microns
Detector Array Size	128 x 128
Focal Length	25.0 cm
Frame Rate	800 frames/sec
Down Sampling Factor	8
Modulation Scheme	Single channel, linear phase
Modulation Frequency	200.0 Hz
Detector Charge Capacity	40 million electrons
Quantization Levels	16
2D NETD	0.008 C
3D MDTD (edge)	0.053 C
Along Track Resolution	0.43 m
Cross Track Resolution	0.45 m
Range Resolution	0.44 m
Coverage Rate	0.05 km^2/min
Height Field-of-View	102.2 m

Optical design techniques (folded reflective grating interferometer, laterally moving demodulation grating, input grating tilt for achromatization, Surrier truss mounting) discussed in an earlier report [7.1] would be used to provide a compact, mechanically robust interferometer module. The size of the optical components is well within the current state-of-the-art in optical component manufacturing.

Detector arrays of a suitable size are also currently available; however, the detector full well and readout rate requirements are not currently met. Both are required to achieve adequate sensitivity. The frame rate requirement (for the LWIR design) corresponds to a 13 MHz pixel rate. Using four parallel channels, a 512 x 512 element HgCdTe array with a 260 fps readout rate is currently under development by Rockwell that achieves a 24 million electron full well. This corresponds to a 17 MHz pixel rate per channel.

The dynamic range and frame rate of the detector array are the critical drivers with respect to sensitivity, especially in the LWIR, because the sensor aperture sizes could be increased if the detector were able to handle the increased photon flux. This, in addition to the need for signal modulation for I and Q sampling, is the driver behind the high frame rates. The path to higher sensitivity, therefore, is dependent on increasing either of these detector attributes. At this time, a substantial advance in performance beyond that discussed in the previous paragraph is difficult to envision in the near future.

While the sensor designs present only modest risks with regard to optical, electro-optical, and mechanical components and subassemblies, the pointing and stabilization requirements are significantly more stressing. Ideally, a capability is needed for steering the sensor line-of-sight to a fixed phase reference point near the ground. The mass stabilized design discussed in Reference 7.1 for an operational system represents a possible approach for an airborne demonstration sensor. The requirements are a bit less stressing, however. In round numbers, the pointing error must change by less than 4 μrad during a frame time (1.25 or 2.5 msec) and be correctable to better than 4 μrad over the synthetic aperture time through either measured pointing information (e.g., inertial data) or autofocusing techniques [see Section 9].

7.1 REFERENCES

[7.1] J.P. Mills et al, *PRISM System Requirements*, ERIM Report to USAF WL/AARI-2, Contract No. F33615-88-C-1749, December 1992 (SECRET), Chapter 4.

Intentionally Left Blank

8.0 RANGE ESTIMATION ALGORITHM DEVELOPMENT

The PRISM sensor acquires a series of 2-dimensional interferometric image data from which a 3-dimensional image is formed. In this section, the image formation algorithm for the PRISM sensor are described and its image characteristics are discussed. The algorithm utilizes a back-projection approach which reconstructs the image by inverting the sensing process. To simplify computation, the virtual fringes along an image plane normal to the sensor line of sight are assumed to be periodic. This far field approximation is good when the target range is sufficiently distant and/or the sensor IFOV is sufficiently narrow. The conditions are met in the field experiments and in the focused search scenario described in this report.

8.1 SENSOR OUTPUT SIGNAL

Consider the imaging geometry in Figure 8-1. The sensor platform flies along a straight line parallel to the x-axis while staring at a fixed point in the target scene. The sensor is also turned to keep a zero optical path difference from the two receiving apertures of the sensor to the fixed point in the target scene throughout the data collection. The point becomes the zero phase reference for the interferometric data and the corresponding x-y plane defines the reference plane where z=0. We note that for a down looking sensor, the x-y plane is approximately parallel to the ground plane. For a size looking sensor, however, the x-y plane will cut the ground plane at an angle.

The hybrid interferometric sensor samples the object scene with a 2-dimensional array of pixels at a spatial frequency given by $(2\pi sr/\lambda)$ $[x\cos\theta + z\sin\theta]$ where R is the distance to the plane being samples and s is the aperture separation at wavelength λ. The complex output of the (m,n) pixel of the detector array is equal to:

$$u(m,n,\theta) = \iiint_{IFOVm,n,\theta} 0(x,y,z)\exp[-i2\pi f(x\cos\theta + z\sin\theta]dxdydz \tag{8-1}$$

where

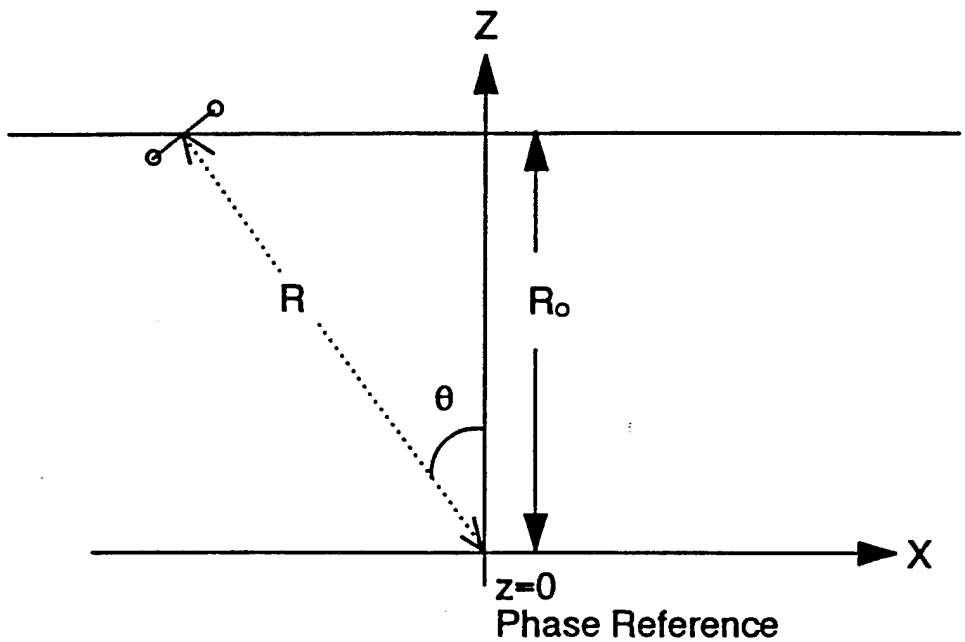

Figure 8-1 Imaging Geometry of PRISM Sensor

$$f = \frac{s}{\lambda\left(\frac{R_0 - z}{\cos\theta}\right)} \tag{8-2}$$

The $IFOV_{m,n,\theta}$ is a column the shape of an elongated pyramid as illustrated in Figure 8-2(a), and $O(x,y,z)$ is the object intensity distribution. To simplify the computation, the sampling frequency is assumed to be uniform across x for a given z. The far field approximation is good if θ and the sensor FOV in the x-direction are both small. However, we have not assumed that the sampling spatial frequency is the same at different z. In the field experiment where the required FOV in the range direction is about 10% of the target nominal range, the spoke like structure of the virtual fringes as shown in Figure 8-2(b) must be taken into account.

With the integration limits defined by the 3-dimensional $IFOV_{m,n,\theta}$, the complex output of the (m,n) pixel can be written as

$$u(m,n,\theta) = \int_{z\tan\theta + \frac{(n+1/2)\rho_x(R_0-z)}{R_0\cos^2\theta}}^{z\tan\theta + \frac{(n+1/2)\rho_x(R_0-z)}{R_0\cos^2\theta}} \int_{(m+1/2)\rho_y}^{(m+1/2)\rho_y} \int_{-00}^{\frac{R_0}{\cos\theta}} 0(x,y,z)\exp[-i2\pi f(x\cos\theta + z\sin\theta)]dxdydz \tag{8-3}$$

Since the sensor flies parallel to the x-axis, the IFOVs of the detector elements are stationary in the y-direction. We can therefore treat the outputs of the rows of detector elements independently, forming M 2-D images. The final 3-D image is obtained by stacking the 2-D slices together. Looking only at a single 2-D slice, Eq. (8-3) can be simplified to:

$$u(m,n,\theta) = \int_{z\tan\theta + \frac{(n+1/2)\rho_x(R_0-z)}{R_0\cos^2\theta}}^{z\tan\theta + \frac{(n+1/2)\rho_x(R_0-z)}{R_0\cos^2\theta}} \int_{-00}^{\frac{R_0}{\cos\theta}} 0(x,y,z)\exp[-i2\pi f(x\cos\theta + z\sin\theta)]dxdz \tag{8-4}$$

The outputs of the PRISM sensor are frames of data from its two-dimensional detector arrays. The 2-D image data can be reformatted into MxN temporal data $u(m,n,t)$ which can be converted into the θ dependent form in Eq. (8-4) via the relationship $\theta = \tan^{-1}(\tan\theta_0 + Vt/R_0)$ where θ_0 is the viewing angle at t-0 and V is the velocity of the sensor platform.

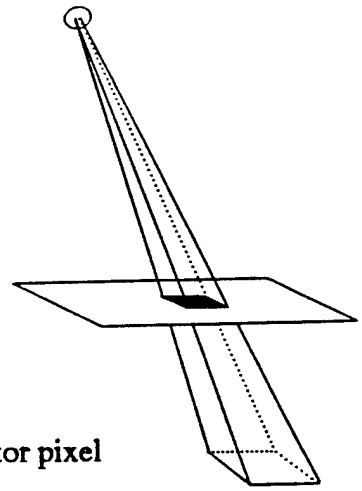

(a)

IFOV of a detector pixel

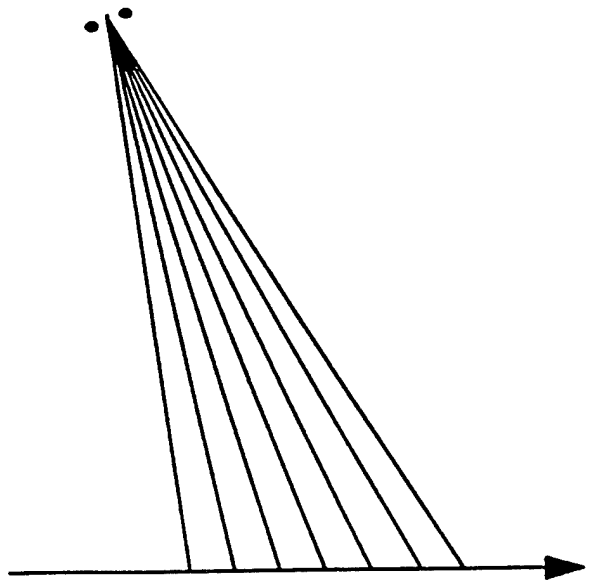

(b)

Spoke-like virtrual fringe pattern

Figure 8-2 Shape of detector IFOV and Sampling Frequency of Virtual Fringes.
(a) Shape of Detector IFOV
(b) Sampling Frequency of Virtual Fringes as function of Range

8.2 IMAGE FORMATION

If a single large detector is used to acquire the interferometric data and the entire target field stays within the region where IFOVs of the detector at different viewing angles overlap (see Figure 8-3), the sensor output can be written as:

$$u(m_0,\theta) = \int_{z\tan\theta+\frac{(-1/2)\rho_x(R_0-z)}{R_0\cos^2\theta}}^{z\tan\theta+\frac{(1/2)\rho_x(R_0-z)}{R_0\cos^2\theta}} \int_{-00}^{\frac{R_0}{\cos\theta}} 0(x,y,z)\exp[-i2\pi f(x\cos\theta + z\sin\theta)]dxdz \qquad (8\text{-}5)$$

Eq. (5) expresses the Fourier transform relationship between the correlation output and the object intensity distribution. The diversity in viewing angles generate an arc shape synthetic aperture as shown in Figure 8-4(a). The image can be constructed directly by the inverse transformation,

$$0(m_0,x,z) = \int_{-\Delta\theta/2}^{\Delta\theta/2} u(m_0,\theta)\exp[i2\pi f(x\cos\theta + z\sin\theta)]d\theta \qquad (8\text{-}6)$$

The impulse response of such an aperture has the shape of a bow-tie as shown in Figure 8-4(b). Since the synthetic aperture created by angle diversity is primarily in the z-direction, the image resolution in the x direction is given simply by the IFOV of the detector. Making the correlation measurements at a single spatial frequency and with a single detector, the image has no spatial information in the x and y directions. To obtain spatial information on the target scene, multiple measurements at different wavelengths or with multiple detectors are required.

In the single detector system, wavelength diversity can be used to generate a large imaging aperture in the x or along track direction, producing multiple pixels within the IFOV of the detector. With the PRISM sensor, image formation in the x and y directions is achieved by utilizing a detector array with M x N detector pixels. The pixelation of the image, however, makes the image formation process more complicated.

In Figure 8-5, the IFOVs of the detectors in the array at different viewing angles are illustrated. As the sensor platform flies over and view the target scene from different

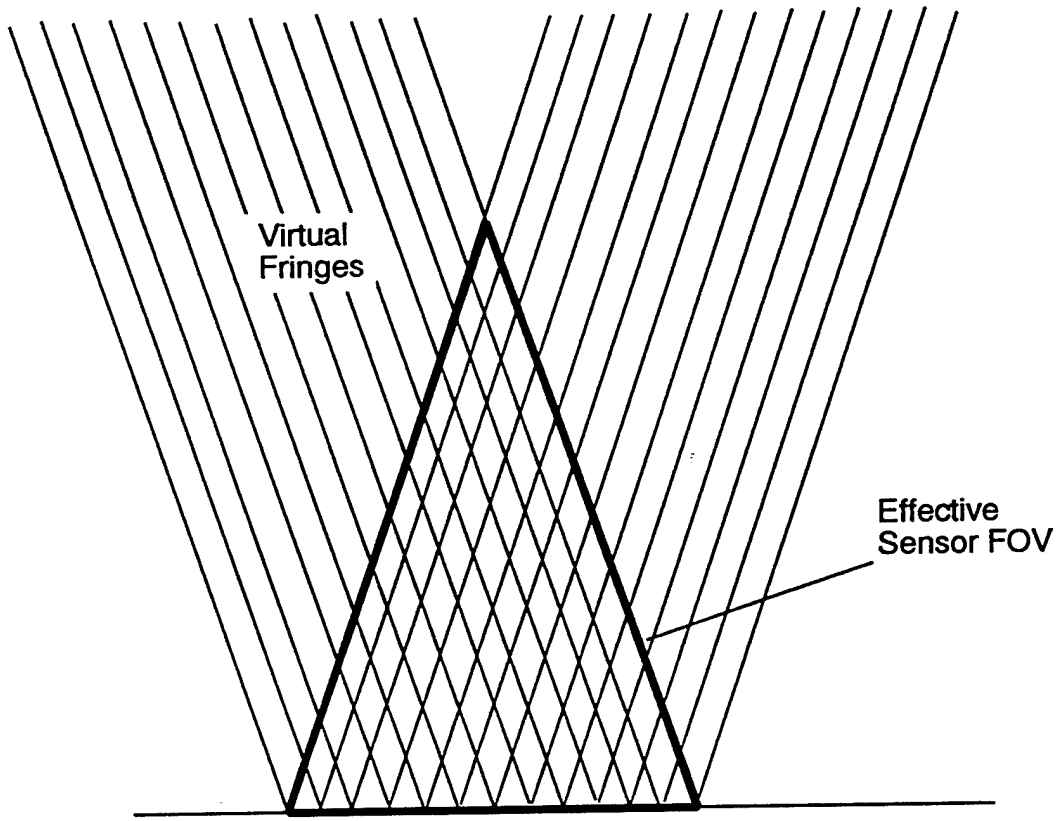

Figure 8-3 Imaging with a Single Large Detector Pixel

Synthetic aperture generated by diversity in viewing angle

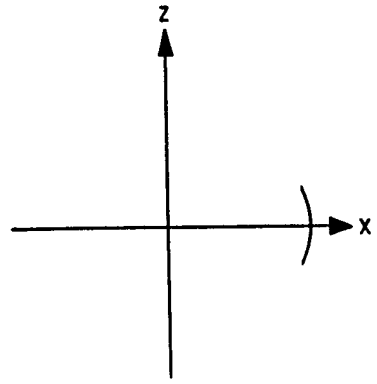

(a)

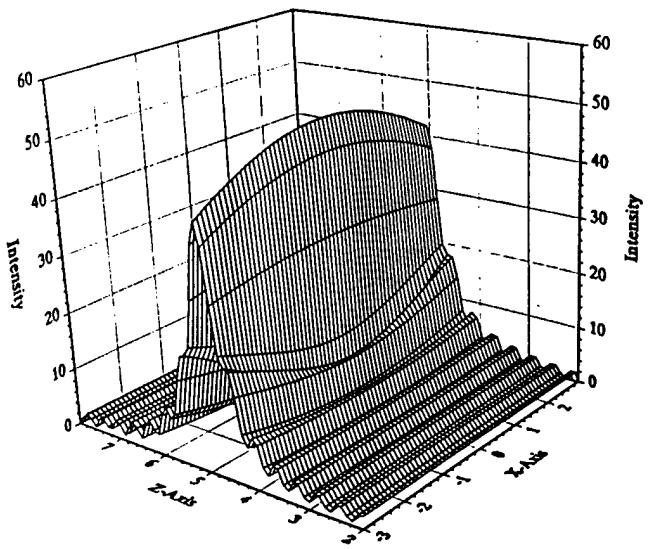

(b)

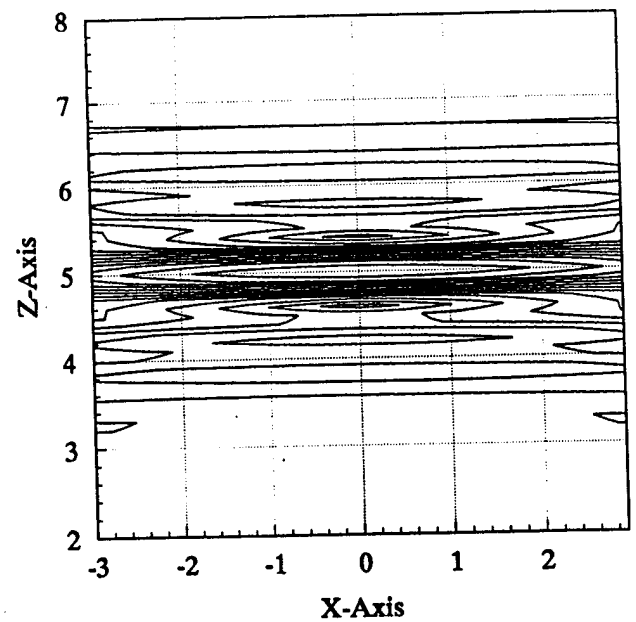

Figure 8-4 Aperture Fill and Impulse Response with a Single Detector and a Single Wavelength.
(a) Synthesized Aperture
(b) Impulse Response

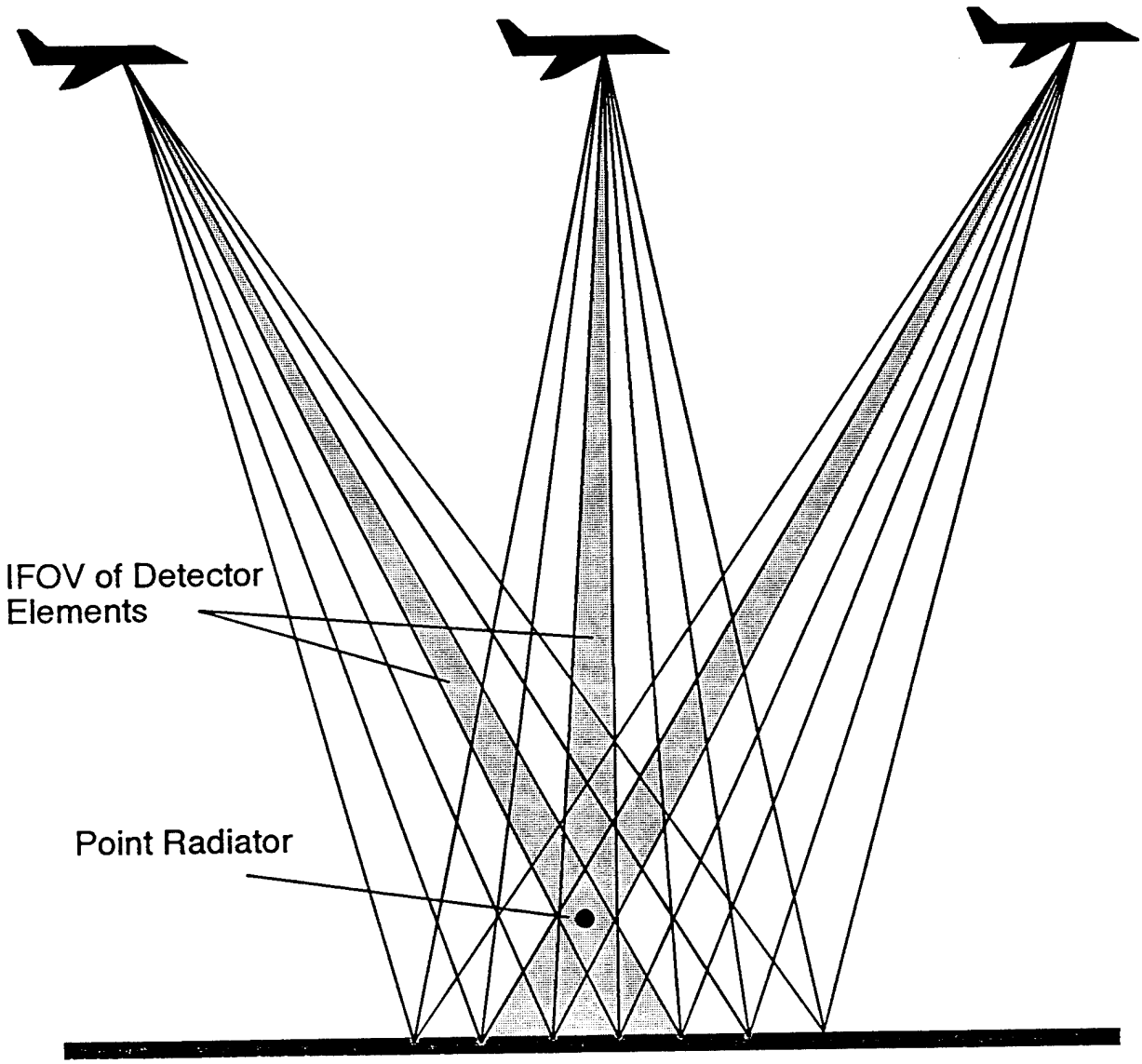

Figure 8-5 Jumping of Point Image From One Detector Element to Another with Change in Viewing Angle

angles, the IFOVs the detector array stay stationary at the reference plane (z=0). At other ranges, however, the IFOVs sweep across the target field in the x or along-track direction. The image of a point radiator located away from the z-0 plane jumps from the IFOV of one detector to the next as the viewing angle changes. This is illustrated in Figure 8-6 which shows the simulated outputs of three adjacent detectors due to a single point radiator in the scene. To form an image of the radiator with full range resolution, the outputs of all the detectors which sensed the emission of the point radiator at different times must be appropriately combined. This is achieved by back projecting virtual fringes over the IFOV of the individual detectors.

To form the PRISM image, complex virtual fringes (i.e. linear phases with the magnitude and phase of the correlation outputs of the detectors at the corresponding viewing angle) are back projected along the IFOVs of the detector elements in the image space as illustrated in Figure 8-7. This is done for the sensor outputs at the various viewing angles and coherently summed. The resulting image is therefore given by:

$$\begin{aligned} 0(m_0,x,z) = & \int_{-\Delta\theta/2}^{\Delta\theta/2} u(m_0,-N/2,\theta)\Sigma_{-N/2}(x,z,\theta)\exp[i2\pi f(x\cos\theta + z\sin\theta)]d\theta \\ & + \int_{-\Delta\theta/2}^{\Delta\theta/2} u(m_0,-N/2+1,\theta)\Sigma_{-N/2+1}(x,z,\theta)\exp[i2\pi f(x\cos\theta + z\sin\theta)]d\theta \\ & + \ldots + \int_{-\Delta\theta/2}^{\Delta\theta/2} u(m_0,N/2,\theta)\Sigma_{N/2}(x,z,\theta)\exp[i2\pi f(x\cos\theta + z\sin\theta)]d\theta \end{aligned} \tag{8-7}$$

where the aperture function, $\Sigma_n(x,z,\theta)$, is the IFOV of the n detector pixel at viewing angle θ which is equal to

$$z\tan\theta + \frac{(n-1/2)\rho_x(R_0-z)}{R_0\cos^2\theta} < x < z\tan\theta + \frac{(n+1/2)\rho_x(R_0-z)}{R_0\cos^2\theta}$$

and

$$-\infty < z < \frac{R_0}{\cos\theta} \tag{8-8}$$

The back projection is performed on the outputs of each row of detectors in the x-direction. The coherently summed data produce a slice of angle-range (x-z) image from each row of detectors. Stacking the two-dimensional images in the y-direction generates a full three-dimensional image of the target scene.

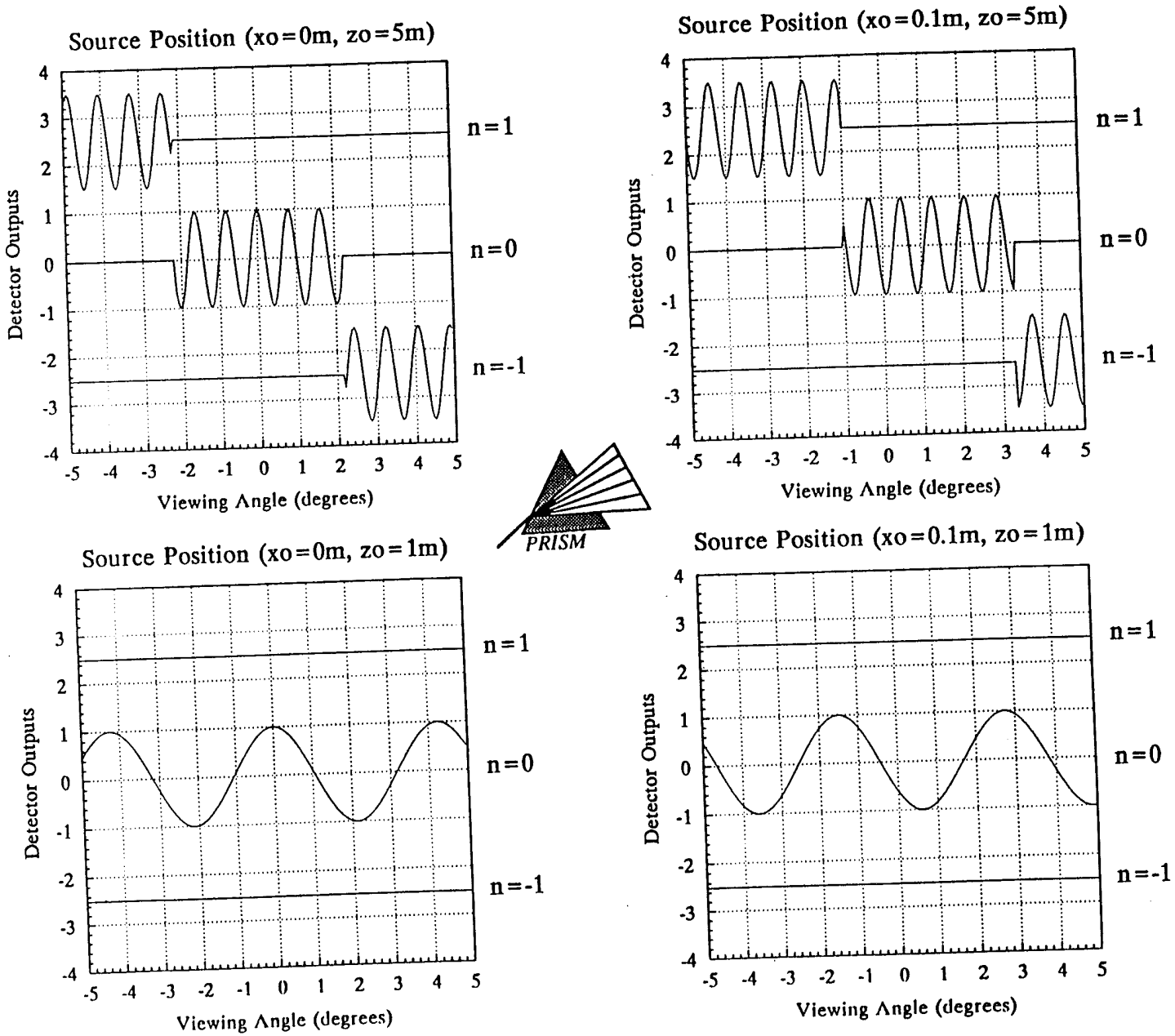

Figure 8-6 Outputs of Three Adjacent Detector Elements Due to a Single Point Radiator at Different Target Locations.

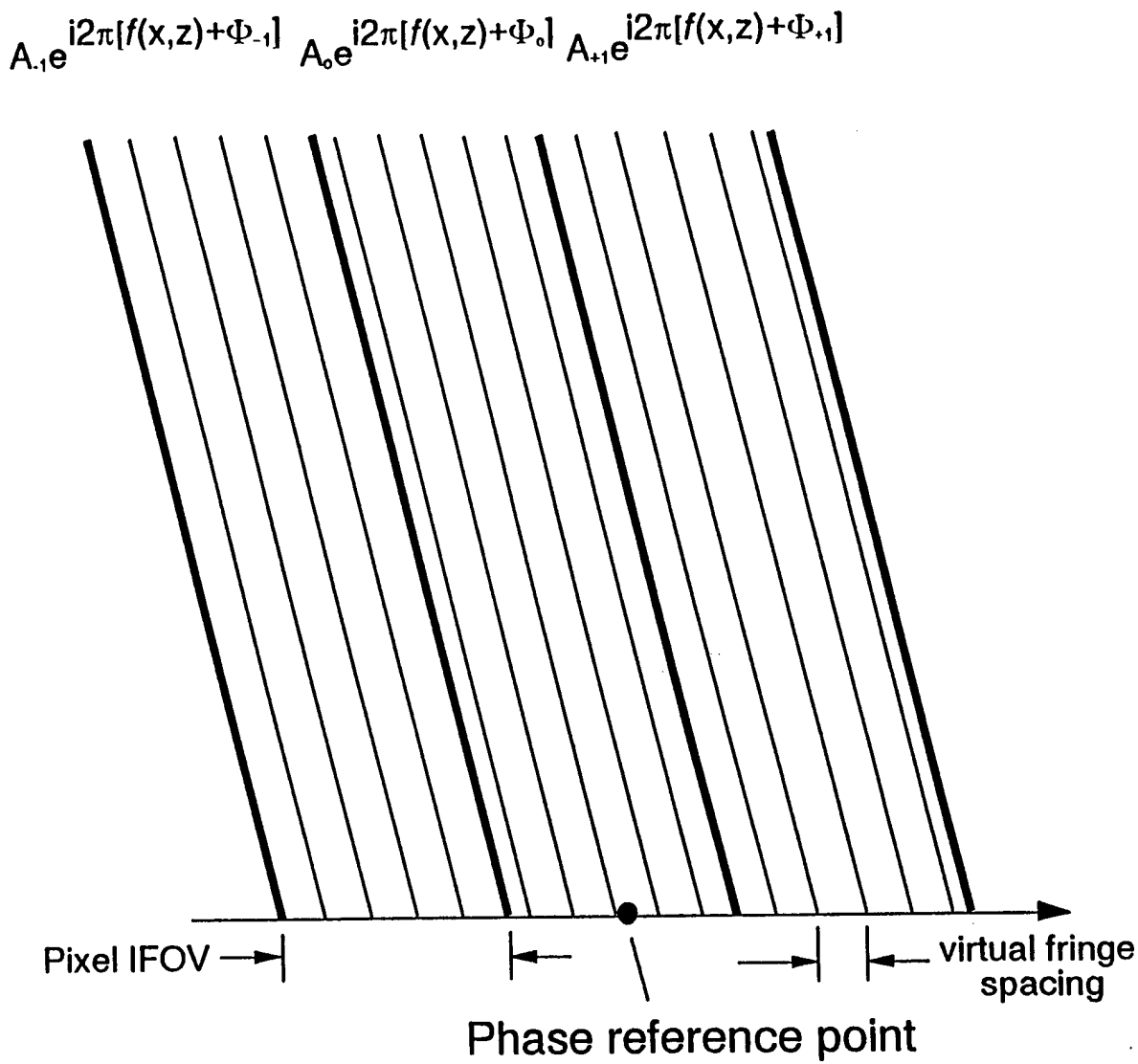

Figure 8-7 Back-projecting Complex Virtual Fringes (Linear Phases) Along the IFOVs of Detector Elements.

8.3 IMPULSE RESPONSE CHARACTERISTICS

Since the aperture function, $\Sigma_n(x,z,\theta)$, is dependent on x and z, the impulse response (IPR) of the PRISM sensor is space-varying. For image points far from the phase reference plane where the virtual fringes is stationary, the IFOVs sweep across the image points continuously in the x direction. The image of point radiators at z>>0 is not pixelated and the shape of the IPR stays approximate constant in the x-direction. The simulated image of a point radiator 5m above the reference plane is shown in Figure 8-8. In the z or range direction, the shape of the IPR in the z direction resembles a sinc function. In the x or along-track direction, the shape of the IPR is given by the convolution of detector FOV with a rect function. We have assumed in the simulation that the focused spot is much smaller than the detector width and the detector IFOV is approximately a rect function. The resulting shape of the IPR in the x-direction is a triangle with a base two pixels wide. The image of a point radiator at the same range but shifted in the x-direction by half a pixel width is shown in Figure 8-9. The IPR is essentially unchanged, demonstrating the PRISM image is continuous and not pixelated for image points sufficiently far away from the phase reference plane. Therefore, given adequate SNR, the position of a point image can be located with a precision much finer than the pixel size of the focal plane sensor.

For a point near the reference plane at z=0, the IPR of its image in the x direction is pixelated since the IFOV of the detectors do not shift significantly with viewing angle. The IPR also becomes more space varying in the x-direction. For a point radiator located near the center of the pixel, it is seen mostly by a single detector element. The IPR of its image is approximately a rect function with the width of a detector pixel as shown in Figure 8-10. If the point radiator is located between the IFOVs of two adjacent detector elements such that it is seen by one detector over half of the viewing angles and by another over the other half, the resulting IPR has a significantly different shape as shown in Figure 8-11.

When the virtual fringes (linear phases) are back projected onto the image space, it can be projected onto a very fine grid producing a highly sampled image. However, the computational load could be unacceptably high. The minimum sampling requirement is dependent on the maximum allowable signal loss and it can be determined from the shape and width of the IPR. The shape of the IPR is triangular in the x-direction and a sinc function in the z-direction. Therefore, signal loss due to mismatches between the location

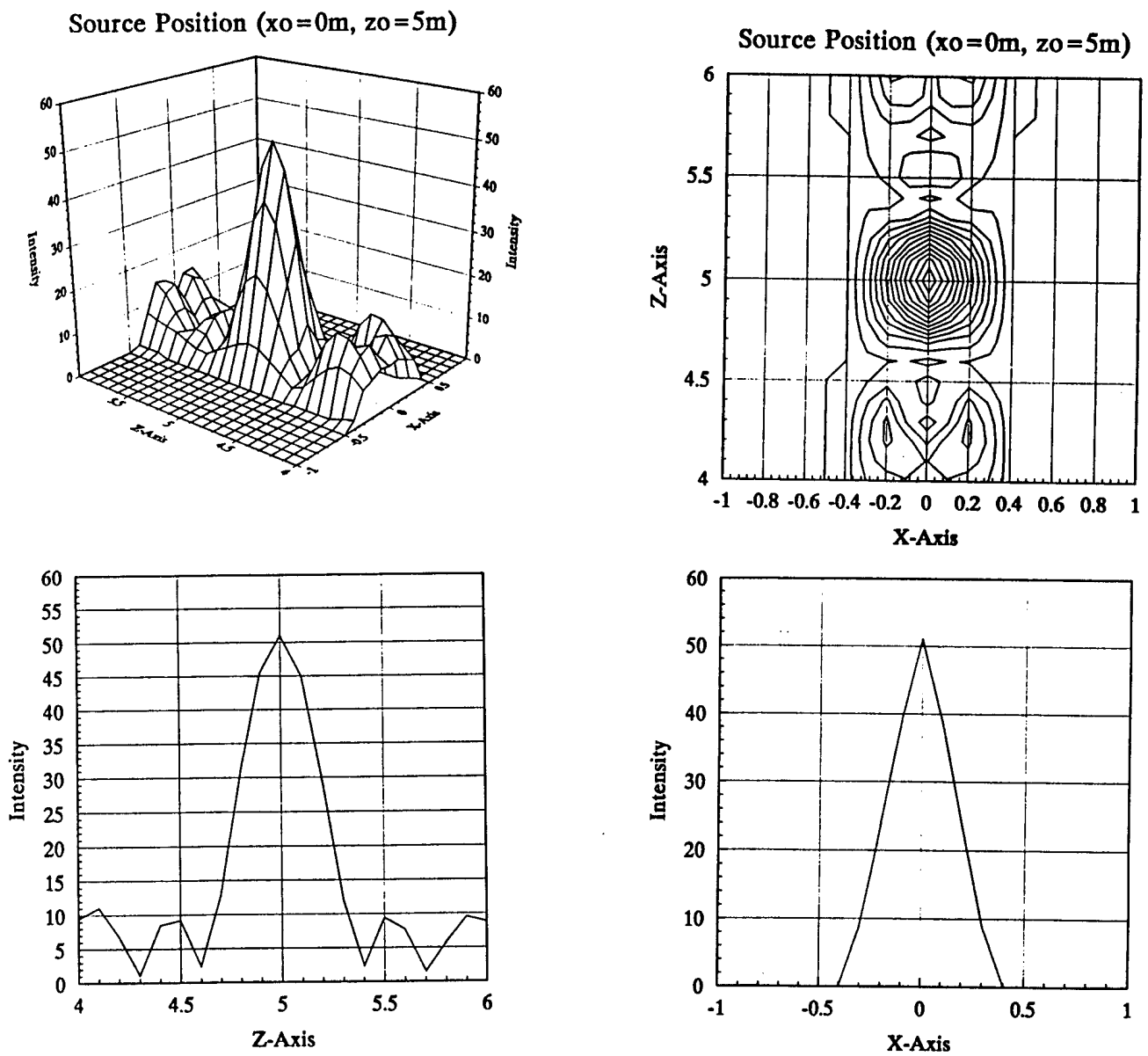

Figure 8-8 Simulated Image of a Point Radiator 5m Above Reference Plane.

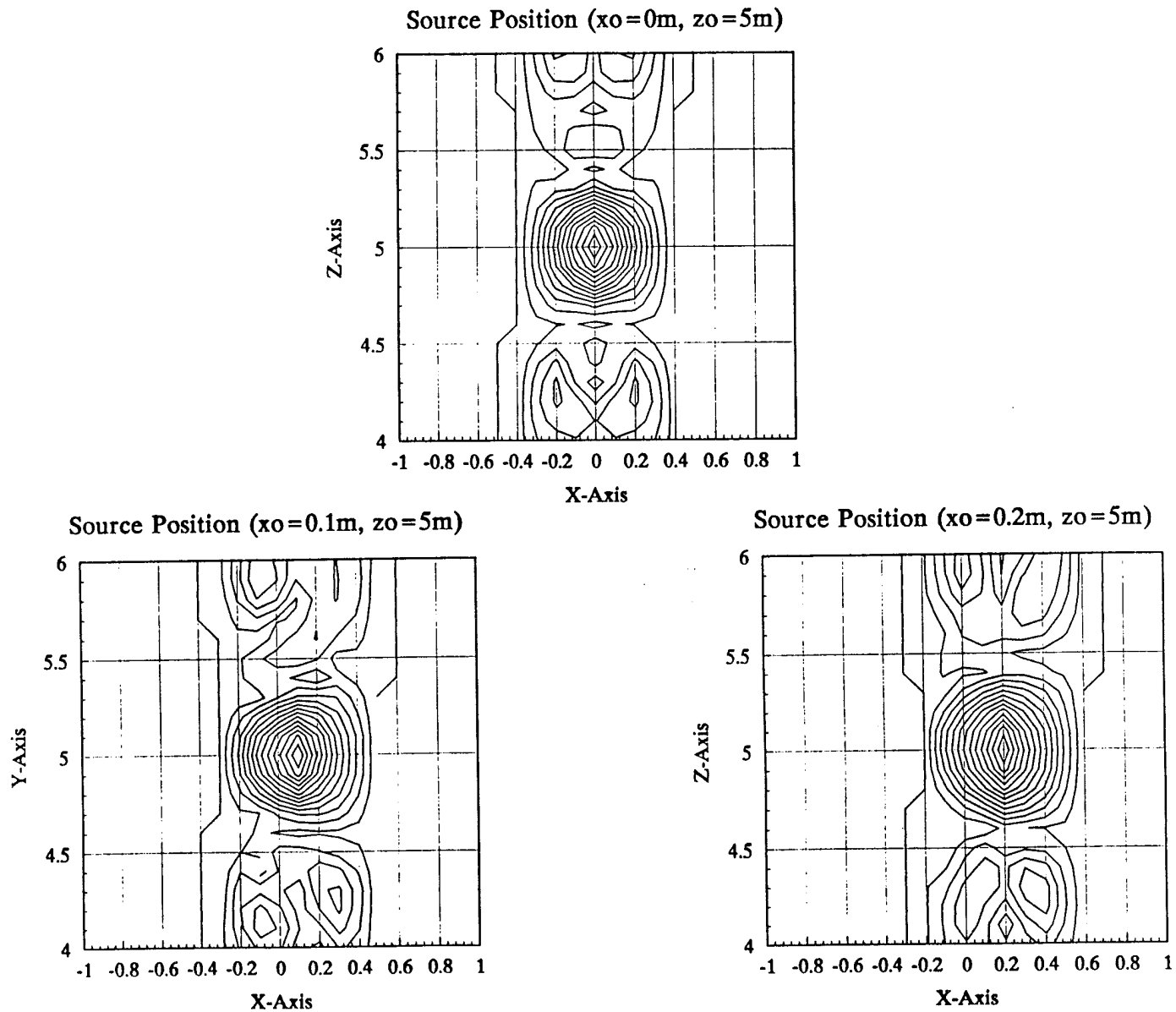

Figure 8-9 Simulated Images of Point Radiators at Different Locations 5m above Reference Plane.

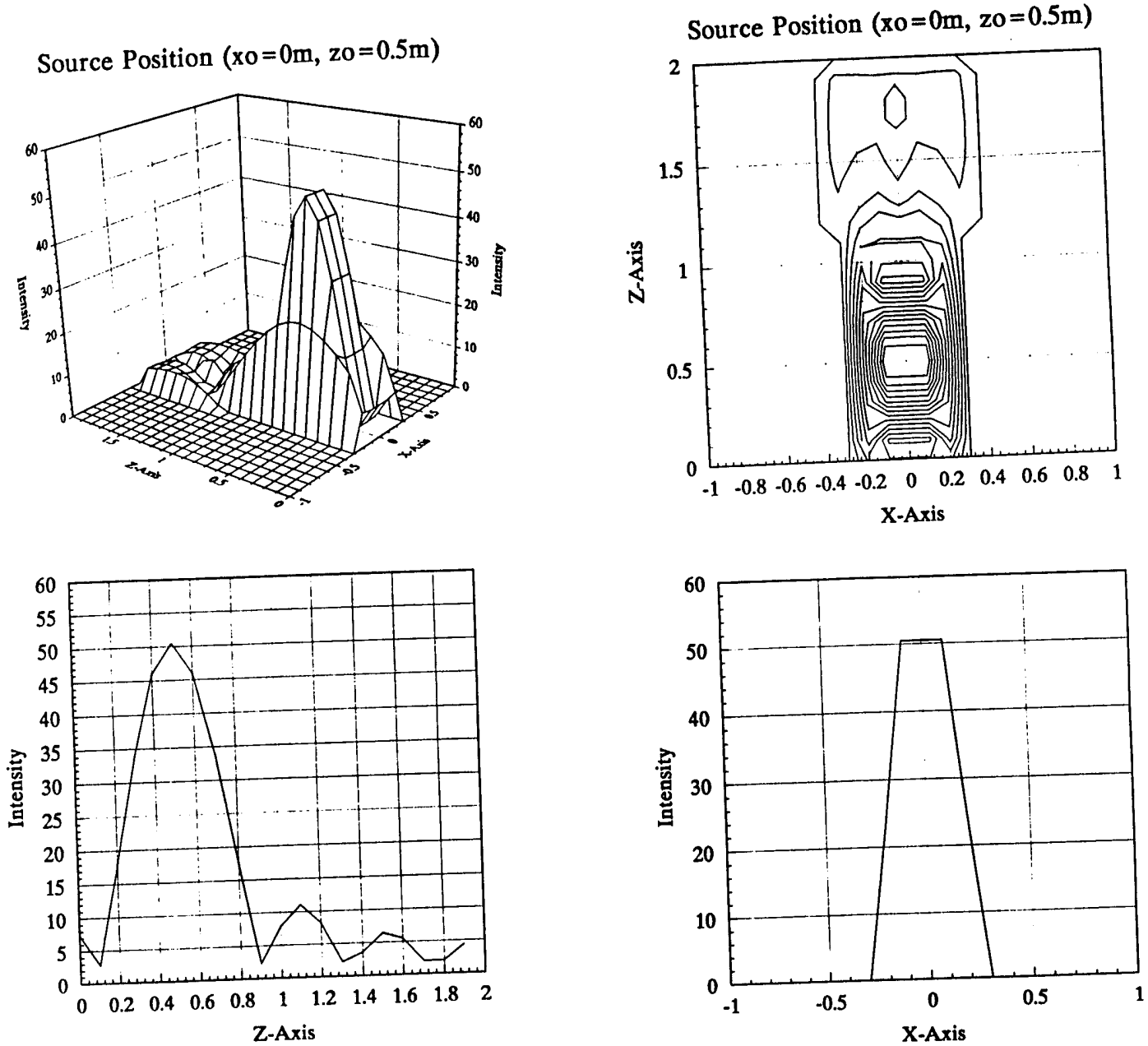

Figure 8-10 Image of Point Radiator Located Near the Reference Plane.

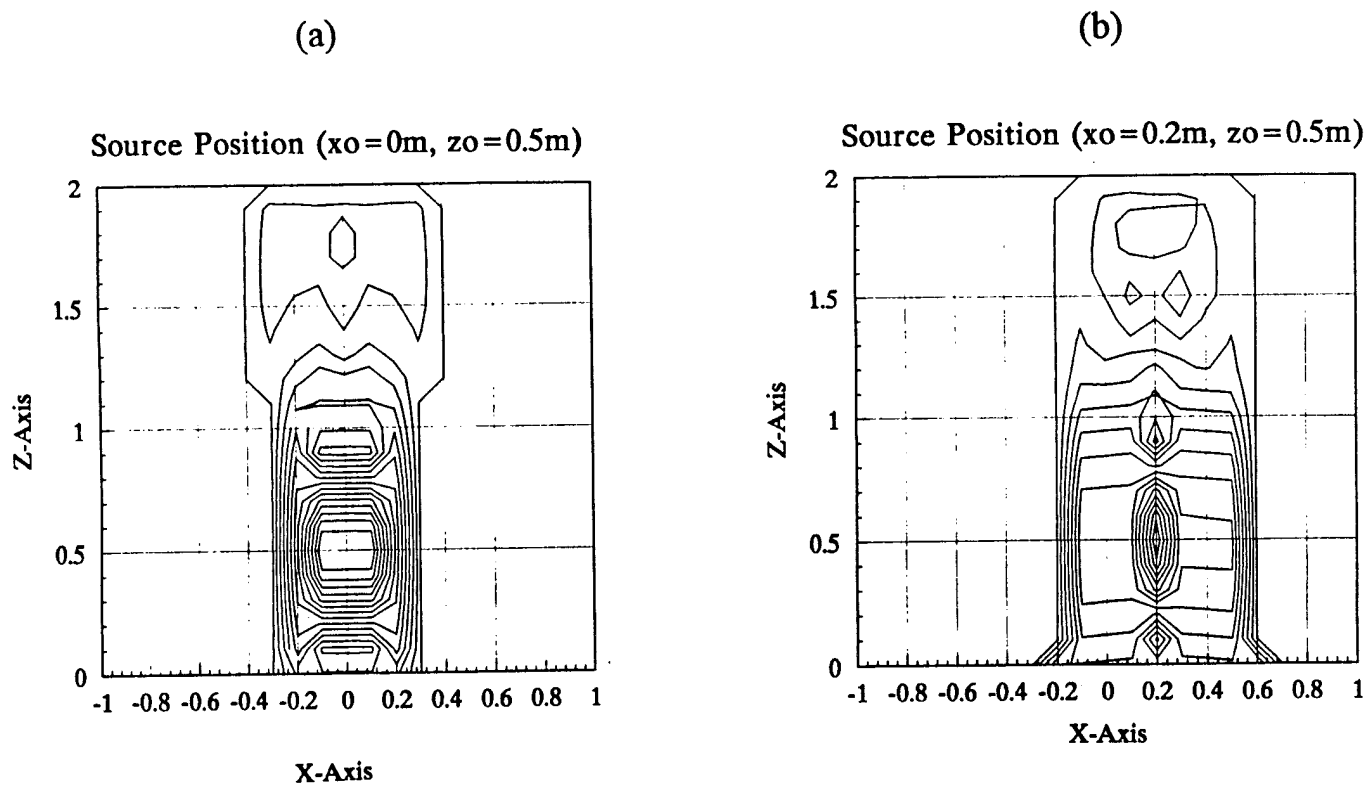

Figure 8-11 Simulated Images of Point Radiators at Different Locations 0.5m above Reference Plane.
(a) Point Radiator at Center of Pixel when Viewed at the Middle of the Angular Range
(b) Point Radiator Between two pixels when Viewed at the Middle of the Angular Range

of the peak of the IPR and the sampling grid can be limited to a maximum of 12.5% (as illustrated in Figure 8-12) by using a sampling period at the image plane equaling to one quarter of the pixel spacing.

8.4 ESTIMATING RANGE OF EXTENDED SURFACES

The range to the target surface is given by the location of the compressed image in the z-direction. For a point target, the target range can be determined from the location of the peak of the point image. Range estimation, however, is more complicated when imaging extended surfaces such as natural ground cover. The image exhibits a speckle characteristic very similar to the one well known in coherent imaging.

An extended surface can be modeled as a superposition of random point radiators. Within the IFOV of a detector pixel, there are several virtual fringes. The correlation output due to a particular radiator can take on any phase value depending on its location relative to the phase of the virtual fringes. With the superposition of many radiators, the correlation output is given by the sum of many sinusoids of the same spatial frequency (since the radiators are at the same range) but with different phases. The reconstructed image is, in turn, a summation of many IPRs with different phases. The resulting image intensity at the target surface can be very bright or very dim, depending of the phase relationship between the interfering point images.

To demonstrate the effect, we created as the input target, a set of random point radiators located at the same target range as shown in Figure 8-13(a). The resulting image is presented in Figure 8-13(b). The intensity distribution is "speckled" with many drop outs. If we simply locate the peak intensity along sample lines separated by one pixel distance, there could be many range estimation errors. To minimize range estimation errors, the following algorithm was used.

1) Form image via back projection over IFOVs of detector pixels with sampling period in x and z direction equal to 1/4 of the detector pixel IFOV.
2) Threshold the 3-D image data above noise level.
3) Group every four samples lines in the x-direction together and determine the z location of the peak value within each group or pixel.

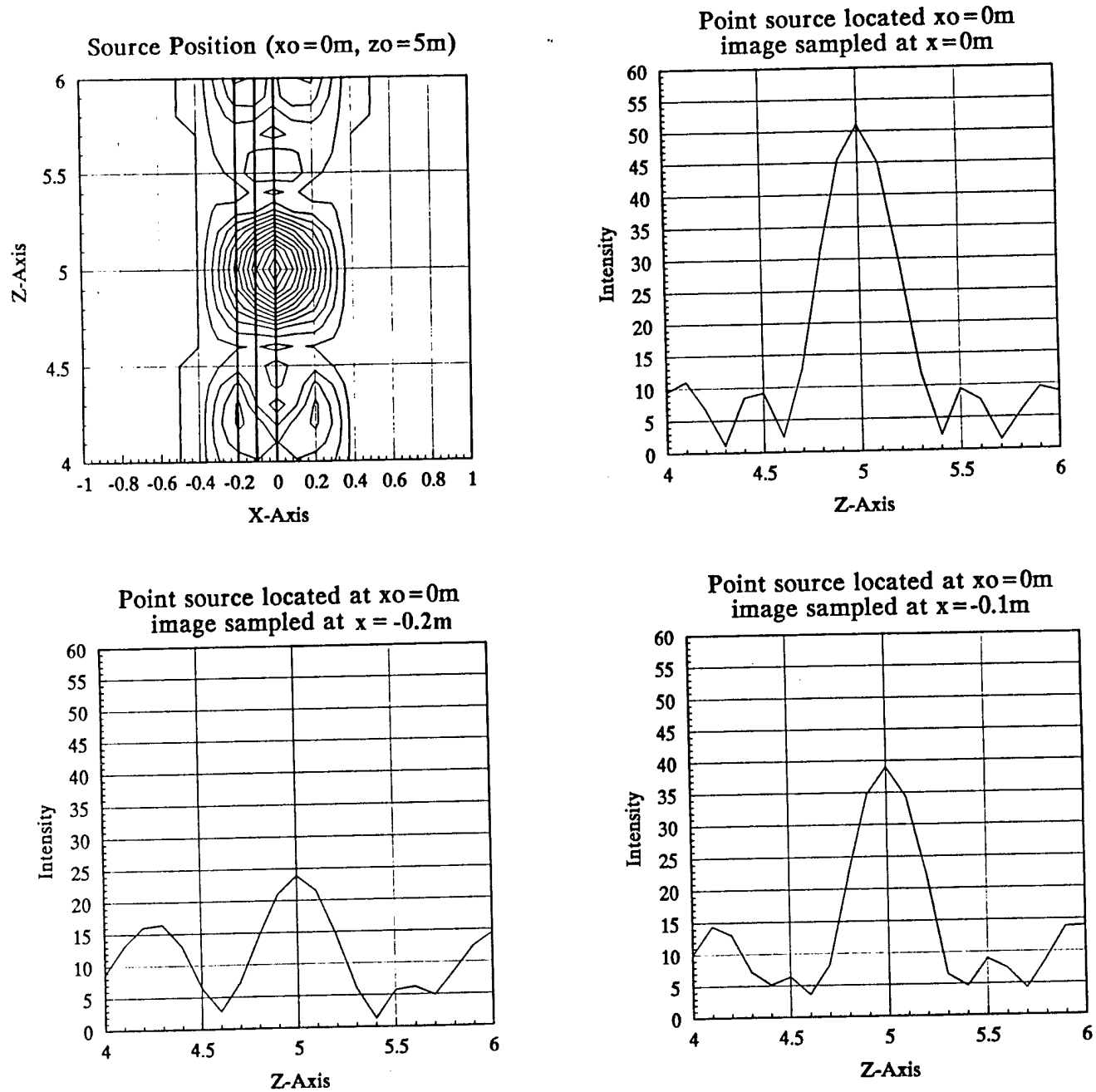

Figure 8-12 Using Sampling Period 1/4 of the Pixel Width to Limit Signal Loss to Less Than 12.5%.

(a)

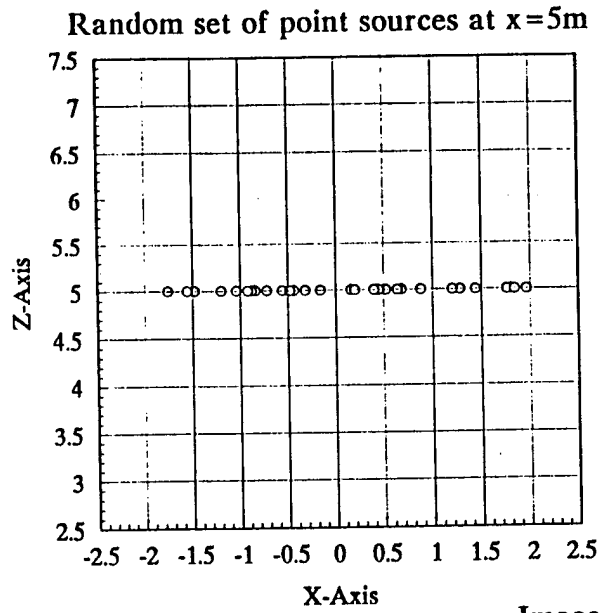

(b)

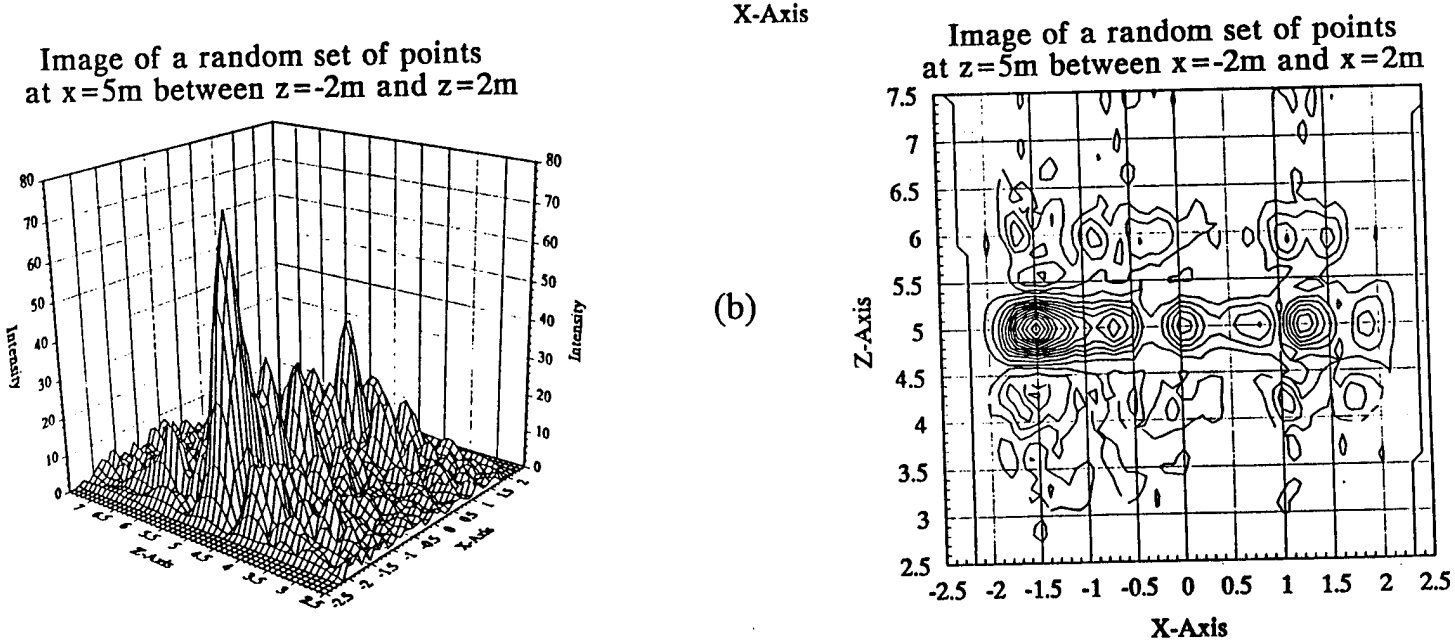

Figure 8-13 Speckle Effect when Imaging Extended Surface with Random Texture.
(a) Radiators Forming Surface
(b) Speckled Image

Forming the image with a sampling period 1/4 of the pixel width ensures that the IPR is sampled near its peak intensity as explained earlier. Grouping every four sample lines together in the x-direction reforms full pixels. Since the average speckle size is one pixel wide, the peak intensity within a group of four sample lines are, in most cases, located at the correct target range in the speckled image. In the simulated example, the algorithm produced the correct range estimates for all the pixels, as shown in Figure 8-14.

The speckle effect is also present for an object extended in the z-direction (e.g. tree canopy). A simulation example is shown in Figure 8-15. The intensity distribution of the image does not correspond directly to the intensity distribution of the extended target and the peak intensity does not necessarily represent the surface at the closest range. However, the image support does correspond to the extent of the object in the range direction.

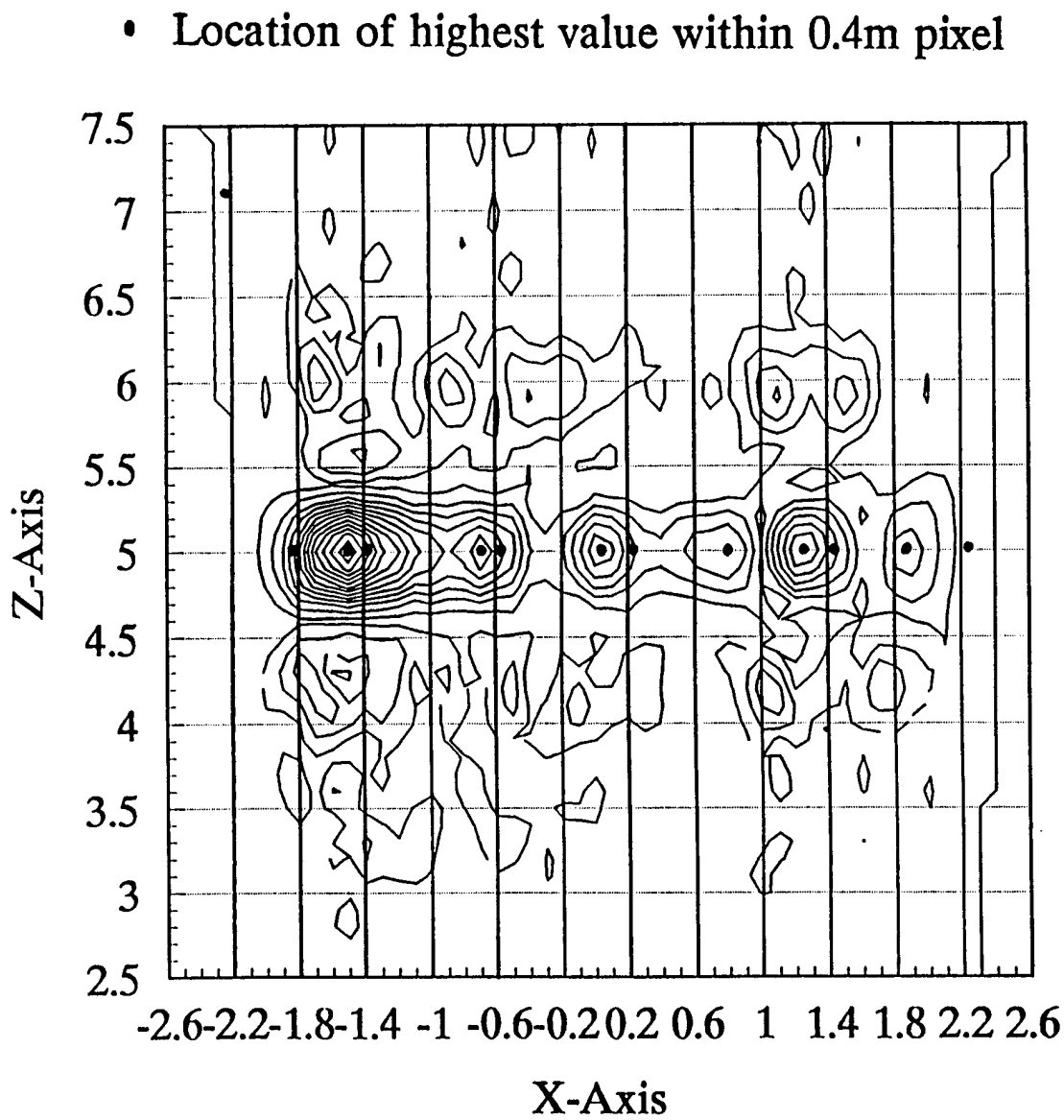

Figure 8-14 Surface Estimation by Grouping Four Sample Lines Together and Determining the Location of the Peak.

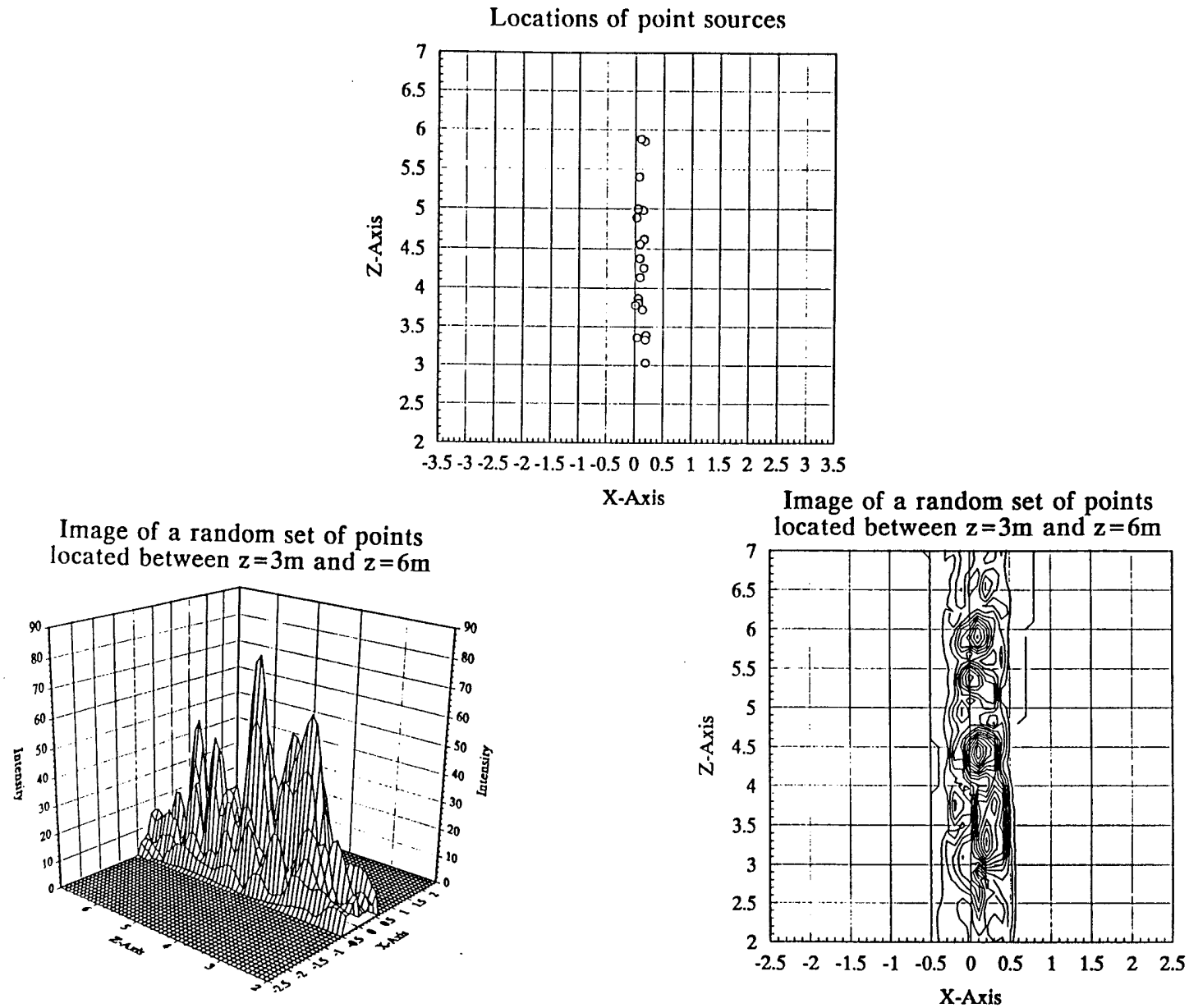

Figure 8-15 Speckle Effect in the Range Direction when Imaging Range Dispersed Targets.

9.0 PRISM FOCUSING

The PRISM sensor places tight tolerances on system stability and atmospheric turbulence effects to avoid phase errors in the time domain. In instances where these tolerances are not met, an unacceptable smearing of the depth information will occur at each x-y pixel. We performed an initial development of a phase-error correction algorithm and demonstrated its ability to correct these errors by post-processing the data, based on the data itself.

Our investigation includes the effects of space-invariant phase errors, such as those due to pointing errors, atmospheric turbulence near the sensor, and path-length errors within the interferometer. We assume the simplest form of the phase error, one that is the same for all x-y pixels and depends only on the time (or look-angle) variable. We assume a simplified model for the depth image being given by the Fourier transform of the data over the look-angle variable.

Several phase-correction algorithms could be applied to the PRISM data. Our first choice was a modified version of the shear averaging algorithm [9.1], where the shear is in the look-angle dimension. We derived a version of shear averaging that includes a weighting function that could emphasize the contributions due to pixels that (a) have the most energy in the PRISM bandpass and (b) are near to the reference plane in the depth dimension. The latter selectivity is to minimize problems with pixel walk associated with depth distance from the reference plane. We tested the shear averaging algorithm on data with simulated phase errors and determined its performance. We found that shear averaging without the weighting function worked quite well, and so we did not progress to the weighting function in practice. We found it necessary to remove the linear trend from the phase-error estimate in order to avoid problems with the PRISM bias term.

Although shear averaging was successful, it would also be useful to implement a second phase-correction algorithm, such as prominent point processing, to determine which algorithm works best. It is also important to perform preliminary analysis to predict performance as a function of signal level and amount and type (quadratic, higher-order, or random) of phase error, compare theory with the simulation experiment results, demonstrate it on real data, and determine the degree to which this might lessen the tolerances on the system.

9.1 SIGNAL MODEL

A simplified model for the signal history collected by the PRISM sensor is as follows:

$$G(x, y, \theta) = F(x, y, \theta) \exp[i\phi_e(\theta)] \tag{9-1}$$

where

(x, y) = pixel coordinates

θ = look angle $\propto$ t = time

$F(x, y, \theta)$ = ideal complex PRISM signal without phase errors

$\phi_e(\theta)$ = phase error

$g(x, y, z) = F\,[G(x, y, \theta)]$ = 3-D image (voxels)

F = 1-D Fourier transform in θ-z dimension

Note that this ignores (1) any component of the error that is space variant [i.e., depends on (x, y)], (2) pixel walk, and (3) PRISM bias terms.

9.2 PHASE-ERROR CORRECTION ALGORITHMS

Several algorithms have been devised for estimating and correcting the phase errors from the corrupted data for synthetic-aperture radar (SAR). The more common ones are summarized in Table 9-1.

Table 9-1. Correction Algorithms for Spatially Invariant Phase Errors

Algorithm	Assumption	Status	Error Order, Size	Image Character Required	Computation Required	Auto-matic?
Single Prominent Point (ERIM)	Have image of bright point source	Mature	Any, Large	Prominent point	Moderate	No
Sub-aperture Processing (Map-drift) (ERIM, Hughes)	Image features invariant with look angle	Mature	Low, Large	Structured image	Moderate	Yes
Shear Averaging (U. Penn., ERIM)	**Signal history correlation is stationary**	**Partial**	**Any, Large**	**None**	**Minimal**	**Yes**
Phase Gradient (PGA) (Shift-and-add) (Sandia)	Have image of bright point source	Partial	Any, Large	None ?	Large	Yes
Phase Retrieval (ERIM)	Finite diameter or known low-return area	New	Any, Large	Limited extent	Very large	No
Image Sharpening (ERIM)	Maximum contrast ==> minimum phase error	Partial	Low, Small	Structured image	Very large	Yes

From this group of phase-error corrections we have selected the shear averaging algorithm because (1) it is, by far, the fastest to compute, (2) it can handle arbitrarily high-order phase errors, (3) it can handle large amounts of phase errors, (4) it makes the minimal assumptions about the image (does not require a prominent point), and (5) it is relatively easy to implement. It does require that the signal history be stationary, i.e., it does not change much during the collection interval.

9.3 EXTENSION OF SHEAR AVERAGING ALGORITHM

We extended the shear averaging algorithm [9.1] to make it operate on PRISM data. We first form the sheared sum

$$S(\theta) = |S(\theta)| \exp[i\theta(\theta)] = \sum_{x,y} w(x, y)\, G(x, y, \theta)\, G^*(x, y, \theta - \delta\theta) \qquad (9\text{-}2)$$

where w(x, y) is an optional weighting function, $\delta\theta$ is the interval between adjacent frames, and G* is the complex conjugate of G.

We can use the weighting function to de-emphasize the contributions due to pixels where the signal is weak or for signals that lie far from the reference plane and would therefore suffer from pixel walk. An example of such a weighting function would be

$$w(x, y) = \exp[-(z - z_{ref})^2/\sigma_z^2] \times \text{Peak-strength}(x, y) \qquad (9\text{-}3)$$

where we assume that the range to the (x, y) pixel has been determined to be z (as, say, the brightest compressed range bin) and the brightness of that brightest range bin is Peak-strength(x, y). In this expression z_{ref} is the reference plane where there would be no pixel walk, and σ_z determines how quickly the weighting function falls off as we depart from the reference plane. Use of such a weighting function would require us to compute the range-compressed image, return to the signal-history domain to apply the weighting function, and then recompute the image. If we do not use the weighting function, then the algorithm is much faster since the range-compressed image must then be computed only once.

The sheared sum $S(\theta)$ is important because its phase is approximately equal to the difference in the phase error between that frame and the previous one. We can show this as follows. Inserting the signal model into the expression for the sheared sum, we have

$$S(\theta) = |S(\theta)| \exp[i\eta(\theta)]$$

$$= \exp[i\phi_e(\theta) - i\phi_e(\theta - \delta\theta)] \sum_{x,y} w(x, y)\, F(x, y, \theta)\, F^*(x, y, \theta - \delta\theta)$$

$$= \exp[i\phi_e(\theta) - i\phi_e(\theta - \delta\theta)]\, I(\theta, \delta\theta)(9\text{-}0) \qquad (9\text{-}4)$$

where the phase error comes out in front of the summation since it is independent of (x, y). The summation

$$I(\theta, \delta\theta) = \sum_{x,y} w(x, y)\, F(x, y, \theta)\, F^*(x, y, \theta - \delta\theta) \qquad (9\text{-}5)$$

resembles the correlation function from statistical optics which, by the van Cittert-Zernike theorem is proportional to the Fourier transform of the object reflectivity in the z direction. However, the van Cittert-Zernike relationship does not strictly hold for this case. Nevertheless, this summation will usually share one important feature with the optical correlation function: it will tend to be independent of θ, so we could write it as

$$I(\delta\theta) = |I(\delta\theta)| \exp[\psi(\delta\theta)] \,, \qquad (9\text{-}6)$$

where $|I(\delta\theta)|$ is the magnitude and $\psi(\delta\theta)$ is the phase of $I(\delta\theta)$. Assuming that $\delta\theta$, the interval between pairs of adjacent frames, is constant, independent of θ, then we have the result that $I(\delta\theta)$ has a constant phase, $\psi(\delta\theta)$. This can be shown explicitly for the case where the scene has just a single height function at each pixel (which would not be true for pixels in which the scene consists of a net with holes in it, for example). Then the image is a delta function in the height dimension [but with a different height, $z(x, y) = h(x, y)$ at each pixel], and its Fourier transform is a height-dependent linear phase function of θ. The object distribution is given by

$$f(x, y, z) = a(x, y)\, \delta(z - z_0(x, y)) \qquad (9\text{-}7)$$

and its Fourier transform, the signal history, is given by

$$F(x, y, \theta) = a(x, y) \exp[i2\pi\alpha\, \theta\, z_0(x, y)/N] \,, \qquad (9\text{-}8)$$

where α is a constant. Inserting this in the expression above yields

$$I(\theta, \delta\theta) = \sum_{x,y} w(x, y)\, F(x, y, \theta)\, F^*(x, y, \theta - \delta\theta)$$

$$= \sum_{x,y} w(x, y)\, a^2(x, y) \exp[i2\pi\alpha\, \theta\, z(x, y)/N] \exp[-i2\pi\alpha\, (\theta - \delta\theta)\, z(x, y)/N]$$

$$= \sum_{x,y} w(x, y)\, a^2(x, y) \exp[i2\pi\alpha\, \delta\theta\, z(x, y)/N] \qquad (9\text{-}9)$$

which is a complex constant independent of θ.

Whenever $I(\theta, \delta\theta) = I(\delta\theta)$ is independent of θ, then the phase of $S(\theta)$ is

$$\eta(\theta) \approx \phi_e(\theta) - \phi_e(\theta - \delta\theta) + \psi(\delta\theta) , \tag{9-10}$$

where $\psi(\delta\theta)$ is the phase of $I(\delta\theta)$.

The second step in shear averaging is to compute the running sum of the $\eta(\theta)$, to give us a phase-error estimate

$$\phi(0) = 0 \ , \ \phi(\theta) = \phi(\theta - \delta\theta) + \eta(\theta) \ . \tag{9-11}$$

Inserting the expression for $\eta(\theta)$ yields

$$\begin{aligned}
\phi(\theta) &\approx \phi(\theta - \delta\theta) + \phi_e(\theta) - \phi_e(\theta - \delta\theta) + \psi(\delta\theta) \\
&= [\phi(\theta - 2\,\delta\theta) + \phi_e(\theta - \delta\theta) - \phi_e(\theta - 2\,\delta\theta) + \psi(\delta\theta)] + \phi_e(\theta) - \phi_e(\theta - \delta\theta) + \psi(\delta\theta) \\
&= \phi(\theta - 2\,\delta\theta) - \phi_e(\theta - 2\,\delta\theta) + \phi_e(\theta) + 2\,\psi(\delta\theta) \\
&= \ldots \\
\phi(\theta) &\approx \phi_e(\theta) + n\,\psi(\delta\theta) ,
\end{aligned} \tag{9-12}$$

where n is the number of frames up to that point (it is proportional to θ). That is, the phase-error estimate, $\phi(\theta)$, is approximately equal to the true phase error, $\phi_e(\theta)$, plus a linear phase term $n\,\psi(\delta\theta)$.

Ordinarily linear phase terms only shift the image without smearing it and are of little concern. However, for PRISM it is important to accurately subtract a bias term, and an unknown linear phase would complicate this.

The third step is to correct the data by subtracting the phase-error estimate from its phase to compute the corrected data:

$$G_{cor}(x, y, \theta) = G(x, y, \theta)\ \exp[-i\phi(\theta)] \ . \tag{9-13}$$

Then the height dimension is formed in the usual way by Fourier transforming in the θ dimension.

9.4 BIAS TERM

A consideration that we did not anticipate at the beginning of this study is the effect of phase errors on the PRISM bias term. The bias term is large compared with the desired signal term, so an accurate subtraction of the bias term is essential for good image quality. In the Fourier (signal history) domain, the bias term [which depends on the (x, y) pixel location] is a constant. In the range-compressed image domain, it becomes the impulse response (in z), which, for an unweighted aperture would be a $\mathrm{sinc}(z) = \sin(\pi z)/(\pi z)$ function. From the discussion above, we see that the phase-error correction algorithm introduces a linear-phase term $n\ \psi(\delta\theta)$, where n is proportional to θ. This will happen for all the phase-error correction approaches with which we are familiar, although the size of the linear phase error may depend on the details of the phase-error correction approach. This results in a translation in the z dimension of the range-compressed image. If the impulse-response term due to the bias is also shifted, then the bias subtraction will be in error and can leave a large residual term (the difference between the inherent bias-related impulse response and the incorrectly translated, subtracted impulse response).

This residual error can be greatly reduced or eliminated in a variety of ways. The simplest way, which we demonstrated, is to subtract from the phase-error estimate any linear-phase terms. This greatly reduced the residual bias term, although it may not have eliminated it entirely. Further research will be required to determine the optimum approach to eliminating the residual bias term.

9.5 SIMULATION RESULTS

To see how well shear averaging performed when correcting phase errors in PRISM signal histories, we used simulated data. This approach gives us the flexibility of changing the type and magnitude of the error and the ability to determine how well the algorithm was doing by directly comparing the added phase error with the phase error estimated by shear averaging.

Using 30 simulated frames of a truck at different aspect angles from the SIRIM system, we produced a simulated PRISM collection. One of the 30 frames we used is shown in Figure 9-1. The other frames view the truck from different angles left-to-right. The simulated data is free of detector noise.

We processed the resulting PRISM signal history to produce the 3-D image shown in Figure 9-2. Since the data produced by the PRISM system is three dimensional, all the images in this section are shown in two dimensions as separate X, Y, and Z projections. The Z projection gives an x-y

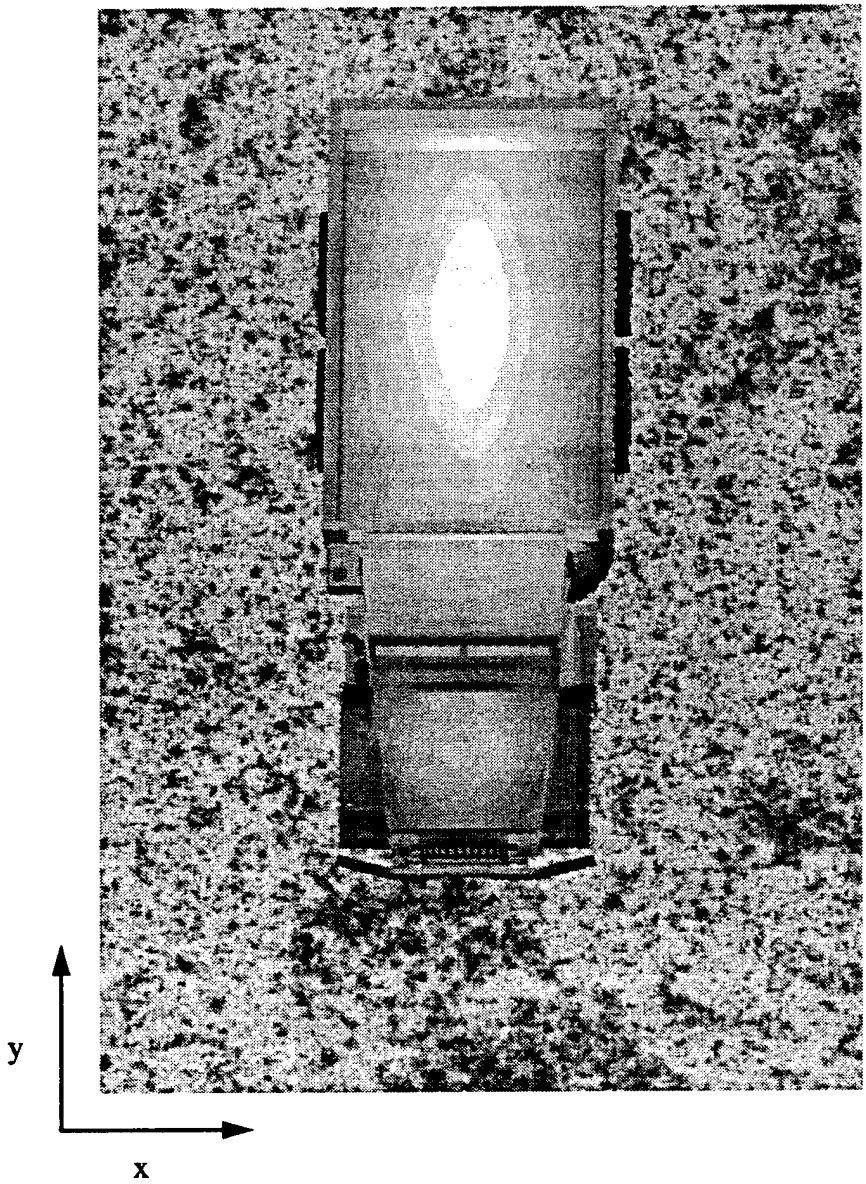

Figure 9-1: Example SIRIM image of a truck (the 10th of 30 images) used in the signal history simulations.

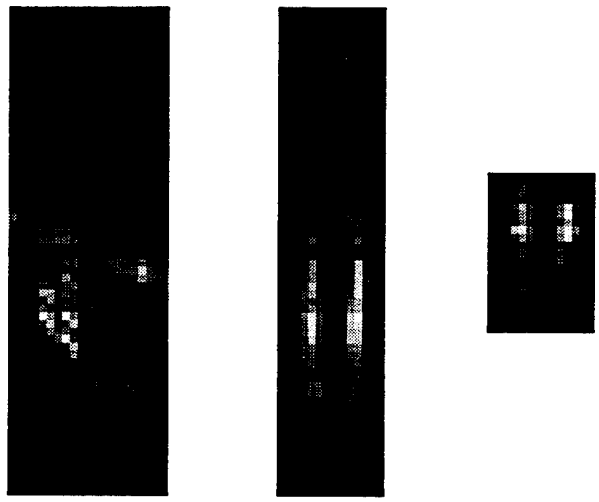

X Y Z

Figure 9-2: The 2-D X, Y, and Z projections of the 3 -D PRISM image used in the simulations.

view of the image, as though viewed from above (much like the picture in Figure 9-1). The X projection gives a y-z view of the image, as though viewed from the front of the truck. The Y projection gives an x-z view of the image, as though viewed from the side of the truck. In the X and Y projections, the z direction is from top-to-bottom; this is the direction in which smearing will occur due to phase errors. All projections on a given dimension are identically scaled across all figures. This causes obvious image saturation in some cases, but it allows us to show the details more clearly in the areas of the images having lower signal levels.

The main result of our work is shown in Figures 9-3, 9-5, and 9-7. These images show the result of applying shear averaging with linear trend removal on simulated PRISM signal histories with added quadratic error. The quadratic error in these examples was 1/4 wave, 1/2 wave, and 1 wave, respectively. The added phase errors and the shear averaging corrections for these three examples are shown in Figures 9-4, 9-6, and 9-8. For these plots we added an inconsequential constant to the phase-error estimate in order to better compare it with the added phase error. The difference between the two curves is the residual phase error left by shear averaging. In all three cases the small residual phase error has negligible impact on image quality. The smearing in the z direction caused by the phase error, most evident in the one-wave case shown in Figure 9-7(a) in the X projection, is completely corrected by shear averaging. The corrected images, shown in columns (b) of Figures 9-3, 9-5, and 9-7, match the ideal images, shown in columns (c), very well.

When we implemented shear averaging in the straightforward way, without linear trend removal, we found that the results were not as good as we had hoped. This was due to the way that phase errors effect the bias term in PRISM images. Figure 9-9 shows a PRISM signal history with an added linear phase error of 1/4 wave. This example shows two things. First, because of the bias subtraction step, the PRISM processor as it is currently implemented is sensitive to linear phase errors, unlike most other sensors, which are generally insensitive to linear phase errors. The linear phase error does not cause a smearing of the image, but in the PRISM sensor it does cause the imperfect subtraction of the bias term. Second, we see an illustration of the fact that shear averaging cannot correct linear phase errors. Figure 9-10 shows the added linear error and the phase error estimated by shear averaging.

Figure 9-11 shows an example of shear averaging without linear trend removal. In it we attempted to correct a 1/4 wave quadratic error like that in Figure 9-3, but did not remove the linear component from the phase-error estimate. The plot of the added phase error and the estimated phase error in Figure 9-12 shows that shear averaging can sometimes introduce large linear phase

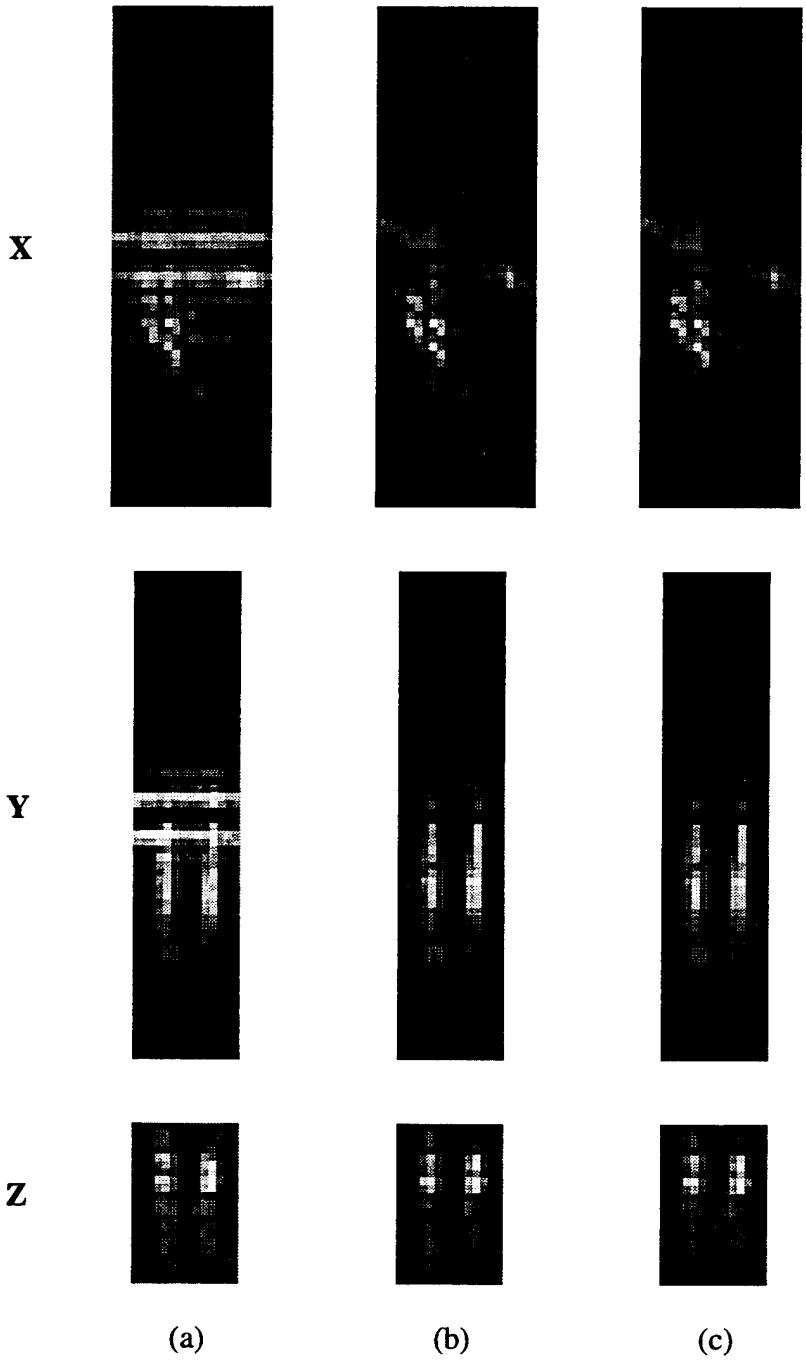

Figure 9-3: The result of applying shear averaging to a PRISM signal history with a peak quadratic phase error of 1/4 wave. The images in column (a) are the 2-D projections of the PRISM 3-D image with the added error. Column (b) shows the projections after correction by shear averaging. The images in (c) are the ideal unaberrated projections for comparison.

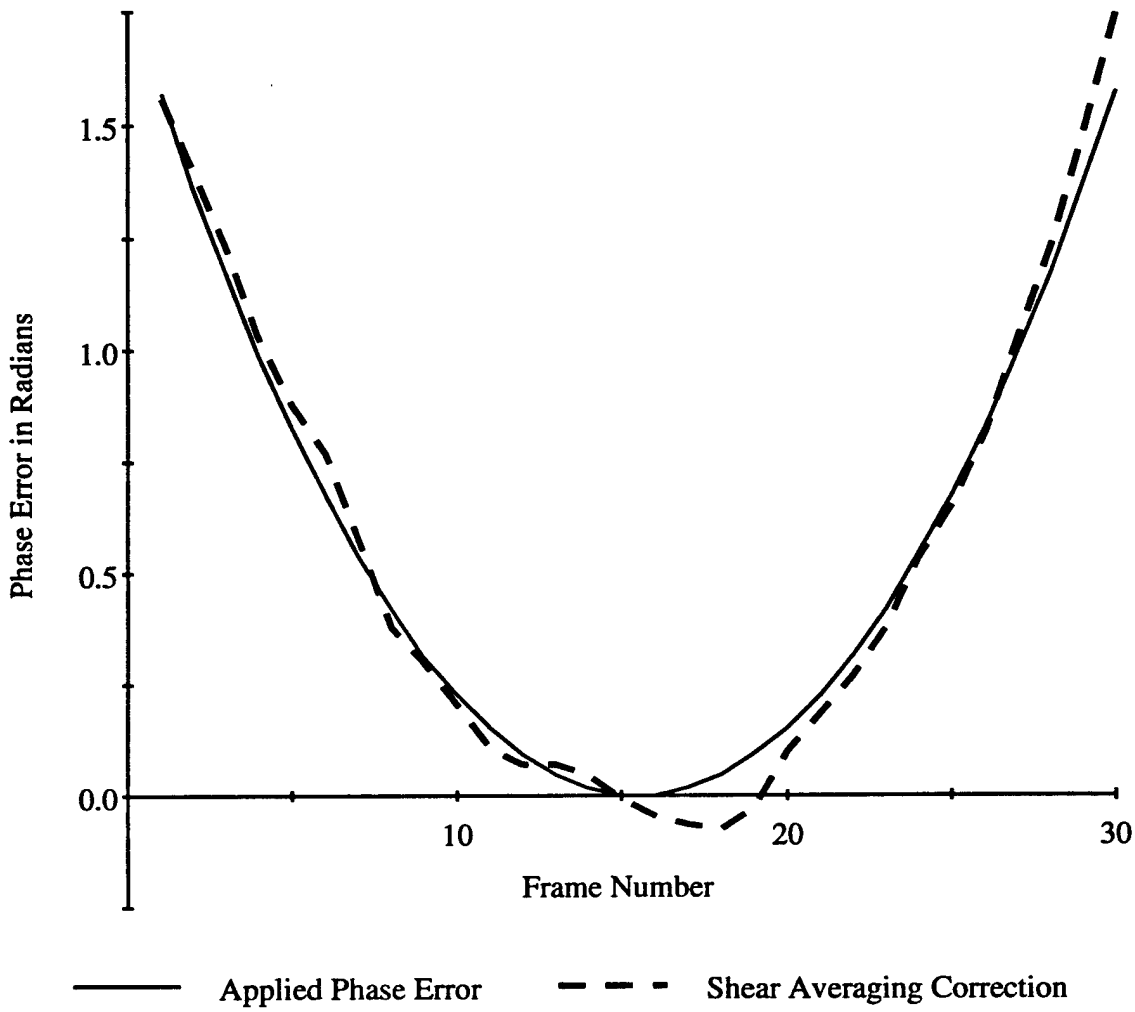

Figure 9-4: Applied phase error vs. shear averaging correction for 1/4 wave peak quadratic error.

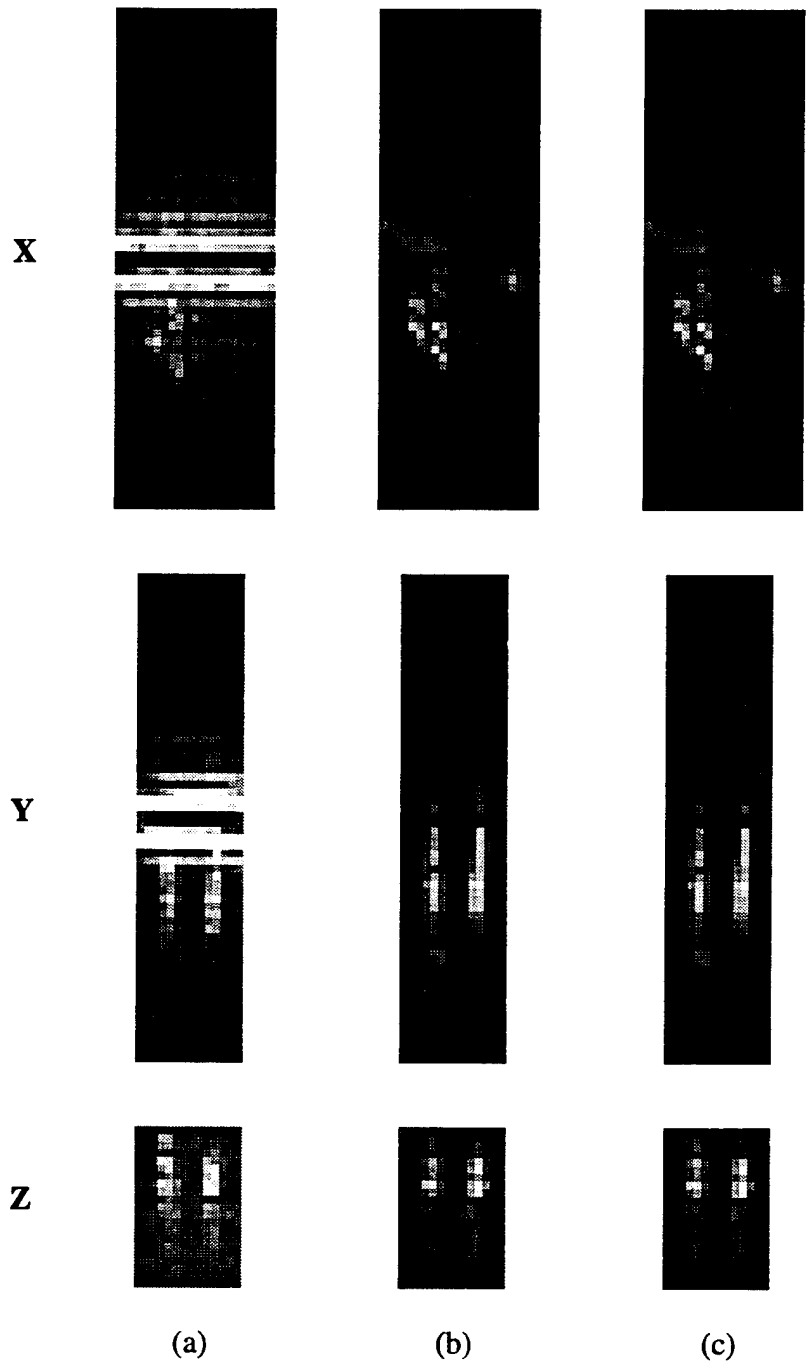

Figure 9-5: The result of applying shear averaging to a PRISM signal history with a peak quadratic phase error of 1/2 wave. The images in column (a) are the 2-D projections of the PRISM 3-D image with the added error. Column (b) shows the projections after correction by shear averaging. The images in (c) are the ideal unaberrated projections for comparison.

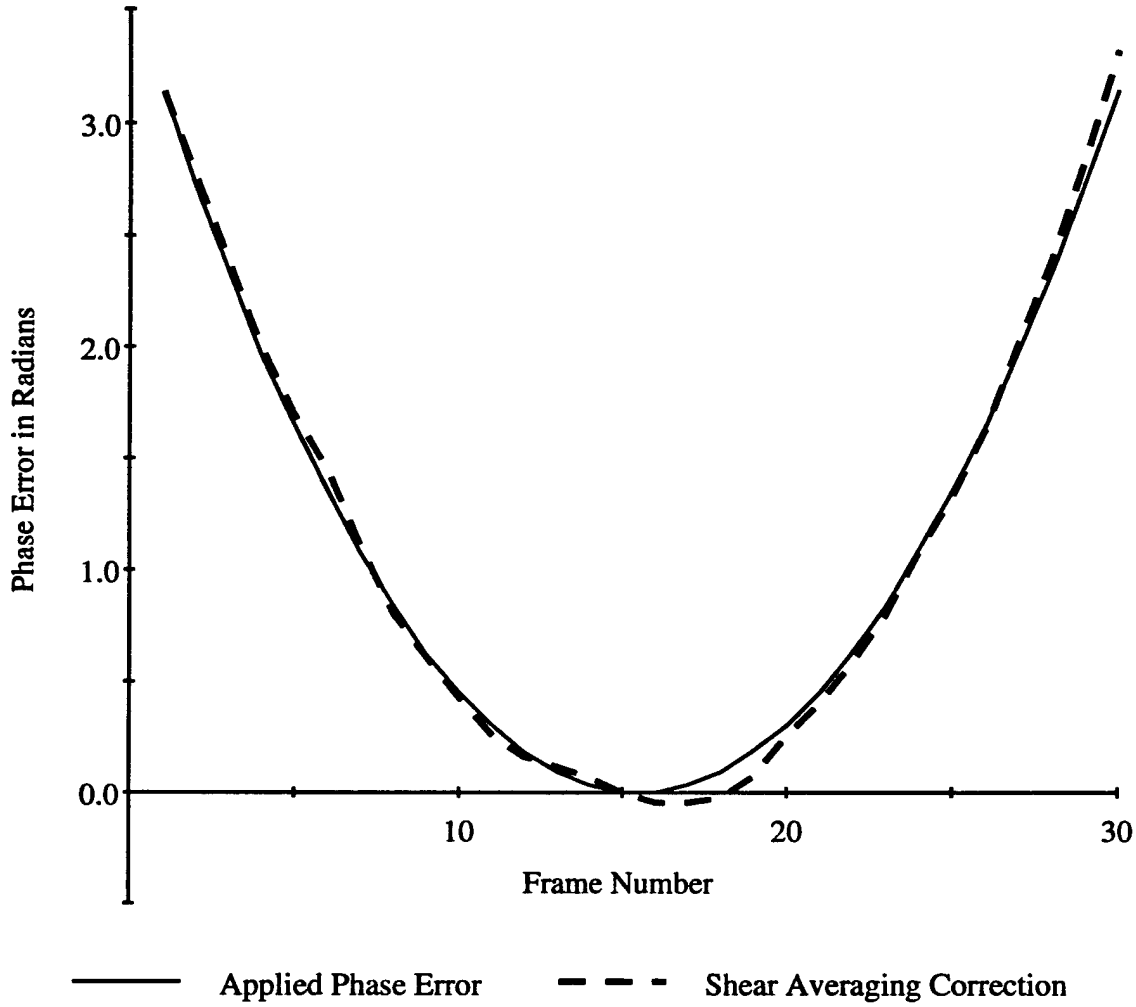

Figure 9-6: Applied phase error vs. shear averaging correction for 1/2 wave peak quadratic error.

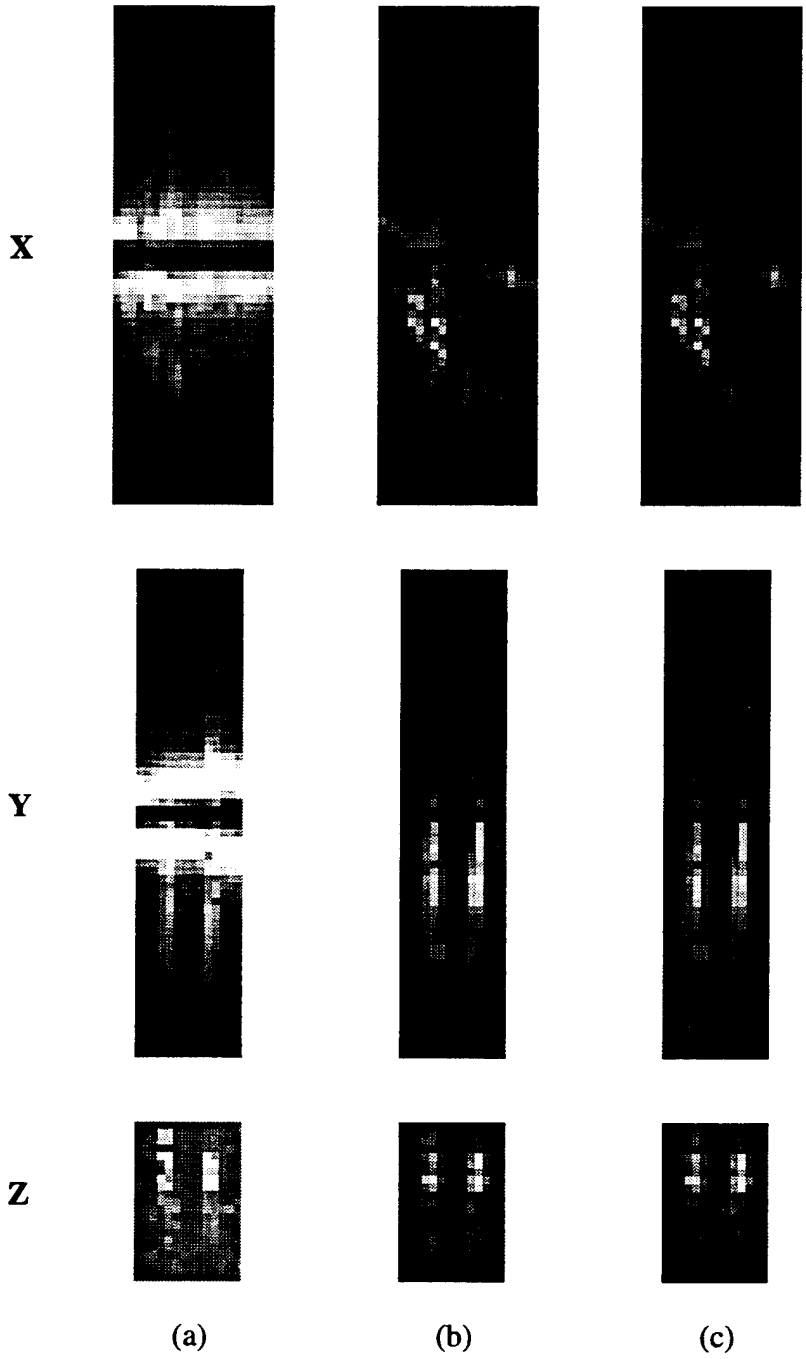

Figure 9-7: The result of applying shear averaging to a PRISM signal history with a peak quadratic phase error of one wave. The images in column (a) are the 2-D projections of the PRISM 3-D image with the added error. Column (b) shows the projections after correction by shear averaging. The images in (c) are the ideal unaberrated projections for comparison.

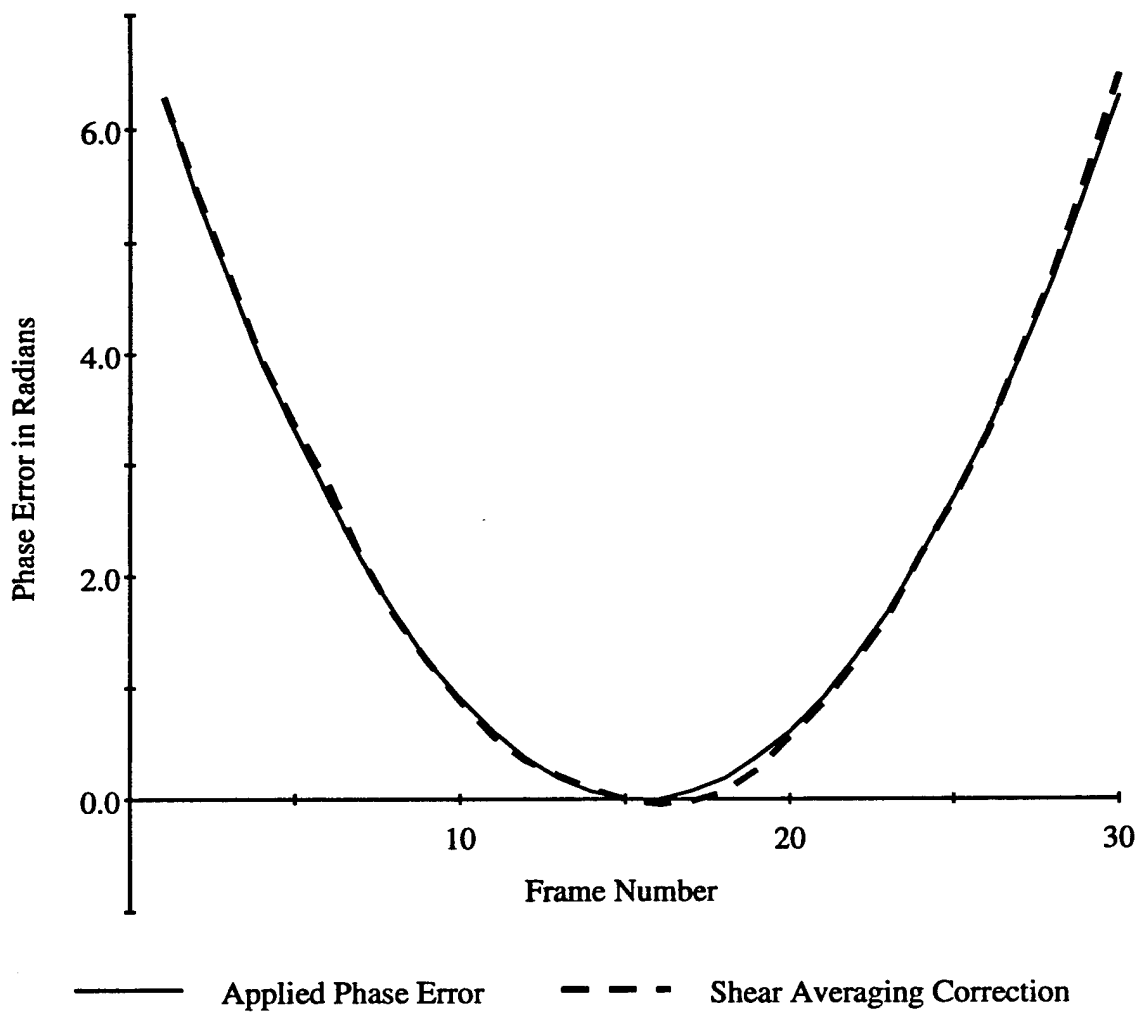

Figure 9-8: Applied phase error vs. shear averaging correction for 1 wave peak quadratic error.

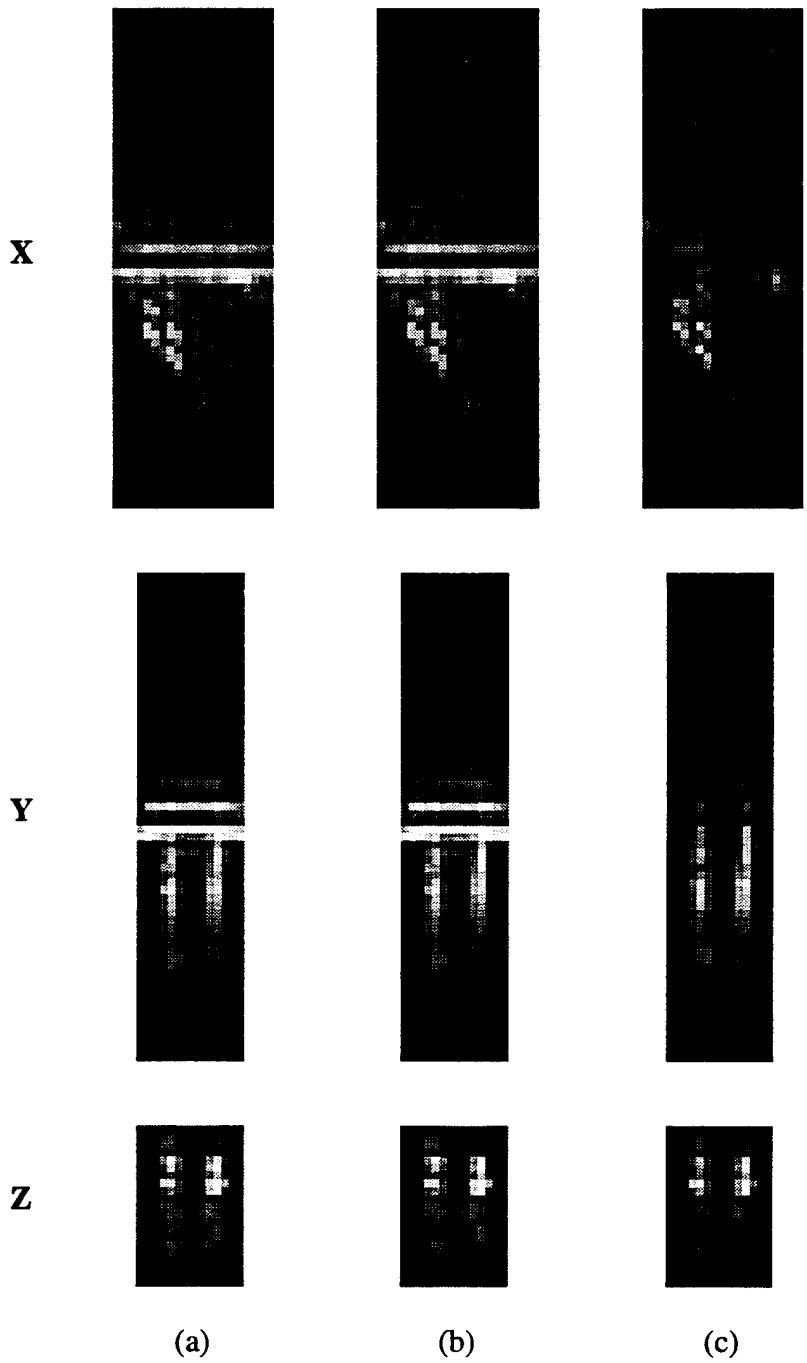

Figure 9-9: The result of applying shear averaging to a PRISM signal history with a peak linear phase error of 1/4 wave. The images in column (a) are the 2-D projections of the PRISM 3-D image with the added error. Column (b) shows the projections after correction by shear averaging. The images in (c) are the ideal unaberrated projections for comparison.

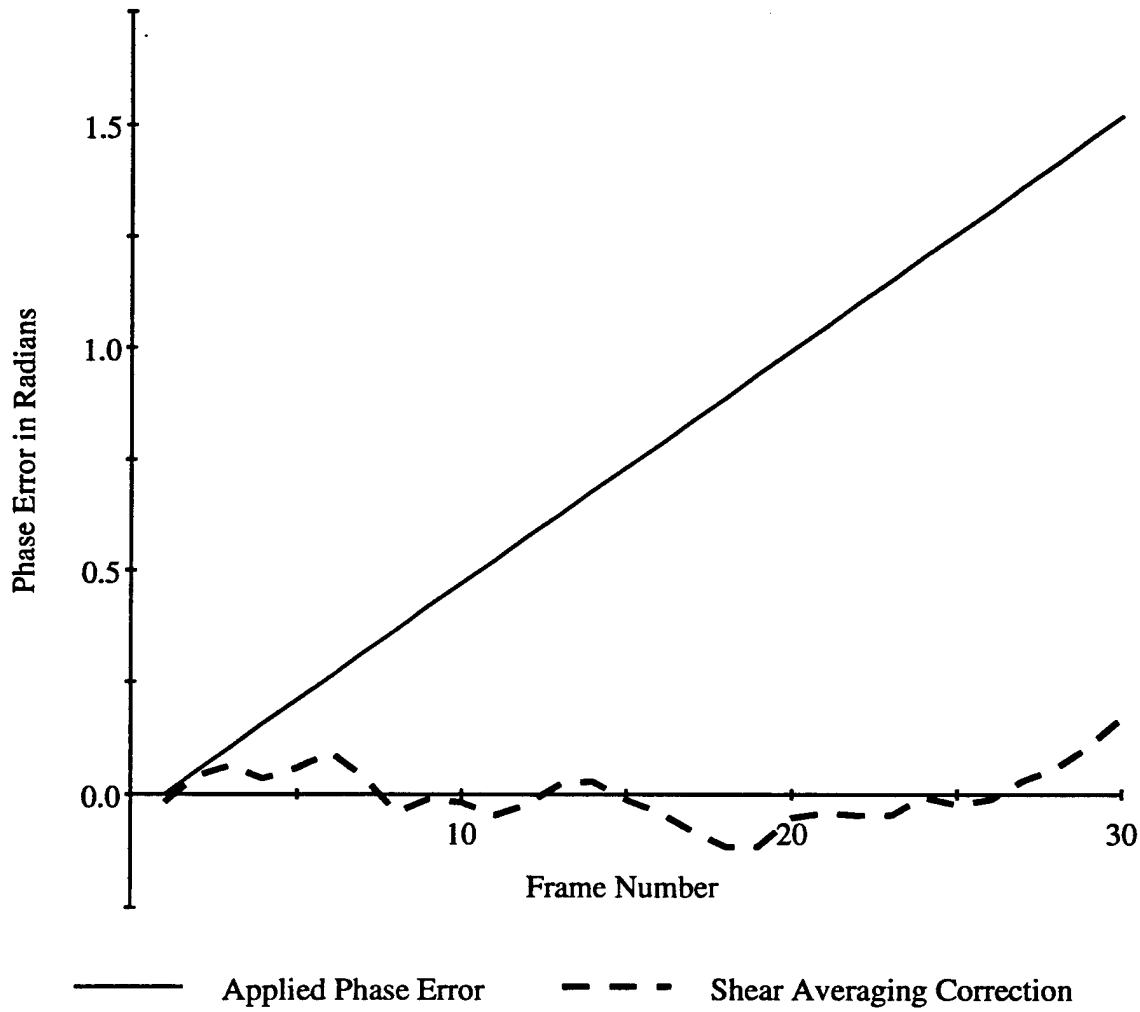

Figure 9-10: Applied phase error vs. shear averaging correction for 1/4 wave peak linear error.

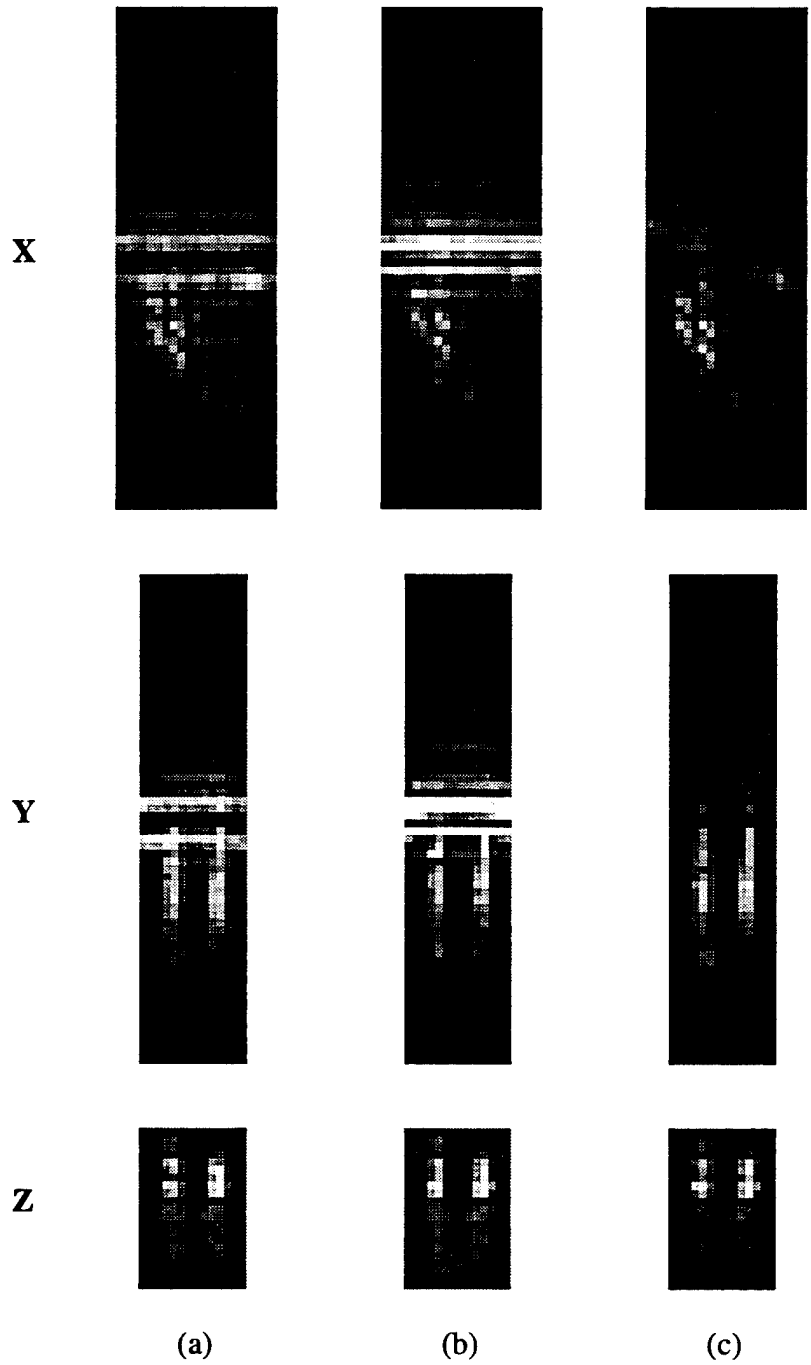

Figure 9-11: The result of applying shear averaging without linear trend removal to a PRISM signal history with a peak quadratic phase error of 1/4 wave. The images in column (a) are the 2-D projections of the PRISM 3-D image with the added error. Column (b) shows the projections after the attempted correction by shear averaging. The images in (c) are the ideal unaberrated projections for comparison.

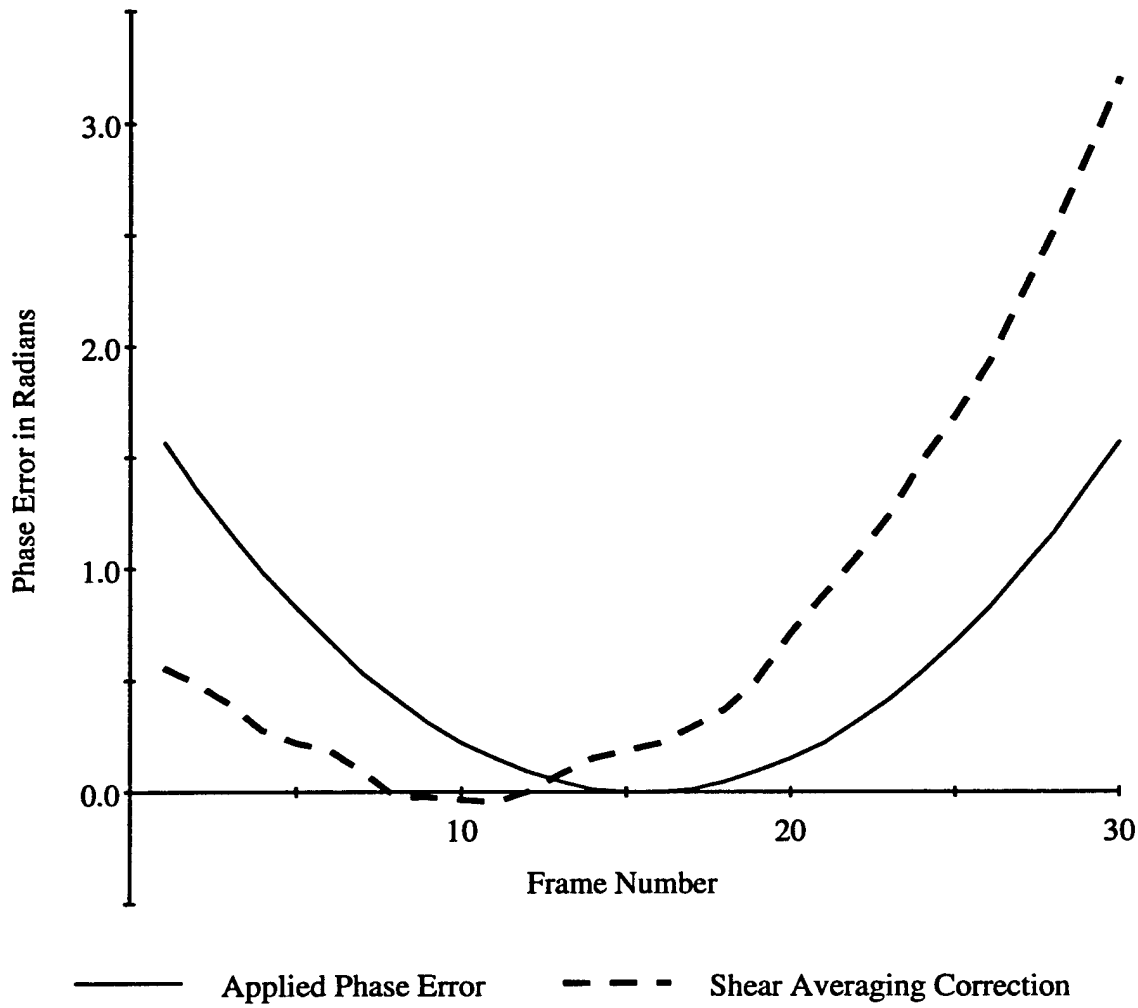

Figure 9-12: Applied phase error vs. shear averaging correction without linear trend removal for 1/4 wave peak quadratic error.

errors. We first tried simply subtracting the line drawn between the first and last values of the estimated phase error samples, but this did not adequately remove the trend from the 1-wave quadratic example. It proved better to do the trend removal with a regression algorithm. Note from Figure 9-9 that trend removal does not help shear averaging to correct linear phase errors; it merely keeps shear averaging from changing the linear component of the error. We conclude that linear trend removal by regression analysis is an essential part of the shear averaging algorithm for correcting PRISM phase errors. This was the technique we successfully used to correct the phase errors the images shown in Figure 9-3, 9-5, and 9-7.

9.6 REFERENCES

[9.1] J.R. Fienup, "Phase Error Correction by Shear Averaging," in Signal Recovery and Synthesis III, digest of papers 14-16 June 1989, N. Falmouth, MA, (Optical Society of America, 1989), pp. 134-137.

10.0 COMPARISON OF PRISM VS. MOTION STEREO

This section offers a comparison of the passive 3D imaging capabilities of PRISM relative to advanced algorithms based on motion stereo. It is shown that the relative performance depends somewhat strongly on the scene spatial content. In fact, the techniques appear to be complimentary in that PRISM works well with some targets (e.g., camouflage nets) for which stereo fails, and vice-versa. After reviewing the motion stereo algorithm considered, we provide here the results of both an analytical comparison of depth (range) estimation precision, and an empirical comparison of 3D imaging based on real visible and infrared data.

10.1 DESCRIPTION OF THE MOTION STEREO ALGORITHM

Motion stereo is based on the idea that the image location of an object point changes predictably as a camera is moved. The magnitude of this displacement is related to the distance from camera to object. If the camera motion is known, this distance can be estimated by measuring the displacement of an object from frame to frame, then calculating the distance which would result in such a displacement. This process will be described in further detail later.

A particular collection geometry of interest is shown in Figure 10-1. In this case, the camera rotates to track a reference point while moving along a straight path. The i-th image is collected from a location which is distance B_i from the first camera position ($B_1 = 0$). It is assumed that the camera is oriented so the vertical image axis is perpendicular to the direction of camera motion. A total of N frames, $f_i(x, y)$, $i = 1, 2, \ldots, N$ are collected.

Assuming the geometry described above, a point at distance z from the baseline will be shifted by $d_i = B_i F(z^{-1} - z_r^{-1})$ in the i-th frame, where z_r is the distance to the reference point, F is the focal length of the lens, and displacement is measured relative to the point's location in the first frame. Based on this result, the i-th image is modeled as:

$$f_i(x, y) = f(x - B_i F[z(x, y)^{-1} - z_r^{-1}], y) + n_i(x, y), \tag{10-1}$$

where $f(x, y)$ is the noise-free continuous image seen from the first camera position,

$z(x,y)$ is the distance from the baseline to the object which appears at location (x, y) in image 1, and

$n_i(x, y)$ is zero-mean white Gaussian noise, independent from frame to frame.

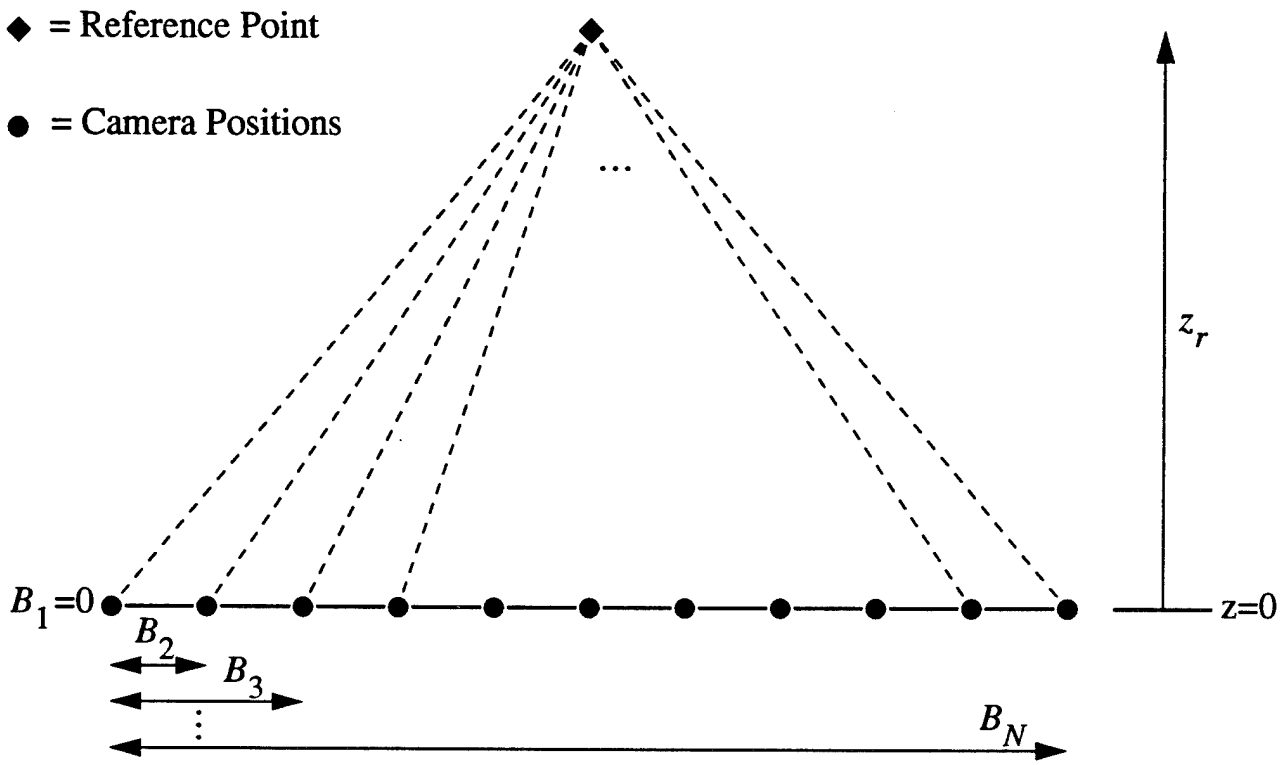

Figure 10-1: Motion stereo data collection geometry

Note that this model does not attempt to account for points which disappear or reappear as the view angle changes. The image shift can be written in terms of inverse distance $\zeta = z^{-1}$, giving the modified image model which will be assumed throughout the rest of this discussion :

$$f_i(x, y) = f(x - B_i F[\zeta(x, y) - \zeta_r], y) + n_i(x, y). \tag{10-2}$$

The motion stereo algorithm we have implemented is based on that proposed by Okutomi and Kanade [10.1]. Given N image frames, P stereo pairs are formed by grouping these images in different ways. The k-th pair is denoted $P_k = (p_{k1}, p_{k2})$, where p_{k1} and p_{k2} are the frame numbers of the two images. Given the desired search range, $\zeta_{min} = z_{max}^{-1}$ to $\zeta_{max} = z_{min}^{-1}$, a set of n_z candidate inverse distances are chosen equally spaced on this interval. Corresponding to each trial ζ is a disparity $d_i(\zeta) = B_i F(\zeta - \zeta_r)$, which represents the distance a point appears to shift from image 1 to image i. For a single stereo pair P_k, we attempt to match each point (x, y) in frame p_{k1} to the corresponding point in frame p_{k2}. Assuming a true constant range ζ_0 in some region W centered at (x, y) in image 1, the image model of Eq. (10-2) indicates $f_{Pk1}(x + d_{Pk1}(\zeta_0), y)$ should match $f_{Pk2}(x + d_{Pk2}(\zeta_0), y)$ within W (ignoring measurement noise). For each trial ζ, the p_{k1}-th image is shifted by $d_{pk1}(\zeta)$, the p_{k2}-th image is shifted by $d_{pk2}(\zeta)$, then the shifted images are compared within W. Image similarity is measured by the sum of squared differences (SSD) given by :

$$e_k(x, y, \zeta) = \sum_{(i,j)\in W} \left(f_{Pk1}(x + d_{Pk1}(\zeta) + i, y + j) - f_{Pk2}(x + d_{Pk2}(\zeta) + i, y + j)\right)^2. \tag{10-3}$$

To estimate distance based on the single pair P_k, $\zeta_{opt}(x, y)$ is chosen to minimize the SSD (3) at each location, then $z(x, y) = \zeta_{opt}(x, y)^{-1}$. To combine range information from multiple stereo pairs, the algorithm estimates $z = \zeta^{-1}$ at each location as that which minimizes the sum of sum-squared differences (SSSD) given by :

$$E_{12...P}(x, y, \zeta) = \sum_{k=1}^{P} e_k(x, y, \zeta) \ . \tag{10-4}$$

This algorithm is a generalization of that proposed by Okutomi and Kanade in the sense that it allows for an arbitrary image pairing scheme, and that the image model has been modified to incorporate camera rotation. The current implementation incorporates two modifications of the

motion stereo algorithm described above. Based on the characteristics of the SSSD curve at each location, an attempt is made to determine where a gross error in the range estimate is likely. Two tests were developed based on empirical observation of SSSD curves in problem areas such as occluded objects or flat intensity regions. The average value of the SSSD curve at each location is required to be above a given threshold. In addition, each side of the curve must rise a minimum percentage above the smallest value. If either test is failed, no estimate is made (defaults to $z = z_r$).

10.2 ANALYTICAL COMPARISON

In this section, we compare the abilities of motion stereo and the PRISM sensor to produce dense 3-D maps of terrain-type scenes from an aircraft looking nominally downward. We assume that for effective target detection we need a depth measurement at every pixel, i.e., a dense 3-D map. Consequently we are interested only in stereo methods such as that just described that work on a pixel-by-pixel basis rather than feature-based, since feature-based methods only give sparse sampling of the depth. The analysis of motion stereo discussed here derives from [10.1, 10.2, 10.3], as that work appears to represent the state-of-the-art in dense motion stereo (as far as we could tell from a limited literature search and from discussions with some of the authors). The analysis of PRISM derives from the sensor signal model discussed throughout this report.

The metric for comparison is the theoretical depth estimation precision. For this comparison, we assumed that we collect the motion stereo image data through an aperture of diameter d_a and detect with a CCD array with pixels of size Dx, whereas PRISM uses two apertures, each of size d_a, separated (center-to-center) by a distance s and detect with the same CCD array as motion stereo. (The conclusions would change if we were to assume, for example, that the motion stereo sensor uses a phase-aligned segmented optical system having two apertures, each of diameter d_a, separated by s.)

10.2.1 Motion Stereo Depth Estimation Precision

As described in Section 10.1, in motion stereo one measures the disparity of the position of a feature in two or more images taken from different camera positions. The disparity, d, in image space is equal to the baseline (the distance between two camera positions) times the focal length of the optics divided by the distance from the camera to the feature: $d = BF/z$. Hence by measuring d, and knowing B and F, one can determine the distance (or depth or height) z. The precision of the depth estimate is given in terms of its standard deviation. For two-frame stereo, the standard deviation of the depth estimate is (as derived in [10.4])

$$\sigma_z = \frac{\sqrt{2}\,\sigma_n\,\Delta x_{obj}}{\Delta\theta\,\sqrt{J/r}\,\sigma_L} \tag{10-5}$$

where

σ_L = the rms per-pixel spatial derivative (in the direction of motion) of the measured irradiance

σ_n = rms noise per image pixel

Δx_{obj} = detector pixel size in object space

$\Delta\theta$ = angular subtense of baseline

J/r = number of detector pixels integrated for depth estimate.

For the special case of an irradiance step of magnitude DL in the x direction (the direction of motion of the camera) in the center of a pixel, the irradiance for three successive pixels is L – DL/2, L, and L + DL/2 and the irradiance derivative is DL/(2Dx). Then, as derived in [10.4], we can express the standard deviation of the depth estimate as

$$\sigma_{z(N=2\ \text{stereo})} = \frac{2\sqrt{2}\,\Delta x_{obj}\,\sigma_n}{\Delta\theta\,\Delta L\,\sqrt{J/r}} = \frac{2\sqrt{2}\,\Delta x_{obj}}{\Delta\theta\ \text{SNR}\ \sqrt{J/r}} \tag{10-6}$$

where SNR $= \Delta L/\sigma_n$. For the special case of photon noise, this expression becomes

$$\sigma_{z(N=2\ \text{stereo})} = \frac{\Delta x_{obj}}{\Delta\theta}\,\frac{2\sqrt{2}}{\sqrt{N_B}\sqrt{J/r}}\,\frac{L}{\Delta L} \tag{10-7}$$

where L is the average irradiance and N_B is the number of photons per detector element per frame.

In areas where the depth changes rapidly, to avoid smoothing the depth estimate we would expect to use a value of J/r of a small number of detector pixels. For a fair comparison with PRISM, for which no such averaging is performed, we should use J/r = 1. (If J/r > 1, then for a fair comparison the depth estimate from PRISM would have to be averaged over J/r detector pixels, in which case its standard deviation would be reduced by $\sqrt{J/r}$ as well.) Note that for the SNR, $\sigma_n/\Delta L$, we take the signal to be the local variations in the image intensity (or the derivative of the image intensity) rather than the image intensity itself.

The standard deviation for the depth estimate for N-frame motion stereo is

$$\sigma_{z(N\text{-stereo})} = \Omega\ \sigma_{z(N=2\ \text{stereo})}\ , \tag{10-8}$$

where

Ω ≥ 1, or $= 1$, or $= \sqrt{6N/[(N+1)(N+2)]} \approx \sqrt{6/N}$ for $N >> 1$

N = number of frames.

The uncertainty in the value of Ω results as follows. Using the method of [10.2, 10.3], obtaining the factor $\Omega = 1$ requires noise in the depth measurements that is perfectly correlated, which may not be realistic, and so achieving $\Omega = 1$ may be difficult in practice. The possibility has been raised [10.2, 10.3] that N-frame motion stereo will give depth estimates with precision (standard deviation) that is about $\sqrt{6/N}$ times that obtainable from a single stereo pair with the longest baseline. At this time, however, there is considerable uncertainty as to whether this improved precision is realizable. Consequently, in what follows, we carry the factor Ω which is unknown for motion stereo, but probably is somewhere between unity and $\sqrt{6/N}$. Note that multiple frames are always valuable, and probably necessary, to resolve ambiguities and increase robustness (which is important for stereo) even if they do not improve precision.

10.2.2 PRISM Depth Estimation Precision

As shown earlier in this report, the Cramer-Rao lower bound for PRISM on the standard deviation of the depth estimate is given by

$$\sigma_{z(\text{CR-PRISM})} = \frac{\sqrt{3}}{\pi} \rho_z \frac{1}{SNR_{3d}} = \frac{\sqrt{3}}{\pi} \rho_z \frac{1}{\sqrt{N\, N_B}} \frac{L_B}{m_s L_S} \tag{10-9}$$

where

L_S = the signal in the interferometer passband

L_B = the signal in the low-pass image (essentially same as L for stereo)

m_s = factor of signal modulation depth (≤ 1) due to limited achromaticity, etc.

SNR_{3d} = signal-to-noise ratio through the system passband

and the height resolution is given by

$$\rho_z = \frac{h\lambda}{s\,\Delta\theta}, \tag{10-10}$$

h = altitude of sensor

s = shear distance (center-center spacing between PRISM apertures)

and where the right-most expression is for the case of photon noise. It has been reported that the actual performance of the PRISM depth estimate is comparable to the Cramer-Rao lower bound, and so this expression approximates the actual performance.

10.2.3 Comparison of Depth Estimation Precision

From Equations (10-5) and (10-9), it can be seen that the depth estimation precision is dependent on scene spatial contrast. An extreme example is a sinusoidal pattern given by $L_1(r) = b + c\cos(2\pi f_0 x)$, with spatial frequency, f_0, falling within the PRISM passband. In this case, the PRISM sensor can have an accurate depth estimate while motion stereo fails completely.

Probably a better case for which to compare PRISM and motion stereo is for the case of an edge. Let us assume that there is an irradiance step of size ΔL centered in the middle of a pixel over a small range of viewing angles. Then the irradiance for three successive pixels is $L - \Delta L/2$, L, and $L + \Delta L/2$. In this case, the depth precision of PRISM is given by [10.5, 10.6]

$$\sigma_{z(\mathrm{PRISM})\mathrm{edge}} = \frac{\Delta x_{obj}}{\Delta\theta} \frac{\sqrt{6}}{\sqrt{N\,N_B}\,m_s} \frac{L}{\Delta L} \quad . \tag{10-11}$$

where photon noise was assumed. Then the ratio of the precisions is given by (for J/r =1)

$$\frac{\sigma_{z(\mathrm{N\text{-}stereo})\mathrm{edge}}}{\sigma_{z(\mathrm{PRISM})\mathrm{edge}}} = 2\Omega \frac{\sqrt{N}}{\sqrt{3}} m_s \quad . \tag{10-12}$$

If N-frame stereo can really get its theoretical performance of $\Omega \approx \sqrt{6/N}$, and if PRISM also has ideal performance with $m_s = 1$, then this expression becomes

$$\frac{\sigma_{z(\mathrm{N\text{-}stereo})\mathrm{edge}}}{\sigma_{z(\mathrm{PRISM})\mathrm{edge}}} = 2\sqrt{2} \, , \tag{10-13}$$

that is the performance of PRISM has a ($2\sqrt{2} \approx 2.8\times$) advantage over N-frame motion stereo for the case of an edge. If in practice $\Omega \approx 1$ and $m_s \approx 1$, then PRISM would have a large advantage; but if $\Omega \approx \sqrt{6/N}$ and $m_s << 1$, then motion stereo would have a decided advantage.

For the most general scene, when photon-limited, the expressions for the precision of the two methods are, grouping terms for easier comparison,

$$\sigma_{z(\text{N-stereo})} = 2\sqrt{2}\,\Omega \frac{\Delta x_{obj}}{\Delta\theta} \frac{1}{\sqrt{N_B}\sqrt{J/r}} \quad \frac{L}{2\sigma_L} \tag{10-14}$$

$$\sigma_{z(\text{CR-PRISM})} = \frac{\sqrt{6}}{\sqrt{N}m_s} \frac{\Delta x_{obj}}{\Delta\theta} \frac{1}{\sqrt{N_B}} \quad \frac{h_o\lambda}{s\Delta x_{obj}} \frac{L_B}{L_S\pi\sqrt{2}} \tag{10-15}$$

$$\frac{\sigma_{z(\text{N-stereo})}}{\sigma_{z(\text{PRISM})}} = 2\sqrt{2}\left(\frac{m_s\Omega}{\sqrt{J/r}} \frac{\sqrt{N}}{\sqrt{6}}\right)\left(\frac{\sigma\Delta x_{obj}}{\lambda h}\right)\left(\frac{\pi}{\sqrt{2}} \frac{L_S}{\sigma_L}\right) . \tag{10-16}$$

The four groups of factors can be interpreted as follows. The first factor of $2\sqrt{2}$ is the advantage PRISM has over stereo for the case of an edge. We obtain this factor of $2\sqrt{2}$ by choosing to include the factor $(\pi/\sqrt{2})$ multiplying L_S/σ_L in the last factor above. The factor $[m_s\Omega/\sqrt{J/r}]$ $[\sqrt{N}/\sqrt{6}]$ includes all the terms that together would be unity if each of the two systems operated ideally. The factor $(\lambda h/\Delta x_{obj}s)$ is the spatial frequency of the interferometer passband relative to the spatial frequency $1/\Delta x_{obj}$, where Δx_{obj} is the resolution of the camera/detector in object space without regard for the interferometer. So the factor $(s\Delta x_{obj}/\lambda h)$ goes as the inverse of the spatial frequency of the PRISM passband. The factor $(\pi/\sqrt{2})$ (L_S/σ_L) is proportional to the strength of the signal within the interferometer passband relative to the strength of the signal in the low-pass image. It depends on how the scene's spatial power spectrum drops off as a function of spatial frequency. For an image spatial power spectrum that varies as $1/(\text{frequency})^2$ [then the square root of its spatial power spectrum falls off as 1/(frequency)], (L_S/σ_L) is proportional to $(\lambda h/\Delta x_{obj}s)$. In that instance the factor $(s\Delta x_{obj}/\lambda h)$ times the factor $(\pi/\sqrt{2})$ (L_S/σ_L) is a constant, independent of the location of the interferometer passband.

Figure 10-2 illustrates these terms. The height standard deviation of PRISM is inversely proportional to the product of three terms: (1) the linear term (the straight line rising from the origin), given by $(s\Delta x_{obj}/\lambda h)$, (2) the power spectrum of the object, and (3) passband of the interferometer (the hump centered about the passband frequency $s/\lambda h$). The second and third of these factors together form the term L_S. For the special case of an edge, the square root of the spatial power spectrum falls off as 1/frequency, as illustrated by the curve that falls from right to left. If the square root of the spatial power spectrum falls off more slowly than 1/(frequency), then PRISM would further outperform stereo relative to the case of an edge; on the other hand, if the

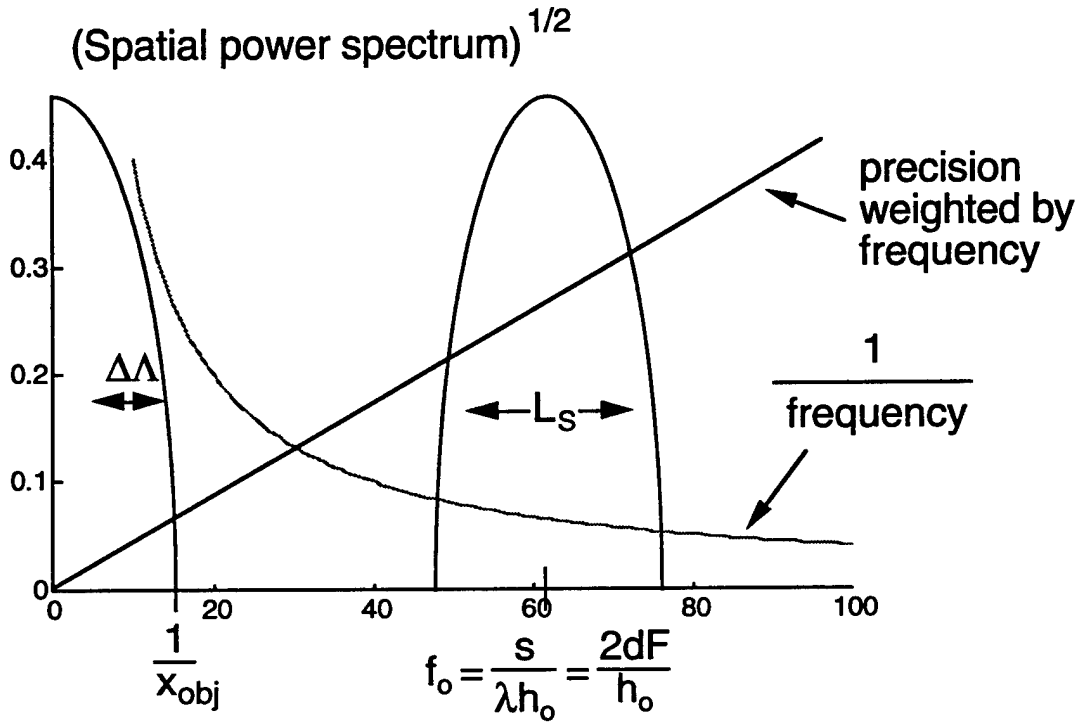

Figure 10-2: Factors in height precision in the spatial frequency domain.

square root of the power spectrum falls off significantly faster than 1/(frequency), then stereo would outperform PRISM relative to the case of an edge.

Examples are as follows. For an ideal edge oriented in the direction of the PRISM bandpass, the square root of the power spectrum drops as 1/(frequency) and the two approaches are related as described in the analysis of an edge given above. For a scene that reveals little additional detail with increased resolution, for example, if all the edges were "soft" relative to Δx_{obj}, then stereo would have superior depth precision. For a scene having a relatively smooth image as seen at a resolution of Δx_{obj}, but having considerable detail that is resolved by the length-s baseline, PRISM would have superior depth precision. Consequently PRISM is best suited for situations in which there exists unresolved detail, as might be the case for targets with camouflage nets.

10.2.4 Multiple Depth Scenario

For certain scenarios, for example targets under camouflage nets or the "deep hide" scenarios in which tree branches above a target may partially obscure it, each image pixel may have two or more depths within it. The ability to determine both depths may be important for determining the type of target that is underneath a partially transparent net or to detect a target partially obscured by overhead tree branches. It is unclear how motion-stereo would be able to sense multiple depths within a pixel. It might be done, for example, by looking for multiple correlation peaks. On the other hand, the ability of PRISM to sense multiple depths within a single pixel has been demonstrated [10.7].

These differing abilities arise from a fundamental difference between stereo and PRISM. Stereo explicitly attempts to determine a single number, the depth, to associate with each 2-D pixel. This is accomplished by determining the depth that corresponds to a disparity (translation) that gives the best match between two images taken at different angles. PRISM, on the other hand, explicitly determines the scene reflectivity at a collection of 3-D pixels, or voxels (volume picture elements). In a subsequent step we can determine a depth at each 2-D pixel by determining the depth coordinate which has the maximum 3-D image intensity. Alternatively we can estimate multiple depths, for example, by calculating all depth coordinates for which the 3-D image intensity exceeds some threshold. When the need arises for determining multiple depths within a pixel, which may often be the case for camouflaged and partially hidden targets, PRISM might hold a decisive advantage over stereo.

10.3 EMPIRICAL COMPARISON

Since the results of the analytical comparison demonstrated a significant sensitivity of both the PRISM and motion stereo techniques to imaged scene structure, we decided to empirical compare approaches based on a subjective assessment of 3D imaging performance for common scene data. The results are presented here, and are based on input data from a prior visible laboratory PRISM demonstration [10.7] as well as a midwave infrared field PRISM demonstration [10.8].

Three data sets were processed using the motion stereo techniques described in the previous section. The first set, titled "TEST2", is a visible test target consisting of several blocks and various other objects on a flat background, as shown in the top image of Figure 10-3. The second, titled "SCENE2", is a sequence of visible images of a realistic terrain board, shown in Figure 10-4. Finally, the infrared collection "RUN25" from the second Kinzua field data collection was processed. One of these frames is shown at the top of Figure 10-5.

10.3.1 Motion Stereo Processing

The stereo processing parameters used in each case are summarized in Table 10-1. Whenever possible, an attempt was made to match the parameters used during previous PRISM processing. Several clarifications and miscellaneous parameters not given in Table 10-1 are listed below:

- The "Okutomi method" of image pairing was used throughout, i.e. each frame is paired with frame 1 for a total of $P = N - 1$ stereo pairs.
- We allow the SSD window W to be sampled on a finer grid than the digital image. However, these data sets showed no noticeable improvement in range estimates when oversampling was incorporated.
- Only the "TEST2" data set showed significant improvement when thresholding and ratio testing of the SSSD error metric were incorporated.
- The SSSD threshold values listed in Table 10-1 are scaled internally by the number of samples in the SSD window W, and by the number of image pairs P.
- Camera motion was from right to left in each case.
- The detector width for the "RUN25" data set is twice that of the physical detector since stereo processing was applied to subsampled images.
- Heights are all measured relative to the reference point.

Intentionally Left Blank

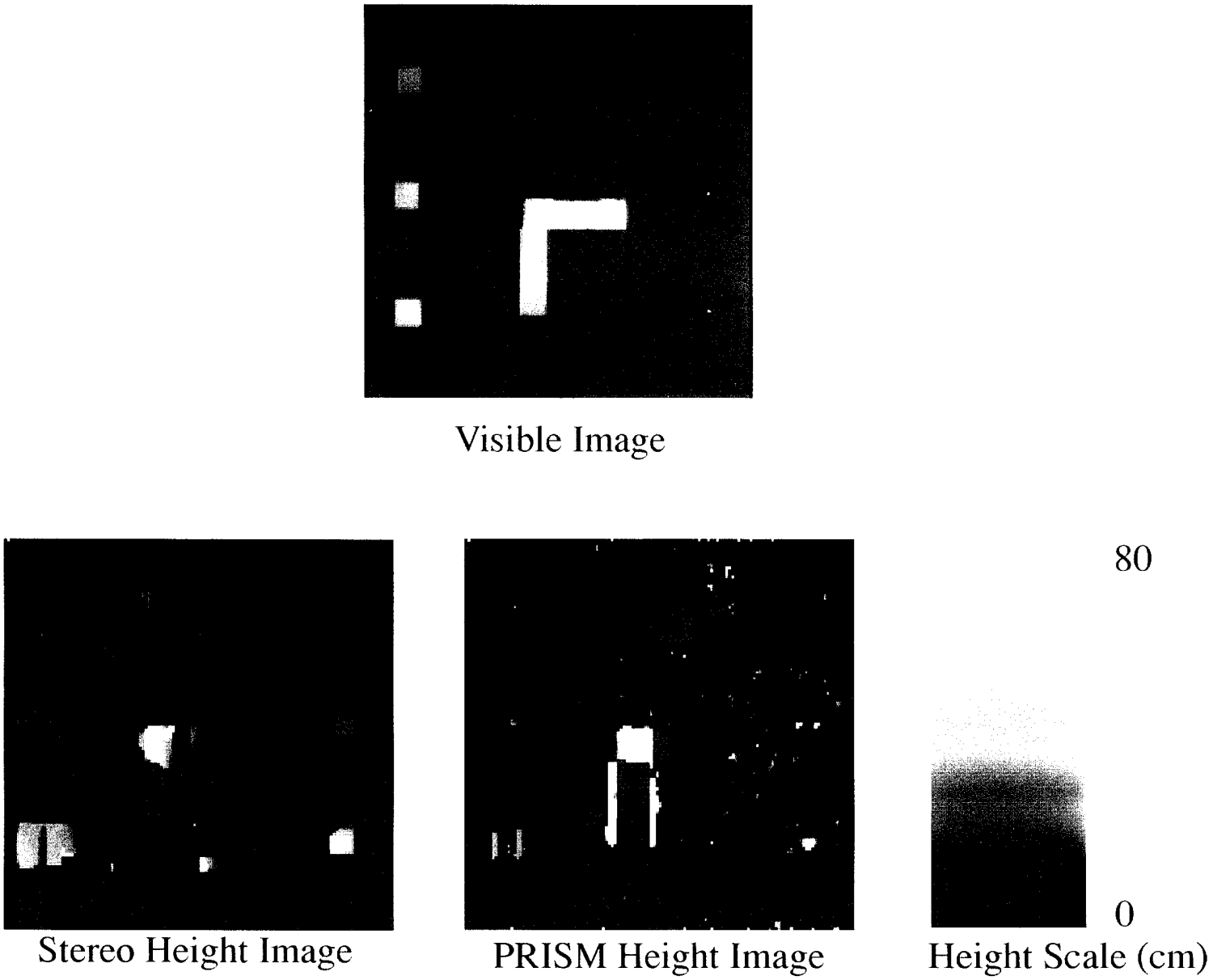

Figure 10-3: Comparison of PRISM and motion stereo imagery for TEST2 data set

Visible Image

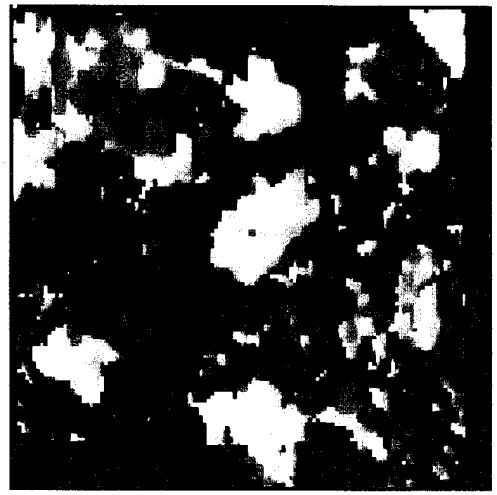

Stereo Height Image

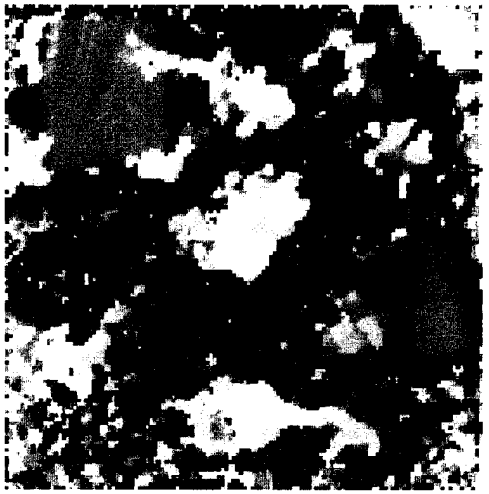

PRISM Height Image

Height Scale (cm)

Figure 10-4: Comparison of PRISM and motion stereo imagery for SCENE2 data set

Contrast-Enhanced Thermal Image

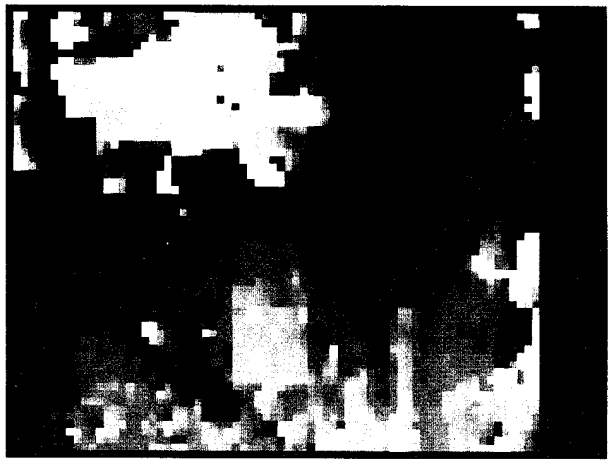

Stereo Height Image

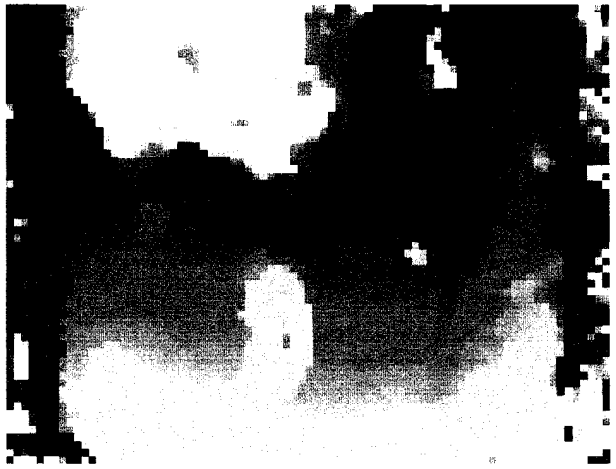

PRISM Height Image

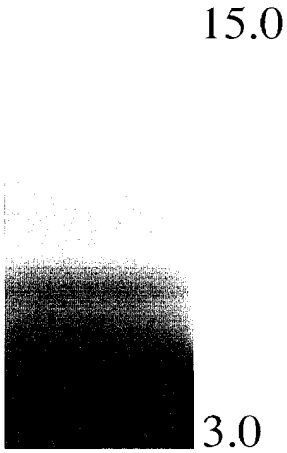

Height Scale (m)

Figure 10-5: Comparison of PRISM and motion stereo imagery for RUN25 data set

Table 10-1: Collection and Processing Parameters

\ Common Parameters	TEST2 (Blocks)	SCENE2 (Terrain Board)	RUN25 (Truck at Kinzua)
Number of Frames	128	128	60
Focal Length (mm)	35	35	25
Detector Pixel Width (μm)	16	16	100
Image Size (rows x cols)	128 x 128	128 x 128	60 x 80
Distance to Reference Pt. (m)	25.0	25.0	100.59
Stereo Parameters			
Window Size (pixels)	5 x 5	3 x 3	3 x 3
Oversampling Rate	1 x 1	1 x 1	1 x 1
Camera Spacing (mm)	29.2	29.2	292.2
Minimum Height (m)	0.0	0.045	3.03
Maximum Height (m)	0.8	0.4	15.0
Number of Height Bins	128	128	80
SSSD Threshold	8000	N/A	N/A
SSSD max/min ratio	1.1	N/A	N/A
Some Relevant PRISM Parameters			
Minimum Height (m)	0.0	0.045	0.0
Maximum Height (m)	0.8	0.4	15
Number of Height Bins	128	128	100
Scale : m / bin	0.00630	0.00279	0.151
Minimum Bin Used	0	0	20
Maximum Bin Used	127	127	99
Threshold	175	0	0
Median Filter Kernel Size	3 x 3	3 x 3	3 x 3

- No post processing (e.g. median filtering) of the height maps is employed. No improvement was seen when a median filter was applied to stereo height maps.

10.3.2 PRISM Processing

A PRISM height map was also generated for each of the three scenes described previously. These were obtained by peak range extraction from processed 3-D PRISM image data. The height at each location (x, y) was determined by the z position of the maximum signal strength over a specified range. If this maximum did not exceed a specified threshold, no estimate was made (set to bin 0). Range bins were converted to heights by scaling and biasing. Median filtering was applied to lessen noise in the height maps. Parameters associated with each of these steps are listed in Table 10-1.

10.3.3 Results and Comparisons

Figures 10-3, 10-4, and 10-5 illustrate the resulting stereo and PRISM height maps for the three data sets. Each is color-coded to indicate height relative to the reference point, as indicated on the scale in each figure. Before proceeding to make some comparisons, it is necessary to point out a fundamental difference between the range maps produced by the two algorithms. The current implementation of motion stereo calculates the range to each point in the scene as viewed from the first camera position. The PRISM images show range to each point in the scene as viewed from the central viewing angle. As a result, objects may appear to be in slightly different locations in the two height maps. While there is a difference in viewing angle, range is calculated as the normal distance from object to baseline in each case.

Both algorithms had some trouble with the "TEST2" data set, especially with the flat background and the vertical edges of the blocks. Much of the apparently flat background in the height maps of Figure 2 corresponds to regions where neither algorithm made an estimate (height set to 0 by default). The failure of stereo in flat intensity regions is due to the fact that there is no contrast to drive the stereo matching algorithm; the SSSD is small in amplitude and very flat. Anomalous behavior at edges is not surprising, considering the image model completely ignores occlusions (it is difficult to match to something which disappears). The PRISM image is most notably in error at the centers of the plain blocks (which fall outside the sensor passband), and at the vertical edges of the vertical row of blocks. The stereo image does show all the interesting objects in the scene, but tends to blur them out, exaggerating their size. The PRISM image seems to be missing the tree in the upper left portion altogether, while the tank is non-recognizable unless

one knows it is there. While the background of the PRISM image has a noisy appearance, the map of Figure 10-3 shows much improvement over the non median filtered version.

Figure 10-4 shows stereo and PRISM height maps for the "SCENE2" data set. There are a few notable differences here. PRISM is certainly superior in detecting the presence of the two nets in the upper left corner and on the right edge slightly below center. These were designed to lie in the PRISM passband, but have detail too fine to be resolved by stereo. The truck on the road shows up clearly in the stereo image, while that in the PRISM image is obscured by noise. The lower tank is seen in the PRISM image only, while the upper is detectable in both. The PRISM image suffers most noticeably from noisy height estimates, while the most objectionable feature of the stereo image is the presence of large height errors, such as at the edges of the trees.

Figure 10-5 shows height maps of a truck near trees, corresponding to "RUN25" of the data taken from a railroad bridge at Kinzua, PA. The PRISM image shows two small objects to the right of the truck and trees, neither of which appear in the stereo image. It appears the upper object is indeed present in the scene, but is missed entirely by stereo, while the lower object is an artifact in the PRISM image. The trees are tallest in the middle according to the stereo image, while the PRISM image shows a depression in the center of the trees. It is not clear which is closer to the true shape of the trees, but the drastic height change indicated by the PRISM image seems unlikely. The ground slope appears smooth in the PRISM image, while it is rough and irregular in the stereo image. Again, it is not clear what the true height profile is, but the amplitude fluctuations in the stereo image are larger than would be expected. As in the previous data set, the stereo image exhibits some smoothing throughout and poor performance at the edge of the trees. Both images exhibit occasional spurious height peaks.

10.3.4 Conclusion

We have demonstrated the ability of motion stereo to produce range information from a sequence of infrared images. Three data sets were processed in order to qualitatively compare the range estimation performance of PRISM and stereo. Several comparisons were made based on these results, but no universal conclusion has been reached regarding the superiority of either algorithm. Empirical results are in agreement with the analytical comparison; that is, the relative performance of these algorithms is shown to depend on scene content (specifically, on the rolloff rate of the spatial power spectrum). In general, it appears PRISM performs better in regions of relatively high spatial frequency, stereo performs better in areas of lower spatial frequency, and neither does well at very low frequencies.

10.4 REFERENCES

[10.1] M. Okutomi and T. Kanade, "A Multiple-Baseline Stereo," IEEE Trans. PAMI 15, 353-363 (1993)

[10.2] L. Matthies, T. Kanade and R. Szeliski, "Kalman Filter-based Algorithms for Estimating Depth from Image Sequences," International J. Computer Vision 3, 209-236 (1989).

[10.3] L. Matthies, R. Szeliski and, T. Kanade "Kalman Filter-based Algorithms for Estimating Depth from Image Sequences," Image Understanding Workshop, pp. 199-213 (1989).

[10.4] J. Fienup, "Comparison of Motion Stereo and PRISM, "ERIM internal memo OSL-93-7541, August 2, 1993.

[10.5] J.P. Mills, J.D. Gorman and M.T. Eismann, *PRISM System Requirements (U)*, ERIM Report No. 240400-15-F to WL/AARI-2, December 1992 (SECRET).

[10.6] D.C. Rife, "Single-Tone Parameter Estimation from Discrete-Time Observations," IEEE Trans. Info. Theory IT-10, 591-598 (1974).

[10.7] I. Cindrich, M.T. Eismann, J.P. Mills, B.D. Neagle, K.S. Schroeder and A.M. Tai, *PRISM Sensor Technology Development for Passive 2-D and 3-D Imaging (U)*, ERIM Report WL-TR-92-1041, September 1992 (CONFIDENTIAL).

[10.8] *PRISM Ground Experiment*, ERIM Final Report No. 246840-1-F to Air Force WL/AARI on Contract DLA900-88-D-0392, Delivery Order 38, March 1995.